

# Characteristics of Upward Lightning Flashes

THÈSE N° 7988 (2018)

PRÉSENTÉE LE 26 JANVIER 2018  
À LA FACULTÉ DES SCIENCES ET TECHNIQUES DE L'INGÉNIEUR  
GROUPE SCI STI FR  
PROGRAMME DOCTORAL EN GÉNIE ÉLECTRIQUE

ÉCOLE POLYTECHNIQUE FÉDÉRALE DE LAUSANNE

POUR L'OBTENTION DU GRADE DE DOCTEUR ÈS SCIENCES

PAR

Mohammad AZADIFAR

acceptée sur proposition du jury:

Prof. P. Frossard, président du jury  
Prof. F. Rachidi-Haeri, Prof. M. Paolone, directeurs de thèse  
Prof. M. Rubinstein, rapporteur  
Prof. V. Cooray, rapporteur  
Prof. A. Skrivervik Favre, rapporteuse



ÉCOLE POLYTECHNIQUE  
FÉDÉRALE DE LAUSANNE

Suisse  
2018



To my family







# Abstract

In addition to the general aims of lightning research such as lightning physics and meteorology, the study of upward lightning is of particular importance in protection of tall objects such as wind turbines and telecommunication towers. It also helps us in better understanding the lightning initiation process and its role in the earth-atmosphere electrical balance.

Within this context, this thesis presents an analysis on various aspects of upward lightning discharge (negative, positive, bipolar) using experimental observation and theoretical modeling for better understanding of its initial stage, the propagation of its electromagnetic field along irregular terrain and its interaction with the ionosphere.

The work carried out in this thesis takes advantage of the data obtained at the unique experimental facility of the Säntis tower to study upward lightning discharges of different polarities and the modeling of its environmental electromagnetic effects. The Säntis Tower is a 124-meter tall tower sitting on the top of the Säntis Mountain (2500 M ASL). During this thesis, several important updates have been implemented to the station. These updates include the upgrade of the digitization system and GPS time stamping, installation of overvoltage protection on the GPS Antenna and on the PXI 6682H card, and the deployment of a wideband electric and magnetic field measuring system which was installed in Herisau, about 15 km away from the Säntis tower.

Our investigation on the superimposed impulsive components of the initial stage of upward negative flashes revealed that they can transfer net negative charges to ground by both M-component and return stroke modes of charge transfer, which can be distinguished by their associated electric field signature. Moreover, we investigated the ability of Lightning Location Systems (LLSs) to locate and detect upward negative flashes. Different aspects of upward negative flashes which might

affect the evaluation performance of LLSs were discussed. It is found that LLSs tend to overestimate the peak current values of RS pulses of upward negative flashes. Using full-wave numerical simulation, it is demonstrated that this overestimation is mainly due to electric field enhancement by wave propagation along mountainous terrain around S antis Tower.

Using simultaneous channel-base current and electric field records of upward positive flashes, we observed that two types of pulsations can be distinguished during the course of progression of upward negative leaders which are very similar to “Classical PBPs” and “Narrow PBPs” of the initial stage of downward negative leaders suggesting a general similarity between upward and downward negative leaders.

We present and discuss current waveforms associated with 13 bipolar flashes recorded at the S antis Tower during the period from June 2010 to January 2015. We have found two flashes of our data base each characterized by a sequence of two upward leaders of opposite polarity within the same flash, a scenario that has never been reported from previous observations at instrumented towers. The obtained results suggest that the traditional classification of bipolar flashes should be revisited.

We present simultaneous channel-base current and wideband electric field waveforms at 380 km distance from the strike point associated with upward flashes initiated from the S antis Tower. The dataset presented in this study represents, to the best of the Author’s knowledge, the first simultaneous records of lightning currents and distant fields associated with natural upward flashes featuring ionospheric reflections. The data are used to infer the characteristics of the ionospheric layers. We present a full-wave 2D FDTD analysis of the field propagation including the effect of the ionospheric reflections and the results are compared with the experimental data. Furthermore, we present a novel semi-analytical simplified approach based on the ray tracing concept to estimate radiated electric fields associated with lightning return strokes, taking into account ionospheric reflections.

**Keywords:** Upward Lightning Flash, Tall Towers, Electromagnetic Fields, Lightning Location Systems, Upward Leaders, Earth-Ionosphere Waveguide, Numerical Simulation, Finite Difference Time Domain, Snell’s Law, Ray Tracing.



## Résumé

En plus des objectifs généraux de la recherche sur la foudre tels que la physique de la décharge et la météorologie, l'étude des décharges ascendantes est particulièrement important pour la protection des objets élevés tels que les éoliennes et les tours de télécommunication. Cela nous aide également à mieux comprendre le processus d'initiation de la foudre et son rôle dans l'équilibre électrique terrestre-atmosphérique.

Dans ce cadre, cette thèse présente une analyse des différents aspects de la décharge orageuses ascendante (négative, positive, bipolaire) en utilisant des observations expérimentales et la modélisation théorique pour une meilleure compréhension de son stade initial, la propagation de son champ électromagnétique sur un terrain irrégulier et son interaction avec l'ionosphère.

Le travail effectué dans cette thèse se base sur des données obtenues lors de l'installation expérimentale unique de la tour de Säntis pour étudier les décharges orageuses de différentes polarités et la modélisation de ses effets électromagnétiques. La tour de Säntis est une tour de 124 mètres de haut située au sommet du mont Säntis (2500 M ASL). Au cours de cette thèse, plusieurs mises à jour importantes ont été effectuées dans la station. Ces mises à jour comprennent l'amélioration et la modernisation du système de numérisation et l'horodatage GPS, l'installation de la protection contre les surtensions sur l'Antenne GPS et sur la carte PXI 6682H et le déploiement d'un système de mesure de champ électromagnétique et à large bande qui a été installé à Herisau à une distance d'environ 15 km de la tour Säntis.

Les études sur les composants impulsifs superposés au stade initial des éclairs négatifs ascendants a révélé qu'ils peuvent transférer des charges négatives nettes au sol par les modes de transfert de charge 'M-component' et arc-en-retour, qui

peuvent être distingués par leur signature de champ électrique associé. En plus, nous avons étudié la capacité des systèmes de localisation de la foudre à localiser et à détecter des éclairs négatifs ascendants. Différents aspects des éclairs négatifs ascendants qui pourraient affecter les performances de tels systèmes ont été discutés. Nos études ont montré que les systèmes de détection ont tendance à surestimer les valeurs de courant maximal des arcs-en-retour des éclairs négatifs ascendants. En utilisant des simulation numériques, il est démontré que cette surestimation est principalement due à l'amplification du champ électrique en se propageant le long d'un terrain montagneux autour de la Tour Sântis.

En utilisant des enregistrements simultanés de courant à la base du canal et de champ électrique des éclairs positif ascendants, nous avons observé que deux types de pulsations peuvent être distingués au cours de la progression des leaders négatifs ascendants qui sont très similaires aux "PBP classiques" et aux "PBP étroits" de la phase initiale des leaders négatifs, suggérant une similitude générale entre les leaders négatifs ascendants et descendants.

Les formes d'ondes associées à 13 décharges bipolaires enregistrées à la tour Sântis pendant la période de Juin 2010 à Janvier 2015 sont présentées et discutées. Deux des éclairs bipolaires enregistrés sont caractérisés chacun par une séquence de deux leaders ascendants de polarité opposée, un scénario qui n'a jamais été signalé par des observations antérieures dans les tours instrumentées. Les résultats obtenus suggèrent que la classification traditionnelle des éclairs bipolaires devrait être revisitée.

Nous présentons des mesures simultanées de courant de foudre et de champ électrique large-bande à 380 km de distance du point d'impact associé aux éclairs ascendants initiés à partir de la Tour Sântis. Les données présentées dans cette étude représente, à notre connaissance, les premiers enregistrements simultanés des courants d'éclair et des champs associés à des éclairs naturels ascendants présentant des réflexions ionosphériques. Les données sont utilisées pour déduire les caractéristiques des couches ionosphériques. Nous présentons une analyse FDTD en 2D de la propagation des ondes en tenant compte de l'effet des réflexions ionosphériques et les résultats sont comparés aux données expérimentales. En plus, nous présentons une nouvelle approche semi-analytique simplifiée basée sur le concept de 'ray-tracing' pour estimer les champs électriques rayonnés par la foudre en tenant compte des réflexions ionosphériques.

**Mots-clés:** Décharges Orageuses Ascendantes, Tours élevées, Champ Electromagnétique, Systèmes de Localisation de la Foudre, Leaders Ascendants, Earth-Ionosphere Waveguide, Simulation Numérique, Différence de Temps Fini Domaine, La loi de Snell, Ray Tracing.



# Acknowledgements

It is a great pleasure for me to thank the people who helped me throughout these years in this short note, whom without their generous help and supports it was quite impossible to make this amazing journey.

First of all, I would like to express my deepest gratitude to my supervisors Prof. Farhad Rachidi and Prof. Mario Paolone.

Indeed, my words would come to shortage if I want to truly thank Farhad for his excellent personality, vast knowledge, kindness and endless supports which made my PhD life a wonderful experience.

To Mario for his hard working spirit, intelligence and creative ideas, whom his presence always inspired not only me, but all ELL family members to work hard and efficient.

I would like to deeply thank Prof. Marcos Rubinstein, one of the most brilliant people I ever met in my life, for the scientific collaboration, all fruitful discussion we had and his amity. A big thank deep from my heart.

My sincere gratitude goes to Prof. Vladimir Rakov, Dr Gerhard Deindorfer, Dr. Wolfgang Schulz, Hannes Pichler, and Dr. Keyhan Sheshyekani for their advice, support and scientific collaboration. Exclusive thanks goes to Dr. Carlos Romero, for the Sántis instrumentation legacy, his excellency and warm friendship. Thanks Azizam!

I would like to address my heartfelt thanks to Dr. Stefan Metz, Dr. Dongshuai Li, Dr. Mirjana Stojilovic, Dr. Abraham Rubinstein and Dr. Arturo Mediano for the fruitful collaborations that we had in these four years and I hope to do more in future.

To Prof. Hesamoldin Sadeghi and Prof. Rouzbeh Moini and Dr. Parisa Dehkhoda, my supervisors during my Master project at AUT for their constant help, support and encouragement. I am deeply grateful to Mrs. Andrée Moinat, Mrs. Eulalia Durussel and Mrs. Sophie Flynn secretaries of the Laboratory, for all their constant availability, sympathy, and kindness. Merci Andrée, Eulalia, et Sophie!

I would like to thank as well our colleagues from Swisscom, Swisscom Broadcast, Armasuisse, and Huber&Suhner, whom kindly supported us during this project. I would like also to acknowledge the Swiss National Science Foundation (Project 200021\_147058) for funding this dissertation.

My time at EPFL was made enjoyable by an amicable environment in the laboratory. Tremendous thanks to all the members of ELL building for the friendly atmosphere and the priceless moments (listed without order): Dr. Rachid Cherkaoui, Jean-Michel Buemi, Dr. Pierre Zweigacker, Dr. Chen Xi, Dr. Daniel Gazzana, Dr. Alexander Smorgonskiy, Dr. Nicolas Mora, Dr. Gaspar Lugrin, Dr. Paolo Romano, Dr. David Beccera, Amirhossin Mostajabi, Lixia He, Zhaoyang Wang, Dr. Stela Sarri, Dr. Omid Alizadeh Mousavi, Dr. Mokhtar Bozorg, Dr. Mostafa Nick, Dr. Maryam Bahramipناه, Dr. Dimitri Torregrossa, Dr. Marco Pignati, Dr. Lorenzo Reyes, Dr. Lorenzo Zanni, Dr. Georgios Sarantakos, Lydie Magnone, Dr. Fabrizio Sossan, Asja Derviskadic, Emil Namor, Asia Codino, Enrica Scolari, Yihui Zho, Hossein Sekhavatmanesh, Mohsen Kalantar, Andreas Kettner, Andrea Polini, and Sylvain Robert.

During my stay in Lausanne, I was fortunate to meet wonderful people with whom I have shared incredible moments. Here, I would like to thank my special friends in Lausanne for their friendship, supports, and kind helps; Masoume, Mohammad, Mohsen, Samira, Mahbube, Elahe, Leili, Sina, Mina, Majid, Arizu, Farhang, Saba, Bitra, Elham, Mahsa, MohammadReza.

Last but not least, my deepest and forever thanks to my beloved parents (Goli and Alireza) for their dedication and many years of support, for their endless love and infinite patience and compassion, they were my best teachers. I wish to express my heartfelt thanks to my brother, Hamed, his beloved wife Narjes, my dearest Dornika, my sister Haniyeh and her husband Hooman.

*Lausanne, October 25, 2017*

Mohammad Azadifar

## Table of Contents

|          |  |           |
|----------|--|-----------|
| <b>1</b> | <b>Introduction.....</b>   | <b>9</b>  |
| 1.1      | Lightning Phenomenology .....  | 9         |
| 1.1.1    | Cloud Electrification Process .....                                  | 10        |
| 1.1.2    | Different Phases of Discharge (Avalanche, streamer, and leader)..... | 11        |
| 1.2      | Types of Lightning Discharge.....                                    | 12        |
| 1.2.1    | Downward Negative Flashes.....                                       | 13        |
| 1.2.2    | Upward Negative Flashes .....  | 14        |
| 1.2.3    | Downward Positive Flashes .....                                      | 14        |
| 1.2.4    | Upward Positive Flashes .....  | 15        |
| 1.3      | Lightning Observation .....  | 15        |
| 1.3.1    | Instrumented Towers.....   | 16        |
| 1.3.2    | Triggered Lightning .....  | 18        |
| 1.3.3    | Lightning Location Systems (LLSs) .....                              | 19        |
| 1.4      | Objectives of the Thesis .....                                       | 19        |
| 1.5      | Organization of the Thesis .....                                     | 20        |
| <b>2</b> | <b>Instrumentation.....</b>  | <b>23</b> |
| 2.1      | Introduction.....  | 23        |
| 2.2      | Säntis Tower and Initial Instrumentation .....                       | 23        |
| 2.3      | Upgrades .....   | 26        |
| 2.4      | Wideband Electromagnetic Field Station.....                          | 27        |
| 2.5      | Far-Distance Electric Field Sensor.....                              | 30        |
| 2.6      | Field Mill.....  | 32        |
| 2.7      | European Cooperation for Lightning Location Detection (EUCLID) ..... | 33        |
| 2.8      | Conclusion .....   | 34        |
| <b>3</b> | <b>Upward Negative Flashes.....</b>                                  | <b>35</b> |
| 3.1      | Introduction.....  | 35        |
| 3.2      | Initial Stage of Upward Negative Flashes.....                        | 37        |
| 3.2.1    | Data .....   | 38        |
| 3.2.2    | Observed ICC Pulses.....   | 40        |

|          |  |            |
|----------|--|------------|
| 3.2.3    | Comparison of RS-Type ICC Pulses and Return Strokes .....  | 44         |
| 3.3      | Ability of LLSs to Detect and Locate Negative Upward Flashes .....   | 50         |
| 3.3.1    | Data Set .....   | 51         |
| 3.3.2    | Detection Efficiency .....   | 52         |
| 3.3.3    | Location Accuracy .....  | 55         |
| 3.3.4    | Peak Current Estimation.....   | 61         |
| 3.4      | Lightning Electromagnetic Field Propagation along Mountainous Terrain .....  | 62         |
| 3.4.1    | FDTD Modeling Scheme .....   | 63         |
| 3.4.2    | Simulation Results.....  | 66         |
| 3.4.3    | Sensitivity Analysis of Parameters .....   | 74         |
| 3.5      | Conclusion.....  | 77         |
| <b>4</b> | <b>Analysis of Upward Positive Flashes .....</b>   | <b>79</b>  |
| 4.1      | Introduction .....   | 79         |
| 4.2      | Recorded Data .....  | 80         |
| 4.2.1    | Type-I Upward Positive Flashes .....   | 81         |
| 4.2.2    | Type-II upward positive flash .....  | 82         |
| 4.2.3    | Downward flashes .....   | 84         |
| 4.3      | Features of Upward Negative Stepped Leader Pulses.....   | 85         |
| 4.3.1    | Observed Characteristics of Individual Pulses .....  | 85         |
| 4.3.2    | Overall waveform characteristics .....   | 88         |
| 4.3.3    | Characteristics of Category A Electric Field Pulses.....   | 91         |
| 4.4      | Comparison Between the Initial Stage of the Current Associated with Upward Positive Flashes and That of Downward Negative Flashes..... | 94         |
| 4.5      | Modeling of Category A Pulses in Upward Positive Flashes.....  | 98         |
| 4.6      | Conclusion.....  | 102        |
| <b>5</b> | <b>Upward Bipolar Flashes .....</b>  | <b>103</b> |
| 5.1      | Introduction .....   | 103        |
| 5.2      | Experimental Observation.....  | 104        |
| 5.2.1    | Current Waveform Belonging to Category I.....  | 105        |
| 5.2.2    | Current Waveforms Belonging to Category II .....   | 108        |
| 5.2.3    | Current Waveforms Belonging to Category III.....   | 110        |



|          |   |            |
|----------|---|------------|
| 5.3      | Suggested Modification to the Traditional Classification of Bipolar Flashes.....                              | 112        |
| 5.4      | Conclusion .....  | 116        |
| <b>6</b> | <b>Lightning Interaction with the Ionosphere .....</b>  | <b>119</b> |
| 6.1      | Introduction.....   | 119        |
| 6.2      | Obtained Experimental Data.....   | 121        |
| 6.3      | Reflection Characteristics of Electromagnetic Field from Ionosphere .....                                     | 125        |
| 6.3.1    | Height of Ionospheric Reflection .....  | 125        |
| 6.3.2    | Variation of the Reflection Height as a Function of Stroke Order.....   | 128        |
| 6.3.3    | Peak Field Versus Peak Current for Groundwave and Skywaves.....   | 128        |
| 6.4      | FDTD Numerical Simulation of Wave Propagation in Earth-Ionosphere Waveguide<br>130                            |            |
| 6.4.1    | Methodology .....   | 130        |
| 6.4.2    | Simulation Results .....  | 133        |
| 6.4.3    | Comparison with Experimental Data .....   | 134        |
| 6.5      | Ray Tracing Approach for Field Calculation of Electromagnetic Field Reflection from<br>Ionosphere Layer ..... | 136        |
| 6.5.1    | General Methodology and Simplifying Assumptions .....   | 137        |
| 6.5.2    | Validation Using FDTD Simulation .....  | 141        |
| 6.6      | Conclusion .....  | 142        |
| <b>7</b> | <b>Conclusions.....</b>   | <b>145</b> |
| 7.1      | Summary and Conclusions.....  | 145        |
| 7.2      | Original Contributions .....  | 148        |
| 7.3      | Future Work: .....  | 149        |
| <b>8</b> | <b>Bibliography .....</b>   | <b>151</b> |



# 1

## Introduction

### Summary

This chapter serves to contextualize the work presented in this thesis, introduce the nomenclature and the objectives of the thesis. In this respect, we first present a brief introduction on the known aspects related to the phenomenology of lightning discharge including the cloud electrification process and various phases of the discharge process. Then, we provide the classification of cloud-to-ground lightning flashes based on the polarity and direction of the leader.

The various means developed along the years to observe the lightning discharge are listed and briefly discussed. Particular attention is given to the use of instrumented tall towers, triggered-lightning and lightning location systems.

At the end of the chapter, we present the objectives and the structure of this thesis.

### 1.1 Lightning Phenomenology

Lightning can be defined generally as a transient discharge which effectively transfers a large amount of charge (up to several hundreds of Coulombs) in between two distant points in a relatively short period of time (less than a second or so). Cumulonimbus clouds with large vertical extent (up to several kilometers) are found to be one of the main cloud structures which can generate lightning discharges [1]. However, in different geographical locations and meteorological conditions, other cloud structures like winter clouds are capable of producing lightning discharges, which show larger horizontal extent rather than vertical extent compared to

cumulonimbus clouds [2], [3]. There are mainly two widely accepted theories of cloud electrification which will be discussed in Subsection 1.1.1.

### 1.1.1 Cloud Electrification Process

Even though the study of cloud microphysics and electrification process began in the early nineteenth century [4], the mechanisms behind charge formation, separation, and accumulation within thunderclouds are still not fully understood.

The most successful mechanism which can explain most observed electrical properties of thunderclouds is the precipitation theory, which is based on simultaneous presence of three phases of water molecule (mixed-phase condition). Heavier particles like graupel move downward due to the gravitational force and collide with lighter particles like ice crystals and smaller precipitation particles which, due to updraft convection, move upward. During these collisions, depending on the surrounding temperature, graupel particles inherit some negative or positive charges and therefore ice crystals gain the opposite polarity [5]. At temperatures higher than  $-15^{\circ}\text{C}$ , graupel particles win positive charges, while at lower temperatures a reverse polarity of charge will be transferred to them. Due to the interaction between downward and upward moving charged particles, three layers of positively charge layer at top, negatively charged layer at the middle, and a lower screening layer of positive charge will be formed (the so-called tripole cloud structure). In addition to that, Krehbiel suggested that positive corona charges accumulated over the ground surface can be transferred to the positive screening layer by updraft convection [6].

Another cloud electrification hypothesis, the deep convection theory, is based on updraft convection of accumulated positive corona charges over the ground surface toward the clouds and their attachment to cloud particles. The positive charges within thunderclouds, attract surrounding negative charges in the air and forms various layers of the charged cloud structure [1].

Figure 1-1 shows the most prominent cloud structure in thunderclouds proposed by Krehbiel [7]. However, it has been established that cloud charge structures could be more complex and that they evolve during the lifetime of thunderstorms [8], [9].

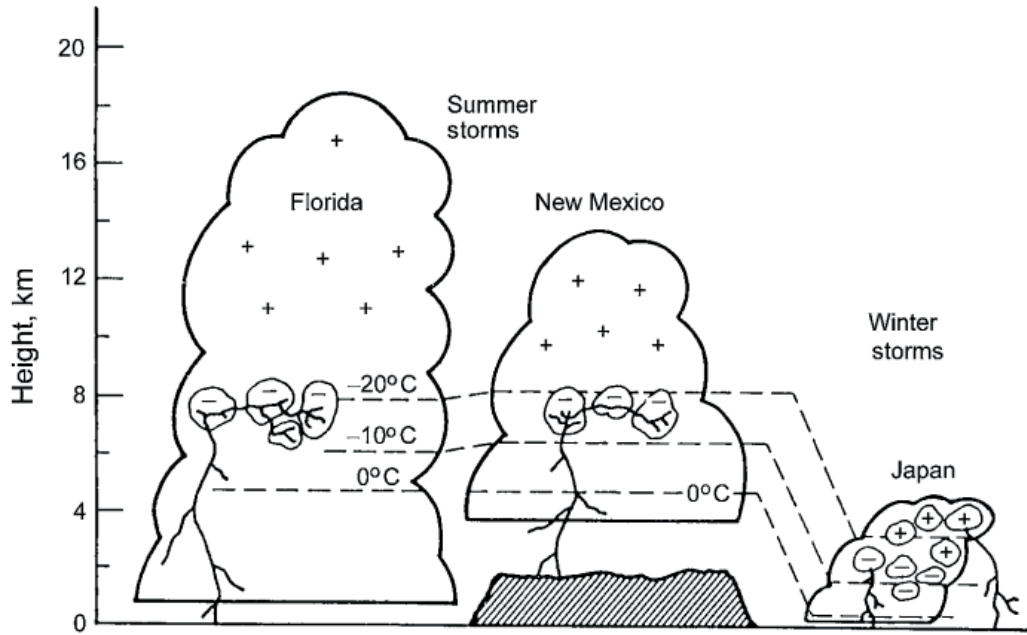


Figure 1-1. Schematic diagram of typical thundercloud structure in different geographical locations [7].

### 1.1.2 Different Phases of Discharge (Avalanche, streamer, and leader)

Relativistic Runaway Electron Avalanche (RREA) was proposed to be the most probable mechanism of initiating lightning discharges in the atmosphere by Gurevich et al. [10]. This theory suggests that the minimum ambient electric field for initiation of lightning (in the so-called breakeven process) is much less than the dielectric breakdown field in the air value ( $3 \times 10^6$  V/m at  $T = 293$  K and  $P = 1$  atm) for the progression of the avalanche at long distances [11]. If the background electric field supports the growth of the avalanche, the electric field at the head of avalanche reaches the air breakdown level, and space charges will start to participate in the ionization process. This phase of the discharge is called streamer [12]. The number of available charged particles for avalanche to streamer transition is estimated to be about  $10^8$ - $10^9$  [13]. The background electric field for positive and negative streamers progression are found to be about  $4.5$ - $6 \times 10^6$  V/m and  $1$ - $2 \times 10^6$  V/m, respectively [14]–[17]. In the streamer phase of discharge, only electrons have the mobility and positive ions are almost stationary with only vibrational movements. However, if the number of available free electrons increases to a certain level, during their collisions to positive ions, they can transfer enough energy to positive ions to make them mobile. The positive ions are massive enough to pass their kinetic energy to neutral atoms, and both of them start to participate in the ionization process (Thermal Ionization). During this process the temperature of electron particles decreases, while positive ions and neutral atoms gain temperature. As a result, all electrons,

positive ions and neutral particles will reach thermodynamic equilibrium and the streamer phase of the discharge develops to create a hot conducting channel [1]. This hot conducting channel is called a leader.

## 1.2 Types of Lightning Discharge

Lightning discharges can be classified by their path of discharge into the following categories [18]:

- Intracloud flashes which occur entirely inside a cloud (IC).
- Cloud-to-cloud (or inter-cloud) flashes which occur between two clouds (CC).
- Cloud-to-ground flashes which occur between a cloud and the ground (CG).
- Air discharge flashes which occur between a cloud and the surrounding air.
- Discharges in the upper and middle atmosphere.

Intracloud flashes (IC) are known to be the most frequent type of lightning discharges which occur in earth atmosphere [1]. Since this kind of lightning flashes occurs inside a thundercloud, mostly remote electric field observations were used to investigate their features. It has been found that IC flashes bridge the gap between middle negative layer of a thundercloud and its upper positive layer [19], [20].

Cloud-to-ground flashes can be classified into four types according to the direction of their initial leader propagation (either upward or downward) and the polarity of effective charge transfer (either positive or negative) [21]. This classification is schematically shown in Figure 1-2. Apart from this conventional classification, an individual lightning flash can transfer both negative and positive charges during its course. This type of lightning discharge is called a bipolar flash, which are as frequent as positive flashes [22].

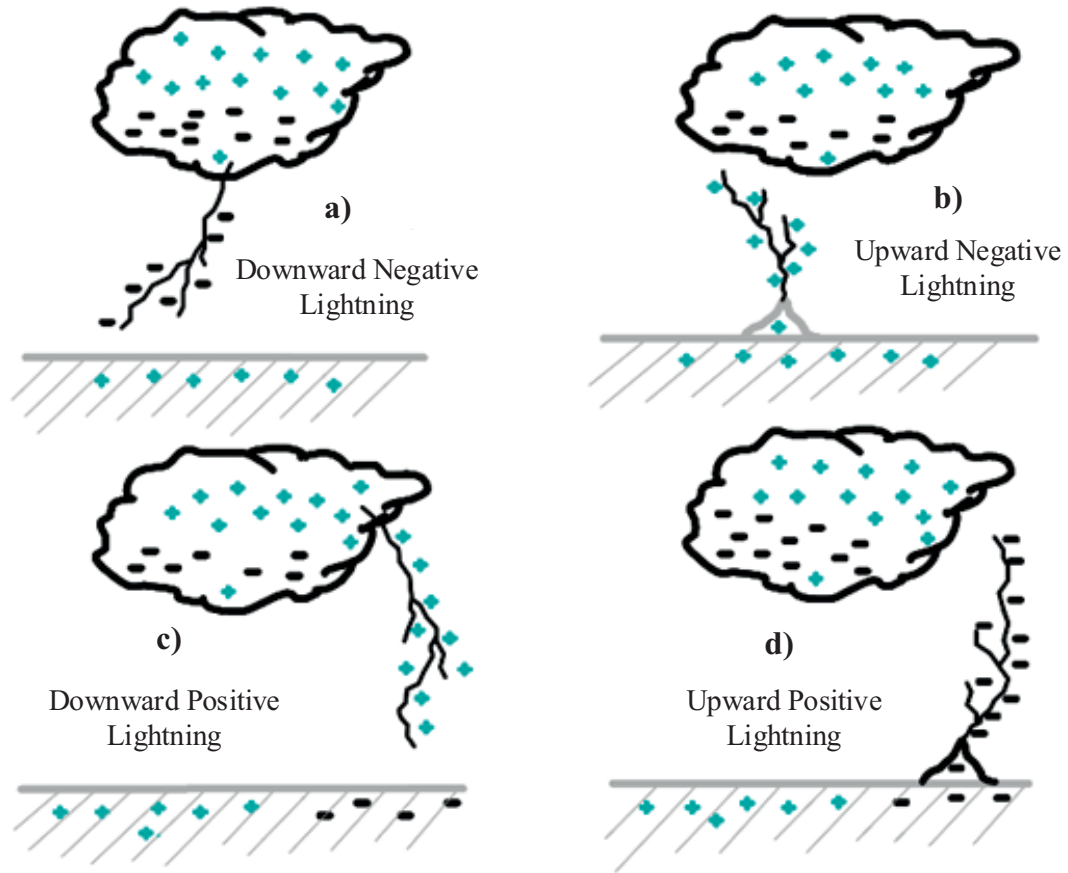


Figure 1-2. Four categories of CG flashes based on the effective polarity of charge transferred to ground and direction of leader (Adapted from [21]).

### 1.2.1 Downward Negative Flashes

Downward negative flashes are the most frequent and well-studied type of lightning discharges [18]. The start of downward negative flashes is usually marked with Preliminary Breakdown Pulses (PBPs), which are a series of downward directed negative breakdowns [23]. These pulses are known to initiate from the main negative charge layer of the thundercloud. Some researchers hypothesized that the presence of the lower positive screening layer is mandatory in the generation of PBPs in downward negative flashes [24], [25], and therefore not all downward flashes include PBPs. However, it has recently been found that PBPs are present in all downward negative flashes [26]. There is an ongoing debate on the charge transfer mechanism of individual PBP pulses, their evolution in time, and their difference from usual downward stepped leader process [27], [28].

After the above-mentioned preliminary discharge, a negative stepped leader is initiated and propagates toward the ground. As the leader tip nears the ground, local electric field at the vicinity of sharp objects enhances, leading to one or more upward

positive connecting leaders [21]. When one of the upward connecting leaders attach to the downward leader (attachment process), available charges deposited along the leaders become neutralized by a ground wave propagating upward with a speed of about half to one-third the speed of light, the so-called first Return Stroke (RS).

If additional charges are available at the top of the channel, one or more dart leader/RS sequences might follow the previously ionized channel to the ground [21].

### 1.2.2 Upward Negative Flashes

Upward negative flashes initiate from tall objects. They occur when the ambient electric field inside thundercloud is not high enough to initiate a negative downward leader [29]. It has been demonstrated that the presence of elevated objects can increase drastically the risk of incidence of lightning discharges [30].

Upward negative flashes initiate with a positive upward leader process which bridges the gap between the grounded object and the cloud [31]. Upward positive leaders were mostly observed to propagate continuously and they are accompanied by a quasi-continuous mode of charge transfer. The upward leader and the associated continuous current form a current signature which is called the Initial Continuous Current (ICC) [18], [32]. Impulsive current pulses can be observed in this stage of discharge, which are called ICC-pulses [33].

After the cessation of the ICC, some downward leader/subsequent return strokes might follow the previously ionized channel [18]. This stage of upward negative flash is quite similar to their downward counterpart [34].

### 1.2.3 Downward Positive Flashes

Although positive downward flashes are found to constitute only about 10% of total downward flashes [22], they are more likely to produce high current strokes with large amount of positive charge transfer to ground. The usual tripole cloud charge structure seems to be less likely to generate downward positive flashes [35]. Figure 1-3 shows possible cloud charge structures or scenarios which might be involved in their formation [3], [8], [36]–[39].

Similar to downward negative flashes, PBPs were observed to precede positive return strokes [40] [41]. Positive downward flashes contain generally one stroke and are less likely to produce subsequent return strokes [42].



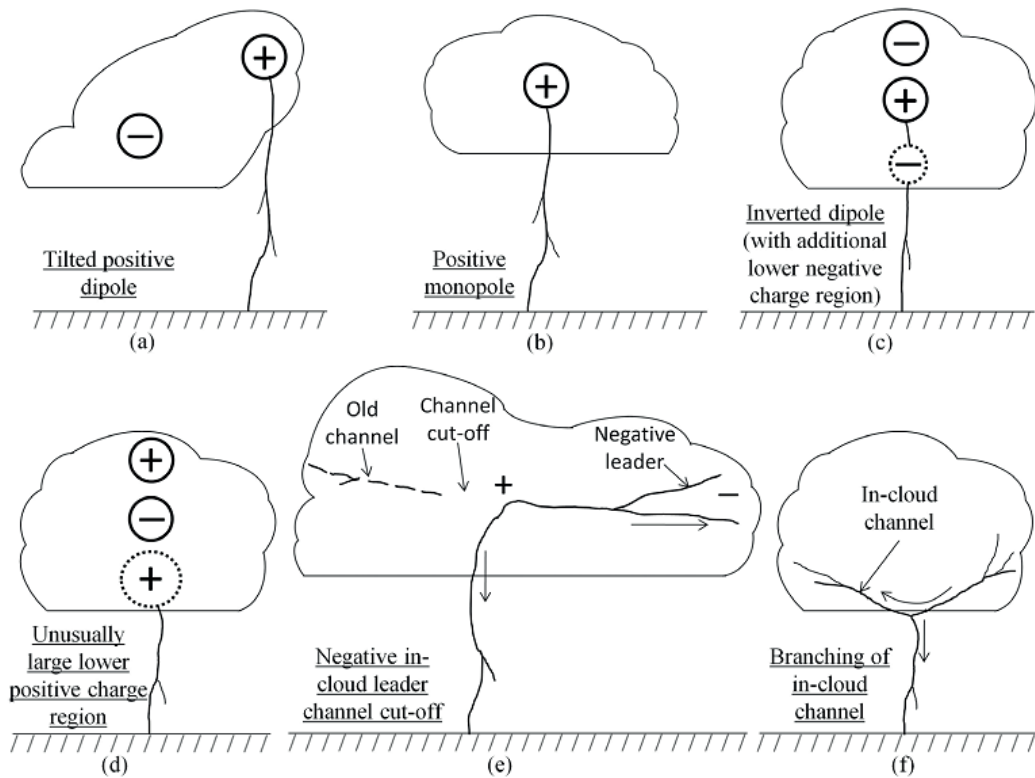


**Figure 1-3. Possible cloud structure and scenarios favoring production of positive downward flashes (Adapted from [43]).**

#### 1.2.4 Upward Positive Flashes

Upward positive flashes initiate by the inception of an upward negative stepped leader [44]. Upward positive lightning discharges and their properties have been studied in a handful of papers [45]–[49]. Due to the sparse available data on this type of lightning discharges, the involved cloud charge structure is not fully known. Based on the recorded data on the channel-base current, a recent analysis [50] has proposed a classification of upward positive flashes into two categories which will be further discussed in Chapter 4.

### 1.3 Lightning Observation

Experimental observation of lightning discharge mainly began at the start of 19th century. At that time, local lightning incidence was measured through a parameter called the number of thunderstorm-days, which corresponds to the number of days in which an observer could hear the thunder.

The first lightning current measurement system was deployed by McEachron in 1937 on the Empire state building in New York [51], [52]. And up to date, lightning

direct current measurement using instrumented towers were conducted in other geographical locations [42].

Along with instrumented towers, triggered lightning has been used to study lightning discharges [18]. Moreover, lightning discharge might produce various signatures of electromagnetic field at its different phases. Hence, electromagnetic field observations at frequencies from 1Hz up to the microwave ranges [53] were used to study, detect, locate, and estimate various processes in lightning discharge [54].

Streak photo cameras were utilized previously to observe visually different phases of lightning discharges. The use of high-speed camera during the past two decades or so has revolutionized lightning research [55].

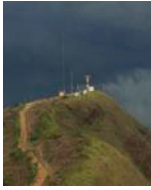





Experimental observation of lightning currents can be obtained either directly using instrumented towers or triggered lightning, or indirectly using lightning location systems. It is worth mentioning that direct measurements can provide us valuable information on the lightning channel-base current and as well the possibility of study of detail analysis of lightning events in a specific location. On the other hand, indirect observations can infer lightning occurrence characteristics over a wide range of area. More discussions on the pros and cons of direct and indirect lightning observation can be found in section 3.3.

#### 1.3.1 Instrumented Towers

However, the critical conditions for the initiation of lightning discharge in nature are not understood very well, experimental observations revealed that local enhancement of electrostatic field at the vicinity of high elevated objects such as tall towers and wind turbines enhances the probability of initiation of lightning discharge or its interaction with previously formed discharges. Hence, tall structures have been widely used to study lightning discharge (See [56] for a recent review). Figure 1-4 shows currently operational instrumented towers (see [56] for detailed description of each tower).

The most extensive study on tower-initiated lightning was performed by Berger and co-workers at the summit of San Salvatore Mountain in Switzerland [57], [58]. Their obtained data set is still a reference in most lightning engineering applications [42]. The site comprised two 70-m tall towers at the top of the San Salvatore Mountain which is 914 m above sea level. Figure 1-5 shows the annual lightning flash incidence rate observed at the two towers of Mont San Salvatore. As it can be seen, due to the moderate height of the mountain and the erected towers, an appreciable number of downward flashes were recorded along with upward events, which makes this study and the obtained dataset unique [42]. Before the instrumentation of the Gaisberg

Tower in Austria [59] and the Säntis Tower in Switzerland [32], the study of Berger et al. formed the largest available data set of lightning current waveforms.

| Morro de Cachimbo   | Giasberg  | Säntis  | Peissenberg   | CN Tower  | Skytree   |
|---|---|---|---|---|---|
| 60 m  | 100 m   | 124 m   | 160 m   | 553 m   | 634 m   |
|  |  |  |  |  |  |
| 1430 m<br>ASL   | 1288 m<br>ASL   | 2502 m<br>ASL   | 940 m<br>ASL  | 76 m<br>ASL   | 37 m<br>ASL   |

**Figure 1-4. Currently operational instrumented towers (as of 2017).**

In 1998, the Gaisberg Tower was instrumented with lightning current measurement equipment and it has been found to be one of the most struck elevated object that had been instrumented so far. The average lightning flash rate was about 57 flashes/year, in which 99% of flashes were upward [60]. It has been observed that about half of upward flashes recorded at the Gaisberg tower are initial-stage-only flashes and do not contain any RS-pulses [61].

The Säntis Tower was instrumented with lightning current measurement facilities since June 2010 and up to June 2016 more than about 562 flashes were successfully recorded. This number of recorded flashes corresponds to an average lightning incidence rate of 93 flashes/year, which is expectedly higher than all other instrumented towers worldwide [62]. Figure 1-6 shows the thunderstorm-day count for the Säntis Tower location. It can be observed that after the erection of the initial 84-m tall tower in 1976 and the new 123-m tall tower in 1997, the number of thunderstorm-days showed a significant increase.

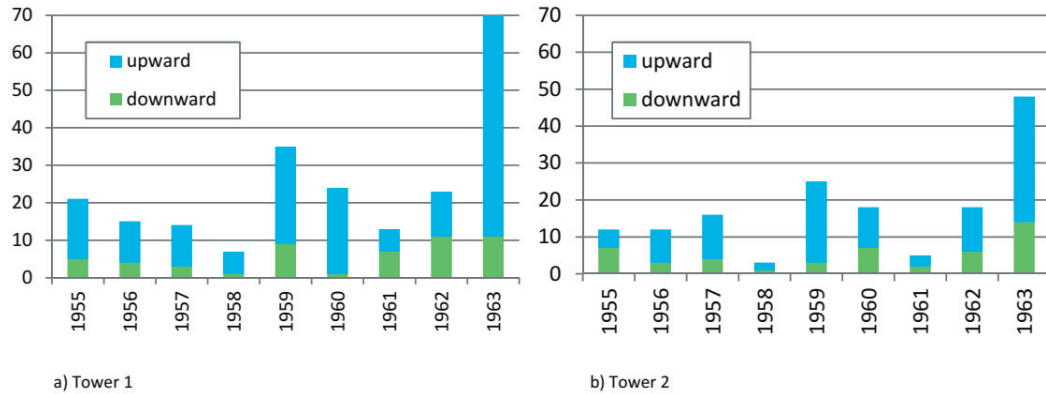


Figure 1-5. Annual lightning incidence to the towers on Monte San Salvatore (Adapted from [60])

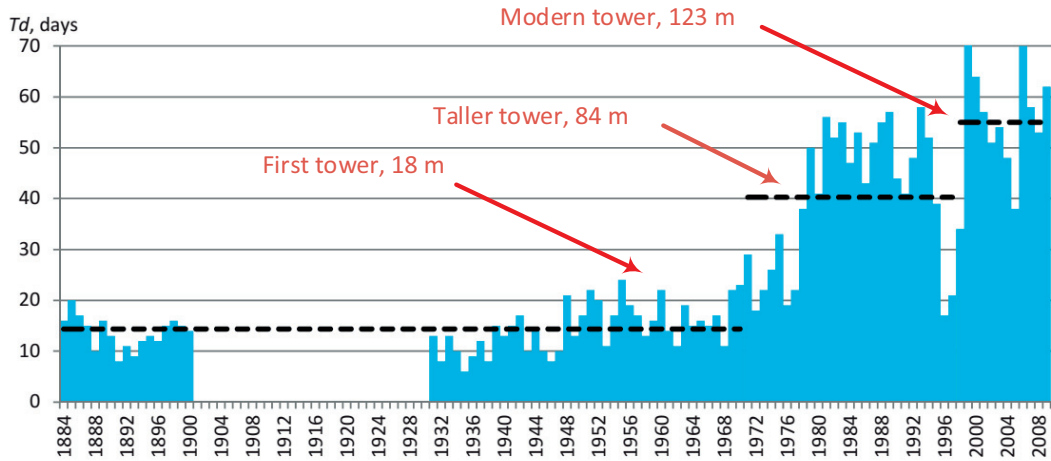


Figure 1-6. Annual lightning flash incidence and evolution of the Sântis Tower (from [60]).

#### 1.3.2 Triggered Lightning

In addition to the instrumented towers, one of the main tools that improved our knowledge of lightning is the artificial initiation of lightning, called also triggered lightning [18]. The most successful means of producing an artificial lightning is by launching a small rocket with a wire (either grounded or ungrounded) extended toward the cloud from the ground. The first inland triggered lightning experiments was conducted by Fieux et al. in France [63] and up to date this method was used by researchers in different locations (e.g., [45], [64]). The comparison between the initial stage of tower-initiated lightning and triggered lightning shows that ICC-pulses in tower-initiated lightning are characterized by larger peaks, shorter rise times, and shorter half-peak widths than triggered lightning [31].

### 1.3.3 Lightning Location Systems (LLSs)

Lightning detection and geolocation is of particular interest for so many applications such as forecasting thunderstorms and their movement in real-time, power utilities protections, lightning warning applications, risk assessment, etc. [65].

Lightning various processes might generate an electromagnetic energy with frequencies ranging from a from few hertz up to  $10^{20}$  Hz [66]. Each of these processes might effectively radiate at specific frequency range. Hence, design of LLS, range of detection, and the interpretation of obtained data might vary according to the discharge process which is target of detection [54]. VLF, LF, MF, HF, VHF frequency ranges were used by ground-based LLSs and optical radiation were used by satellite-based LLSs. Table 1-1 summarizes various frequency ranges, the associated discharge processes that can be detected, and mode of electromagnetic field propagation.

**Table 1-1. Various frequency ranges of LLS observations (Adapted from [54]).**

| Frequency range     | Discharge processes                                   | Mode of propagation                               |
|---------------------|---|---|
| VLF (3-30 kHz)      | CG RSs/CIDs*/PBP                                      | Groundwave and Earth-ionosphere waveguide         |
| LF-MF (30 kHz-3MHz) | CG RSs/CIDs/PBP/K-changes/CG leader steps             | Groundwave and Earth-ionosphere waveguide         |
| HF (3-30 MHz)       | Various incloud and leader processes                  | Mixed of groundwave and line of sight propagation |
| VHF (30 – 300 MHz)  | Breakdown of virgin air, dart leader, K-changes, CIDs | Line of sight propagation                         |
| Near IR/optical     | Hot current carrying channel                          | Line of sight propagation                         |

\* Compact Intracloud Discharges

## 1.4 Objectives of the Thesis

The main objectives of this thesis can be divided into two folds:

- Study of various processes of upward lightning flashes initiated from the Săntis tower with special focus on their initial stage with the particular interest in better understanding of physics of discharge, insulation coordination of power utilities and wind turbines, and developing of meteorological research.

- Study of electromagnetic field radiation of upward lightning flashes either along the mountainous Alp region or the very far ranges including its interaction with the ionosphere, which is essential in the evaluation and improvement of the performance of Lightning Location Systems along mountainous areas and moreover can provide us more insight on propagation of electromagnetic waves in the earth-ionosphere waveguide.

More specifically, the objectives of this thesis can be summarized as follows:

- Analysis of superimposed ICC-pulses of upward negative flashes and investigation of their charge transfer mode.
- Study of the ability of LLSs to detect upward negative flashes and lightning electromagnetic field propagation in mountainous areas.
- Study of upward positive flashes including the involved upward negative stepped leader and its comparison to downward negative leader.
- Study of upward bipolar flashes recorded at the Säntis Tower.
- Analysis of the interaction of upward lightning with the earth-ionosphere waveguide and proposing theoretical approaches to calculate the associated field interaction with the ionosphere layer.

## 1.5 Organization of the Thesis

In Chapter 2 we review the current measurement facilities of the Säntis Tower, along with updates and upgrades that have been conducted to improve the performance of the system. We briefly describe the installed field mill, close range, and distant electric field stations that were utilized to obtain the field signature of Säntis events. In addition, a general overview of the Lightning Location System whose data were used extensively in this thesis is given.

Chapter 3 is devoted to explore various aspects of upward negative flashes, which makes them different from their downward counterparts. We examine the superimposed pulses on the initial stage of upward negative flashes using simultaneous far field observation and current records at the Säntis Tower in order to find the involved charge transfer modes in their formation. Furthermore, the ability of Lightning Location Systems to detect and locate upward negative flashes is discussed. Finally, a full wave numerical method is developed to evaluate lightning electromagnetic field propagation along mountainous areas.

Chapter 4 presents a summary of the characteristics of upward positive flashes recorded at the Säntis Tower. In the following, the characteristics of upward negative stepped leaders are investigated using simultaneous channel-base current and vertical electric fields recorded at 14.7 km. We compare electric field signatures of the initial stages of downward negative flashes and upward positive flashes. At the end, we attempt to propose a model to calculate electric field radiation of oscillatory

(microsecond-scale) pulses superimposed on the initial rising portion of Type-II upward positive flashes based on the expected background physical process.

Chapter 5 reports on 13 bipolar lightning flashes recorded at the Säntis Tower in Switzerland during the period of June 2010 to January 2015. Based on our observations and the existing literature, we suggest a modification to the traditional classification of bipolar flashes.

Chapter 6 is devoted to investigate the interaction of upward flashes with the ionosphere layer. We present simultaneous current and wideband electric field waveforms at 380 km distance from the strike point associated with upward flashes initiated from the Säntis Tower. The dataset presented in this study represents, to the best of the Author's knowledge, the first simultaneous records of lightning currents and distant fields associated with natural upward flashes featuring ionospheric reflections. A full-wave, finite-difference time-domain (FDTD) analysis of the field propagation including the effect of the ionospheric reflections is presented and the results are compared with the experimental data. Moreover, we present a novel semi-analytical simplified approach based on the ray tracing method to estimate radiated electric fields associated with lightning return strokes, taking into account ionospheric reflections.





# 2

## Instrumentation

### 2.1 Introduction

The knowledge of lightning current parameters is of great importance to both engineering applications of lightning research such as protection of power grids, sensitive electric and electronic systems, and to scientific curiosity for better understanding of the involved physical processes [67]. Direct channel-base current measurements can provide salient parameters including peak current, maximum current derivative, current risetime, current duration, charge transfer and action integral. Lightning current measurements along with their associated electromagnetic field observation and high speed video imaging can be the source of valuable information to improve our understanding of the physics of the lightning discharge and its electromagnetic effects.

In this chapter, we present the Säntis Tower measurement system along with the upgrades that have been implemented to improve its performance. We will also describe the structure of the electromagnetic field measurement stations which have been installed to date. A section is also devoted to present the European Lightning Location System, whose data have been widely used in this thesis.

### 2.2 Säntis Tower and Initial Instrumentation

The Säntis Tower was instrumented in May 2010 to measure accurately currents of lightning discharges striking the tower [32]. The Säntis Tower is a 124-m-tall tower sitting at the top of the 2502-m-tall Säntis Mountain (see Figure 2-1). The Säntis Mountain is located in the northeast of Switzerland in the Appenzell region ( $47^{\circ}14'57''\text{N}$ ,  $9^{\circ}20'32''\text{E}$ ). The tower is made of a conical metallic structure with an

outer Plexiglas cover which protects the interior installed telecommunication infrastructure.

The lightning current waveform and its time derivative are measured at two different heights of 24 m and 82 m above ground level, using Rogowski coils and B-dot sensors (see [68], [69] for more detailed information).

Figure 2-2 shows the schematic diagram of the installed electronics which includes sensors, heating system, power supply, microcontrollers, Ethernet links, signal conditioning and protection (i.e., integrator, attenuator and surge arrester) and analog-to-digital converter. The analog outputs of the sensors are relayed to a digitizing system by means of A/D – D/A 12\_bit optical fiber links with an overall bandwidth of DC to 25 MHz (Terahertz LTX5515). The initial data acquisition system included an industrial PC, two National Instrument PCI 5122 high-speed digitizers (operating with a maximum sampling rate of 100 MS/s and capable to record a maximum time window of 1.2 s with 240 ms of pre triggering time) and a Meinberg GPS 170 PCI card. The system allows over-Internet remote maintenance, monitoring and control.

Table 2-1 presents the response characteristics of the installed PEM and ROCOIL Rogowski coils. Due to the resonance of the Rogowski coils at the frequency range of about 1 MHz, B-dot sensors are used to recover the frequency response of the current above 120 kHz. The combination of the Rogowski coil and the B-dot sensor outputs at each height is used to obtain the current waveform with an overall bandwidth of 0.01 Hz up to 3 MHz (see [32] for more information on the data analysis).



**Figure 2-1. The Säntis Tower**

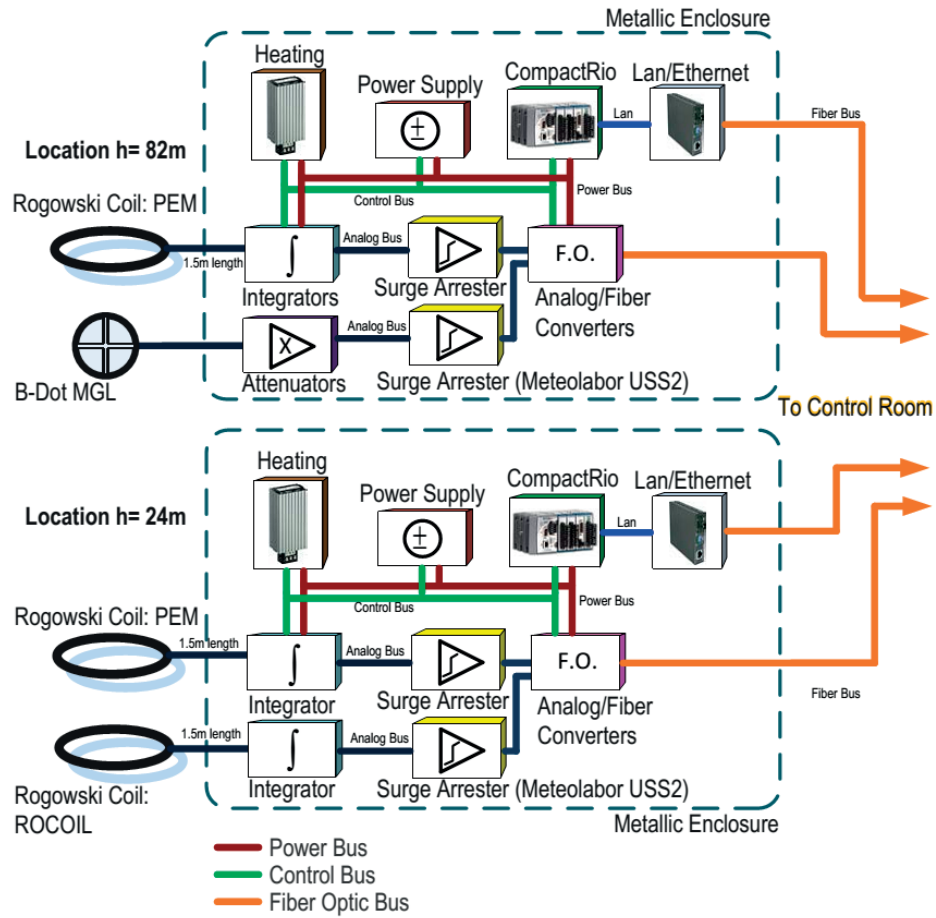


Figure 2-2. Schematic diagram of the primary installation (From [32]). From May 2010 until July 2013.

Table 2-1. Characteristics of the installed Rogowski Coils (Adapted from [32])

| Parameter                | ROCOIL @ 24 m       | PEM @ 24 m         | PEM @ 82 m         |
|--------------------------|---------------------|--------------------|--------------------|
| LF (-3 dB)               | 0.1Hz               | 0.01Hz             | 0.01Hz             |
| HF (-3 dB)               | 5MHz                | 3MHz               | 3MHz               |
| Noise level              | 20mV <sub>p-p</sub> | 2mV <sub>p-p</sub> | 2mV <sub>p-p</sub> |
| Coil transfer admittance | 1 kA/V, 10 kA/V     | 20 kA/V            | 20 A/V             |

### 2.3 Upgrades

In this section, we present a number of upgrades that were made in 2013-2014 on the tower measurement system.

As it was mentioned in Section 2.2, the initial data measurement and acquisition system included an industrial PC, two National Instrument PCI 5122 high-speed digitizers and a Meinberg GPS 170 PCI card, in which the incompatibilities between digitizers and GPS card led to inaccurate GPS time stamps. In order to solve this issue, a system based on the PXI platform of National Instruments was implemented. PXI combines the conventional electrical bus of PCI with modular Eurocard mechanical packaging of Compact PCI and adds specialized synchronization buses and key software features. In addition to the PCI bus, timing and triggering buses have been added to the PXI backplane. A 10 MHz system reference clock, PXI trigger bus, star trigger bus and slot-to-slot local bus make PXI particularly efficient in terms of synchronization, timing and triggering. The timing and synchronization are provided by the PXI 6682H card along with an upgraded GPS antenna of BULLET III, which are able to provide time stamping with a  $100 \pm 13$  ns accuracy.

Other updates include the installation of overvoltage protection on the GPS Antenna and on the PXI 6682H card.

In the initial installation, only one multigap B-dot sensor was installed on the tower at the upper position (82 m). On June 29, 2013, a second multigap B-dot sensor was installed at 24 m, so that  $di/dt$  waveforms are available now at two different heights (see the updated schematic diagram in Figure 2-3).

In addition to that, the sampling rate of the system was reduced from 100 MS/s to 50 MS/s, which leads to pre-triggering time of 960 ms compared to former value of 240 ms and time window of 2.4 s instead of former time window of 1.2 s. This update led to an expanded time window which allows us to capture the initial continuous current section of upward negative flashes. It should be noted that the new sampling rate (50 MHz) is much higher than the higher frequencies of the lightning return stroke (Some megahertz), so the obtained current waveforms are expected not to be affected by this update.

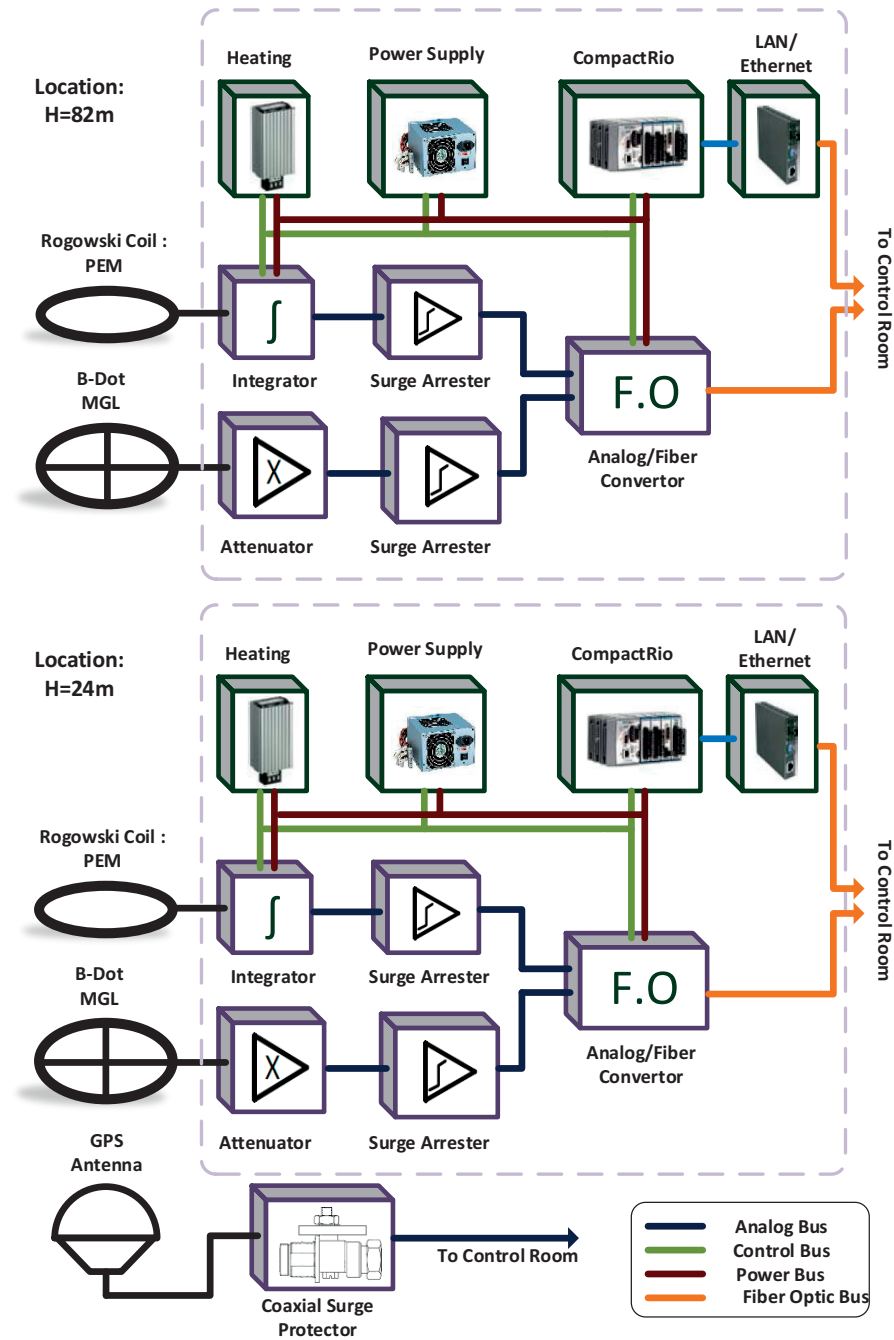


Figure 2-3. Schematic diagram of upgraded current measurement system at two heights (From [70]). System operation from 29 June 2013 up to day.

## 2.4 Wideband Electromagnetic Field Station

A field measurement station was deployed on 23 July 2014 and was operational until 28 October 2014 to record vertical electric fields and horizontal magnetic fields associated with flashes striking the Sântis Tower.



Figure 2-4 shows the geographical location of the Säntis Tower and the temporary field station installed in Herisau (47°23'N, 9°16'E), 14.7 km away from the Säntis Tower. The electric and magnetic field sensors were installed on the roof of a 25 m building belonging to the Huber+Suhner Company. The installed sensors on the roof of the building along with the schematic diagram of the deployed system are shown in Figure 2-5.

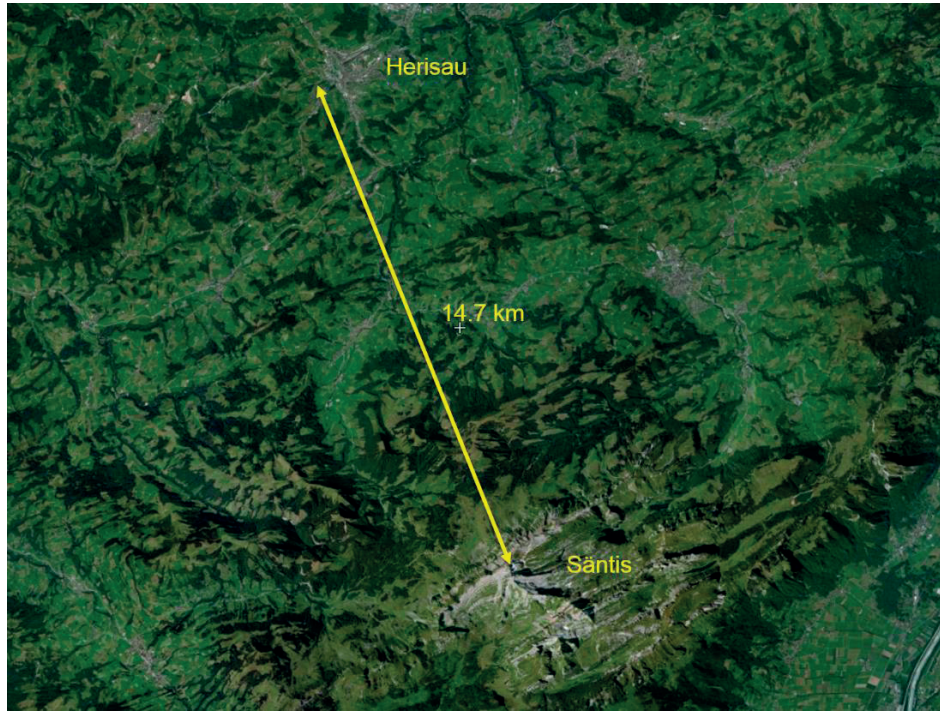
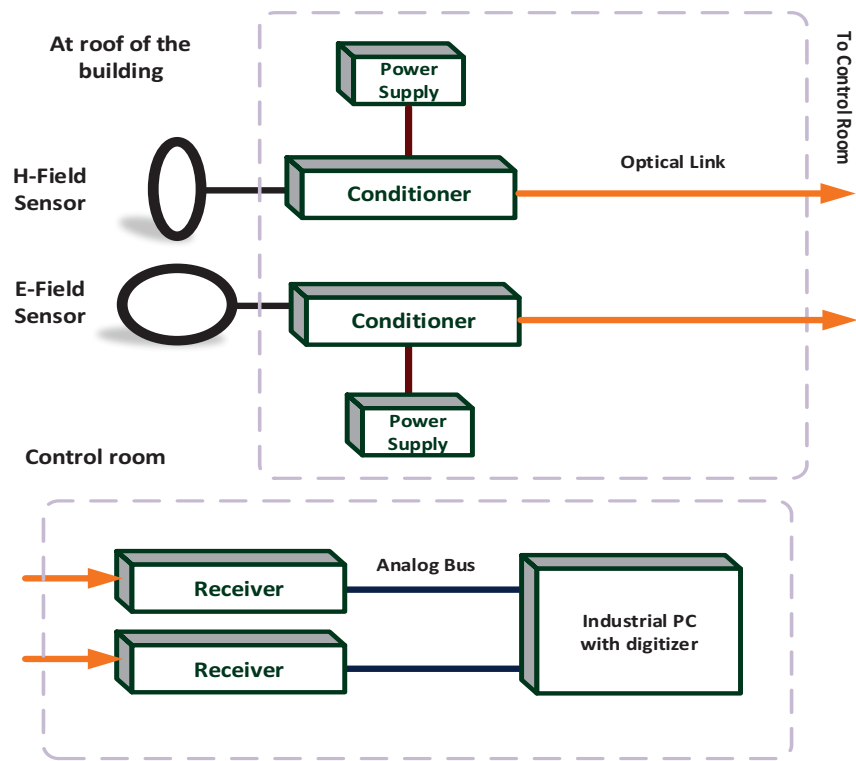


**Figure 2-4. Location of the Säntis Tower and the field measuring station located in Herisau (Appenzell Ausserrhoden, Switzerland).**

The system included two Thales (former Thomson CSF) Mélopée sets, each including a sensor, a conditioner, fiber optic connection and a receiver. A PCI 5122 platform with sampling rate of 50 MS/s was used to digitize and record the field waveforms. The frequency bandwidth of the Mélopée system for the electric field is reported by the manufacturer to be 1 kHz to 150 MHz, and that for the magnetic field is 2 kHz to 150 MHz.

During the operation period of the field measurement station (23 July to 28 October 2014), a total of 26 upward flashes were simultaneously recorded at the Säntis Tower and at the Herisau field station [71]. Out of these 26 flashes, 21 were negative and 5 were of positive polarity. Figure 2-6 presents an example of simultaneous records of current and vertical electric field at 14.7 km distance which occurred on 22 October 2014. The recorded current waveform is characterized by the typical current waveform of negative upward flashes including the initial continuous current section followed by two subsequent return strokes.



a)



b)

Figure 2-5. Wideband electromagnetic field system. a) Schematic diagram of deployed system. b) The installed Mélopée sensors on the roof of 25-m-tall building (From [72]).

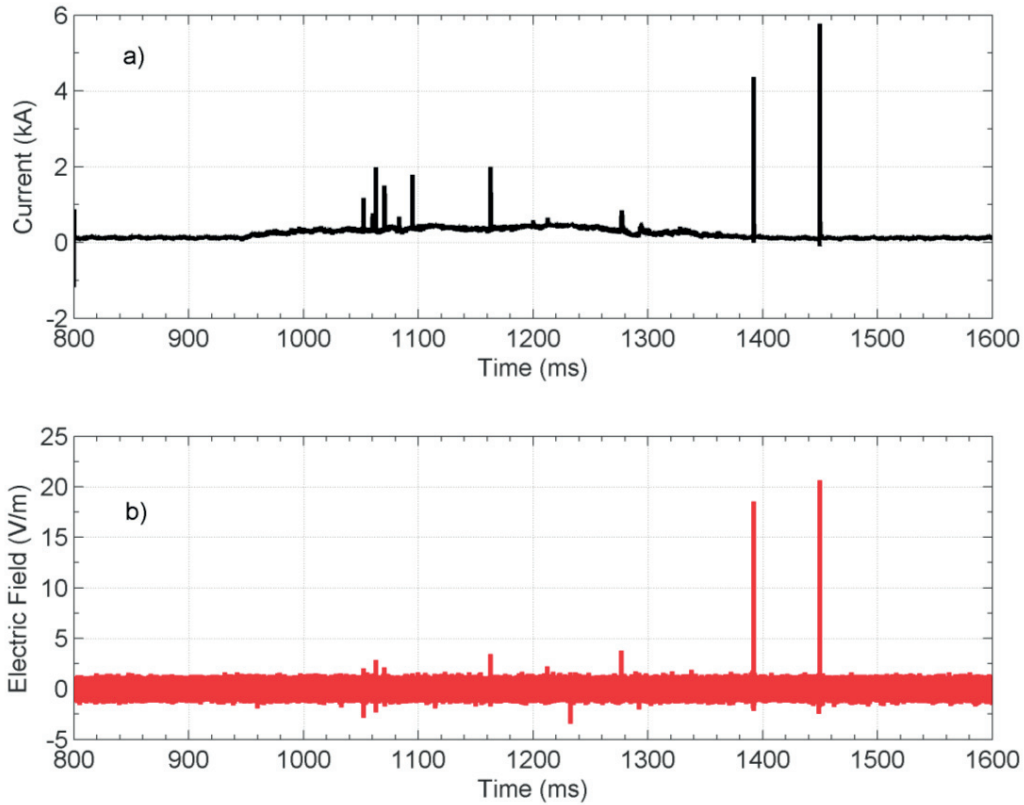


**Figure 2-6. Example of recorded waveforms associated with a flash that occurred on 22 October 2014 at 00:56 AM a) Current waveform. b) E-field waveform at 14.7 km (From [71]).**

## 2.5 Far-Distance Electric Field Sensor

A TCP/IP over the Internet triggering scheme was deployed to trigger an electric field sensor installed in Neudorf, Northern Austria, which measures the vertical component of the electric field. Figure 2-7 shows the location of the electric field sensor 380 km away from the Säntis Tower.

The electric field sensor includes a flat plate antenna and an integrator with a decay time constant of 500  $\mu$ s, corresponding to a low cutoff frequency of 300 Hz. The field waveforms were recorded with a sampling rate of 5 MS/s. More information on the electric field sensor can be found in [73].

During the period of April to October 2014, simultaneous current and electric field waveforms of 29 flashes initiated from the Säntis Tower, were successfully recorded. Among the 29 flashes, 25 were negative and 4 were of the bipolar category. Figure 2-8 presents an example of measured current and vertical electric field waveforms of an upward negative flash occurred on 21 October 2014.





Figure 2-7. Location of the Säntis Tower and the field measurement station in Neudorf, separated by 380 km.

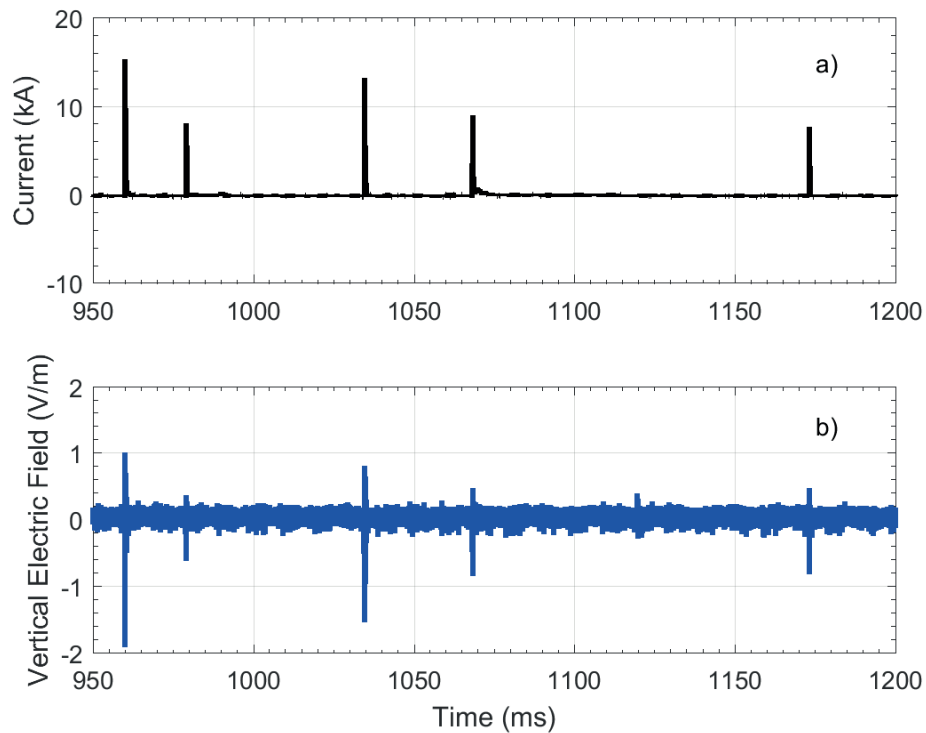


Figure 2-8. Example of measured waveforms associated to an upward negative flash occurred on 21 October 2014, at 20:23:22. a) Current waveform. b) Vertical electric field at 380 km.

## 2.6 Field Mill

The knowledge of the electrostatic field prior, during and after the flashes at Sântis will certainly help in improving our understanding the conditions conducive to the initiation of upward flashes from tall structures.

An EFM-100 field mill has been installed since 15 July 2016 to measure the electrostatic electric field in the immediate vicinity of the Sântis tower. The distance in between the installed field mill and the tower base is about 85 m. EFM-100 can detect even lightning activity up to distances of about 40 km from the tower.

Figure 2-9 shows the position of the installed position of the field mill near the tower base. The field mill sensor is mounted inside a building in which there are metallic bars and concrete structures. Therefore, the observed electric field values are relative and non-calibrated. The system is set to continuously record the field with a sampling time of 50 ms. The highest range of electric field that can be recorded is  $\pm 20$  kV/m. Figure 2-10 shows an example of electrostatic field recorded by field mill during the thunderstorm occurred on 31 July 2016.

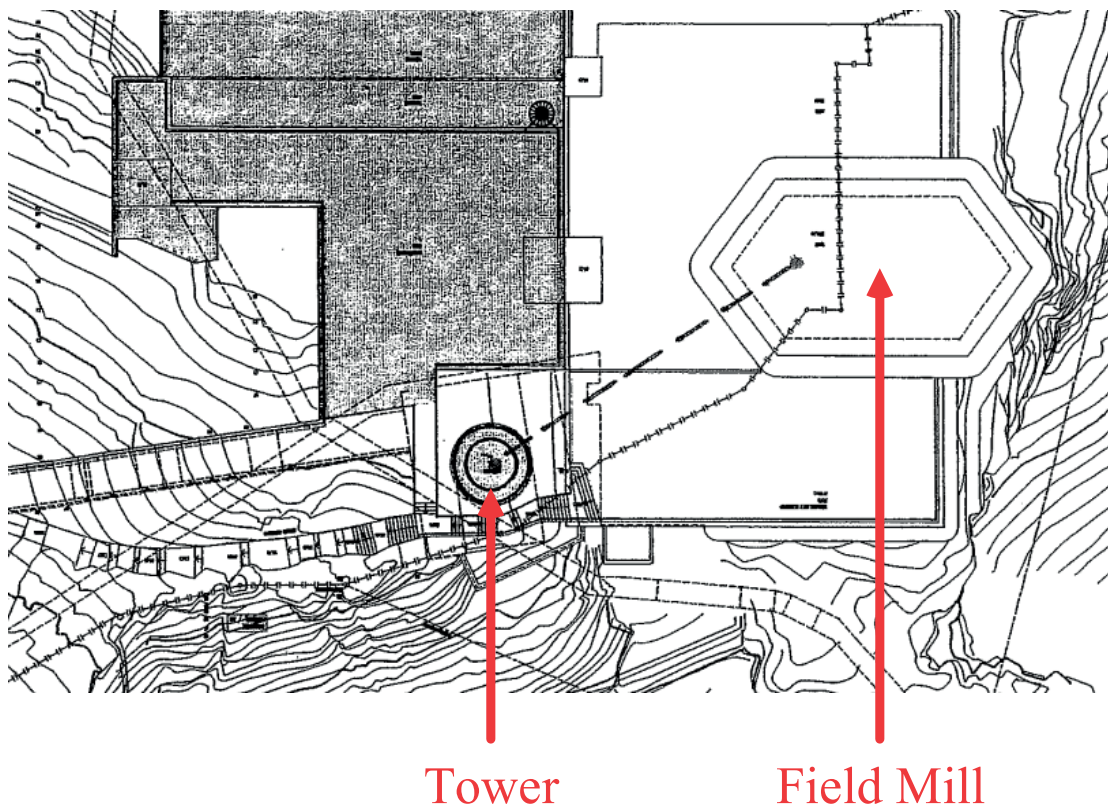
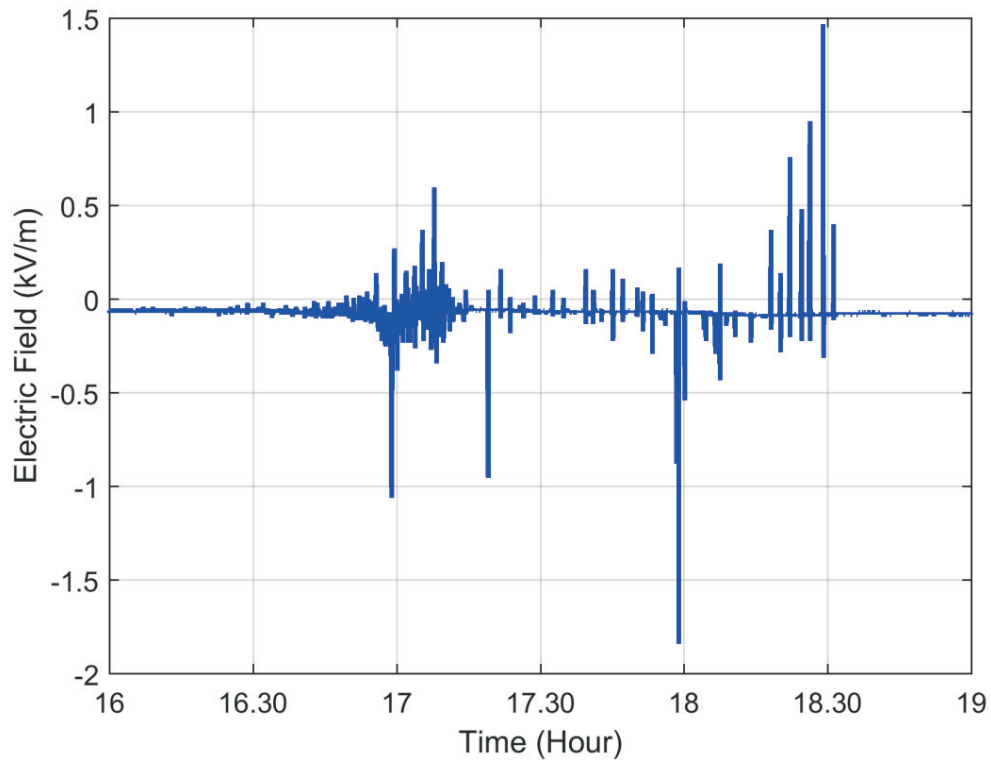


Figure 2-9. Mounted EFM-100 field mill sensor at the vicinity of tower.



**Figure 2-10.** An Example of electrostatic field evolution during the passing by storm of 31 July, 2016.

## 2.7 European Cooperation for Lightning Location Detection (EUCLID)

EUCLID (European Cooperation for Lightning Detection) is a consortium of 19 national lightning detection networks with the aim of identifying and detecting lightning all over the European area (<http://www.euclid.org>). Up to December 2014, the EUCLID network consisted of 149 sensors, including 7 LPATS, 10 IMPACT, 31 IMPACT ES/ESP and 101 LS700x, characterized by a typical bandwidth of 400 Hz to 400 kHz (VLF/LF) [74], [75].

Lightning location systems can provide basic information on the parameters of occurred lightning flashes such as the occurrence time, ground termination coordinates, estimates of return stroke peak current, etc. The knowledge of performance characteristics of lightning location systems is an essential measurement for customers such as power utilities, meteorological services and other sensitive facilities. Due to mountainous terrain and none even coverage of utilized networks, nonuniform values for the Detection Efficiency (DE) and Location Accuracy (LA) are expected [76].

In this thesis, we use the provided data by EUCLID to study the ability of lightning location systems to detect and locate upward lightning flashes in a complex mountainous terrain (European Alps). Figure 2-11 shows the location of six EUCLID sensors at the vicinity of the Säntis Tower.

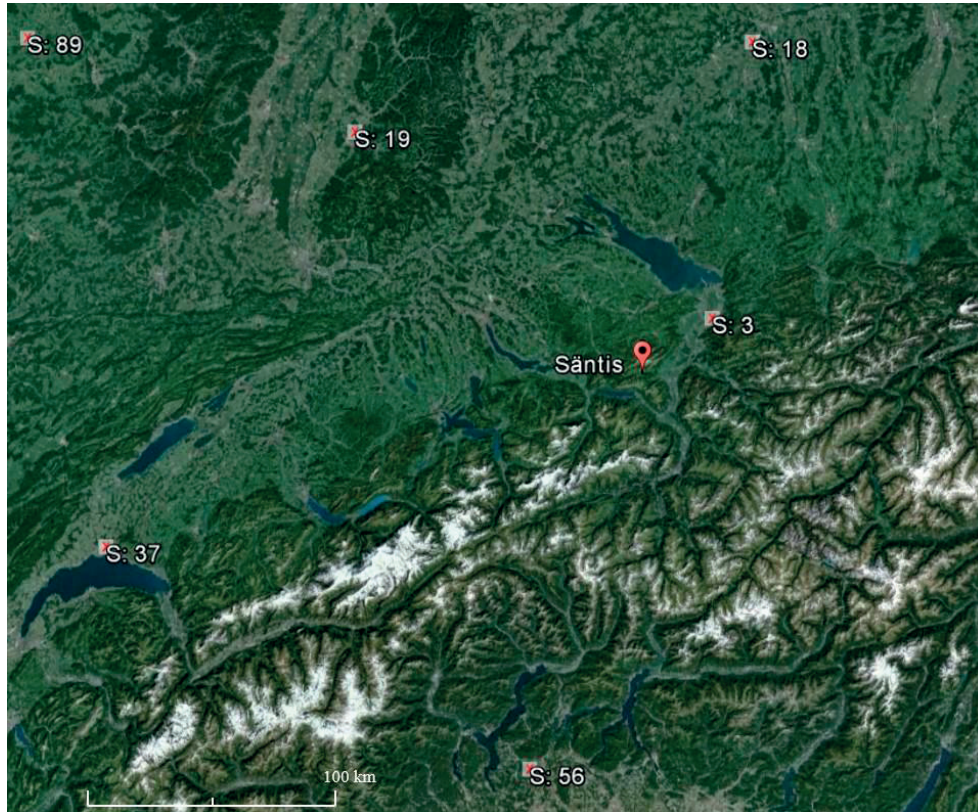


Figure 2-11. Location of EUCLID sensors around the Säntis Tower.

## 2.8 Conclusion

In this section, we described briefly the current measurement system of the Säntis Tower. A certain number of updates and upgrades were conducted in order to improve the performance of the system.

In addition to that, electric field measurement campaigns were deployed at three different distance ranges to record associated electric field of lightning events.



## Upward Negative Flashes

### 3.1 Introduction

Upward lightning flashes have been studied by means of either instrumented towers or rocket-triggered lightning (e.g. [32], [61], [64], [77], [78]). Laboratory long spark gap experiments have shown that a lower value of ambient electrostatic field is required for the initiation of positive leaders compared to negative ones [16], [79], [80]. Due to this fact and favorable cloud charge structure of storms during most periods of their lifetime [6], negative upward lightning (initiated by upward leaders) is known to be more frequent than the positive and bipolar ones [50].

While the ambient electric field inside the thunderclouds is not high enough to initiate downward negative leaders, the presence of tall objects leads to local enhancement of the ambient electric field at their tip up to the critical value for the launch of positive leaders.

Expectedly, there are fundamental differences between the first stages of upward negative flashes and their downward counterparts. Upward lightning flashes are initiated by positively-charged stepped or continuous leaders followed by a continuous discharge phase which effectively transfers negative charges from the negatively charged clouds to ground [31]. The associated current of the upward positive leader and its following continuous current is called the Initial Continuous Current (ICC).

Figure 3-1 presents schematically typical current waveforms of downward (top) and upward (bottom) negative flashes. It can be seen that apart from the differences in the initial stages, similar processes consisting of sequences of downward leader and

return strokes, with or without continuous currents, can be observed in both upward and downward flashes.

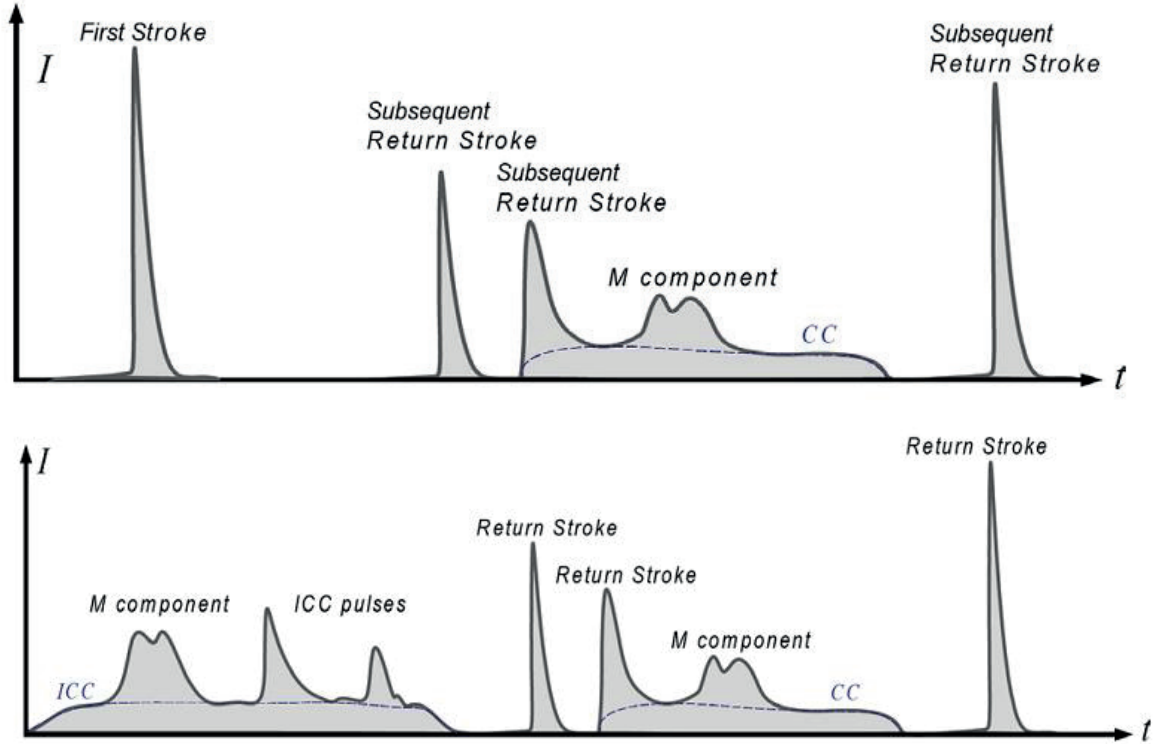


**Figure 3-1.** Typical current waveforms of negative flashes (Adapted from [32]). a) Downward negative flash. b) Upward negative flash.

As it can be observed in Figure 3-1b, some pulses might be superimposed on the ICC which are called ICC-pulses. After the extinction of the ICC and a no-current interval, the initial stage can be followed by one or more downward-leader-return-stroke sequences, similar to those in downward lightning discharges.

In this chapter, we discuss some aspects of upward negative lightning, which makes them different from their downward counterparts. In Section 3.2, we examine the superimposed pulses on the initial stage of upward negative flashes using simultaneous far field observations and current records at the Säntis Tower in order to find the involved charge transfer modes in their formation. In Section 3.3, we discuss the ability of lightning location systems to detect and locate upward negative flashes and in Section 3.4, we propose a full-wave method to calculate lightning wave propagation along mountainous areas in which the occurrence of upward lightning is more probable. The content of this chapter is heavily driven from [72], [76], [81].

## 3.2 Initial Stage of Upward Negative Flashes

There is an ongoing scientific debate on both the initiation mechanisms of ICC pulses and their corresponding charge transfer modes in the initial stage of upward negative flashes. It has been demonstrated by Miki et al. that the ICC pulses in tower-initiated lightning are characterized by larger peaks, shorter risetimes and shorter half-peak widths compared to their rocket-triggered counterparts [31]. Further investigation of fast ICC pulses using video observations suggested that they are more likely to occur in low-altitude branches [82].

The analysis of ICC pulses recorded at the Peissenberg tower has suggested that two types of ICC pulses exist: (1) ICC pulses with relatively long risetime (greater than  $8\text{ }\mu\text{s}$ ), which transfers effectively negative charges to ground in an M-component type mode of charge, (2) fast ICC pulses with short risetimes (smaller than  $8\text{ }\mu\text{s}$ ), which are associated to a return stroke mode of charge transfer.

Upward negative lightning flashes are known to be highly branched [83]. The presence of ICC itself during their initial stage confirms the existence of at least one branch which transfers negative charges continuously to ground. Therefore, ICC pulses occur as a result of the interaction of some other pockets of charge with the branches that carry the continuous current.

Using VHF imaging, close electric field and current records of triggered lightning, Yoshida et al. found that ICC pulses can be initiated by either recoil leaders on previously luminous channels or stepped leaders on newly formed branches [84]. A similar observation using close electric field, high-speed video camera and current measurements at the Gaisberg Tower suggests that the height of the interception of the leader (either recoil or stepped) with the continuous current channel is the critical parameter that affects the charge transfer mode of the ICC pulses. They used the term “mixed mode of charge transfer” to ground for the ICC pulses associated with the occurrence of leader/return stroke mode of charge transfer in a decayed or newly formed channel connected at low altitude to the ICC-carrying channel (see Figure 15 of [33]).

Unlike previous data associated with instrumented towers, in which fields only at relatively close distances up to 190 m are generally available, we obtained simultaneous measurements of lightning currents and relatively distant fields at about 15 km, associated with pulses superimposed on the initial continuous current in upward flashes.

Two different types of pulses superimposed on the initial continuous current can be identified in our dataset: (1) M-component type pulses which are very similar to the pulses presented in [85], and, (2) fast pulses which are very similar to return stroke pulses. These fast pulses have been commonly observed in current records of upward

flashes from tall structures, but relatively rarely in rocket-triggered lightning (see Figure 9b of [86]).

#### 3.2.1 Data

During the operation period of the field measurement station (23 July to 28 October 2014), which was described in Section 2.4, a total of 26 flashes were simultaneously recorded at the S antis Tower and at the Herisau field station. Out of these 26 flashes, 21 were negative.

We examined current and E-field waveforms from 9 upward negative flashes (out of the 21 recorded). The remaining 12 flashes were discarded from the analysis because their current waveform contained at least one pulse that could not be classified unequivocally as ICC pulse or return stroke. Typically, these pulses occurred either at the very end of the ICC or very shortly after its extinction.

Figure 3-2a presents the current waveform associated with an upward negative flash that occurred on 22 October 2014 at 1:14 AM. Figure 3-2b shows the filtered waveform using a low-pass zero-phase filter (Type II Chebyshev with the order of 100) with a cutoff frequency of 1 kHz. In the filtered waveform, one can clearly distinguish the ICC (with 7 superimposed pulses), followed by six return strokes. Figure 3-2c presents the associated electric field waveform. Note that the electric field waveforms have been shifted in time to align the return stroke pulses with their current counterparts.

It should be noted that the atmospheric electricity sign convention is used in this study for the electric field data and a positive sign is used for the current waveform associated with negative return strokes, which effectively transfer positive charge upward or, equivalently, negative charge to the ground.



### 3.2 Initial Stage of Upward Negative Flashes

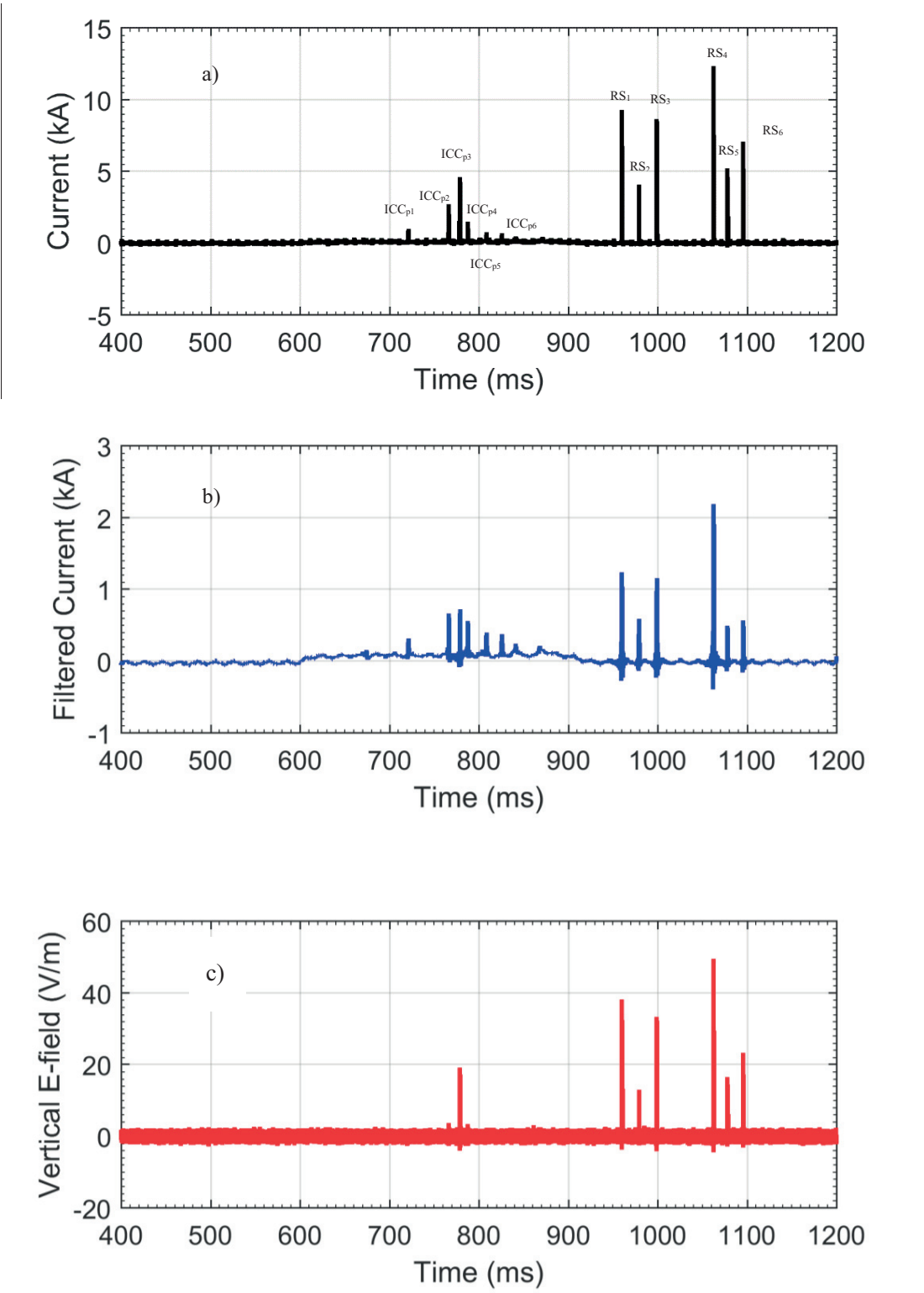
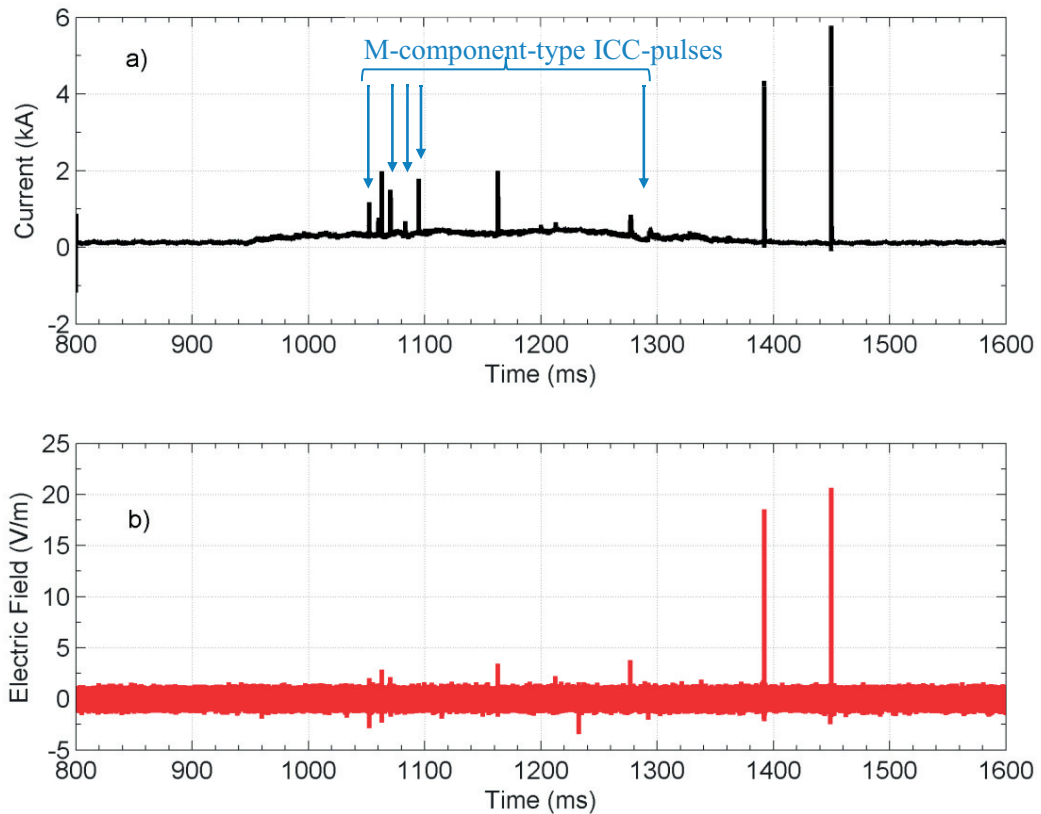


Figure 3-2. Waveforms associated with a flash occurred on 22 October 2014 at 1:14 AM. a) Original Current waveform. b) Current waveform filtered with 1 kHz low-pass filter. c) E-field waveform at 14.7 km (From [87]).

### 3.2.2 Observed ICC Pulses

Based on the characteristics of simultaneous records of current and electric field waveforms, two different types of ICC pulses were observed in our measurement results. We observed that some of the ICC pulses have quite similar features to those of M-component pulses observed in downward negative flashes, and some resemble subsequent return stroke pulses.

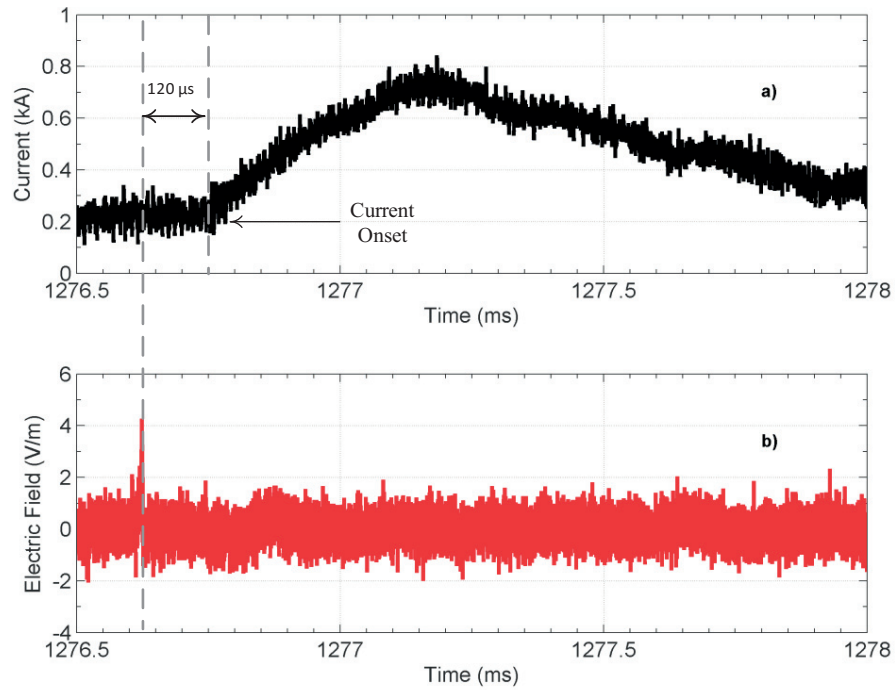
*M-component type pulses.* These pulses are characterized by a slow current waveform with a risetime of the order of a few hundreds of microseconds. Figure 3-3 shows the current waveform associated with an upward negative flash that occurred on 22 October 2014 at 00:56 AM, in which M-component-type ICC-pulses are marked with blue arrows.



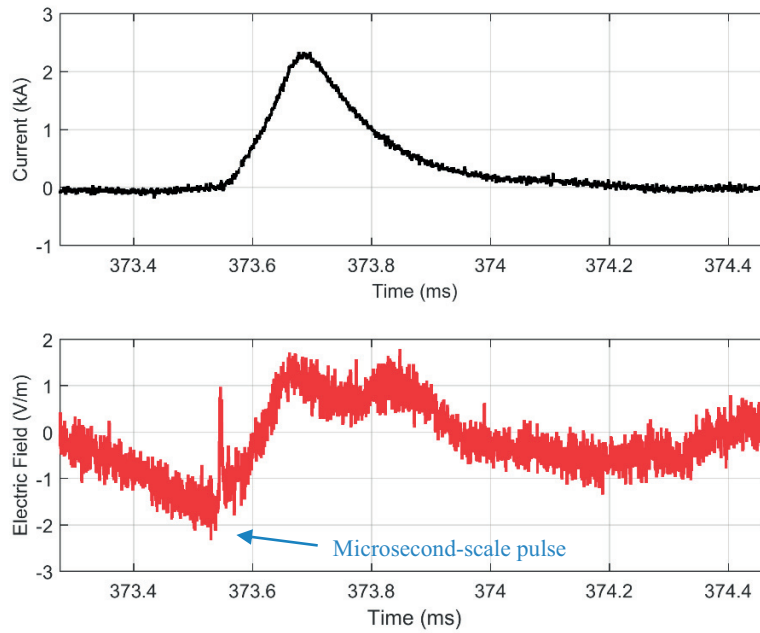
**Figure 3-3.** Waveforms associated with a flash that occurred on 22 October 2014 at 00:56 AM. a) Current Waveform. b) E-field waveform at 14.7 km (From [87]).

Figure 3-4 presents an expanded view of the current and field waveforms of one ICC pulse of this type, which occurred at a time of about 1276 ms. It can be seen that the microsecond-scale electric field pulse occurs about 120  $\mu$ s prior to the onset of the current pulse. This time shift is in agreement with observations in [85], [88],[73], in

which the microseconds-scale field pulse was attributed to intracloud activity preceding and possibly initiating the M-component. Shao et al. [89], using electric field measurements along with VHF observations, suggested that these microsecond pulses might be associated with the initiation of M-component type process. A slow field waveform following the microsecond fast pulses can be observed in the case of some M-component events. An example of M-component type ICC pulse with both microsecond field pulse and slow field waveform is shown in Figure 3-5.



**Figure 3-4. Expanded View of the M-component-type ICC pulses that occurred in the flash shown in Figure 3-3. a) Current pulse. b) E-field pulse at 14.7 km (From [87]).**



**Figure 3-5. Simultaneous current and electric field of an M-component type pulse of an upward negative flash to the S antis Tower occurred on 21 October 2014, 20:41:29 (From [87]).**

*Return-stroke type pulses.* Figure 3-6 shows an expanded view of the current and field waveforms of an ICC pulse of this type in the flash shown in Figure 3-2. The current is characterized by a peak value of 4.6 kA and a 10-90% risetime of 2.1  $\mu$ s. The corresponding E-field peak is 21.4 V/m and the E-field risetime is 2.3  $\mu$ s.

As can be seen, unlike the M-component type pulse shown in Figure 3-4, the onset of the field matches that of the current pulse, indicating that the source of radiation is near the base of the channel.

Furthermore, the radiated electric field pulse appears to be similar to radiated fields associated with return strokes. This can be seen by examining Figure 3-7, which shows an expanded view of the current and field waveforms of a return stroke in the same flash. The current has a peak value of 9.4 kA and a 10-90% risetime of 1.0  $\mu$ s, and the E-field has a peak value of 40.7 V/m and a risetime of 2.0  $\mu$ s. In the next section, we will present a more detailed comparison between return-stroke type (RS-type) ICC pulses and return strokes.

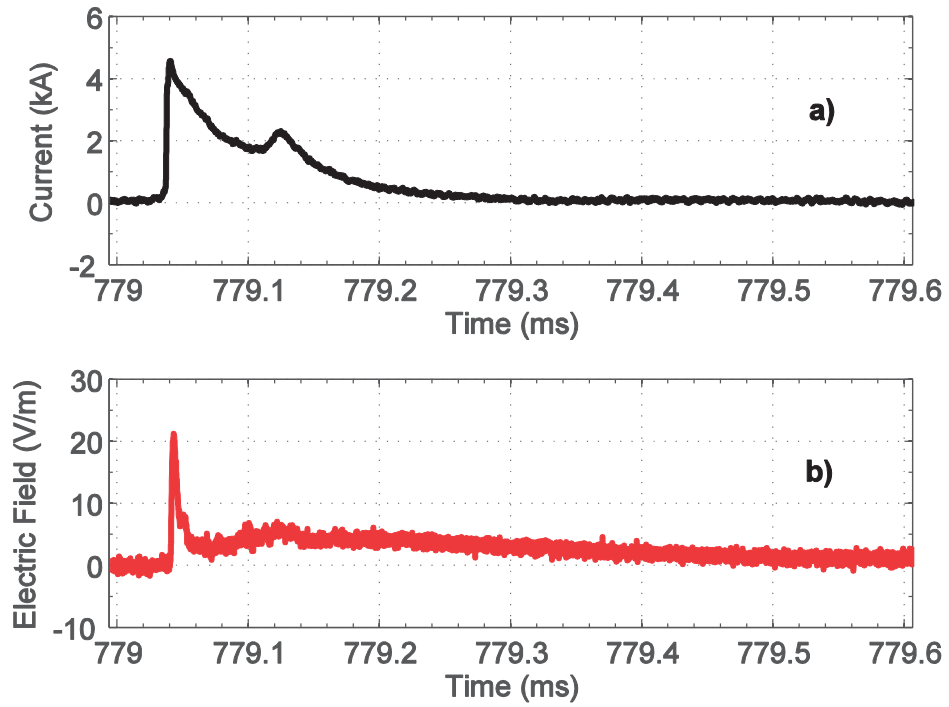
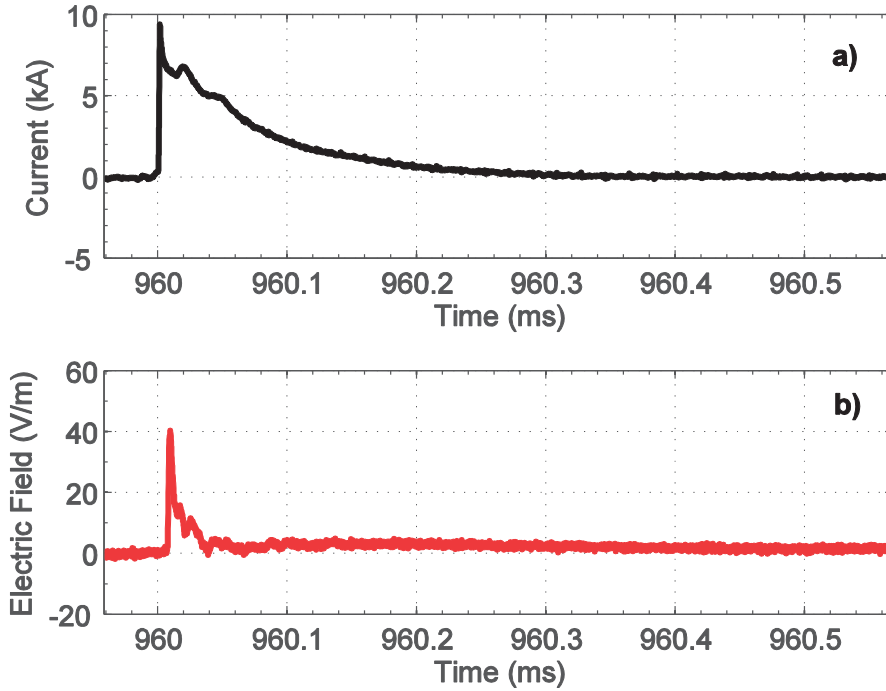


Figure 3-6. Current and E-field waveforms associated with an RS-type ICC pulses in the flash that occurred on 22 October 2014 at 1:14 AM (Figure 3-2). a) Current. b) E-field (From [87]).



**Figure 3-7.** Current and E-field waveforms associated with a return stroke in the flash that occurred on 22 October 2014 at 1:14 AM (Figure 3-2). a) Current. b) E-field (From [87]).

### 3.2.3 Comparison of RS-Type ICC Pulses and Return Strokes

In this section, individual characteristics of RS-type ICC pulses and return strokes are investigated based on their current and radiated electric field waveforms. Figure 3-8 shows a scatter plot of peak E-field versus peak current for all considered RS-type ICC pulses (blue circles) and return strokes (red circles).

It can be seen that the RS-type ICC pulses have, in general, smaller current and field peaks compared to return strokes. On the other hand, the two datasets are characterized by very similar linear regression slopes, namely 3.67 V/(m. kA) for the ICC pulses and 3.77 V/(m. kA) for return strokes. It should be noted that regression lines are forced to go through the origin.

Assuming the field-current relation based on the single-wave transmission line (TL) model (e.g., [90]), and considering a factor of 2 accounting for the enhancement of the electric field associated with the mountainous profile of the field propagation path (which will be elaborated in sections 3.4 and 3.5), the estimated value for the apparent speed of both RS-type ICC pulses and return strokes is about  $1.4 \times 10^8$  m/s, which is in agreement with the reported range of values (about 1/3 to half of the speed of light) found for return strokes in other studies [91]. Strictly speaking, the single-wave TL model is not applicable to ICC-pulses that in general involve two

overlapping waves, but we believe that for fast ICC-pulses, the upward (RS-like) wave is dominant, as further discussed in Section 5.

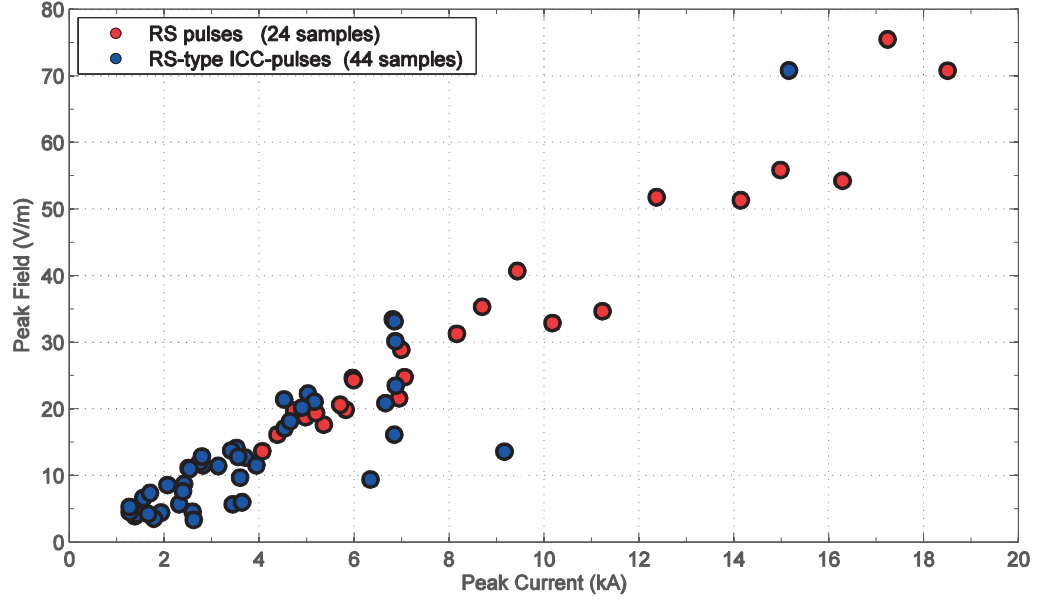


**Figure 3-8.** Scatter plot of electric field peak versus current peak for RS-type ICC-pulses (blue circles) and return strokes (red circles) (From [87]).

Figure 3-9 presents the cumulative probability distribution of the current peak. The straight lines correspond to the best fitting lognormal distributions. Statistical characteristics for the current peak and field peak are summarized in Table 3-1 and Table 3-2, respectively. We have also included in these tables, the 90% confidence interval for the mean values. Note that in Table 3-2, the E-field peak values have been normalized to 100 km.

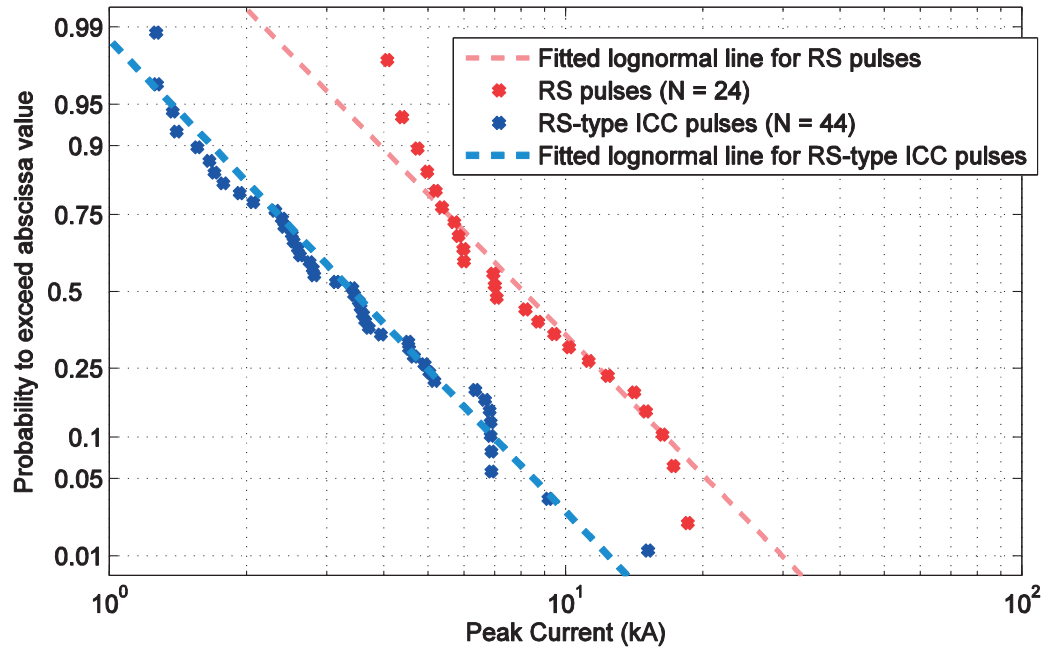


Figure 3-9. Cumulative peak current distributions for the return strokes (red) and RS-type ICC pulses (blue). The straight lines correspond to lognormal approximation (From [87]).

Table 3-1. Characterization of current peak (kA) for 44 RS-type ICC pulses and 24 return strokes.

|                        |    |     |      |      |         | Percentage exceeding tabulated value |     |      |
|------------------------|----|-----|------|------|---------|--------------------------------------|-----|------|
|                        | N  | Min | Max  | Mean | 90% CI* | 95%                                  | 50% | 5%   |
| <b>ICC-pulses</b>      | 44 | 1.3 | 15.2 | 3.3  | 2.9-3.9 | 1.3                                  | 3.4 | 8.6  |
| <b>Return Stroke s</b> | 24 | 4.1 | 18.5 | 8.0  | 6.8-9.4 | 3.7                                  | 8.0 | 17.3 |
| <b>All</b>             | 68 | 1.3 | 18.5 | 4.6  | 4.0-5.2 | 1.5                                  | 4.6 | 13.9 |

\* 90% CI is the 90% confidence interval of the mean value.



### 3.2 Initial Stage of Upward Negative Flashes

**Table 3-2. Characterization of E-field peak (V/m) for 44 RS-type ICC pulses and 24 return strokes. Peak values are normalized to 100 km.**

|                       |    |     |      |      |         | Percentage exceeding tabulated value |     |     |
|-----------------------|----|-----|------|------|---------|--------------------------------------|-----|-----|
|                       | N  | Min | Max  | Mean | 90 % CI | 5%                                   | 50% | 95% |
| <b>ICC-pulses</b>     | 44 | 0.5 | 10.4 | 1.6  | 1.3-1.9 | 0.4                                  | 1.5 | 5.0 |
| <b>Return Strokes</b> | 24 | 2.0 | 11.1 | 4.4  | 3.7-5.2 | 2.0                                  | 4.4 | 9.7 |
| <b>All</b>            | 68 | 0.5 | 11.1 | 2.3  | 1.9-2.7 | 0.6                                  | 2.3 | 8.4 |

\* 90% CI is the 90% confidence interval of the mean value

Figure 3-10 presents the scatter plot of the 10-90% E-field risetimes versus the 10-90% current risetimes excluding pulses with E-field peaks lower than about 10 V/m, for which the determination of the risetime might be significantly affected by noise (19 out of 44 RS-type ICC pulses were left out). For the plotted pulses (25 RS-type ICC-pulses and 24 return strokes), the radius of each circle is proportional to the current peak value.

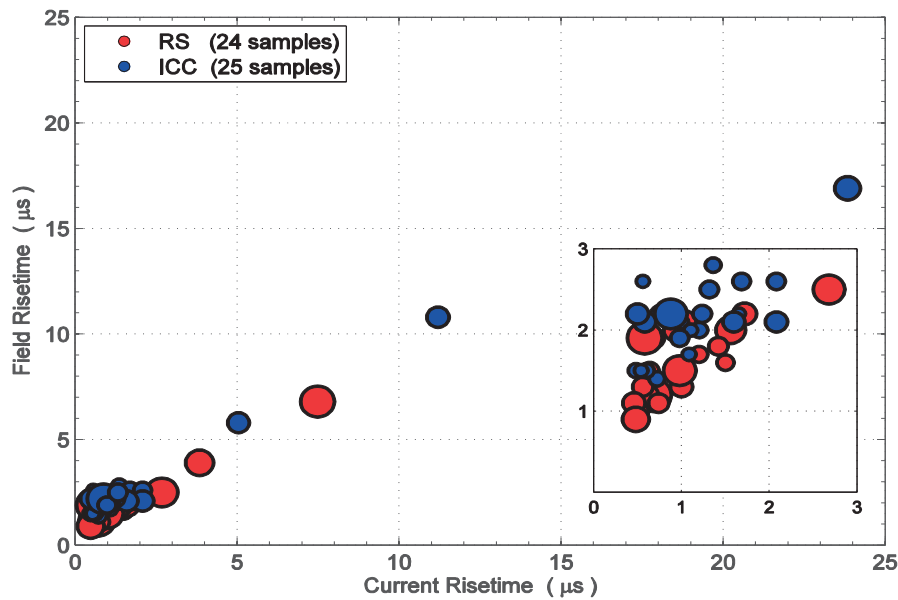


**Figure 3-10. Scatter plot of electric field 10-90% risetime versus current 10-90% risetime for RS-type ICC pulses (blue) and return strokes (red). The radius of each circle is proportional to the associated peak current. The inset shows an expanded view of the scatter plot for risetimes less than 3 μs (From [87]).**

The linear correlation coefficient between the E-field risetime and the current risetime for RS-type ICC-pulses is 0.99. Note that a very similar correlation coefficient (0.97) can be observed between the E-field risetime and current risetime for return stroke pulses.

It is worth noting that the current waveforms associated with both, RS pulses and RS-type ICC pulses sometimes exhibit an initial peak followed by a larger, overall peak. A typical example of double-peak current and associated field waveforms is shown in Figure 3-11, in which the two peaks can be clearly seen. In the plots presented in Figure 3-10, the peak values and risetimes are associated with the initial peak of the current waveform.

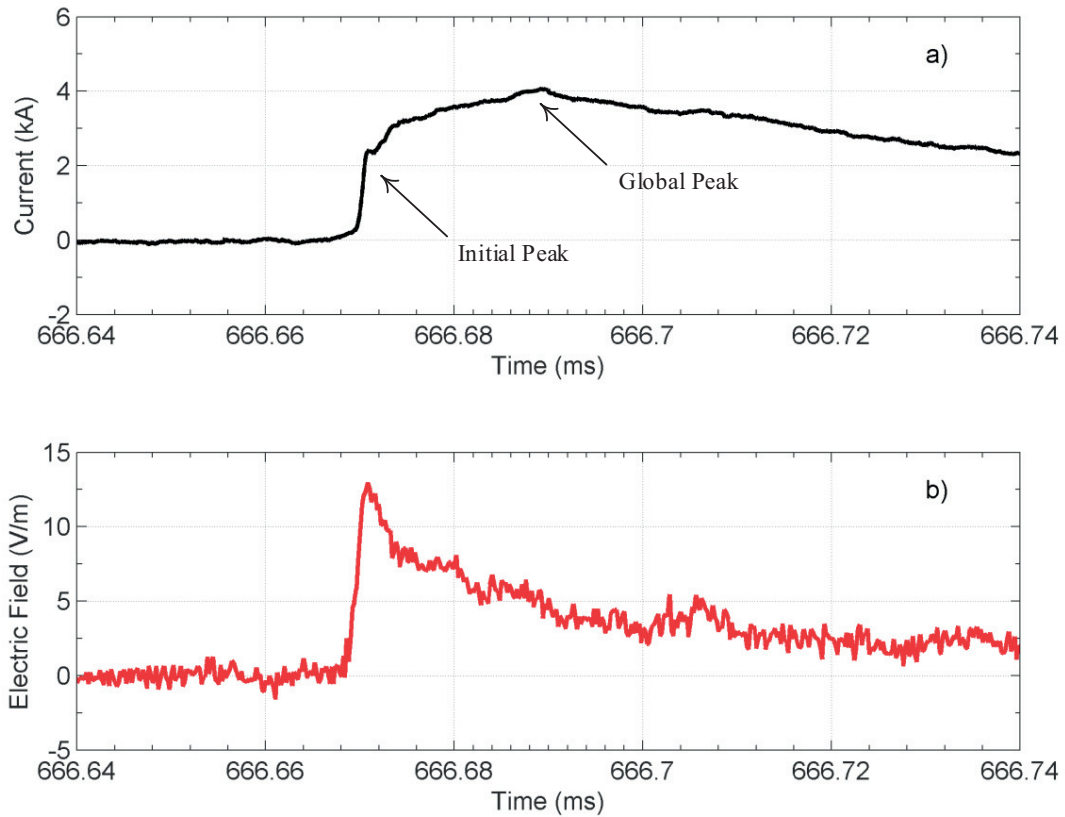


**Figure 3-11. Double-peak current and associated E-field waveforms of RS-type ICC pulse for the flash that occurred on 21 October 2014 at 8:41 PM. (a) Current. (b) E-field (Adapted from [87]).**

The similarity of RS-type ICC pulses with return strokes suggests that these fast pulses are associated with the so-called mixed mode of charge transfer to ground, as defined in [33].

Zhou et al. [33] suggested that ICC pulses are initiated by a downward leader propagating along a previously created, but decayed channel branch that connects

to the grounded ICC-carrying channel. When the height of the junction point is in excess of a kilometer or so (in the cloud), an M-component mode of charge transfer occurs resulting in a long-front incident M-wave. On the other hand, when the height of the junction point is relatively low (about 100 m or so from the tower top), a ‘mixed-mode’ of charge transfer occurs, resulting in a leader/return stroke type process separated from the tower top by a relatively short conducting channel section (see Figure 15 of [33]). In the mixed mode, the return-stroke-like process can start at the tower top or at the junction point between the downward leader and the ICC carrying channel. In the latter case, the strike object can be viewed as being composed of the tower and the conducting channel section below the junction point, attached to the tower top. In either case, the upward propagating RS-like wave should be dominant.

In our dataset, the number of ICC-pulses (44) is larger than the number of return-strokes pulses (24). A similar trend was reported for the Peissenberg and Gaisberg Towers [77], [92], with 90 ICC-pulses versus 35 return strokes and 139 ICC-pulses versus 97 return strokes, respectively. Figure 3-12 shows an example of a current waveform recorded at the Säntis Tower with more than 20 ICC pulses and only one return stroke.

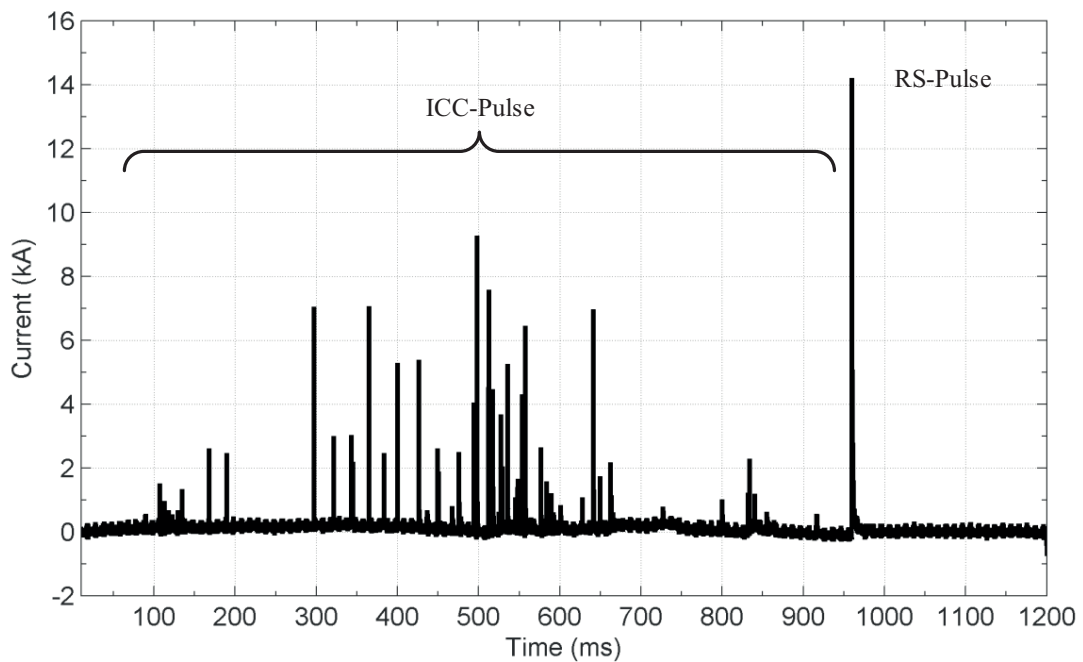


**Figure 3-12.** Current waveform associated with a flash that occurred on 21 October at 8:42 PM and exhibited many ICC-pulses and only one return stroke (Adapted from [87]).

A question arises as to why the number of ICC pulses is significantly larger than the number of return strokes. An explanation for this can be given by making reference to the M-component and mixed modes of charge transfer to ground as defined in [33],

in both of which a channel parallel to the existing one is involved in the charge transfer, with a common channel section between the junction point and the strike object (see Figure 15 of [33]). The difference between the two modes of charge transfer is essentially the height of the junction point, which is at a relatively short distance from the tower top (about 100 m or so) for the mixed-mode, and at larger distances (in excess of a kilometer) for the M-component mode. As evidenced by photographic observations (e.g., [83]), upward discharges can have multiple parallel channels involved in the charge transfer, which potentially results in a higher number of ICC pulses (whether due to M-component mode or mixed mode of charge transfer) relative to the number of “classical” leader/return sequences mostly following the main channel.

### 3.3 Ability of LLSs to Detect and Locate Negative Upward Flashes

In this section, we use the negative upward lightning flashes recorded at the Säntis Tower to assess the ability of lightning location systems to detect and locate upward negative flashes. Instrumented towers along with rocket-triggered lightning were used also to investigate the performance of lightning location systems (LLS). Both of these methods can provide valuable data on different characteristics of LLS like detection efficiency (DE), location accuracy (LA) and peak current estimation accuracy. A discussion on the differences between the DE and the LA obtained from direct tower measurements and other methods, such as video and continuous electric field recordings is in order.

- The DE and LA from tower data are valid for the tower position and they may be different for other parts of the region around the tower. The performance parameters obtained from video recordings, on the other hand, are valid for the region where a sufficiently unobstructed view can be guaranteed, preferably from more than one recording site. On the other hand, direct measurements using towers or triggered lightning provide exact locations, which is not the case for video or electric field recordings.
- Tower data are essentially based on upward lightning, which are characterized by the absence of the first return stroke, and the presence of an initial continuous current (ICC) with or without superimposed pulses. It is important to note that an appreciable number of upward flashes from towers might contain only an initial continuous current with neither superimposed pulses nor return strokes [30] and, therefore, cannot be detected by LLS. For example, the percentage of upward flashes containing only an ICC was 64% at Mount San Salvatore [57], and 48% at Gaisberg [61].

The presence of the tower might affect the location accuracy of LLS in different ways. On the one hand, the presence of a straight, tall strike object results in ‘clean’

electromagnetic field waveforms with enhanced amplitudes [93]. This effect is expected to have a beneficial impact on the location accuracy of LLS. On the other hand, the transient process along a tall strike object can cause distortions of the field waveforms that might negatively affect the performance of LLS. For example, the waveforms of the electric and magnetic fields associated with lightning strikes to the CN Tower in Toronto exhibit a first zero crossing about  $5\text{ }\mu\text{s}$  after the onset of the return stroke [94], which is due to the reflection of the current at the base of the tower. In general, the flash DE of a LLS is also affected by the number of strokes per flash. The more strokes occur in a given flash, the higher is the probability to detect this flash, because a flash is reported (detected) if at least one stroke (first or subsequent) is detected. Therefore, the flash DE can be much higher than any form of stroke DE. A more detailed description of the differences in the ground truth data evaluation methods can be found in [54].

We use current waveforms associated with upward negative flashes measured at the S antis Tower from June 2010 to December 2013 to evaluate the performance characteristics of the EUCLID network. Note that the majority of the recorded flashes at S antis are of upward type and only a few downward negative flashes were recorded in the period of analysis which were excluded from this study. It is worth noting that LLSs do not distinguish between upward and downward flashes.

#### 3.3.1 Data Set

In the period from June 2010 to December 2013, a total number of 327 flashes were recorded, out of which 273 flashes were classified as negative, 46 flashes as positive and 8 as bipolar. The great majority of the measured waveforms are associated with upward flashes. Among the 327 recorded flashes, based on the measured current waveforms, only 4 were identified as downward (3 negative and 1 positive).

It is worth noting that GPS time stamps were not available for some of the events due to a defective GPS card (138 out of 327 flashes). In those cases, the S antis data and EUCLID events were time correlated by analyzing the interstroke interval patterns which were used to calculate time offsets of S antis events due to a drift of the internal clock. Events from the S antis Tower and from EUCLID were considered synchronized if the two following criteria were satisfied after time drift correction: i) the time stamps of events (EUCLID and S antis) were within a time difference of 1ms, and ii) the location of events proposed by EUCLID were within a 5 km circle centered at the S antis Tower. Sometimes upward lightning is preceded and possibly initiated (note that the causality has not been established at this time) by a nearby downward lightning to ground and the applied 1ms time difference should be sufficient to avoid an erroneous correlation of the preceding lightning located by EUCLID and the discharge measured at the tower. Out of the considered 273

upward negative flashes, one was discarded because it was not possible to accurately correct time drift.

For the analysis of the performance of the EUCLID network on detection of upward lightning flashes, we will consider altogether negative return strokes (pulses occurring after the extinction of the ICC) and ICC pulses (superimposed on the initial continuous current fulfilling two conditions: a risetime lower than 8  $\mu$ s and an amplitude greater than 2 kA). These pulses are believed to be associated with the leader/return stroke mode of charge transfer, as opposed to slower pulses which are associated with the M-component charge transfer mode [95]. It should be mentioned that the 2 kA current amplitude criteria was applied based on the study by [96] in which the smallest value of the return stroke current amplitude that can exist in nature lies in the range of 1.5 to 3.0 kA. Note, in addition, that ICC pulses with risetimes greater than 8  $\mu$ s are rarely located by EUCLID as those slow rising currents do not radiate sufficient fields to be detected by several sensors.

It should be noted that throughout Section 3.4, both return strokes and ICC pulses fulfilling the above two conditions will be referred to as pulses.

It is important to note that upward flashes containing only an initial continuous current ICC (with neither superimposed pulses with peaks higher than 2 kA, nor return strokes) were not considered in the present analysis. These flashes (labeled ‘ICC<sub>Only</sub>’ in [61]) were excluded for two reasons. First, LLS’s are not able to detect ICC<sub>Only</sub> flashes. Second, the lightning measurement system currently installed at the S antis Tower is triggered by the di/dt signal measured by the B-dot sensor and, therefore, it is likely that the system misses most of the flashes containing ICC<sub>Only</sub>.

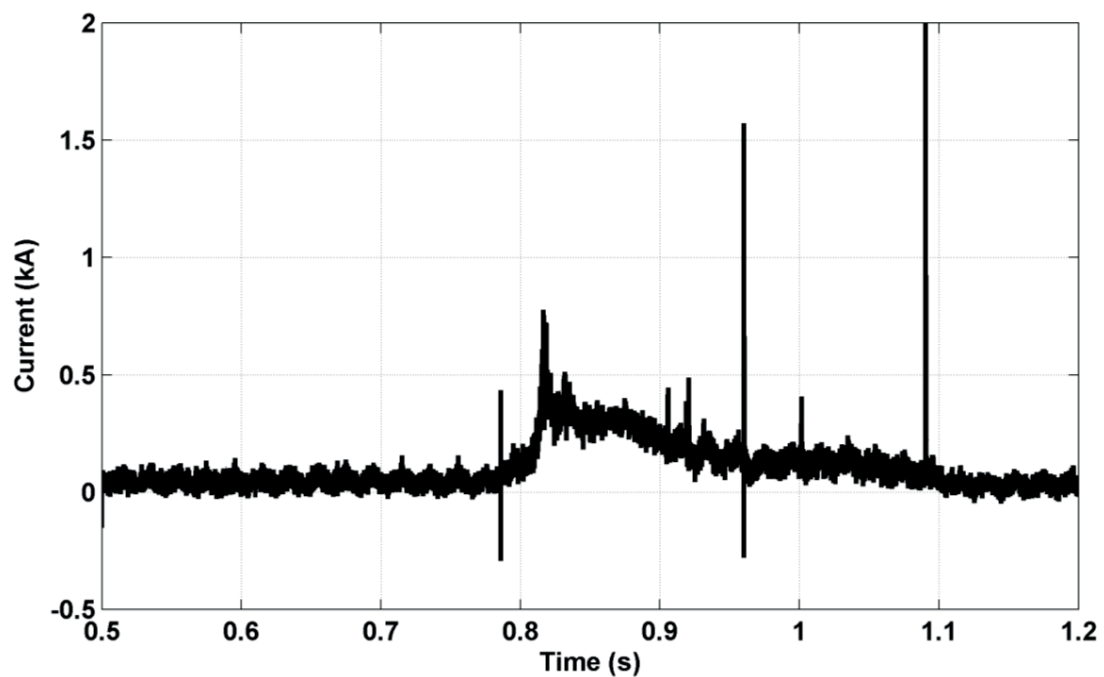
#### 3.3.2 Detection Efficiency

Table 3-3 presents the flash detection efficiency for negative flashes to the S antis Tower observed in the mentioned period, during which 269 upward flashes were recorded by the current measurement system with available timestamps. Out of these 269 flashes, 7 (2.6%) were characterized by an ICC with no pulses satisfying the higher than 2 kA peak current and were not considered in the analysis. Figure 3-13 shows an example of a negative flash with just an ICC and low amplitude ICC pulses. Out of the considered flashes, 253 were detected by the EUCLID network, resulting in a flash detection efficiency of 97%.

It is worth noting that the number of pulses per flash (multiplicity) for upward flashes measured at S antis has a median value of about 8 [97], which is about twice as high as the multiplicity of downward flashes [42]. This might explain the obtained high value for the EUCLID efficiency in detecting S antis flashes, despite the fact that upward flashes do not have first strokes.

**Table 3-3. Flash detection efficiency of the EUCLID network associated with negative lightning flashes to the Sántis Tower.**

|   |     |
|---|-----|
| Number of recorded upward negative flashes with available corrected time stamp at the Sántis Tower                  | 269 |
| Number of recorded ICC <sub>Only</sub> flashes (ICC and minor ICC pulses (peak current < 2 kA)) at the Sántis Tower | 7   |
| Number of detected flashes by the EUCLID Network  | 253 |
| Flash detection efficiency of the EUCLID Network excluding ICC <sub>Only</sub> flashes                              | 97% |



**Figure 3-13. Measured current waveform associated with an upward negative flash recorded on 18:40:15, 25 August 2012. The current is characterized by a low amplitude ICC and ICC pulses with no return strokes.**

A total of 2795 pulses classified either as return strokes or as ICC pulses satisfying the risetime and amplitude criteria were identified. Figure 3-14 shows the peak current distribution of these pulses, featuring a maximum value of 29.6 kA, a median of 7.1 kA, and a geometrical mean value of 6.3 kA.



Figure 3-15 presents the pulse detection efficiency as a function of measured peak current at the Sântis Tower. As expected, the detection efficiency of the EUCLID network increases with the peak current value. The overall pulse detection efficiency is 73%. For pulses with peak values higher than 5 kA, the pulse detection efficiency is about 83%.

It is interesting to note that, among the total number of 2036 detected pulses, 73% of the time-correlated pulses were classified as cloud pulses by EUCLID. This can be explained by the fact that ICC pulses with short current risetimes are believed to be associated with leader/return stroke mode discharges to an existing channel branch at some height above the tower top [33], [95]. Another reason for misclassification is that electric fields radiated from return strokes to a tall tower might feature a shorter peak-to-zero time [73] or an undershoot (for very tall structures) [98].

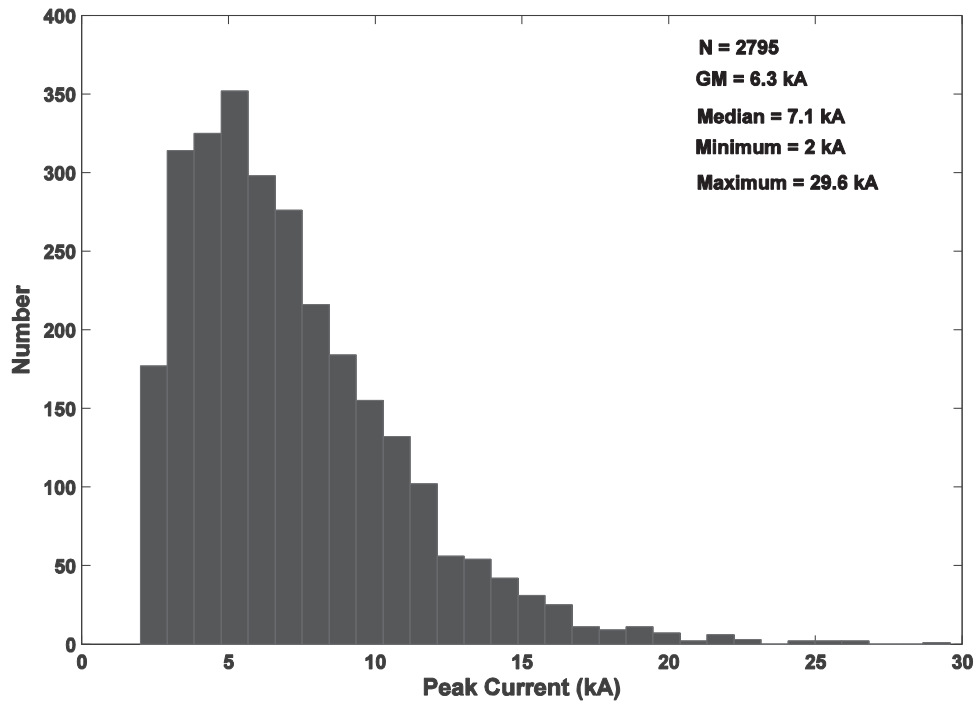


Figure 3-14. Peak current distribution of pulses associated with upward negative flashes measured at the Sântis Tower (Adapted from [76]).



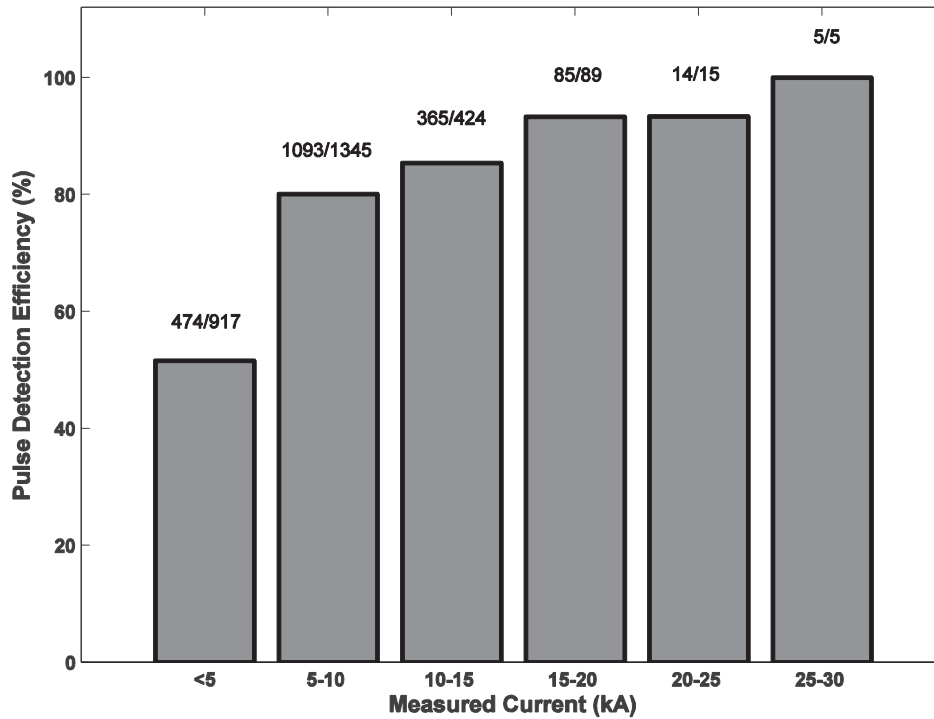


Figure 3-15. EUCLID detection efficiency as a function of pulse peak current measured at S antis (the bin size of 5 kA) for upward negative events (Adapted from [76]).

#### 3.3.3 Location Accuracy

Figure 3-16 presents a plot of pulse locations estimated by the EUCLID network for the S antis Tower pulses. In that figure, the location of each pulse is marked with a circle whose radius is proportional to the peak current value measured at the S antis Tower. It can be seen that most of the pulse locations are around the tower. However, a secondary cluster is located in the south of the tower. As shown in Figure 3-17, these larger location errors are related to low peak pulses (lower than 10 kA or so), most of which are associated with ICC pulses. As discussed in [76], ICC pulses with short risetimes are due to return strokes attaching to an existing channel and often involve strongly tilted channel branches at low altitudes. As a result, larger location errors are associated with them.

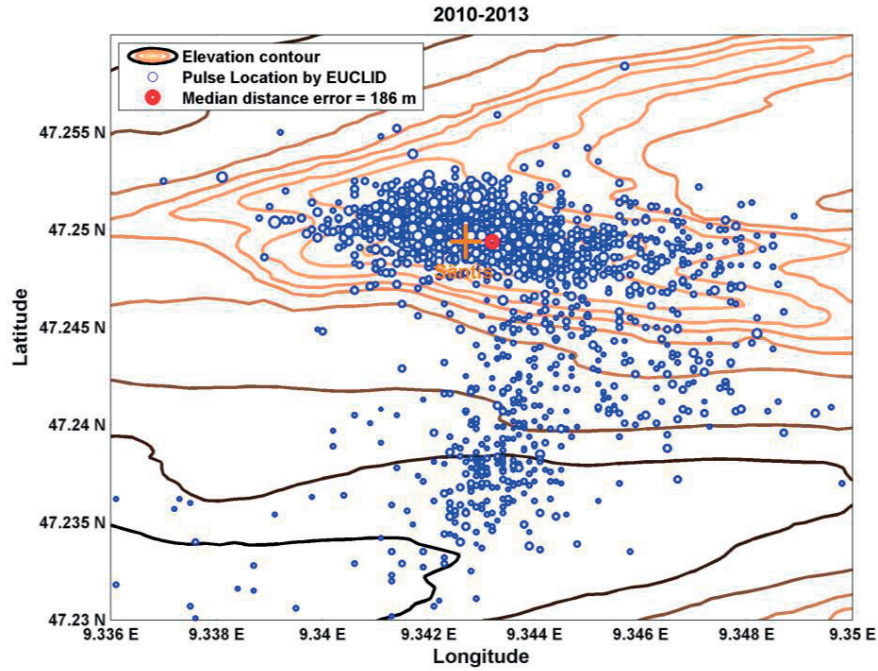


Figure 3-16. Plot of EUCLID pulse locations for upward negative flashes recorded in the period of analysis. The size of the circles is proportional to the current peak measured at Sântis. The base and height of the shown area are respectively 3.34 and 1.06 km (From [76]).

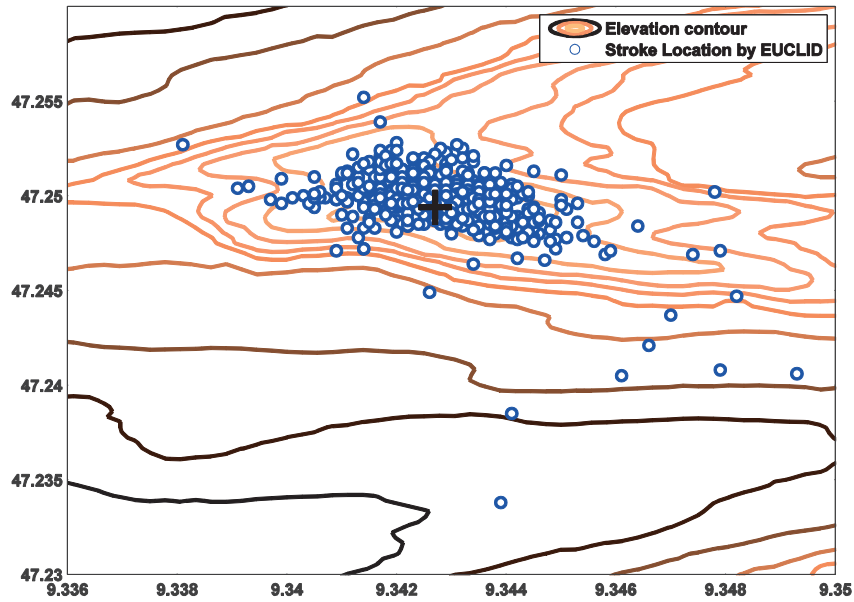


Figure 3-17. Plot of pulse locations estimated by EUCLID excluding pulses with peak values lower than 10 kA (From [76]).

On the other hand, the location accuracy seems not to be appreciably affected by the current risetime, as can be seen in Figure 3-18 in which the absolute location errors of the EUCLID network are presented as a function of the 10-90% current risetime. In this figure, the radius of each circle is proportional to the current peak value. It can be seen that no clear correlation can be found between current rise time and the absolute location error. It is worth noting that, for pulses with much larger risetimes (8  $\mu$ s and larger), it is expected that the probability of detection decreases considerably. Data at the Gaisberg Tower have revealed that only 3% of the pulses with current risetimes greater than 8  $\mu$ s were detected by EUCLID [Diendorfer, 2015].

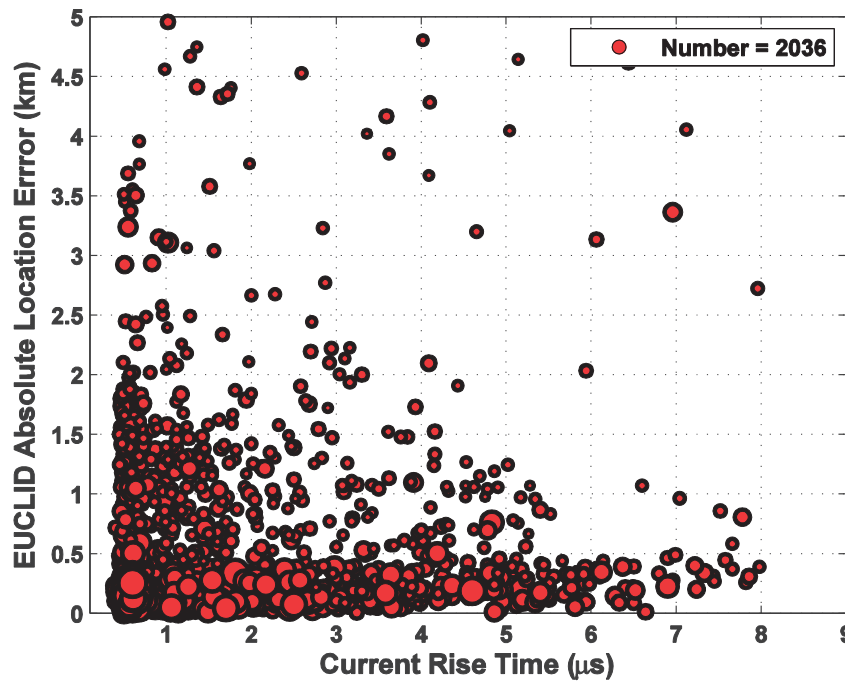


Figure 3-18. EUCLID absolute location error versus measured 10-90% current rise time for upward negative pulses. The radius of each circle is proportional to the current peak value (From [76]).

The median of the absolute distance error, defined as the median distance between the Sântis Tower location and EUCLID's stroke locations, is 186 m. The absolute location error as a function of the peak current measured at the Sântis Tower is presented in Figure 3-19 in separate plots, one for each study period year. It can be seen that large location errors are associated with pulses whose measured current peaks are lower than 10 kA. It can also be seen from Figure 3-19 that the location accuracy of the EUCLID network improved considerably in 2013 following an upgrade in the used location algorithms to account for propagation effects [74]. Table

3-4 presents the evolution of the median and the mean values for the absolute distance error.

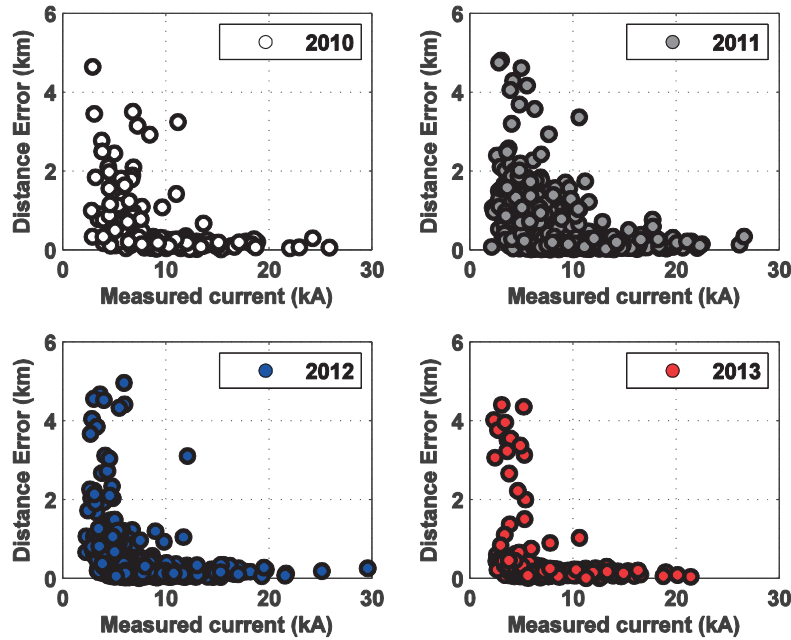


Figure 3-19. EUCLID absolute location error versus Sântis Tower measured peak current for pulses of upward negative events. Data are presented in different plots and different colors are associated with each of the four years of considered in this study (From [76]).

Table 3-4. Evolution of the median and mean values of absolute distance error for pulses detected by the EUCLID network.

| Year                | 2010 | 2011 | 2012 | 2013 |
|---------------------|------|------|------|------|
| Number of Pulses    | 167  | 1104 | 494  | 271  |
| Median (m)          | 219  | 191  | 186  | 160  |
| Arithmetic Mean (m) | 587  | 487  | 449  | 386  |

An important factor that might affect location accuracy of the system is the number of reporting sensors for each pulse. Figure 3-20 shows EUCLID absolute location

error versus the number of its reporting sensors for each pulse. As expected, the absolute distance error decreases with an increase of the number of reporting sensors.

Figure 3-21a shows a scatter plot of EUCLID's semi-major axis length of the 50% confidence ellipse for each pulse versus measured peak current. It can be seen that the majority of large semi-axis values are associated with low peak current values. A plot of EUCLID's semi-major axis length of the 50% confidence ellipse versus location error is presented in Figure 3-21b. In this figure, pulses characterized by peak currents lower than 10 kA are shown in red, while those associated with peak currents greater than 10 kA are shown in blue. It can be seen that the peak current is the critical parameter determining the location accuracy. It is worth noting that using the median confidence ellipse as a measure of the median location error of LLS's is widely accepted and its accuracy was validated based on lightning to the Gaisberg Tower [99].

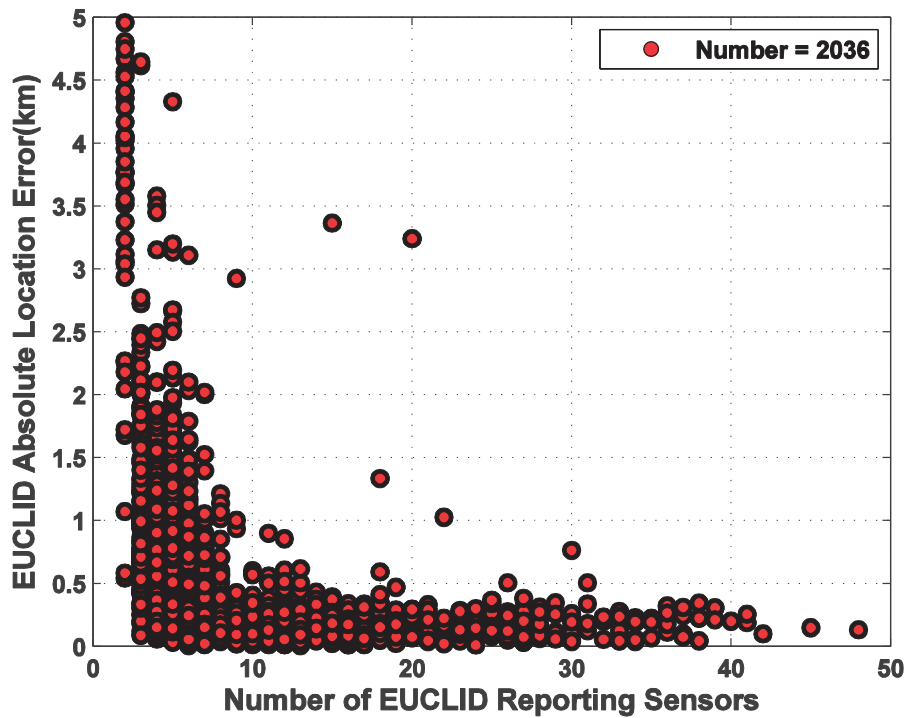
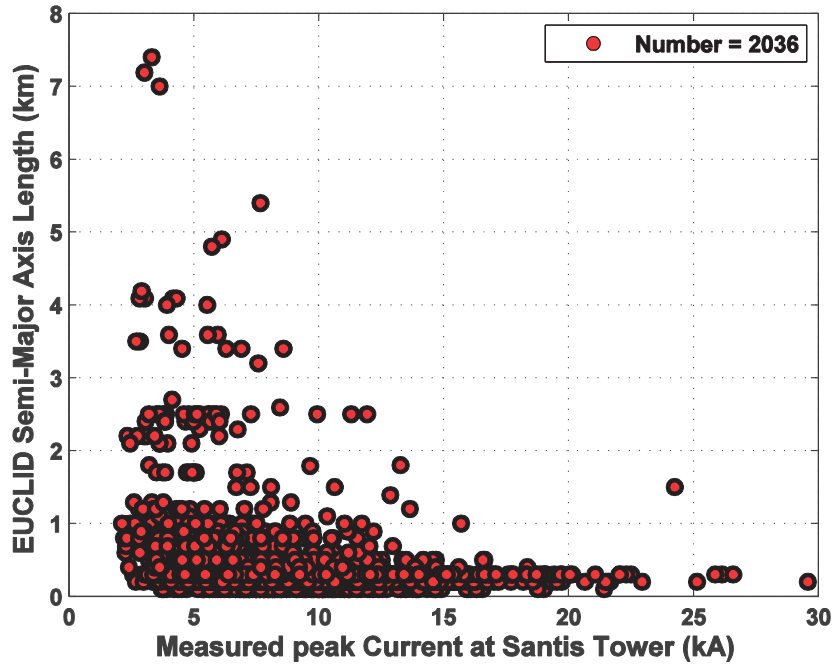
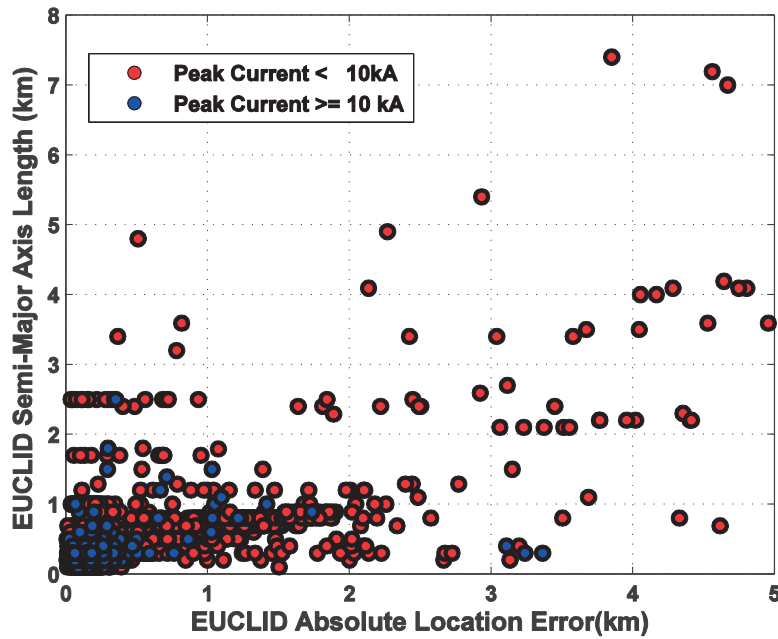


Figure 3-20. EUCLID absolute location error versus the number of EUCLID reporting sensors (From [76]).



(a)



(b)

Figure 3-21. a) EUCLID semi-major axis length of the 50% confidence ellipse versus peak current value of upward negative pulses measured at the Sântis Tower, b) EUCLID semi-major axis length of the 50% confidence ellipse versus absolute location error of upward negative pulses (From [76]).

### 3.3.4 Peak Current Estimation

The problem of indirect estimation of lightning return stroke currents from remote electromagnetic field measurements has been thoroughly discussed in the literature (see, e.g. [90] ). From a theoretical point of view, it has been shown [100] that a statistical estimation (e.g. in terms of mean values and standard deviations) of the current peak is possible from remote field measurements. However, due to the high variability of key parameters such as the return stroke speed, it is impossible to determine the lightning current accurately from the remotely measured electric or magnetic field for a given event. On the other hand, triggered lightning was used to test peak current estimates provided by LLSs. It was shown that the ratio of directly measured and estimated current peaks was characterized by an arithmetic mean of 1.1 [101].

Figure 3-22 presents peak current estimates provided by the EUCLID network as a function of the peak currents directly measured at Säntis. It can be seen that EUCLID tends, in general, to overestimate the peak current. The best-fit linear regression, forced to go through the origin, is also shown in Figure 3-22 which shows that the current estimates provided by EUCLID are typically about 1.8 times higher than those from direct measurements. Note that this difference is well above the uncertainty associated with the current measurement system (Rogowski coil), which has been estimated to be less than 3% [102].

The overestimation of the peak current can be attributed to the enhancement of the radiated electromagnetic fields due to the presence of the tower and the mountain (e.g. [98], [103]–[105]). In the next section, we present a full-wave FDTD analysis [72] supported by experimental observations consisting of simultaneous records of lightning currents and electric fields which reveals that the combined effect of tower and mountainous terrain topography around the Säntis Tower results in an enhancement of the radiated electric field, which is consistent with the overestimation of the EUCLID Network.

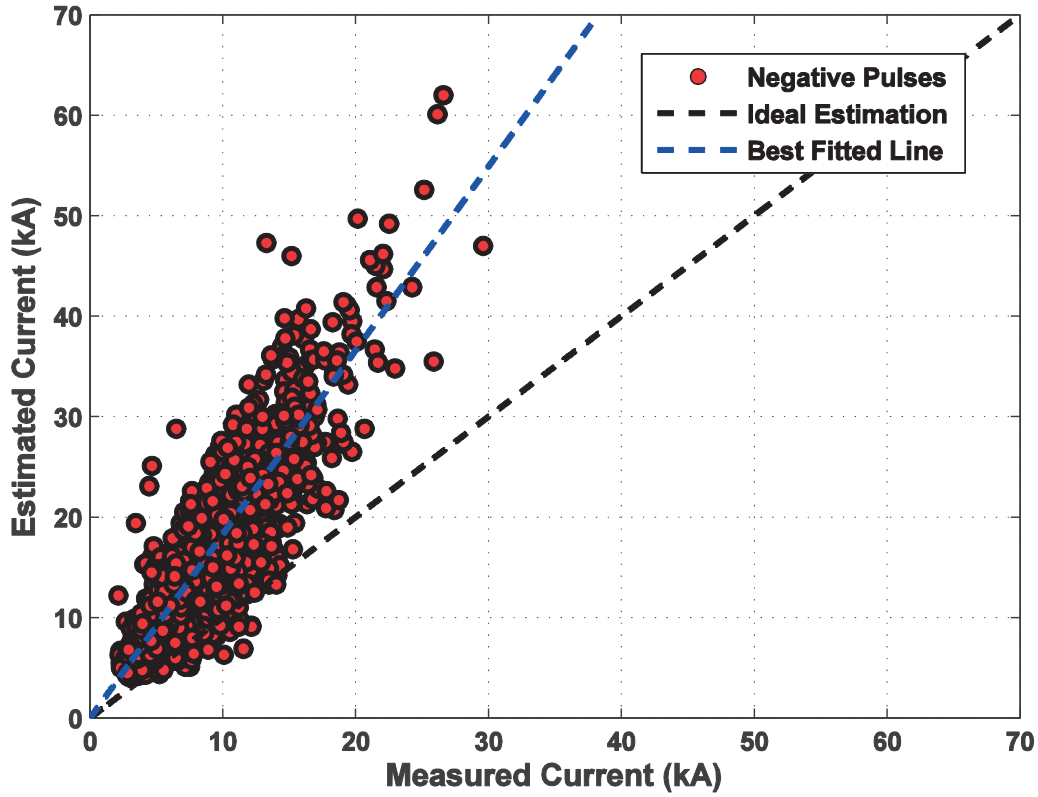


Figure 3-22. EUCLID peak current estimates versus peak currents directly measured at the S antis Tower (From [76]).

### 3.4 Lightning Electromagnetic Field Propagation along Mountainous Terrain

As it was found in Section 3.3, the reported peak current values of S antis strokes were overestimated by EUCLID by a factor of about 1.8, while the performance analysis of EUCLID using Gaisberg Tower data doesn't show such an enhancement [92]. Due to the fact that the lengths of the two tower structures are not that much different (73 m for Gaisberg Tower and 124 for S antis Tower), we speculated that the different geographical terrain of the S antis Tower must be the reason behind the enhancement of the radiated field.

The topic of wave propagation of lightning stroke fields along none-flat terrain has recently received some attention. Soto et al. [106], [107] presented FDTD calculations of lightning electromagnetic fields for a lightning discharge striking the top of a cone-shaped mountain. Paknahad et al. presented, for a similar configuration, FEM (Finite-Element Method) simulations for both, above-ground and underground fields [108]. These studies showed that lightning electromagnetic



fields could be affected by a none-flat ground configuration. Schulz and Diendorfer have attempted to consider a real terrain model by evaluating the length of the propagation path using the terrain model, and correcting the time errors related to the signal path elongation [109]. They noted that the location accuracy of lightning location systems could be improved after considering such correction [110].

All the studies considering a non-flat ground are based either on a fractal method to represent a rough surface or on simplified representations of the mountain (conical, pyramidal). In this section, we present a theoretical analysis of the propagation effects of lightning electromagnetic fields over a mountainous terrain. The analysis is supported by experimental observations consisting of simultaneous records of lightning currents measured at the Säntis tower and associated electric fields measured at a distance of 14.7 km from the tower.

#### 3.4.1 FDTD Modeling Scheme

In order to take into account the real geographical terrain between the Säntis Tower and the field measurement station, the global digital elevation model version 2 (GDEM V2) from advanced space-borne thermal emission and reflection radiometer (ASTER) (henceforth referred to as “ASTER GDEM”) has been adopted. ASTER GDEM was developed jointly by the U.S. National Aeronautics and Space Administration and Japan’s Ministry of Economy, Trade, and Industry, which covers 99% of the Earth’s landmass and spans from 83°N to 83°S at a spatial resolution of 1 arc-second (approximately 30 m at the equator) [111]. The overall accuracy of ASTER GDEM V2 is about 17 m at the 95% confidence level evaluated by the ASTER GDEM validation team [111]. Figure 3-23 shows the topographic map in the region of interest that includes the Säntis tower and the field measurement station. Figure 3-24 shows the two-dimensional (2-D) cross-section of the topographic map along the direct path between the tower and the field measurement station (see red-dashed line in Figure 3-23).

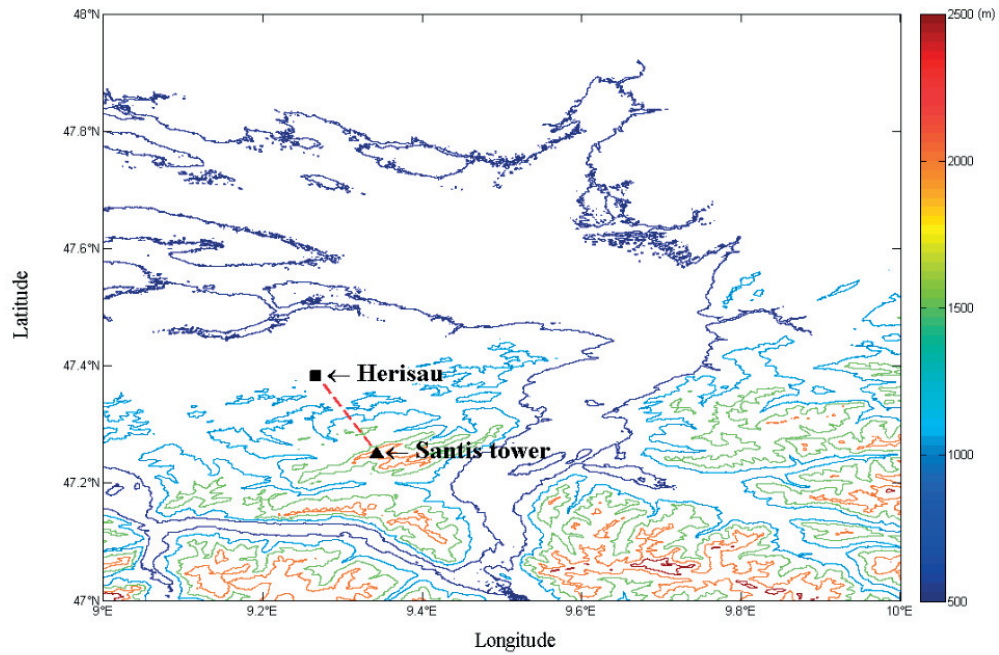


Figure 3-23. Topographic map of Säntis Mountain region along with the location of Herisau field Station. Data was obtained from ASTER GDEM. (From [72]).

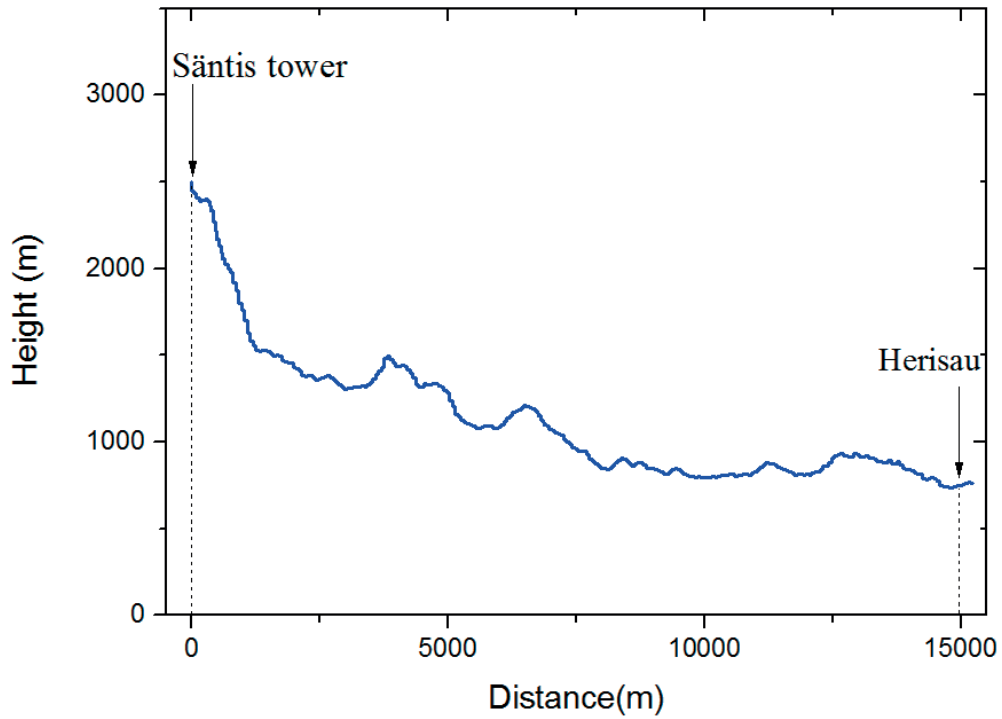


Figure 3-24. Two-dimensional cross-section of terrain in between Säntis Tower and Herisau field station (From [72]).

Because of the distance between the Sântis tower and the field measurement station (about 15 km), a three-dimensional (3-D) FDTD simulation taking into account the topography would require prohibitive computation time and memory requirements. We have therefore considered in this study a 2-D axial symmetric model using the topographic data shown in Figure 3-24, which was imported into our FDTD simulation code. The geometry of the problem is shown in Figure 3-25a. The adopted 2-D axial symmetric assumption appears to be reasonable since, in our case, the tower is located on the top of the Sântis Mountain, which is the highest point in the considered region (see Figure 3-25a). Additionally, this assumption allows a significant reduction of the computational complexity of the problem.

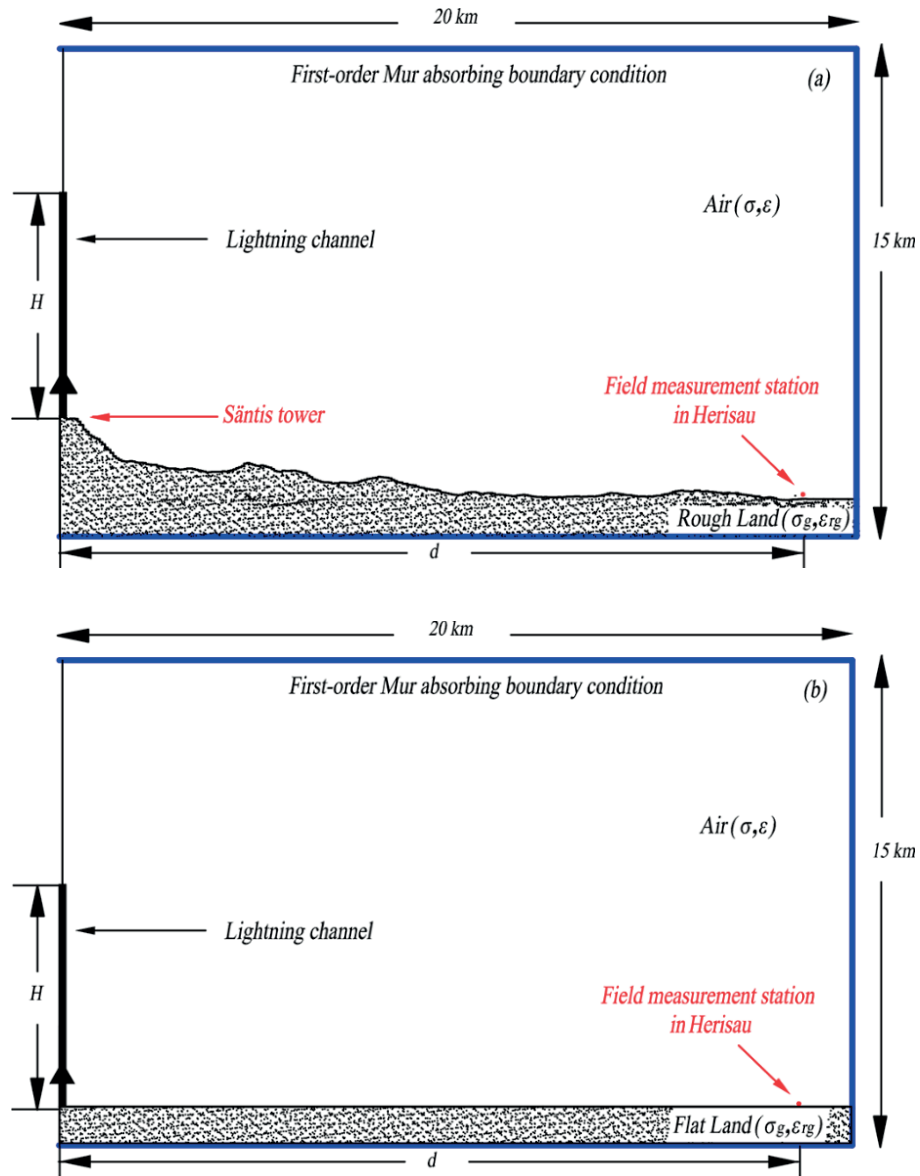


Figure 3-25. Geometry for the FDTD simulation domain. a) Taking into account the 2-D topography of the terrain. b) Assuming a flat ground (From [72]).

In order to analyze the effect of the field propagation along an irregular terrain, we also considered the commonly used assumption of a flat ground as shown in Figure 3-25b. Note that, in our case, the effect of the presence of the Säntis tower can be neglected, due to the small round-trip time along the tower relative to the risetime of current waveforms (e.g., [104], [112]).

As already mentioned in Chapter II, the field sensors were located on the roof of a building. As discussed in the literature (e.g., [98], [113], [114]), the presence of the building might result in an enhancement of the electric field. This issue will be discussed further in Section 3.5.3.

For the FDTD analysis, cylindrical coordinates are adopted and the first-order Mur absorbing boundary conditions are employed to truncate the computational domain [115]. The air and the ground are both represented by Yee's grid units [116]. The FDTD simulation domain of 20 km×15 km is illustrated in Figure 3-25. The spatial discretization was  $\Delta r = \Delta z = 10\text{m}$  and the time increment was set to 19.2 ns, which satisfies the time and space stability condition for FDTD. The ground was characterized by a conductivity  $\sigma_g$  and a relative permittivity  $\epsilon_{rg}$ .

The lightning channel was set in the symmetry axis of the 2-D axial symmetric model and the current distribution along the return stroke channel was specified according to the modified transmission line model with exponential decay (MTLE) [117], [118], assuming a current decay constant  $\lambda = 2\text{ km}$  [119]. The channel height is assumed to be  $H = 7.5\text{ km}$  and the return stroke speed was set to  $v = 1.5 \times 10^8\text{ m/s}$ . A discussion on the influence of the return stroke model and the adopted value for the return stroke speed will be given in Section 3.5.3.

The simulations were carried out on a computer with an Intel Xeon E5450 processor and 32 GB of available memory. The developed FDTD simulation code has been thoroughly validated against results obtained using FEMs [120].

#### 3.4.2 Simulation Results

We use the simultaneous current and electric field waveforms of the lightning flash occurred on October 22, 2014 at 1:14 AM (presented in Figure 3-2) to validate the proposed FTDT simulation.

The current waveform is typical of upward negative flashes with an initial stage comprising the so-called initial continuous current (ICC) which corresponds to an upward positive leader (see, [18] ch. 6). ICC pulses [labeled as  $\text{ICC}_{p1}$  through  $\text{ICC}_{p6}$  in Figure 3-2a] are superimposed to this ICC. After the extinction of the ICC, the waveform features six other pulses resulting from downward leader–return stroke sequences [labeled as  $\text{RS}_1$  through  $\text{RS}_6$  in Figure 3-2a]. We have selected three return strokes (labeled as  $\text{RS}_2$ ,  $\text{RS}_5$ , and  $\text{RS}_6$ ) and one ICC pulse (labeled as  $\text{ICC}_{p3}$ ) for the analysis.

*Return Stroke Pulses.* The channel base currents associated with the considered return strokes were not directly used in the FDTD simulations because of the superimposed noise. Instead, they were represented using the sum of two Heidler's functions Eq. (4.1) [121].

The parameters of Eq. (4.1) were determined using a genetic algorithm (GA) [122]. Figure 3-26 presents the measured current waveforms associated with the three considered return stroke pulses along with their analytical representations using Heidler's functions. The determined parameters of the functions for each waveform are given in Table I.

$$\begin{aligned}
 i(0,t) &= \frac{I_{01}}{\eta_1} \frac{(t/\tau_{11})^{\eta_1}}{[(t/\tau_{11})^{\eta_1} + 1]} e^{-t/\tau_{12}} + \frac{I_{02}}{\eta_2} \frac{(t/\tau_{21})^{\eta_2}}{[(t/\tau_{21})^{\eta_2} + 1]} e^{-t/\tau_{22}} \\
 \eta_1 &= \exp\left(-\frac{\tau_{11}}{\tau_{12}} \cdot \left(n_1 \frac{\tau_{12}}{\tau_{11}}\right)^{1/n_1}\right) \\
 \eta_2 &= \exp\left(-\frac{\tau_{21}}{\tau_{22}} \cdot \left(n_2 \frac{\tau_{22}}{\tau_{21}}\right)^{1/n_2}\right)
 \end{aligned} \tag{4.1}$$

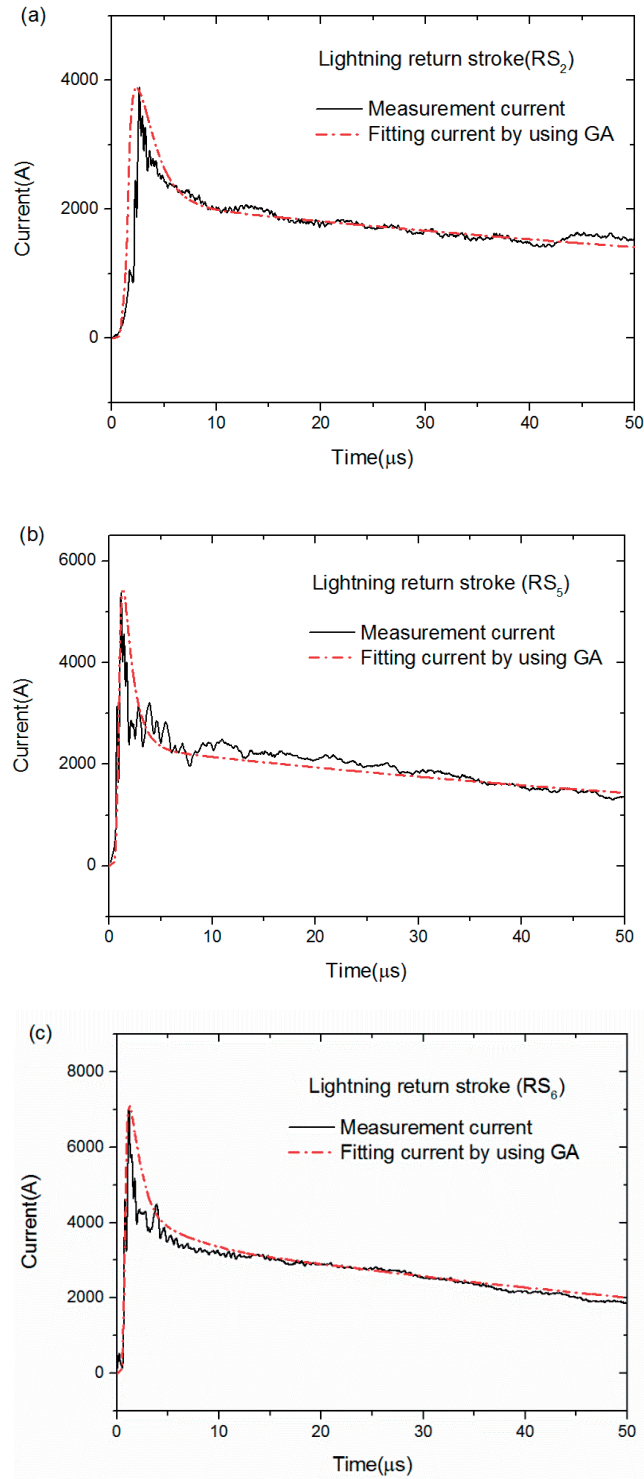


**Figure 3-26. Measured current waveforms associated with the three selected return strokes (solid line) and their analytical representations using Heidler's functions (dashed line). (a) Case1: RS<sub>2</sub>, (b) Case2: RS<sub>5</sub> and (c) Case3: RS<sub>6</sub> (Adapted from [72]).**

**Table 3-5. Parameters of the Heidler's functions used to represent the return stroke current waveforms.**

| Lightning return stroke | <b>I01</b><br>(kA) | <b><math>\tau_{11}</math></b><br>( $\mu$ s) | <b><math>\tau_{12}</math></b><br>( $\mu$ s) | <b>n1</b> | <b>I02</b><br>(kA) | <b><math>\tau_{21}</math></b><br>( $\mu$ s) | <b><math>\tau_{22}</math></b><br>( $\mu$ s) | <b>n2</b> |
|-------------------------|--------------------|---|---|-----------|--------------------|---|---|-----------|
| <b>Case 1 : RS2</b>     | 2.6                | 2.0   | 1.5   | 2.0       | 2.1                | 1.0   | 120   | 9.0       |
| <b>Case 2: RS5</b>      | 4.0                | 0.1   | 1.0   | 7.0       | 2.3                | 1.0   | 100   | 6.0       |
| <b>Case 3: RS6</b>      | 7.3                | 0.8   | 3.0   | 7.0       | 3.0                | 5.0   | 80  | 3.0       |

Figure 3-27 presents a comparison between FDTD simulation results and the obtained experimental data for the vertical electric fields generated by the three return strokes. For the comparison, we have considered the two terrain profiles illustrated in Figure 3-25, namely an irregular ground model based on a 2D representation of the topographic map (Figure 3-25a), and a flat ground (Figure 3-25b). The conductivity and the relative permittivity of the ground were set to  $\sigma_g = 0.01$  S/m and  $\epsilon_{rg} = 10$ , respectively. A discussion on the influence of the ground conductivity will be given in Section 3.5.3.



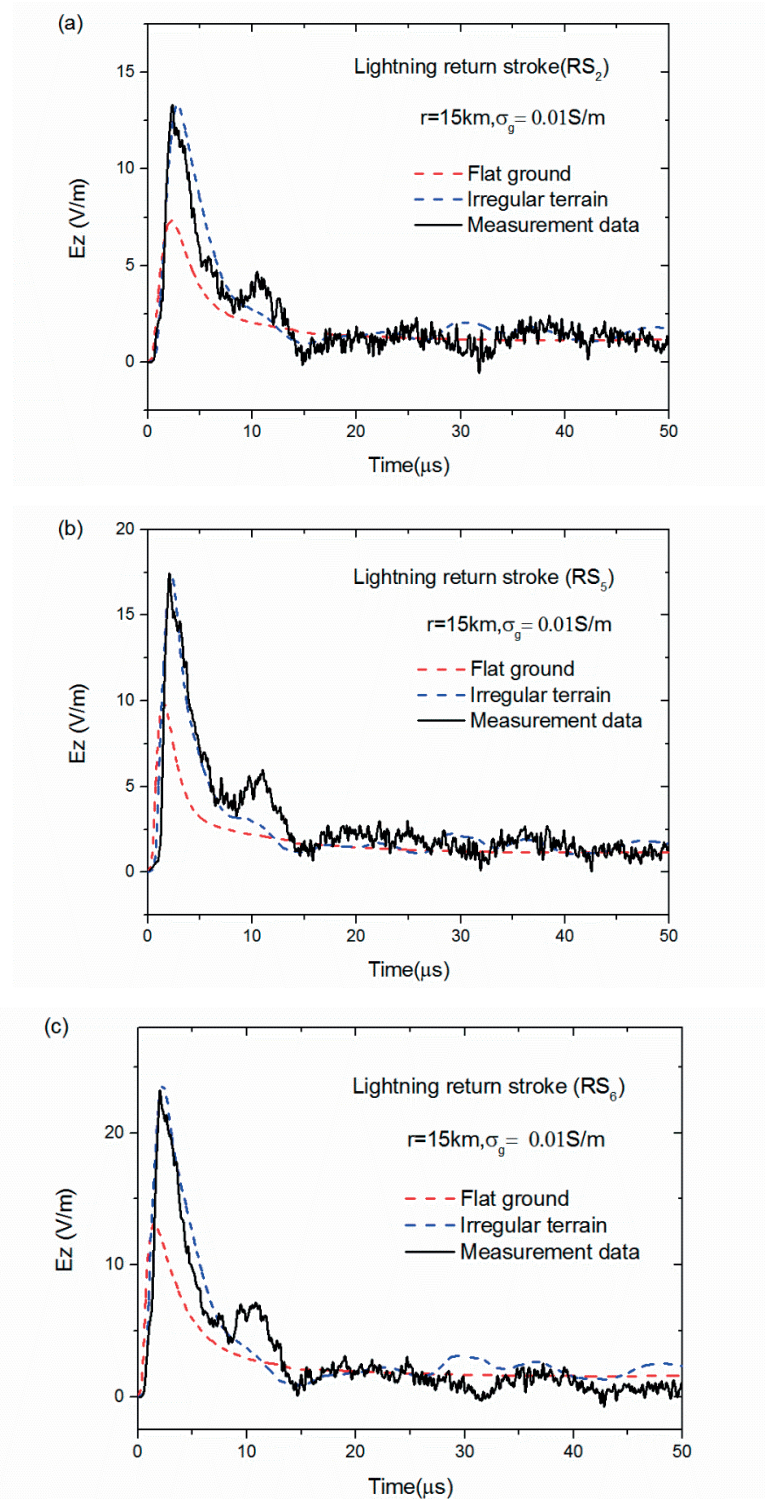


Figure 3-27. Vertical electric fields at 15 km associated with return stroke pulses shown in Fig. 9. Solid line: Measured waveforms; Red dashed lines: simulated waveforms assuming a flat ground; Blue dashed lines: simulated waveforms taking into account the terrain profile. (a) Case 1: RS<sub>2</sub>, (b) Case2: RS<sub>5</sub> and (c) Case3: RS<sub>6</sub>. Ground parameters:  $\sigma_g = 0.01$  S/m,  $\epsilon_{rg} = 1$  (From [72]).



It can be seen that, considering the real irregular terrain between the Säntis tower and the field measurement station, both the waveshape and amplitude of the simulated electric fields are in excellent agreement with the measured waveforms. On the other hand, the assumption of a flat ground results in a significant underestimation of the peak electric field.

It is interesting to note that the obtained results are consistent with the performance analysis of the European lightning detection network (EUCLID) presented in Section 3.4.4, in which it was shown that the peak current estimates provided by the EUCLID network were about 1.8 times higher than those from direct measurements. This overestimation can be attributed to the enhancement of the radiated electromagnetic fields associated with the presence of the irregular, mountainous terrain around the Säntis Tower.

A discussion is in order on the observed enhancement of the electric field. It is well known that a tall tower struck by lightning results in an enhancement of the radiated electromagnetic fields (e.g., [93], [123], [124]). As mentioned earlier, the effect of the presence of the Säntis tower on the radiated field is negligible because of the small round-trip time along the tower relative to the risetime of the current waveforms. The question, however, is whether the observed enhancement in this case is due to the presence of the tall mountain on which the tower is sitting.

To address this question, we have considered an alternative profile in which we have approximated the mountain by a cone over a flat ground (red shape in Figure 3-28), and compared it with the results considering the irregular terrain (represented in blue in the same figure). Figure 3-29 shows the simulated fields for the two profiles, along with the measured waveform. It can be seen that the red profile results in a significant enhancement effect on the field, which, to some extent, can be considered as similar to the presence of a tall strike object. On the other hand, the propagation along the irregular terrain around the tall mountain appears to produce a counterweight to this effect, resulting in a simulated electric field which is in excellent agreement with the measured one.

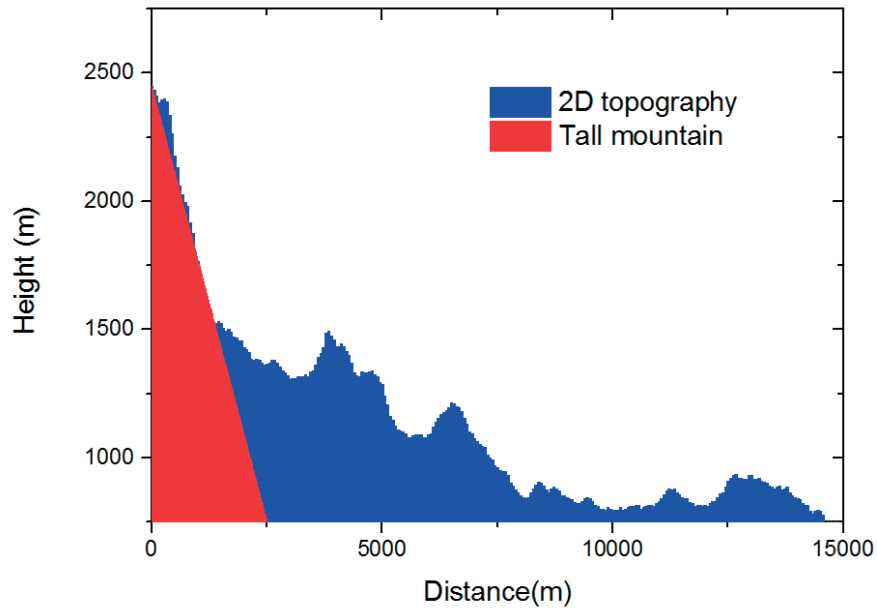


Figure 3-28. Analysis of the effect of the enhancement. Red profile: approximation of the mountain using a cone over a flat ground. Blue profile: 2D topography of the terrain (Adapted from [72]).

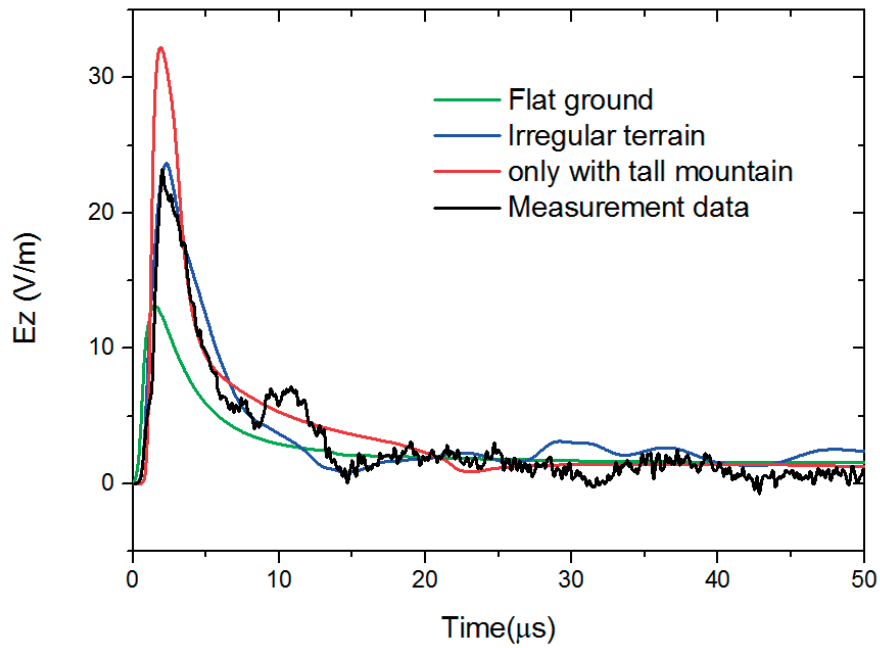
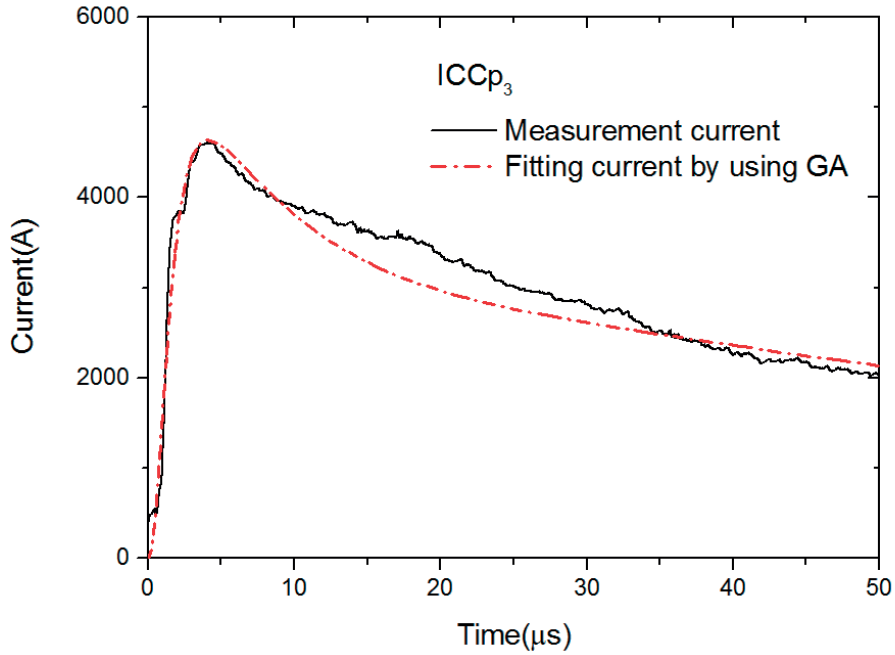


Figure 3-29. Comparison between simulated fields associated with a flat ground (green line), irregular terrain (blue profile in Figure 3-28) and the ground with a tall mountain (red profile in Figure 3-28). The black curve corresponds to the measured waveform (Adapted from [72]).

*ICC Pulses.* In this subsection, we present simulation results for the electric fields associated with an ICC pulse labeled ICCp3 in Figure 3-2. This ICC current pulse is characterized by a 10-90% risetime of  $2.26 \mu\text{s}$  and a peak amplitude of  $4.6 \text{ kA}$ . As for the return stroke waveforms, the ICC current pulse was represented by the sum of two Heidler's functions whose parameters were determined using a GA approach, with  $I_{01} = 4.2 \text{ kA}$ ,  $\tau_{11} = 2.0 \mu\text{s}$ ,  $\tau_{12} = 6.0 \mu\text{s}$ ,  $n_1 = 2.0$  and  $I_{02} = 2.5 \text{ kA}$ ,  $\tau_{21} = 8.0 \mu\text{s}$ ,  $\tau_{22} = 90.0 \mu\text{s}$ ,  $n_2 = 2.0$ . Figure 3-30 presents the measured current waveform associated with ICCp3 (solid line). In the same figure, the analytical representation is also shown in dashed line.



**Figure 3-30.** Measured current waveform associated with the selected ICC pulse (ICCp3 in Figure 3-2) in solid line, and its analytical representations using Heidler's functions in dashed line (Adapted from [72]).

The vertical electric field associated with the ICC pulse was determined following the same approach as the one used for the return stroke pulses. The same model (MTLE) and the same parameters for the return stroke speed were also adopted. presents the comparison between FDTD E-field simulation results and the obtained experimental data. It can be seen that the simulation results taking into account the terrain profile are in reasonable agreement with the measured data, suggesting that the hypothesis of Flache et al. [95] on the charge transfer mechanism is appropriate. Further studies, however, are needed to confirm this hypothesis. The observed difference in the peak value of the field is about 21%. Similar to the results obtained for the return strokes, it can be seen that the assumption of a flat ground results in a significant underestimation of the peak electric field associated with the ICC pulse.

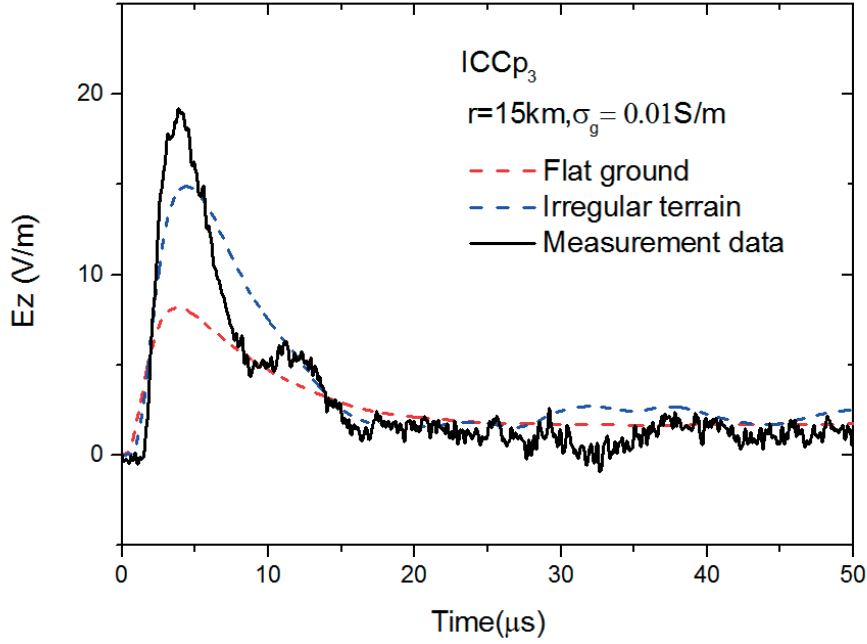


Figure 3-31. Vertical electric fields at 15 km associated with the ICC pulse shown in Figure 3-28. Solid line: Measured waveforms. Red dashed lines: Simulated waveforms assuming a flat ground. Blue dashed lines: Simulated waveforms taking into account the terrain profile. Ground parameters:  $\sigma_g = 0.01$  S/m,  $\epsilon_{rg} = 10$  (Adapted from [72]).

### 3.4.3 Sensitivity Analysis of Parameters

In this section, we discuss the effect of various parameters of simulation such as ground conductivity, the return stroke speed, the adopted return stroke model and the presence of the building on which the field sensors were located.

*Ground Conductivity.* Figure 3-32 shows the FDTD simulations considering three different conductivities for the ground associated with the return stroke (RS6) in Figure 3-2: (i) Perfectly conducting, (ii)  $\sigma_g = 0.01$  S/m, and (iii)  $\sigma_g = 0.001$  S/m. The relative permittivity was set to  $\epsilon_{rg} = 10$  in all cases.

It can be seen that the ground conductivity affects essentially the early-time behavior of the vertical electric field (see [125] for a review on the effect of propagation along a lossy ground). A decrease of the conductivity from 0.01 S/m to 0.001 S/m results in a decrease of the peak electric field of about 15%. The effect of the ground conductivity appears therefore to be less significant compared to the effect of the propagation over the considered rough terrain. Note that we have considered a simple, homogeneous model for the ground with constant, frequency-independent electrical parameters. A more thorough analysis taking into account the soil inhomogeneity (e.g., [126], [127]) and frequency dependence (e.g., [112], [128], [129]) is beyond the scope of this study.

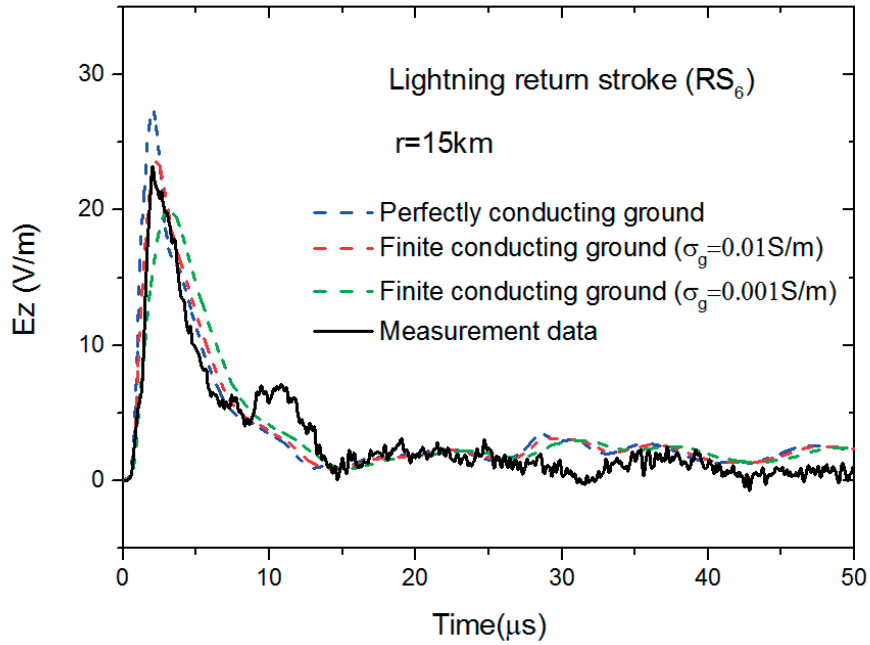


Figure 3-32. Effect of the finite conductivity on the vertical electric field at a distance of 15 km from the lightning channel and along the irregular path. Case 3 : RS6 (Adapted from [72]).

*Return Stroke Speed.* The return stroke speed is an important parameter that can vary from one stroke to another [42]. At distant observation points at which the field is essentially determined by its radiation component, the field peak is nearly proportional to the return stroke speed [90]. On the other hand, at shorter distances, an increase of the return stroke speed might result in a slight reduction of the electric field [130]. The effect of the return stroke speed is illustrated in Figure 3-33. In the analysis, we have considered three different values for the return stroke speed, namely  $1.0 \times 10^8$  m/s,  $1.5 \times 10^8$  m/s, and  $2.0 \times 10^8$  m/s. It can be seen that an increase of the return stroke speed from 1 to  $1.5 \times 10^8$  m/s, and from 1.5 to  $2 \times 10^8$  m/s will result in an increase of about 20% of the peak electric field.

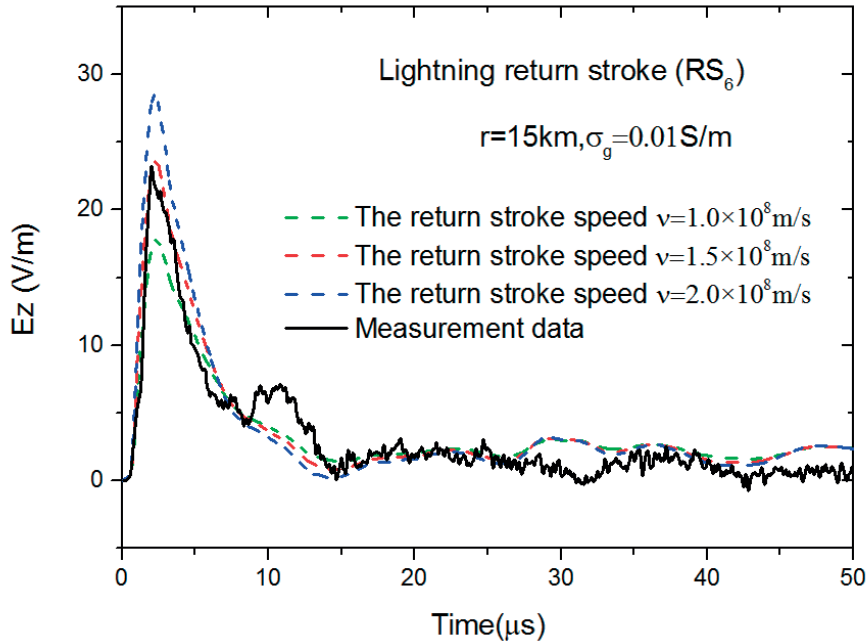


Figure 3-33. Effect of the return stroke on the vertical electric field at a distance of 15 km from the lightning channel and along the irregular path. Case 3: RS<sub>6</sub>. (Adapted from [72]).

*Return Stroke Model.* Figure 3-34 shows the simulated results using three different return stroke models: MTLE [117], [118], TL [131] and MTL [132]. It can be seen that, as far as the early-time response of the field is concerned, the three models provide very similar results. The fact that the TL model fails in reproducing the late-time response is well known and due to the absence of any attenuation of the current pulse along the channel (e.g., [133]). In summary, it can be said that the adopted return stroke model will affect to some extent the results (see also [134]). However, the general conclusion that the propagation along the considered irregular terrain results in an overall enhancement of the field remains valid regardless of the used model.

*Presence of the building on which the field sensor is located.* Finally, it is well known that the presence of the building on which the field sensors are located might affect the measured waveform (e.g. [113], [114]). In particular, the electric field measured on the roof of a building might experience an enhancement that depends on several factors related to the building (shape, material, presence of conducting beams, etc.) and on the position of the field sensor. Representing the building by a conducting block with a conductivity equal to that of the ground would result in an enhancement of the peak electric field of about 25%. However, in the present configuration, the building on which the field sensors were located is surrounded by several other buildings which makes it difficult to evaluate the enhancement effect, either by measurement or by simulation.

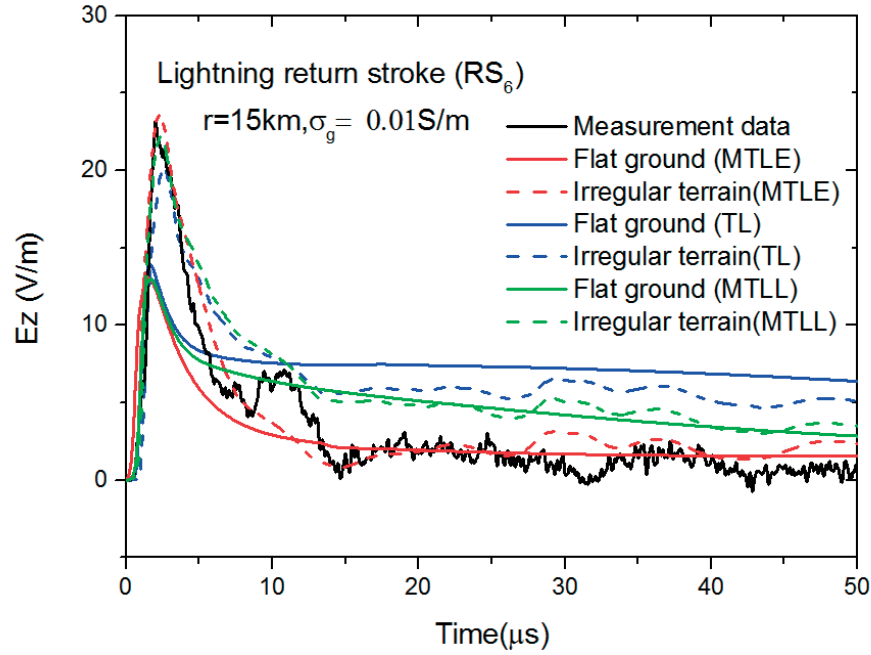


Figure 3-34. Effect of the return stroke model on the vertical electric field at a distance of 15 km from the lightning channel and along the irregular path. Case 3: RS6 (Adapted for [72]).

### 3.5 Conclusion

This chapter was devoted to the analysis of the data obtained at the Säntis Tower associated with upward negative flashes.

We examined superimposed pulses on the initial continuous current of upward negative discharges. Experimental data consisting of lightning current waveforms recorded at the instrumented Säntis Tower in Switzerland, along with electric fields recorded at a distance of 14.7 km from the tower, revealed that two modes of charge transfer along with the continuous current mode could be involved in the initial stage of upward negative flashes.

Superimposed pulses on the initial continuous current were identified: (1) M-component-type ICC-pulses for which the microsecond-scale electric field pulse occurs significantly earlier than the onset of the current pulse, and, (2) RS-type ICC-pulses for which the onset of the field matches that of the current pulse.

In addition, we investigated the ability of LLSs to locate and detect upward negative flashes. Different aspects of upward negative flashes, which might affect the evaluation performance of LLSs, were discussed. It has been found that LLSs tend to overestimate the peak current values of RS pulses of upward negative flashes.

We presented a theoretical analysis method to assess the propagation effect of lightning electromagnetic fields over a mountainous terrain. The propagation of

lightning electromagnetic fields along the mountainous region around the Säntis tower is simulated using a full-wave approach based on the finite-difference time-domain method and using the two-dimensional topographic map along the direct path between the tower and our field measurement station. We showed that, considering the real irregular terrain both the waveshape and amplitude of the simulated electric fields associated with return strokes and fast initial continuous current pulses are in excellent agreement with the measured waveforms. On the other hand, the assumption of a flat ground results in a significant underestimation of the peak electric field.



# Analysis of Upward Positive Flashes

## 4.1 Introduction

Upward positive flashes are initiated with negative upward leaders from the top of elevated structures [48]. They might be followed by some return-stroke-type processes.

This kind of flash is less frequent compared to other lightning discharges and as a result, the knowledge of upward positive flashes is limited to a low number of observations (e.g., [46], [48], [50]). Upward positive flashes can be classified based on their channel-base current waveform into two distinct types [50]. Type-I upward positive flashes exhibit a large, unipolar pulse with a risetime of tens of microseconds, which is preceded by a slow rising current of several milliseconds. The start of the rising portion of the slow current is marked with fast superimposed pulses with risetimes of some microseconds. Type-II upward positive flashes are mainly characterized by a millisecond-scale current waveform, with fast (microsecond-scale) superimposed oscillatory pulses on its rising portion.

Using simultaneous channel-base current and close-range electric field measurements, Heidler et al. [46] proposed that upward positive flashes can be classified based on the preceding lightning activity into self-triggered and other-triggered events. They hypothesized that other-triggered events are downward lightning flashes with long upward connecting leaders.

Using recorded channel-base currents and an assumed stepped leader velocity, Zhou et al. inferred leader lengths of about 168 to 945m with an average leader step length of 2.4 to 13.3m [48].

The only study reporting simultaneous records of high-speed video observations and channel-base currents of upward positive flashes is the one of Miki et al. [47]. They reported step lengths of 6 to 273 m, longer than the values reported by Zhou et al. However, they stated that the limited spatial resolution of their camera might have resulted in an overestimation of the leader step length. In addition, this issue could have prevented the different phases of the stepping process to be resolved in video observation.

In addition to the fact that upward positive flashes are characterized by extensive branching, Miki et al. have found the same features of space stem and propagation of space leader, which are also observed in downward negative stepped leaders (e.g., Biagi et al. [135]). Space stems which form at the head of downward negative leaders, have been observed for the first time in long laboratory spark gap experiments [136]. The reasons behind their formation are still under investigation [18]. Experimental observations have revealed [136] that through thermalization development, space stems transform to space leaders with positive and negative ends which propagate bidirectionally to bridge the gap and further elongate the leader channel.

In this chapter, we present a summary of characteristics of upward positive flashes recorded at the Säntis Tower. The characteristics of upward negative stepped leaders were investigated using simultaneous sets of channel-base currents and vertical electric field recorded at 14.7 km. Electric field signatures of the initial stages of downward negative flashes and upward positive flashes are compared. Finally, an attempt to model electric field radiation of oscillatory (microsecond-scale) pulses superimposed on the initial rising portion of Type-II upward positive flashes based on the expected background physical process is presented.

## 4.2 Recorded Data

During the study period (May 2010 – June 2016), a total of 562 flashes were recorded at the Säntis Tower. About 12% of the recorded flashes (66) were positive and about 4% (23) were classified as bipolar.

Figure 4-1 presents the monthly distribution of the number of flashes to the Säntis Tower in the considered period. As can be seen, both negative and positive flashes are concentrated in the summer months, August being the month during which most of them occurred (122 negative and 21 positive).

The recorded positive lightning flashes at the Säntis Tower can be classified into three categories based on the recorded current waveforms. Out of the 66 recorded positive flashes, only two were classified as downward, five as Type-I upward positive flashes, and 59 as Type-II upward positive flashes.

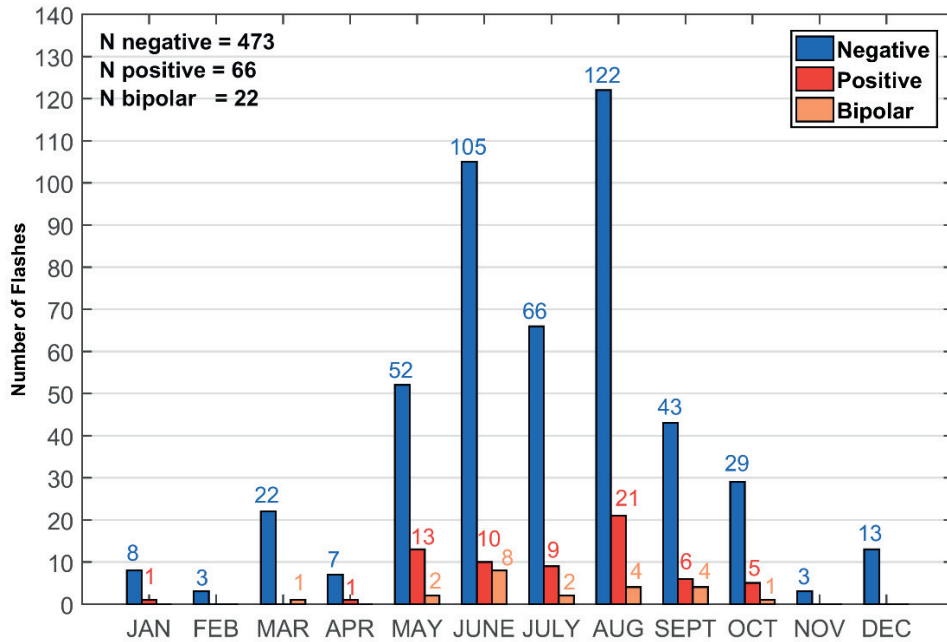


Figure 4-1. Monthly distribution of the number of flashes to the Sántis Tower during the study period (May 2010 – June 2016)

#### 4.2.1 Type-I Upward Positive Flashes

The current waveforms of the first type (occurring in 5 flashes out of the total of 66) are characterized by the presence of a large unipolar current. In the majority of Type-I flashes (4 out of 5), the main current pulse is preceded by bursts of fast pulses typical of upward negative stepped leader, superimposed on a continuous current. Figure 4-2 shows an example of a Type-I upward positive channel-base current which occurred on July 7th, 2010, 21:05:07 (local time). As it can be seen in the expanded view in the figure inset, the flash starts with fast (microsecond-scale) pulses superimposed on the slow-rising continuous current. These pulses are associated with upward negative leader steps. Type-I flashes contain also an impulsive current component as can be clearly seen from the figure.

This type of lightning flashes was also observed by Berger [34] at Monte San Salvatore. Table 4-1 presents median values of lightning current parameters of this study in comparison with the observed parameters by Berger [34]. As it can be seen, the observed flashes in Berger's study are characterized by pulse peak values, flash charges, and front durations in the same order or magnitude compared to our dataset, but with longer durations and, as a result, larger values of action integral. This discrepancy is of course subjected to the different sample size between the two studies.

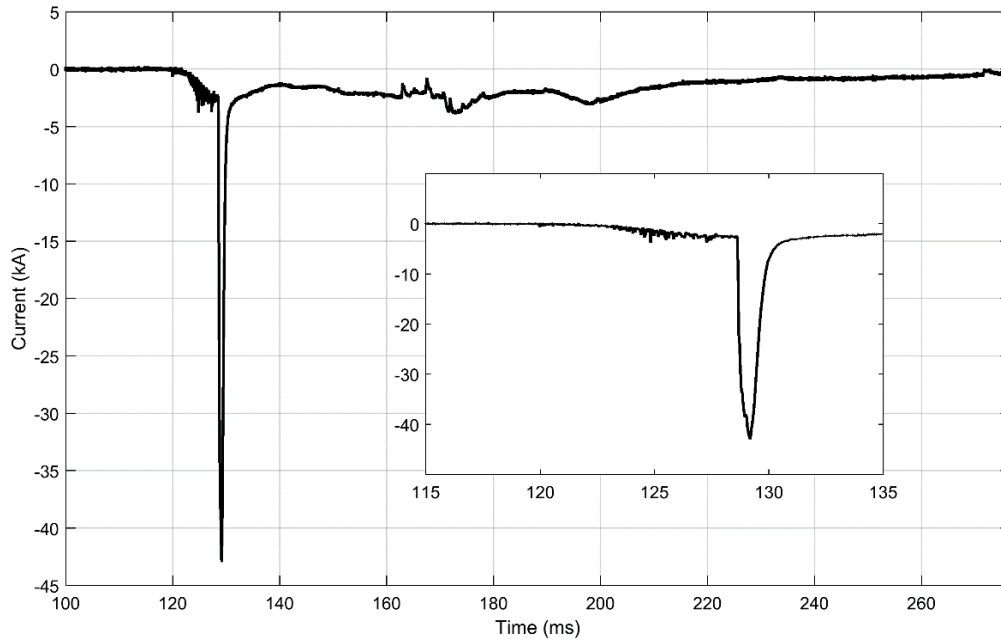


Figure 4-2. An example of Type I upward positive flash occurred on July 7<sup>th</sup>, 2010, 21:05:07 UTC time. Expanded view of initial rising portion is shown in the inset.

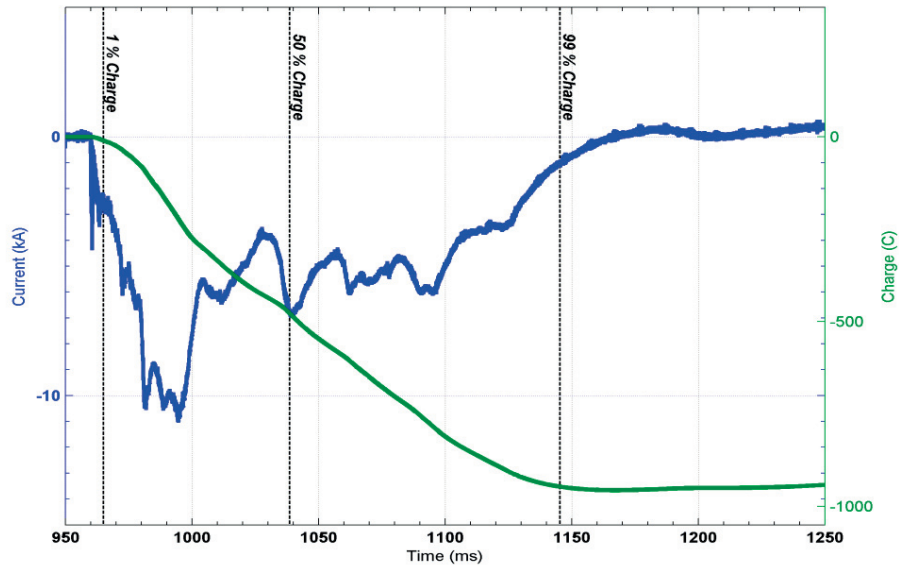
Table 4-1. Comparison of median values of current parameters for Type-I upward positive lightning of this study with those for Berger's study flashes with large impulsive currents (Sample size is given in parenthesis).

| Data   | Pulse Peak (kA) | Flash Charge (C) | Flash Duration (ms) | Action Integral ( $\leftrightarrow 10^6 A^2s$ ) | 10-90% Front Duration ( $\mu s$ ) |
|--|-----------------|------------------|---------------------|---|-----------------------------------|
| Type-1 flashes in this study                                   | 31.5<br>(5)     | 68<br>(5)        | 39.8<br>(5)         | 0.27<br>(5)                                     | 33.6<br>(5)                       |
| Flashes with large impulsive components in Berger's study [34] | 36<br>(35)      | 84<br>(35)       | 68<br>(34)          | 0.66<br>(35)                                    | 39<br>(23)                        |

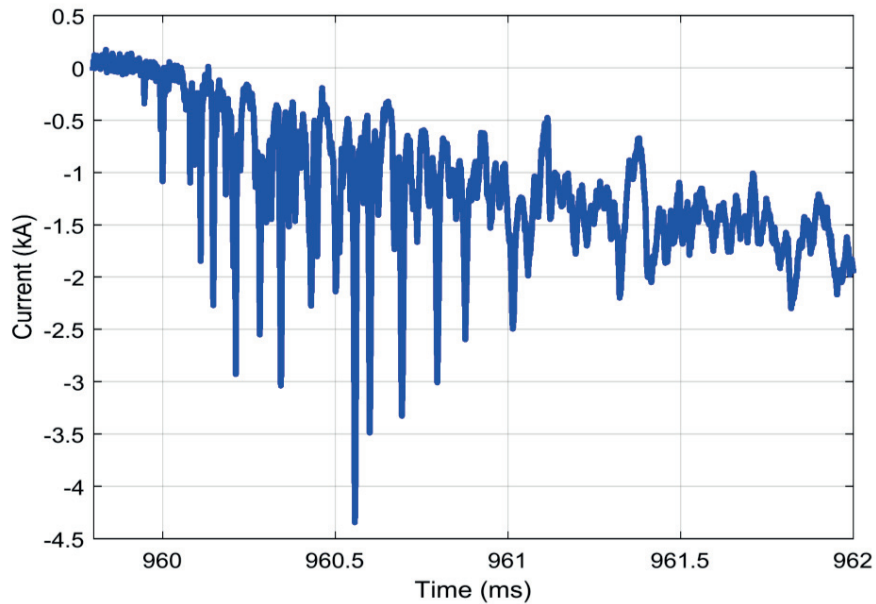
#### 4.2.2 Type-II Upward Positive Flashes

The second type of the observed flashes is characterized by a relatively long duration continuous current in the order of some milliseconds along with oscillatory pulse trains mainly at the start of slow current. The fast oscillatory pulses are believed to be due to the upward negative stepped leader. It should be noted that no impulsive current similar to Type-I flashes is present in this type of flash. Out of 66 recorded positive flashes, 59 flashes (89%) were classified as Type-II upward positive flashes.

Figure 4-3a presents an example of a Type-II upward positive flash occurred on September 27<sup>th</sup>, 2013, 00:56 (local time) which is characterized by a peak value of 11 kA and the highest charge amount of charge transfer (947 C) to ground ever measured at the S antis Tower.



(a)



(b)

Figure 4-3. a) Current waveform associated with a Type-II upward positive flash that occurred on 27 September 2013, 00:56. This flash transferred 947 C of positive charge to ground. Current (left scale) is shown in blue and charge (right scale) in green. b) Expanded view of oscillatory pulses at the start same flash.

Table 4-2 presents the statistical parameters of Type-II upward positive flashes observed at the S antis Tower in comparison to Berger’s study [34]. It can be seen that flashes of this study are characterized by larger peaks and higher charge transfer compared to flashes recorded at Monte San Salvatore by Berger [6].

**Table 4-2. Comparison of Median Values of Current Parameters for Positive Lightning of Type-2 with those for Berger’s flashes without Large Impulsive Currents (sample size is given in parentheses)**

| Data   | Peak<br>(kA)                                | Flash Charge<br>(C) | Flash Duration<br>(ms) |
|--|---|---------------------|------------------------|
| Type-2 flashes in this study   | 11 (pulse peak)<br>4.3 (flash peak)<br>(59) | 48.8<br>(59)        | 78.7<br>(59)           |
| Flashes without large impulsive components in Berger et al. study [34] | 1.5<br>(132)                                | 26<br>(137)         | 72<br>(138)            |

#### 4.2.3 Downward flashes

Out of the 66 recorded positive flashes, two were classified as downward. Figure 4-4 presents an example of a downward positive flash recorded on June 6<sup>th</sup>, 2014, 15:14:26 (local time) with a peak current of 27.5 kA and a rise time of 9.3  $\mu$ s. The expanded view of the initial portion of this flash is shown in the inset of Figure 4-4. As it can be seen, there is no evidence of long upward negative stepped leaders typical of upward positive flashes observed in Type-I or Type-II upward positive flashes. Some initial stepping pulses can be observed which occur very close in time to the return stroke pulse and, as a result, they should correspond to an upward negative connecting leader.

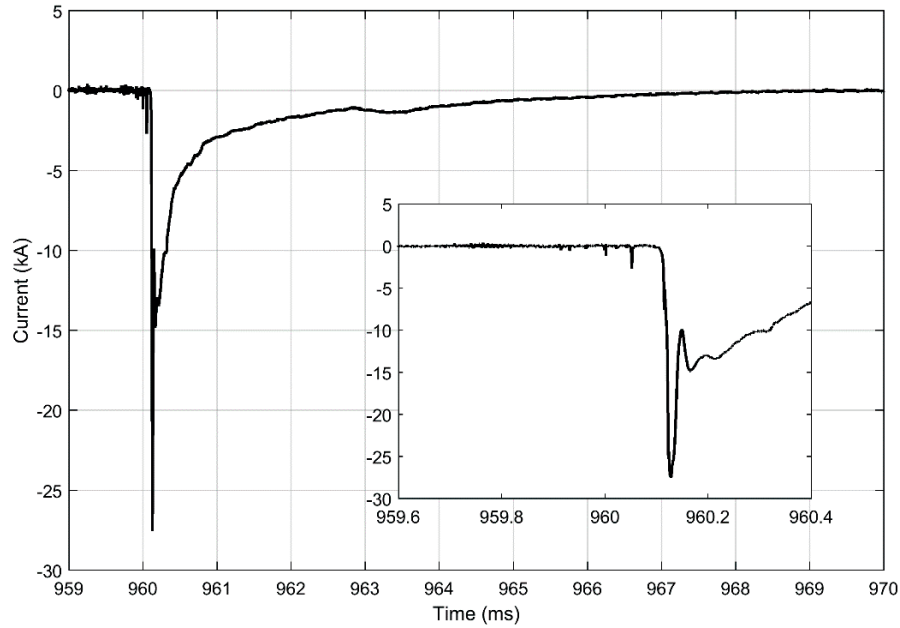


**Figure 4-4.** The presumably downward positive flash occurred on 6<sup>th</sup> June 2014, 15:14:26 (local time). The expanded view of early time of return stroke is shown in the inset.

## 4.3 Features of Upward Negative Stepped Leader Pulses in Type-II Positive Flashes

In this section, we present an analysis of simultaneous channel-base current and electric field records of Type-II upward positive flashes. The vertical component of the electric field was measured at 14.7 km away from the S antis Tower. More information about the field measurement system can be found in Section 2.4.

During the field measurement campaign (July 23 to October 28, 2014), five (out of 26) upward positive flashes were recorded, all of which were classified as Type-II upward positive flashes, characterized by a millisecond-scale slow current waveform with microsecond pulses superimposed on the initial rising portion (see Figure 4-3 for an example of this kind of flash). It should be noted that during this observation period no GPS timestamps were available and the two sets of waveforms were synchronized using the patterns of inter-pulse intervals of their pulsations.

### 4.3.1 Observed Characteristics of Individual Pulses

Herein, we investigate features of individual pulses recorded during the course of the upward negative leader. Figure 4-5 presents the overall current and electric field waveforms of an upward positive flash which occurred on October 21, 2014 at 23:56:46. As already mentioned there were no GPS time stamps available during the

observation period the physics sign convention is used for the electric field representation.

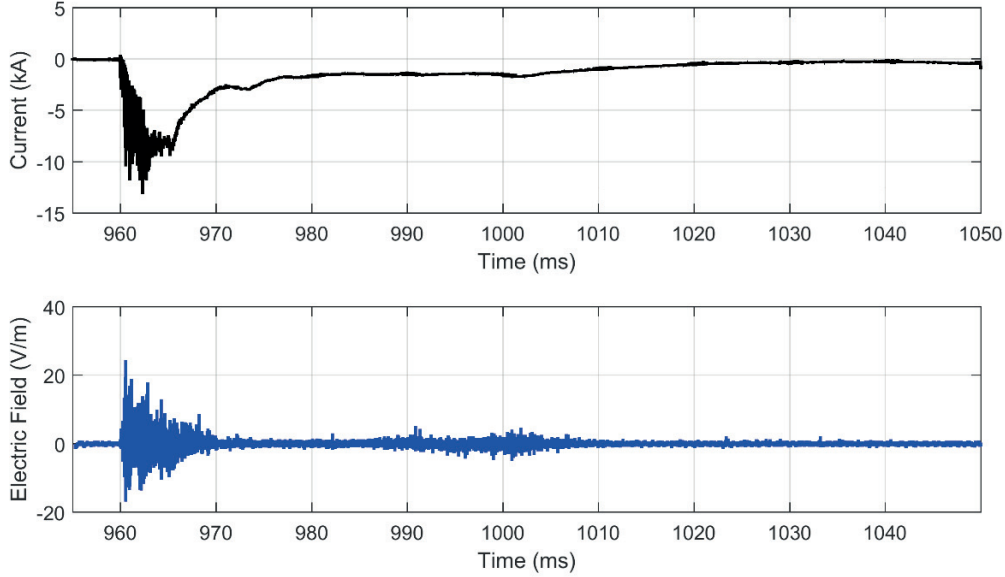


**Figure 4-5. Current (top) and E-field (bottom) wave forms associated with a Type-II upward positive flash that occurred on 21<sup>th</sup> October 2014, 23:56:46 (local time).**

A closer inspection of the recorded current and field waveforms of upward positive flashes reveals that individual pulses can be classified into two major categories: (i) pulses with a bipolar E-field signature with mostly an initial positive half-cycle which usually can be correlated with a negative unipolar current pulse, (ii) mainly unipolar positive or negative pulses which are not correlated with any major current pulse.

The first category of observed pulses is illustrated in Figure 4-6, in which the current and E-field pulses can be clearly correlated together. Furthermore, the electric field pulse shows a bipolar behavior with an initial excursion of positive polarity and an overall duration of about 23  $\mu$ s. For future reference in this chapter, we label this type of pulses “Category A”.

Figure 4-7 and Figure 4-8 show examples of electric field pulses of the second category, which are not correlated with any major current pulse. These E-field pulses are characterized by a much narrower pulse width and can be either unipolar of either polarity or bipolar. We label this type of pulses “Category B”.



### 4.3 Features of Upward Negative Stepped Leader Pulses in Type-II Positive Flashes

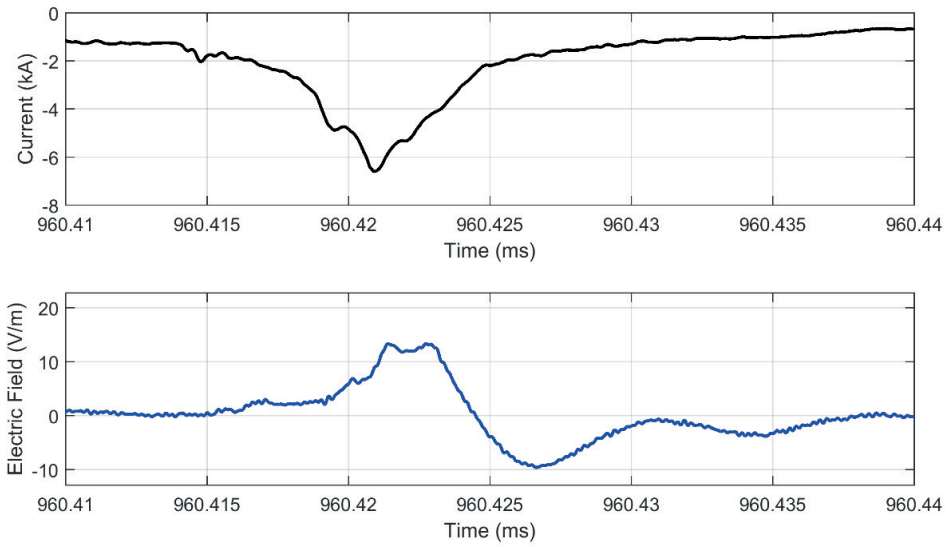


**Figure 4-6.** The first category of observed pulses (Category A pulse). Current (top) and electric field (bottom). The overall waveforms are shown in Figure 4-5.

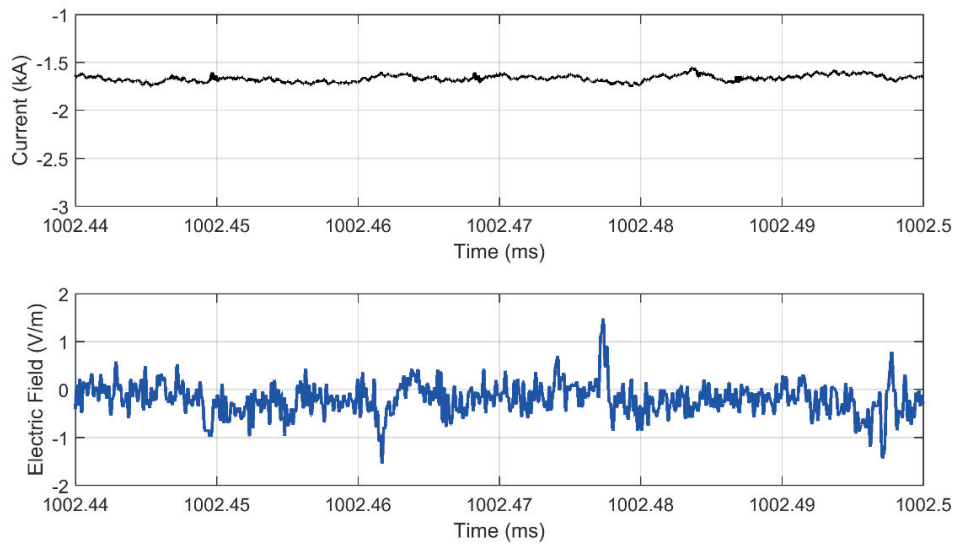


**Figure 4-7.** Examples of unipolar electric field pulses of the Category B without any major current pulse. Current (top). Electric field (bottom). The overall waveform is shown in Figure 4-5.

Comparison of field signature of pulses of Categories A and B reveals that Category B pulses are faster than Category A pulses (pulse width of some microseconds compared to some tens of microseconds).

As it is shown in Figure 4-9, Category B pulses could occur simultaneously with Category A pulses.

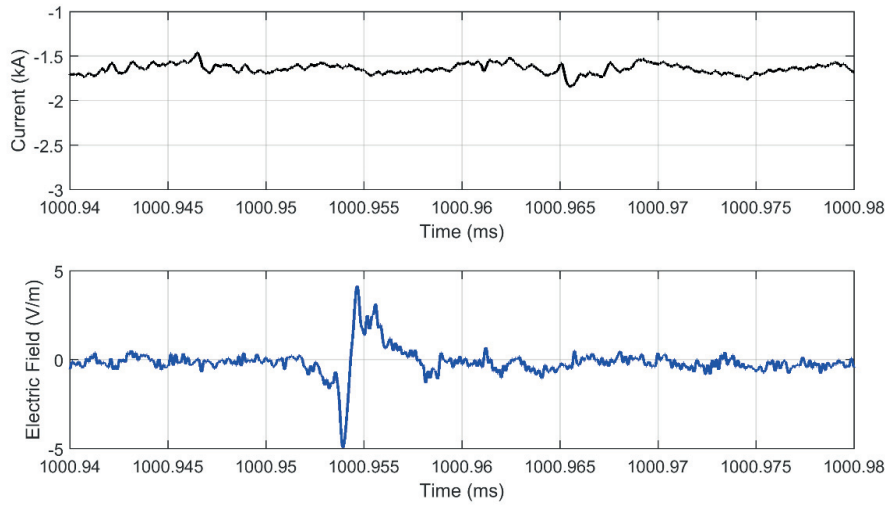


**Figure 4-8.** An example of unipolar electric field pulse of the Category B without any major current pulse. Current (top). Electric field (bottom). The overall waveform is shown in Figure 4-5.

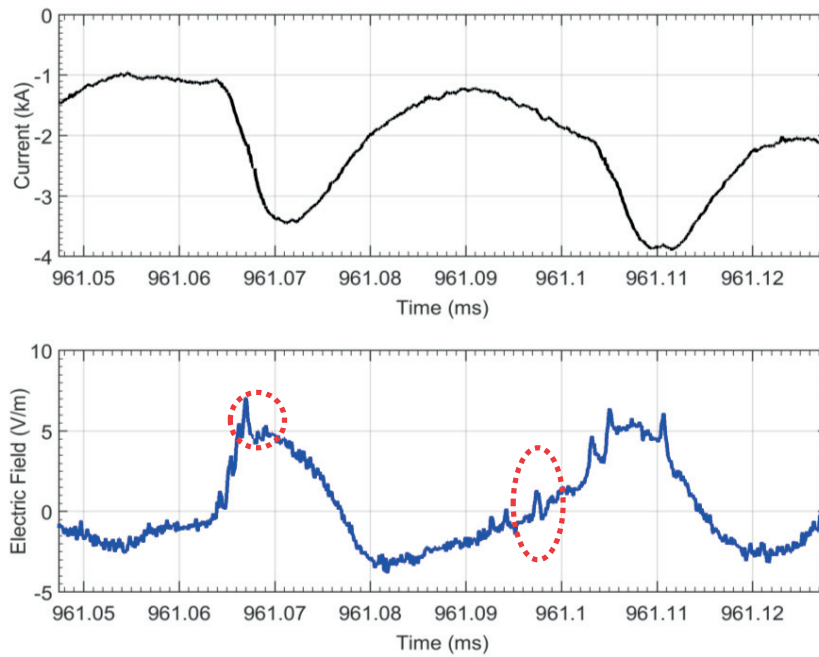


**Figure 4-9.** Superimposed Category B pulses on Category A pulses (Bimodal distribution).

#### 4.3.2 Overall waveform characteristics

As it can be observed in Figure 4-5, the current waveform is characterized by a millisecond-scale waveform with large, oscillatory pulse trains superimposed on its rising portion, while the electric field waveform can be characterized by two distinct periods of pulsations with an intermediate no-pulse time-interval.

Expanded views of the first pulsation period are shown in Figure 4-10 and Figure 4-11. This stage contains generally Category A pulses, which might have some superimposed Category B pulses. The characteristics of pulses evolve as we proceed in time. We can observe that as we go in time:

- Category A pulses become more frequent (inter-pulse time interval decreases, see Figure 4-10).
- Category A pulses become slower (risetime and width of pulses increase, see Figure 4-10 and Figure 4-11).
- The correlation between current and field for Category A pulses decreases (current pulses vanish while field pulses are still discernible, see Figure 4-11).
- Current pulses of Category A become less significant in amplitude and as a result they radiate less (Figure 4-11).
- As the fields due to Category A pulses vanish, Category B pulses start to dominate (Figure 4-11).

During the time period from 974 to 982 ms, the current is characterized by a slow-millisecond-scale waveform and the associated field is nearly equal to zero. Neither the current nor the field present any pulses in this stage.

During the time period from 982 to 1010 ms presented in Figure 4-12, the field is characterized by chaotic bipolar and unipolar fast pulses of Category B. It should be noted that no current-pulses can be observed in this stage.

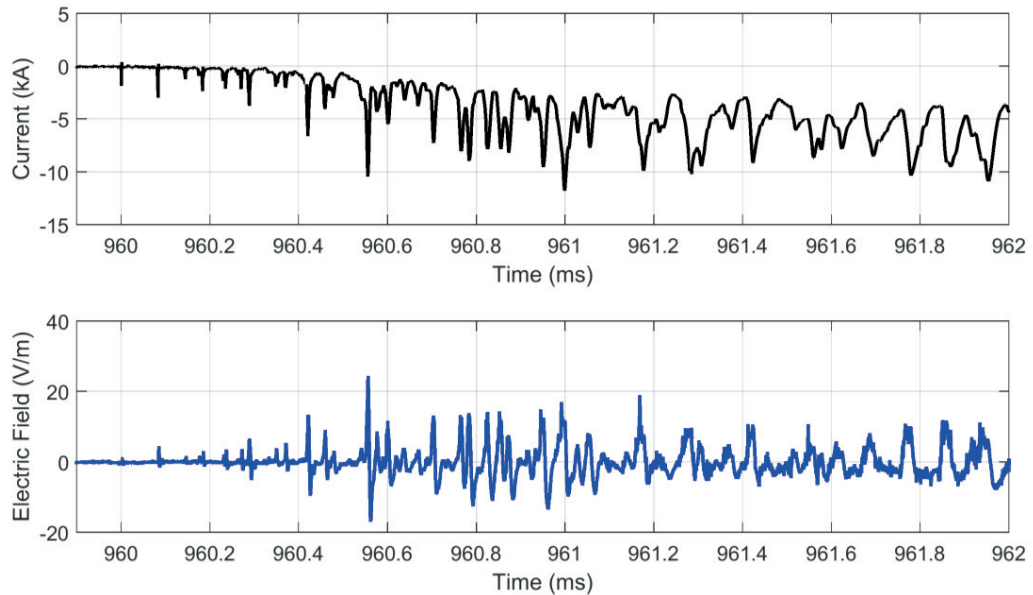


**Figure 4-10.** Expanded View of the rising portion (first stage) of the current (top) and E-field (bottom) waveforms of the flash presented in Figure 4-5.

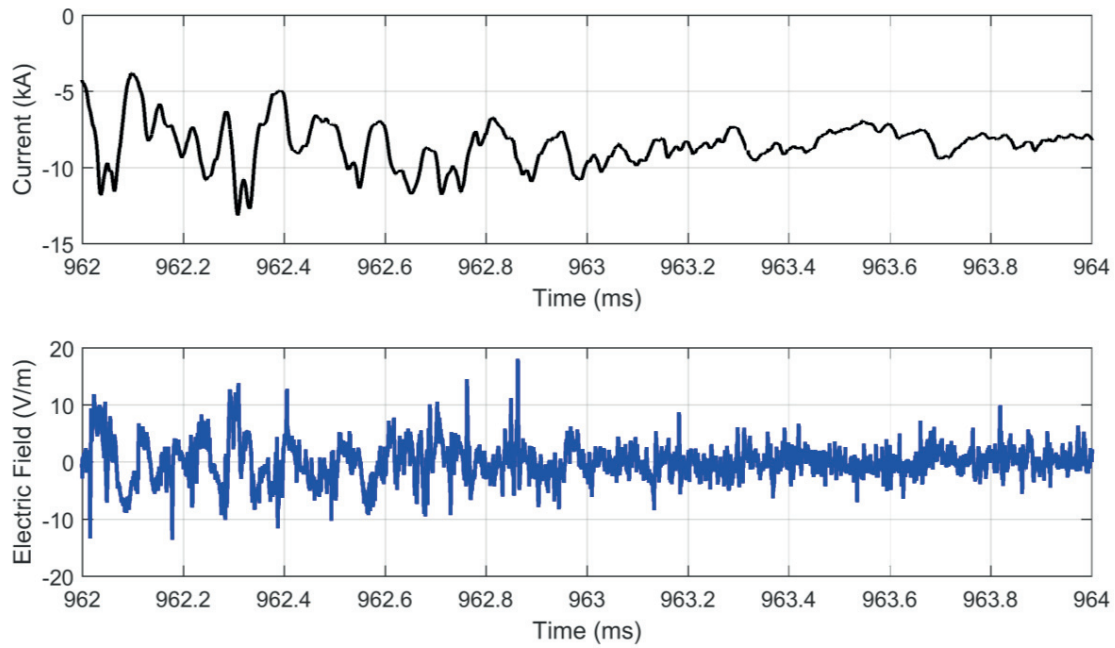


**Figure 4-11. Continuing of Figure 4-10**

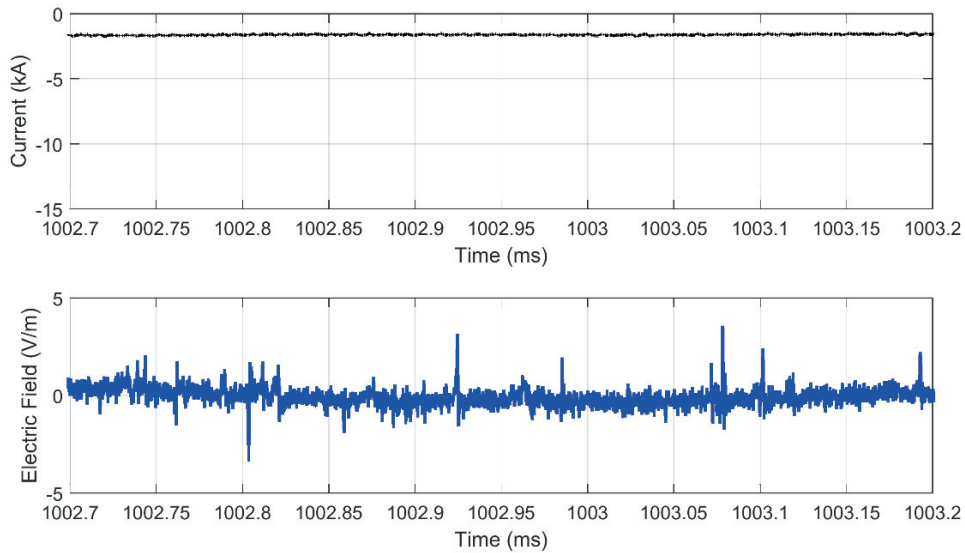


**Figure 4-12. Expanded view of the third stage of upward positive flash presented in Figure 4-5, in which only Category B pulses are present.**

It is worth noting that all recorded upward positive flashes in our dataset include these three stages described above. In some cases, pulses associated with the third stage (Category B pulses on the field with no correlated current pulses) can be seen repeatedly.

In the following, we present an example of such a flash with multiple third stage (Category B pulses on the field with no correlated current pulses).

Figure 4-13 shows simultaneous current and electric field recording associated with a Type-II upward positive flash, which shows slightly different features compared to the case presented in Figure 4-5. Similar to the case presented in Figure 4-5, Category A pulsations occur during the first stage and at about 960 to 966 ms. After a very short intermediate silent phase of no current or field pulses (about 966 to 967 ms), another phase of the discharge starts with an impulsive current and field (about 968 to 982 ms), in which both types of slow pulses (Category A) and fast pulses (Category B) are distinguishable.

This flash is followed by another intermediate stage and a fast pulsation of the field with no correlated current pulsation.

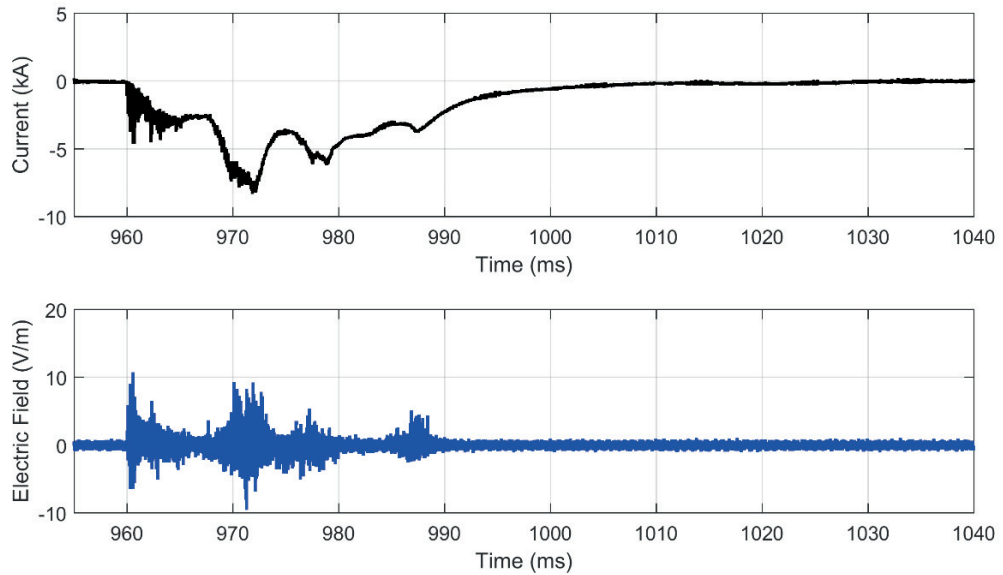


**Figure 4-13.** Current (top) and E-field (bottom) wave forms associated with a Type-II upward positive flash that occurred on 22<sup>th</sup> October 2014, 00:12:21 (local time).

#### 4.3.3 Characteristics of Category A Electric Field Pulses

As it is clear in Figure 4-6 and Figure 4-7, Category A pulses seem to be less chaotic compared to Category B pulses. Therefore, their systematic study is more straightforward compared to Category B pulses.

In this subsection, we present the parameters of the electric field pulses of Category A. Pulses with peak field value smaller than 5 V/m were disregarded (in order not to be affected by the noise level of the field measuring system). We have also excluded consecutive pulses separated by short time intervals, for which it is impossible to accurately determine some of their parameters. Based on the aforementioned

criteria, 33 Class-A pulses from five upward flashes were selected and their characteristics are presented in Table 4-3. The presented parameters of Table 4-3 are defined in Figure 4-14. Furthermore, the peak values are normalized to 100 km in this table.

**Table 4-3. Statistics of characteristics of the first category electric field pulses (Category A). Peak values are normalized to 100 km. Size: 33.**

| Parameter                                  | Value                               |
|--|-------------------------------------|
| Width of the initial half cycle (T1)       | $12.7 \pm 6.1 \text{ } \mu\text{s}$ |
| Width of the second half cycle (T2)        | $13.0 \pm 5.9 \text{ } \mu\text{s}$ |
| 50-50% Width (HPBW)                        | $5.5 \pm 2.8 \text{ } \mu\text{s}$  |
| 10-90% Rise time (R1)                      | $6.4 \pm 3.8 \text{ } \mu\text{s}$  |
| Peak of the initial half cycle (A1)        | $1.4 \pm 0.5 \text{ V/m}$           |
| Peak of the second half cycle (A2)         | $-0.85 \pm 0.47 \text{ V/m}$        |
| Ratio of initial to secondary peak (A1/A2) | $1.8 \pm 0.6$                       |

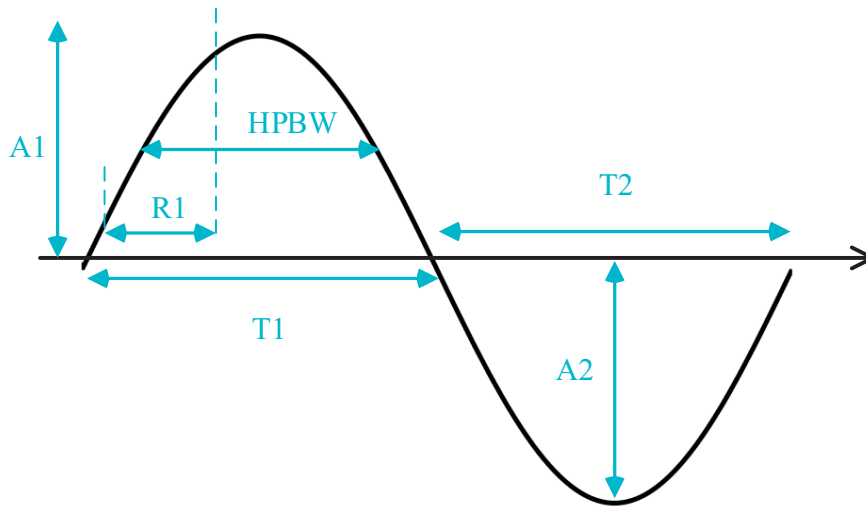


**Figure 4-14. Schematic definition of field parameters of first category pulses (Category A) presented in Table 4-3.**

Figure 4-15 presents the scatter plot of the peak E-field versus peak current in which the current pulse peak is determined using (5.1), where  $I_{Peak\_global}$  is the overall peak

of the pulse,  $I_{start}$  is the current at the start of the pulse and  $I_{end}$  is the current at the end of pulse. (5.1) is used to remove the background slow current.

$$I_{Peak\_local} = I_{Peak\_global} - \left( \frac{I_{start} + I_{end}}{2} \right) \quad (5.1)$$

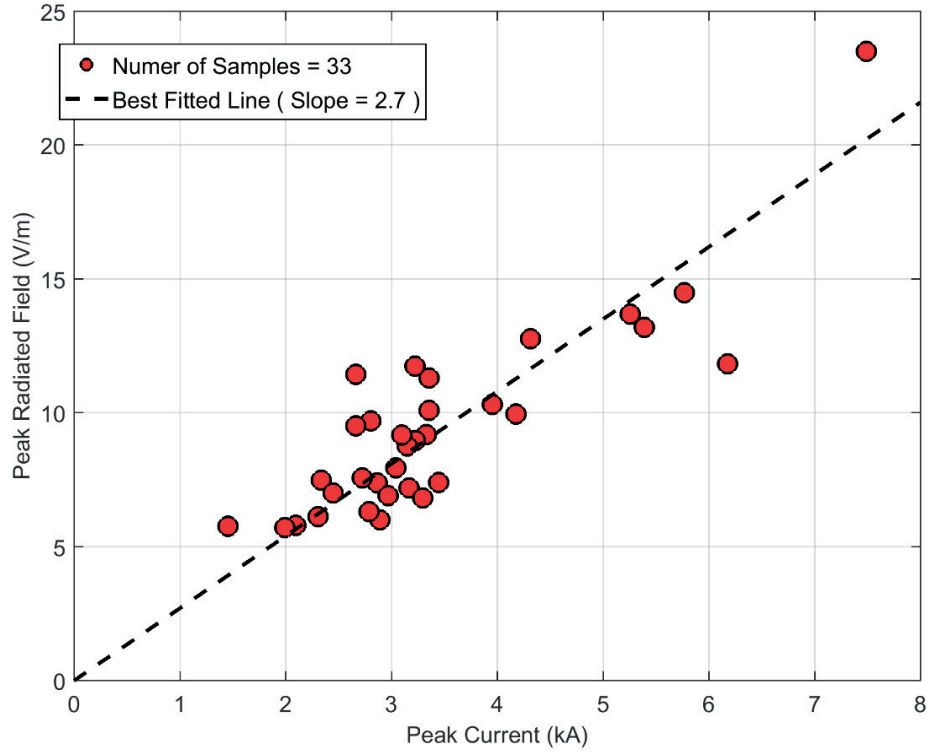
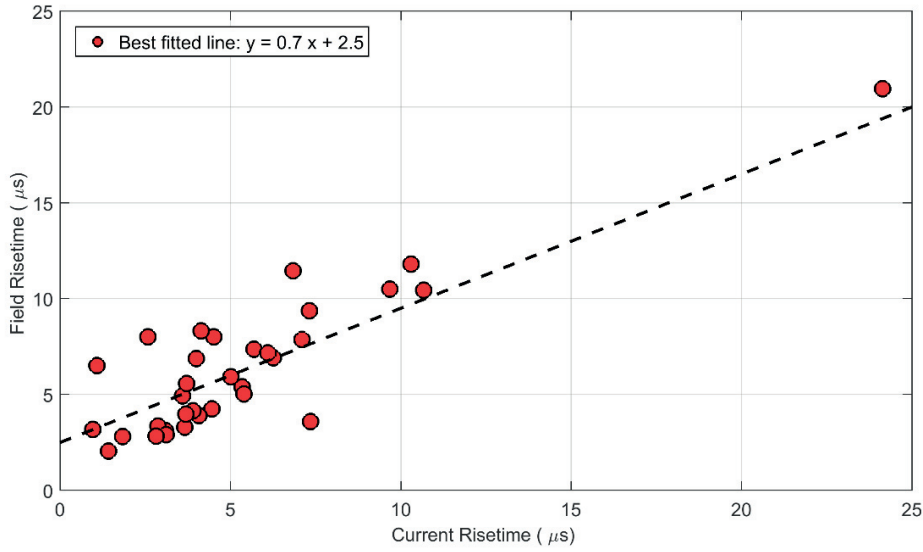


Figure 4-15. Scatter plot of peak field versus current peak associated with Category A pulses.



#### 4.4 Comparison Between the Initial Stage of the Current Associated with Upward Positive Flashes and That of Downward Negative Flashes



**Figure 4-16. Scatter plot of E-field 10-90% risetime versus current 10-90% risetime associated with the first category pulses (Category A).**

A linear correlation can be found between the E-field peak and the current peak, with a slope of 2.7 (V/m. kA) and an R-square of 0.74. Figure 4-16 presents the scatter plot of 10-90% E-field risetimes versus 10-90% current risetimes. The best fitted line can be estimated by  $y = 0.7x + 2.5$  with an R-square of 0.73. In particular, it can be seen from Figure 4-16 that the E-field pulses are generally characterized by a faster risetime compared to the current pulses. This could be due to the fact that field observation point is 14.7 km away from the lightning strike point and expectedly the recorded field peak is mainly due to the radiation term, which is proportional to derivative of current.

#### 4.4 Comparison Between the Initial Stage of the Current Associated with Upward Positive Flashes and That of Downward Negative Flashes

Numerous studies have been conducted up to date to investigate the initiation process of downward negative flashes using various means including electric field observation, VHF mapping, and optical observations (e.g., [24], [137]–[139]).

Clarence and Malan proposed a three-phase mechanism including Breakdown, Intermediate and Leader (BIL) prior to the first return stroke of a downward flash [140] and they hypothesized that the initial breakdown (Stage B) process must be entirely different from the stepped leader process (Stage L). It is worth noting that other studies based on VHF observations suggested that similar discharge processes should occur in stages B and L [138].



#### 4.4 Comparison Between the Initial Stage of the Current Associated with Upward Positive Flashes and That of Downward Negative Flashes

The difference in the underlying physical mechanisms of the B and L processes, and the reason behind the presence of stage I is an ongoing debate.

Two types of electric field pulsation were suggested by Nag et al. [141] to occur during the B and L stages, which are called “Classical” and “Narrow” preliminary breakdown pulses, respectively. Examples of these types of pulses adapted from [137] are shown in Figure 4-17 in which the atmospheric sign convention was used to depict the data.

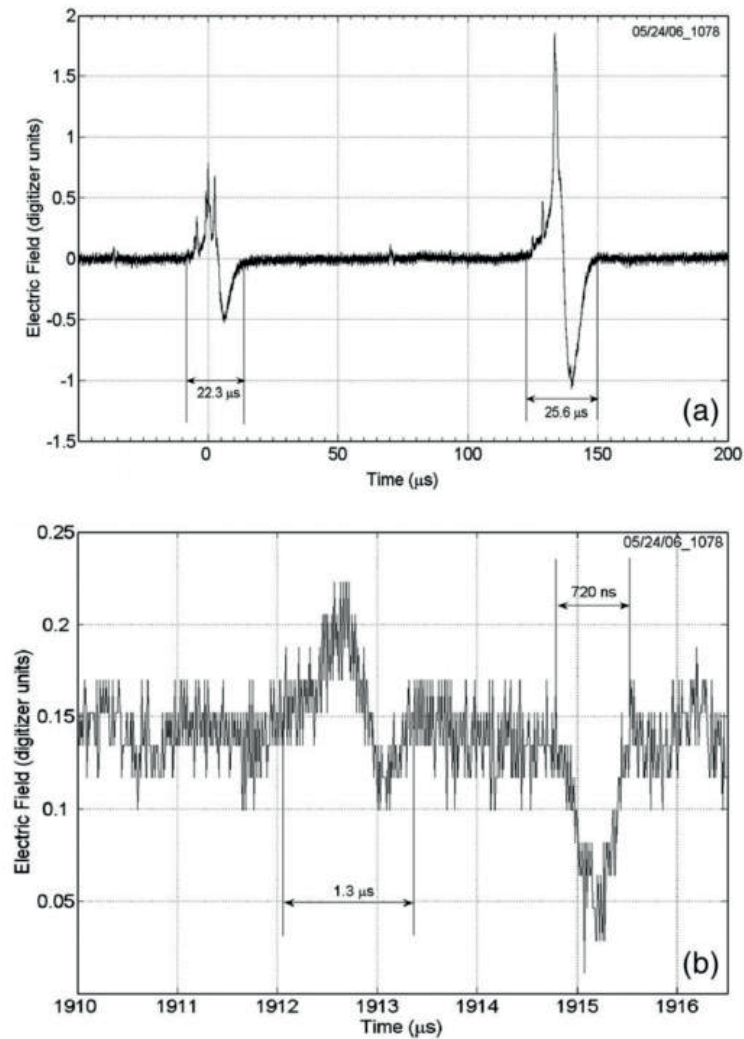


**Figure 4-17. Examples of (a) Classical and (b) Narrow PBPs in a downward negative flash (Adapted from [137])**

Recently, Stolzenberg et al. using a high speed video camera introduced the concept of “initial leader” for initial breakdown pulses (in stage B), which differs from normal stepped leaders (in stage L) [27], [142]. They suggested that the initial leader process can be characterized by the following steps:

#### 4.4 Comparison Between the Initial Stage of the Current Associated with Upward Positive Flashes and That of Downward Negative Flashes

---

- A dim linear feature moves downward from the initiation point (a slow decrease in E-change).
- An impulsive breakdown at the lower end of the initial leader.
- An upward-moving brightness.

They hypothesized that the initial leader pulses stop to occur because the previous initial leaders moved enough charge to reduce the ambient electric field near the initiation point.

On the contrary, Campos and Saba observed that the channel extension in stage B is quite similar to the ordinary leader extension observed in stage L [139].

More recently, Petersen and Beasley [28] observed a bimodal distribution of the stepping process, involving both long (i.e., 200+ m length) and short (i.e., 10+ m length) steps. Figure 4-18 shows examples of pulses in the B and L stages. The same kind of pulsation observed in stage L (So-Called “Narrow PBP”) was observed in stage B, superimposed on less fast pulses (So-called “Classical PBP”).

They suggested the presence of distant space leaders with their negative ends stepping downward and generating narrow pulses (like pulses in section L), while their positive ends will generate classical pulses when they attach to the previous main leader channel (major pulses in Stage B). When the ambient electric field is reduced by the descent of the leader, less distant space leaders would occur, which leads to the generation of only narrow pulses.

#### 4.4 Comparison Between the Initial Stage of the Current Associated with Upward Positive Flashes and That of Downward Negative Flashes

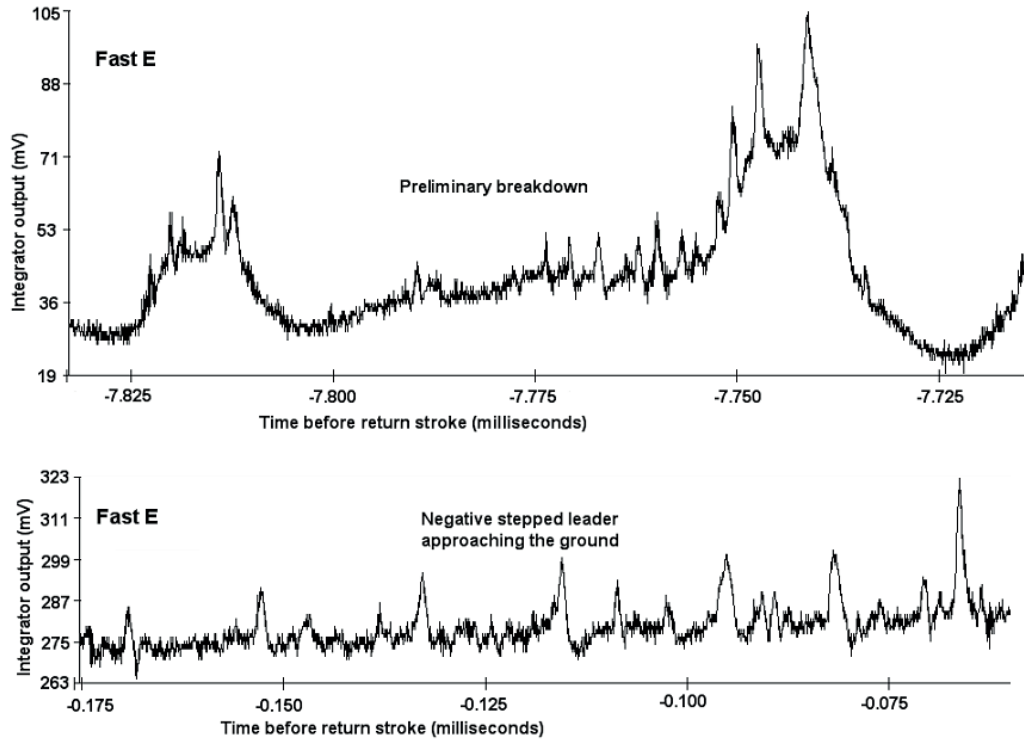
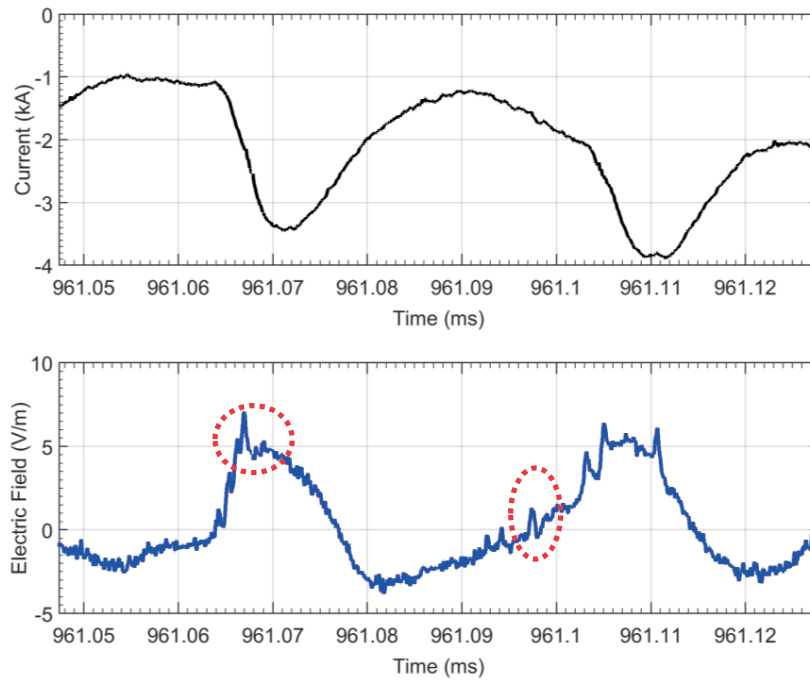


Figure 4-18. Electric field pulses recorded during (top) stage B, (bottom) stage L (Adapted from [28]).

Figure 4-19 (Category A) and Figure 4-20 (Category B) show two main typical individual pulses observed in our dataset associated with upward negative stepped leaders, which are very similar to Classical PBPs and Narrow PBPs observed in preliminary breakdown pulses of downward negative flash (Figure 4-17).

In addition to that, the simultaneous presence of Category A and B pulses as shown in Figure 4-19 can also be seen as a result of a bimodal distribution of stepping processes similar to what is observed in downward flashes [28].

However, further measurements and analysis are needed to draw more general conclusions.



**Figure 4-19. Typical pulses observed in the Category A of upward negative stepped leaders along with bimodal presence of Category B pulses.**

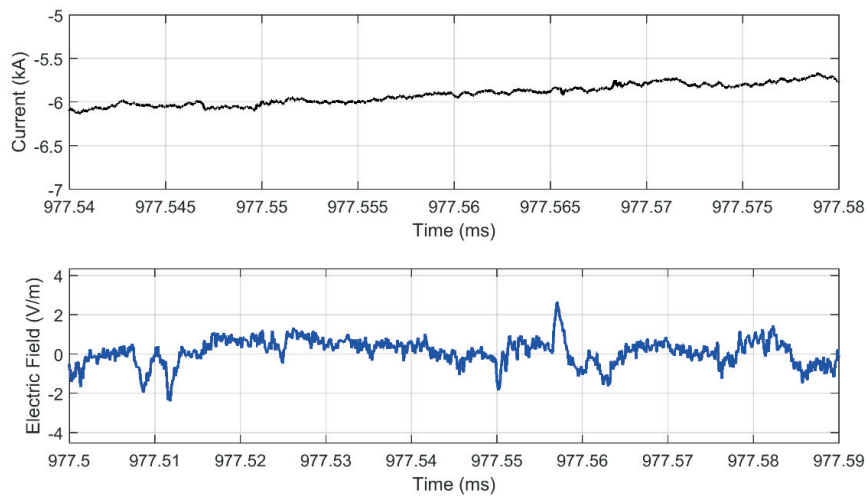


**Figure 4-20. Typical fast pulses (Category B) observed in the third phase of upward negative stepped leaders.**

#### 4.5 Modeling of Category A Pulses in Upward Positive Flashes

As it was discussed in Section 4.3.1, Category A pulses are mainly characterized by a bipolar E-field signature with mostly an initial positive half-cycle which usually can be correlated with a negative unipolar current pulse. The similarity between

Category A pulses of upward positive flashes and Classical PBP pulses in the initial stage of downward negative flashes has been discussed in Section 4.4. Using the available simultaneous current and electric field records of this type of pulses and the concept of attachment of the positive end of space leader to the negative leader tip (similar to classical PBP pulses), we will attempt in what follows to propose a charge transfer model for upward negative leaders considering the presence of a tall tower.

The model allows to calculate electric field radiated from pulses recorded during the first Phase-I (Category A pulses) associated with upward negative stepped leaders.

As illustrated in Figure 4-21, a traveling current pulse is assumed to travel downward from the upper extremity of the leader channel, as of the positive end of the space leader makes connection with main leader channel.

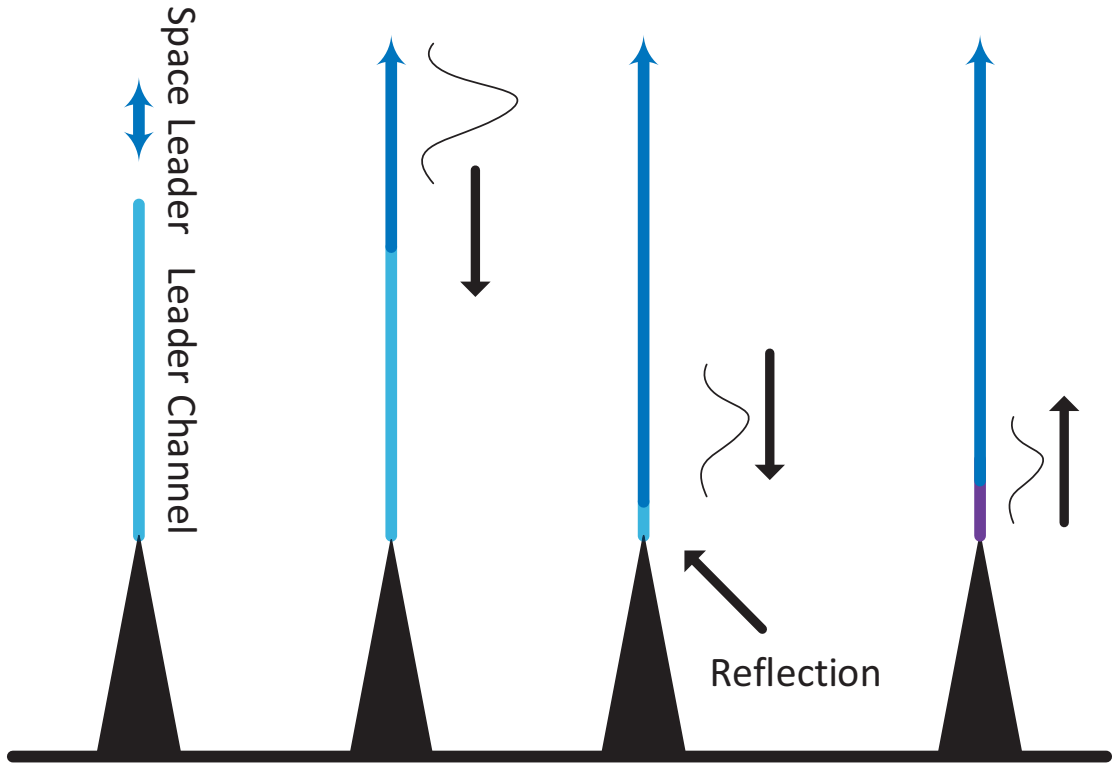


**Figure 4-21. Schematic diagram of the interaction of downward traveling wave with a tall tower.**

An exponential attenuation factor of  $f_d(z') = \exp[(z' - h_{tower}) / \lambda_d]$  is introduced to the downward traveling wave equation to consider corona charge availability limitation along the channel. We assume full reflection of the current at the tower tip ( $R_g = 1$ ). The upward travelling wave is assumed to have an exponential attenuation factor  $f_u(z') = \exp[(z' - h_{tower}) / \lambda_u]$ . We expect the upward traveling wave to suffer less

attenuation compared to downward traveling wave, as the conductivity of the channel is increased by the downward traveling wave.

This model can be mathematically formulated using equation (5.2)

$$i(z', t) = \begin{cases} i(H, t - (H - z')/v) \times f_d(z') & t < (H - h_{lower})/v \\ i(H, t - (H - z')/v) \times f_d(z') + \\ i(H, t - (H + z')/v) \times f_u(z') \times R_g & t \geq (H - h_{lower})/v \end{cases} \quad (5.2)$$

in which  $H$  is the height of the upper extremity of the leader and  $v$  is the speed of the wave-front propagation.

The radiated field can be obtained using

$$dE_z(r, z=0, z', t) = \frac{dz'}{2\pi\epsilon_0} \left[ -\frac{r^2}{c^2 R^3} \frac{\partial i(z', \tau - R/c)}{\partial t} \right] \quad (5.3)$$

We used a Gaussian current wave shape (equation (5.4)) proposed by Karunarathne et al. [143] to represent the undisturbed current wavelshape. Figure 15 shows the represented Gaussian current in comparison to the measured waveform.

$$I(t) = \begin{cases} Ae^{-[\alpha(t-t_1)]^2} & t < t_1 \\ Ae^{-\left[\frac{(t-t_1)t_1}{(t_2-t_1)}\right]^2} & t \geq t_1 \end{cases} \quad (5.4)$$

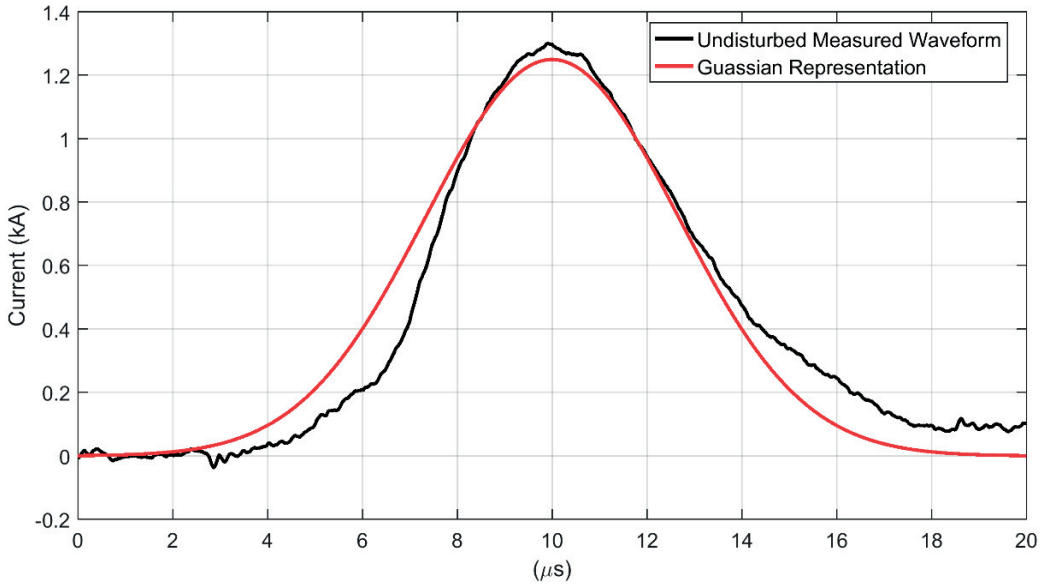
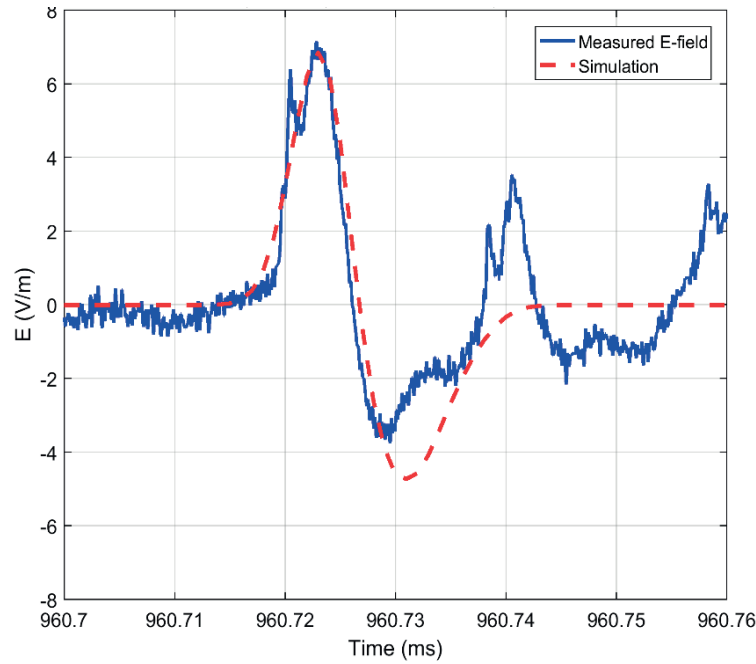


Figure 4-22. Undisturbed measured waveform in comparison to its Gaussian representation.

Adopting the abovementioned model and the assumed current waveform, the field can be calculated by specifying the four parameters which are the leader length ( $H$ ), front-wave speed ( $v$ ), downward wave attenuation ( $\lambda_d$ ) and upward wave attenuation ( $\lambda_u$ ).

Figure 4-23 shows the estimated versus measured vertical electric field by assuming parameters presented in Table 4-4. A quite fair agreement can be observed between the measured electric field and the simulated one.

The parameters are chosen by trial and error to reproduce the best fitted electric field waveshape. The obtained values are consistent with the length of the upward negative leader estimated by Zhou et. [48] and the reported length and wave-front speed value by Karunarathne et al. [144]. More investigation on the sensitivity analysis of parameters is needed to draw more general conclusions.



**Figure 4-23. Simulated radiated electric field in comparison to measured electric field.**

**Table 4-4. The assumed parameters of the proposed model.**

| Parameter   | Value                 |
|-------------|-----------------------|
| $H$         | 1200 m                |
| $V$         | $1.5 \times 10^8$ m/s |
| $\lambda_d$ | 2000 m                |
| $\lambda_u$ | 400 m                 |

## 4.6 Conclusion

This chapter was devoted to investigate the features of upward positive lightning discharges and the involved upward negative leader.

During the study period (May 2010 – June 2016), a total number of 562 flashes was recorded at the Säntis Tower. About 12% of the recorded flashes (66) were positive. The recorded positive lightning flashes at the Säntis Tower can be classified into three categories based on the recorded current waveforms. Out of the 66 recorded positive flashes, only two were classified as downward, five as Type-I upward positive flashes and 59 as Type-II upward positive flashes.

Using simultaneous channel-base current and vertical electric field records of Type-II flashes, we distinguished two types of pulsations:

- Category A pulses with a bipolar E-field signature with mostly an initial positive half-cycle which usually can be correlated with a negative unipolar current pulse.
- Category B pulses, mainly unipolar positive or negative pulses which cannot be correlated with any major current pulse.

We have found that our Category A and B pulses are very similar to “Classical PBPs” and “Narrow PBPs” which have been observed in the initial stage of downward negative leaders. In addition to that, the overall electric field signature of our Type-II events is very similar to the field associated with the Breakdown, Intermediate, Leader (BIL) stages of downward negative flashes. However, more extensive observations are needed to confirm this hypothesis.

Finally, we presented an engineering model that allows calculation of electric field radiated from pulses recorded during Phase-I (Category A pulses) associated with upward negative stepped leaders. The predicted fields are in good agreement with experimental observations.



## Upward Bipolar Flashes

### 5.1 Introduction

Bipolar lightning discharges transfer both negative and positive charges to ground. They are usually initiated by upward leaders from tall structures, but they can also occur in classical downward flashes. Current waveforms associated with bipolar flashes were first reported by McEachron from his studies at the Empire State Building [51]. The overall percentage of bipolar lightning discharges is relatively low, with a probability of occurrence which is believed to be about the same as that of positive lightning [42]. Table 5-1 gives a summary of studies reporting bipolar flashes observed at instrumented towers and in rocket-triggered lightning experiments.

The types of cloud structure and discharge processes involved in the formation of bipolar flashes are still not clearly understood, although some scenarios have been suggested in the literature (e.g., [145]–[147]).

In this chapter, we present 13 bipolar lightning flashes recorded at the Säntis Tower in Switzerland during the period of June 2010 to January 2015. All the 13 bipolar flashes were upward discharges.

In view of the limited number of well-documented bipolar flashes being found in the literature (see Table 5-1), the dataset collected in this thesis does represent a useful source of information for studying the physics of bipolar flashes. Based on our observations with respect to the existing literature, we suggest a modification to the traditional classification of bipolar flashes.

The content of this chapter heavily draws from [148] and [149].

**Table 5-1. Summary of observations of bipolar lightning (Adopted from [149]).**

| Reference                   | Country     | Experiment                              | Number of events             | Percentage (%) |
|-----------------------------|-------------|---|------------------------------|----------------|
| Hagenguth and Anderson [52] | USA         | Empire State Building                   | 11 (10 years of observation) | -              |
| Berger [34]                 | Switzerland | Mount San Salvatore                     | 68 (out of 1196)             | 5.7            |
| Hubert and Mouget [150]     | France      | Triggered lightning                     | 1                            | -              |
| Nakahori et al. [151]       | Japan       | Fukui chimney                           | 2 (out of 14)                | 14.3           |
| Gorin and Shkilev [152]     | Russia      | Ostankino Tower                         | 6 (out of 90)                | 6.7            |
| Akiyama et al. [153]        | Japan       | Triggered lightning                     | 2                            | -              |
| Heidler et al. [154]        | Germany     | Peissenberg Tower                       | 2                            | -              |
| Miki et al. [155]           | Japan       | Fukui chimney                           | 43 (out of 213)              | 20.2           |
| Jerauld et al. [156]        | USA         | Triggered lightning                     | 1                            | -              |
| Wang et al. [157]           | Japan       | Windmill and lightning protection tower | 3                            | -              |
| Zhou et al. [158]           | Austria     | Gaisberg Tower                          | 21 (out of 652)              | 3.2            |
| This Study                  | Switzerland | Säntis Tower                            | 13 (out of 427)              | 3.0            |

## 5.2 Experimental Observation

During the considered period (June 2010 to January 2015), 427 flashes were recorded at the Säntis Tower, out of which 58 (13.5%) were classified as positive flashes and 13 (3.0 %) as bipolar flashes. In 2014, 7 from a total 100 recorded flashes

were bipolar, a fraction that is considerably larger than in previous years (a total of 6 bipolar flashes were recorded in the time period from June 2010 to December 2013).

In [22] Rakov proposed to classify bipolar flashes into three categories. The classification relies on the following peculiar characteristics of the flash:

- (1) a polarity reversal during the initial continuous current with a possible no-current interval between the two polarities;
- (2) different polarities of the initial-stage current and the following return stroke or strokes; and
- (3) return strokes of opposite polarity.

**Table 5-2. Summary of Săntis Tower bipolar flashes. Categories I through III (Adopted from [149]).**

| Date and Time       | Category (according to [22]) | Current waveform example |
|---------------------|------------------------------|--------------------------|
| 2011-08-27 07:20:34 | IIIa                         | Figure 5-7               |
| 2011-08-27 08:05:26 | Ia*                          | Figure 5-4               |
| 2011-08-27 08:42:42 | II                           | Figure 5-5               |
| 2012-07-04 18:45:09 | Ia*                          | Figure 5-1               |
| 2012-08-24 01:28:22 | Ia*                          | -                        |
| 2012-09-11 16:05:05 | Ia*                          | -                        |
| 2014-05-07 20:42:26 | Ib*                          | Figure 5-9               |
| 2014-05-07 20:46:00 | Ia*                          | Figure 5-3               |
| 2014-06-23 16:07:45 | II                           | Figure 5-6               |
| 2014-06-23 16:55:13 | Ia*                          | -                        |
| 2014-09-21 15:14:09 | Ia*                          | Figure 5-2               |
| 2014-09-21 15:22:51 | Ib*                          | Figure 5-8               |
| 2014-10-20 23:47:00 | Ia*                          | -                        |

\*) Ia and Ib will be illustrated in section 5.3.

### 5.2.1 Current Waveforms Belonging to Category I

This category of bipolar flashes is characterized by a change of polarity of the current during the initial stage [22]. A majority of the recorded bipolar flashes (10 out of 13) belong to this category. Figure 5-1 shows the current waveform of an upward flash of

this category recorded on July 4th, 2012. The waveform corresponds to an upward positive leader followed by an initial continuous current (ICC). This flash contained no return strokes. Several pulses are superimposed on the ICC, including one positive pulse which resulted in a polarity reversal of the current. An expanded view of the positive pulse is presented in the inset. The positive current pulse is characterized by a peak value of 3.6 kA and a risetime of 940  $\mu$ s. The latter is much longer than that characteristic of return strokes.

Figure 5-2 presents another example of a Category-I upward bipolar flash recorded on September 21, 2014. The waveform starts with an initial stage current with tens of ICC pulses, including one large positive pulse. An expanded view of the positive pulse is presented in the inset of the figure. The positive pulse is characterized by a peak value of 39.6 kA and a 10-90% risetime of 31  $\mu$ s. Note that the ICC level (100 A) prior to the positive pulse is not discernible (not resolved on the tens-of-kilo amperes amplitude scale).

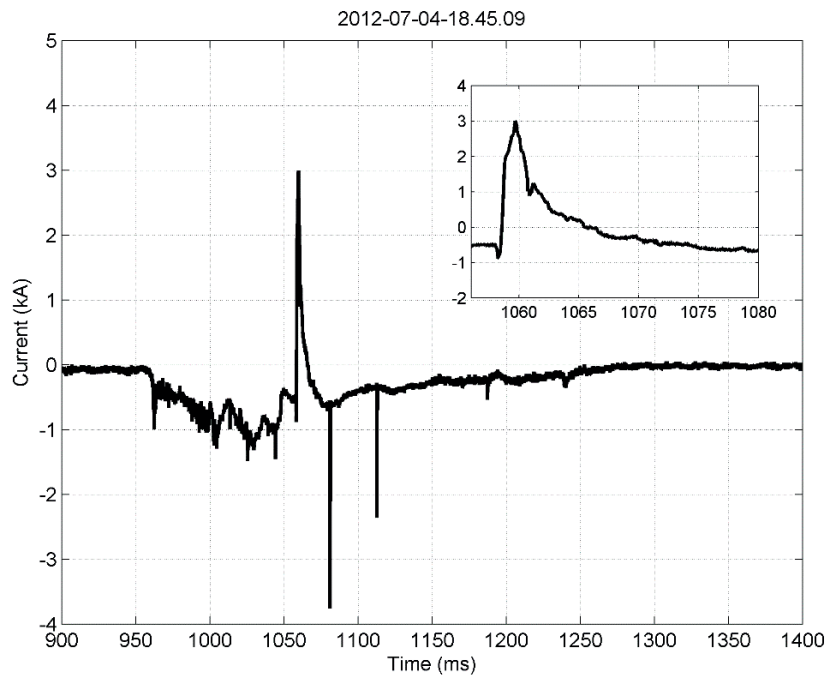


**Figure 5-1. Bipolar flashes of Category I that occurred on 4 July, 2012, 18:45:09. An expanded view of the positive pulse is presented in the inset. This flash contained not return strokes (Adopted from [149]).**

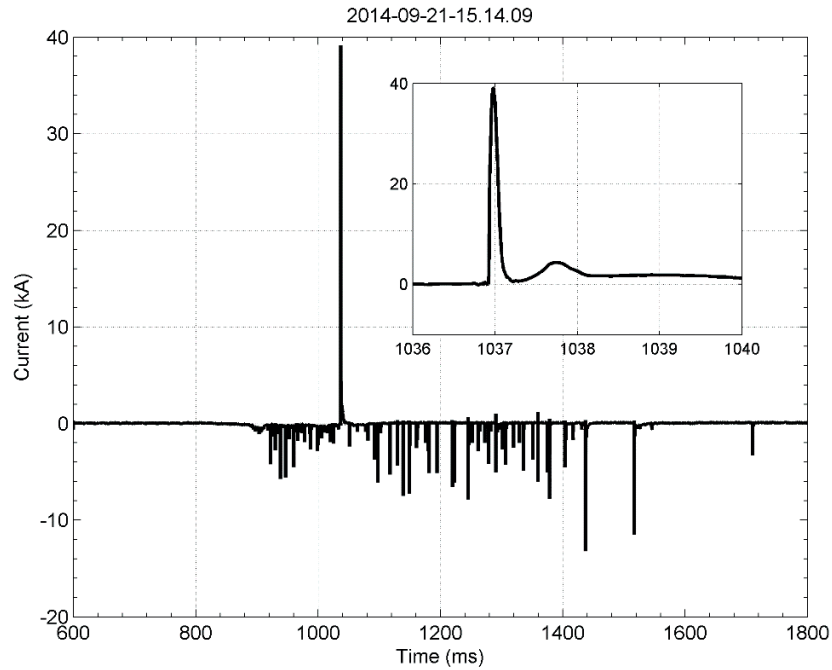


Figure 5-2. Bipolar flash of Category I that occurred on 21 September 2014, 15:14:09. An expanded view of the positive pulse is shown in the inset. The positive pulse is characterized by a peak value of 39.6 kA and a risetime of 31  $\mu$ s (Adopted from [149]).

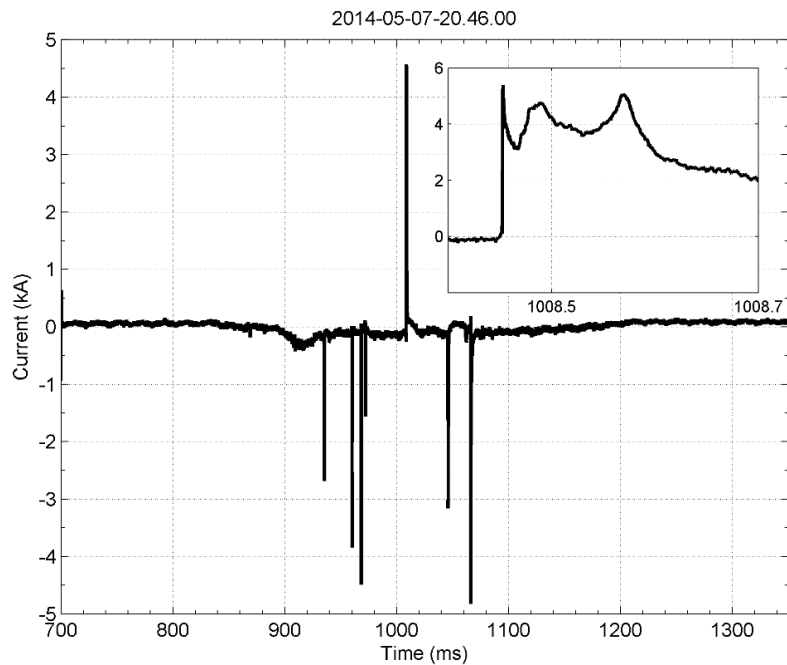
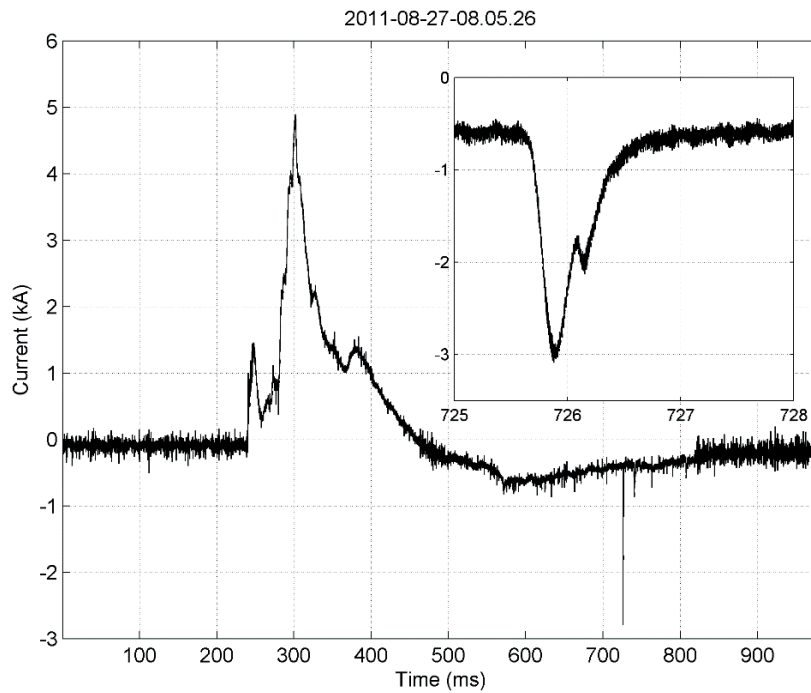


Figure 5-3. Bipolar flash of Category I that occurred on 7 May 2014, 20:46:00. An expanded view of the positive pulse is shown in the inset. The positive pulse is characterized by a peak value of 5.4 kA and a risetime of 0.46  $\mu$ s. This flash contained no return strokes (Adopted from [149]).

A similar example is presented in Figure 5-3. In this case, the positive current pulse is characterized by a peak value of 5.4 kA and an unusually fast risetime of 0.46  $\mu$ s. The ICC level prior to this pulse was 150 A.

Note that the characteristics of positive pulses in the two bipolar flashes presented in Figure 5-2 and Figure 5-3 are similar to those observed in positive flashes of type I [50].

Figure 5-4 presents another example of a measured current waveform associated with a Category-I bipolar flash. In this flash, the current exhibits first a positive excursion (corresponding to a positive charge transfer to ground) followed by a reversal of current polarity from positive to negative. Note that a negative 3-kA ICC pulse occurred after the ICC polarity reversal. An expanded view of this pulse is shown in the inset of the figure.



**Figure 5-4.** Bipolar flash of Category I that occurred on 27 August 2011, 8:05:26. An expanded view of the negative ICC pulse occurring during the late part of the bipolar ICC is presented in the inset. This flash contained no return strokes (Adopted from [149]).

### 5.2.2 Current Waveforms Belonging to Category II

Category II is characterized by different polarities of the initial stage current and the following return strokes [22]. Two out of 13 bipolar flashes of the present study belong to this category. In both cases, the initial stage current waveform corresponds to a type-II positive flash [50]. Type-II positive flashes are defined in Romero et al. as “classical” upward flashes characterized by millisecond-scale waveforms with

large oscillatory pulse trains superimposed on their rising portion, which are inferred to be due to upward negative stepped leaders.

Figure 5-5 and Figure 5-6 present two waveforms corresponding to this category recorded, on 27 August 2011 and 23 June 2014, respectively.

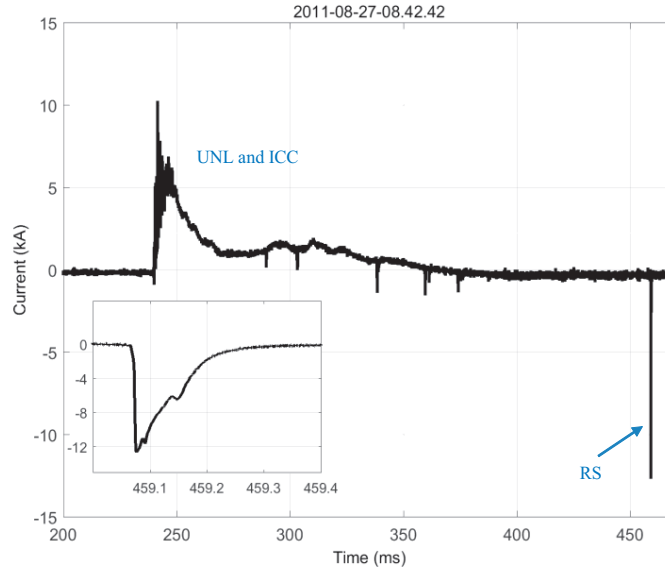


**Figure 5-5.** Bipolar flash of Category II that occurred on 27 August 2011, 8:42:42. An expanded view of the negative pulse associated with the only negative return stroke of this flash is presented in the inset. The negative return stroke current is characterized by a peak value of 12.6 kA and a risetime of 5.1  $\mu$ s. UNL Stands of upward negative leader, ICC for initial continuous current, and RS for return stroke (Adopted from [149]).

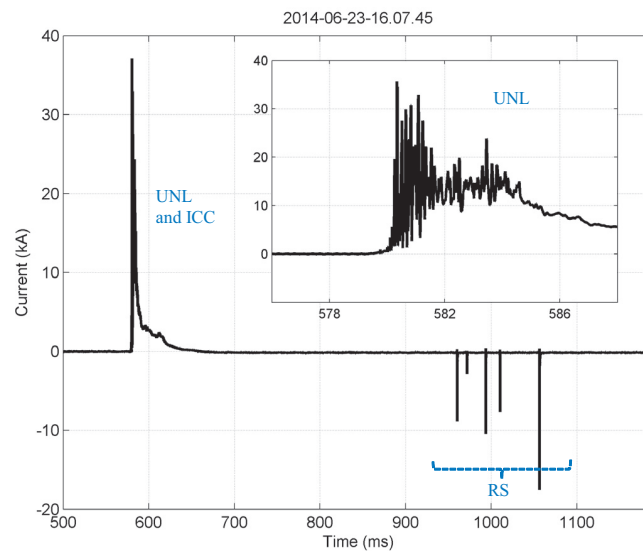


**Figure 5-6.** Bipolar flash of Category II that occurred on 23 June 2014, 16:07:45. An expanded view of the upward negative leader (UNL) is presented in the inset (Adopted from [149]).

For the first waveform (Figure 5-5), the peak of the initial positive pulse train is about 10 kA. The long steady current following the peak features several M-component-like superimposed pulses of negative polarity. After the cessation of the steady current and a no-current interval of about 100 ms, a negative return stroke (12.6 kA peak and 5.1  $\mu$ s risetime) occurred. For the second waveform (Figure 5-6), the largest positive pulse has a peak value of about 38 kA, followed by a no-current interval of nearly 300 ms and 4 negative return strokes.

### 5.2.3 Current Waveforms Belonging to Category III

This category involves return strokes of different polarities within the same flash. Rakov distinguished between upward or triggered lightning flashes (Category IIIa) and downward flashes (Category IIIb) [159]. Only 1 out of the 13 bipolar flashes in our dataset could be classified as a Category-IIIa bipolar flash. The current waveform for this flash is presented in Figure 5-7a. Note that the pre-trigger time of this record was not long enough to capture the whole initial stage process. We can see, however, the late part of the initial continuous current associated with an upward positive leader (negative charge transfer to ground), which ceased at about 100 ms, followed by two return-stroke pulses of opposite polarity at 200 ms and 240 ms. Expanded views of the negative and positive RS pulses are presented in Figure 5-7b and Figure 5-7c, respectively. The negative RS pulse has a peak of 7.1 kA and a risetime of 75  $\mu$ s. This event would not be classified as an RS based on the current risetime (typical RS current risetimes are one to two orders of magnitude shorter). We treated it as a RS, because it was preceded by a 98 ms no-current interval. The positive RS pulse has a peak of 11 kA and a risetime of 0.88  $\mu$ s. Similar current records showing return-stroke pulses of opposite polarity have been reported in [155], [156], [160].



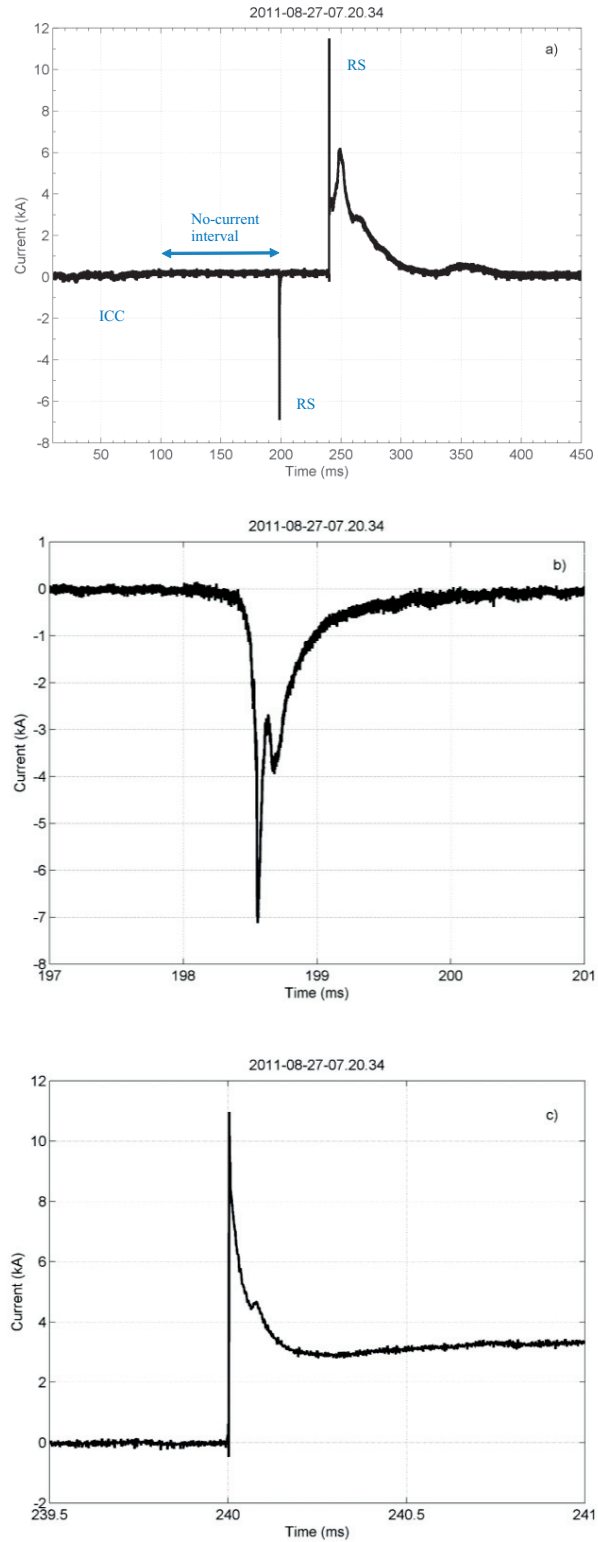


**Figure 5-7.** (a) Bipolar flash of category III that occurred on 27 August 2011. (b) Expanded view of the negative RS pulse (peak of 7.1 kA and a risetime of 75  $\mu$ s). (c) Expanded view of the positive RS pulse (peak of 11 kA and a risetime of 0.88  $\mu$ s), (Adopted from [149]).

### 5.3 Suggested Modification to the Traditional Classification of Bipolar Flashes

Two bipolar flashes without return strokes in this study were each characterized by a current waveform that could be formally assigned to Category I proposed in [22], but showed evidence of two upward leaders of opposite polarity initiated from the tower. In Category-I bipolar flashes, the polarity reversal is usually assumed to be associated with in-cloud processes. We suggest that the traditional classification of bipolar flashes should be modified to distinguish between two types of Category-I flashes: those in which the polarity reversal during the initial stage is associated with in-cloud processes (Category Ia) and those in which the polarity reversal is due to initiation of two opposite-polarity leaders from the tower (Category Ib).

Current waveforms of the two bipolar flashes of Category Ib are presented in Figure 5-8 and Figure 5-9. In Figure 5-8, the current features an initial-stage current associated with transporting the negative charge to ground with 6 superimposed ICC pulses, followed by a waveform characteristic of a type-II upward positive flash initiated by an upward negative leader from the tower [50]. The time interval between the end of the negative waveform and the start of the initial positive pulse (shown in the inset) is about 77 ms. During this time interval, the current reversed polarity from negative to positive. The steady positive current was about 150 A. This polarity change is indicative of Category-I bipolar flash. However, the steady inactive positive current interval was abruptly ended by the upward negative leader developing in virgin air, as further discussed at the end of this section.

Figure 5-9a presents the second case, which starts with a millisecond-scale waveform of positive polarity, superimposed on which are numerous large pulses, characteristic of a type-II upward positive flash [50]. This waveform is followed by a slow-varying current waveform of negative polarity with superimposed pulses of both polarities. An expanded view of the negative waveform, which is indicative of negative charge transfer to ground and, hence, of an upward positive leader, is shown in Figure 5-9b. The inactive time interval between the end of the positive waveform and the start of the negative one is about 15 ms, during which a steady positive current of about 20 A was observed.

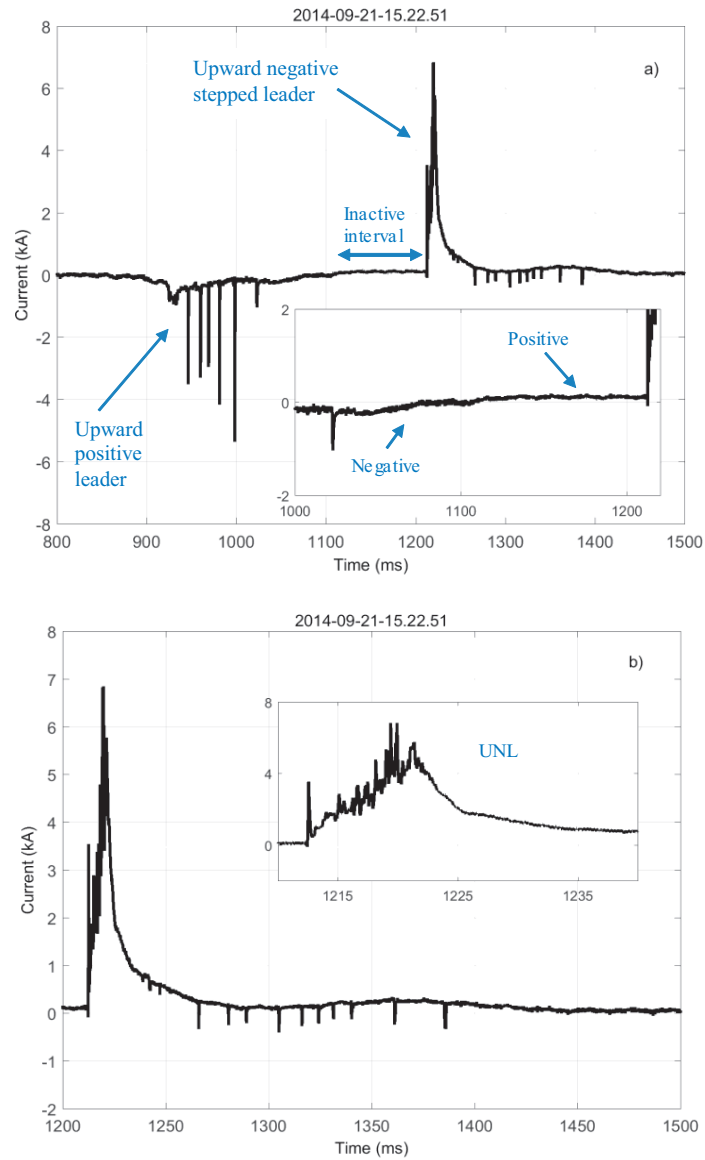


**Figure 5-8. Bipolar flash that occurred on 21 September 2014. a) Overall current waveform. An expanded view of the time interval including the reversal of current polarity is shown in the inset. b) An expanded view of positive current pulse associated with upward negative leader. The pulse train in the initial rising portion of the current waveform is shown in the inset. This flash contained no return strokes (Adopted from [149]).**

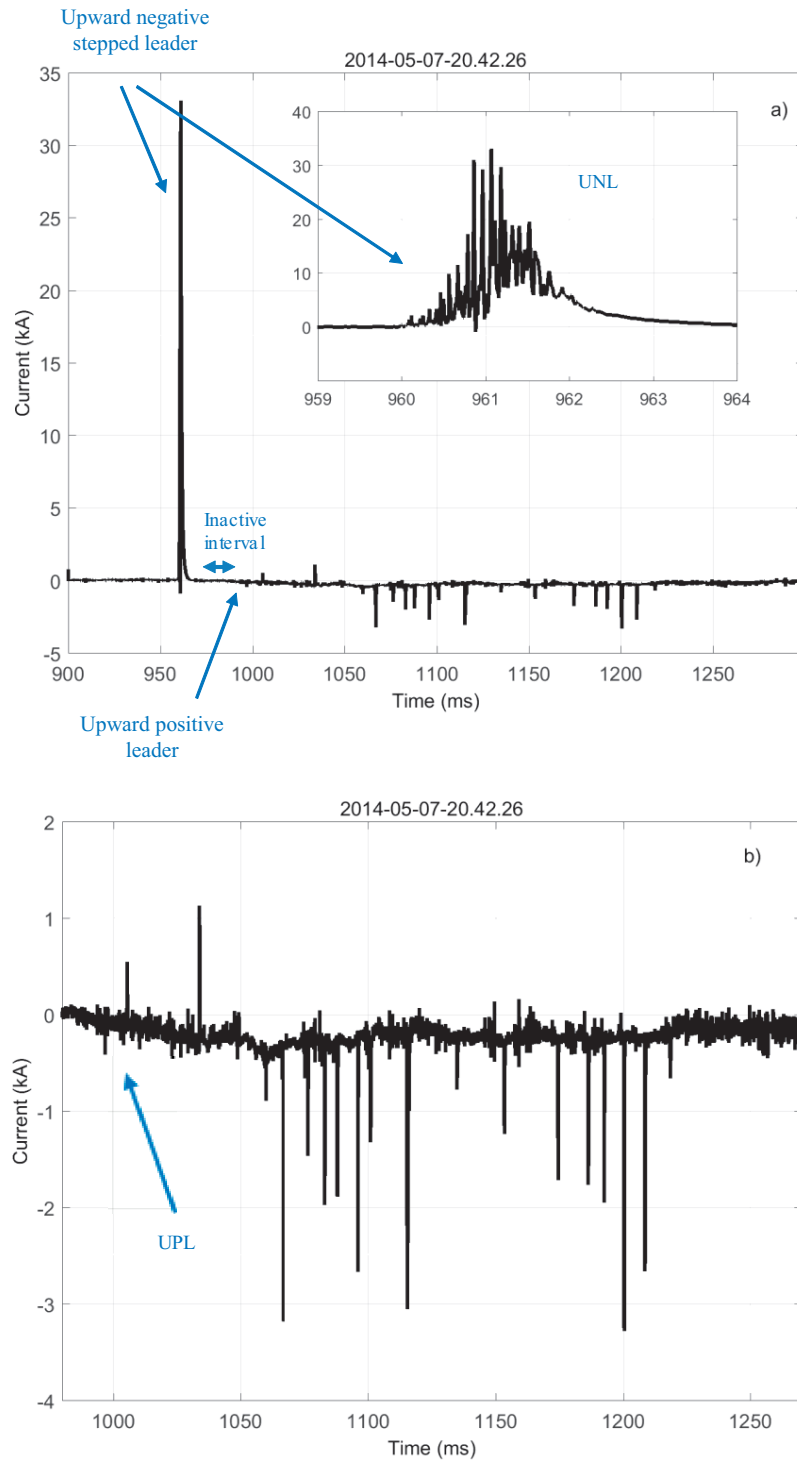
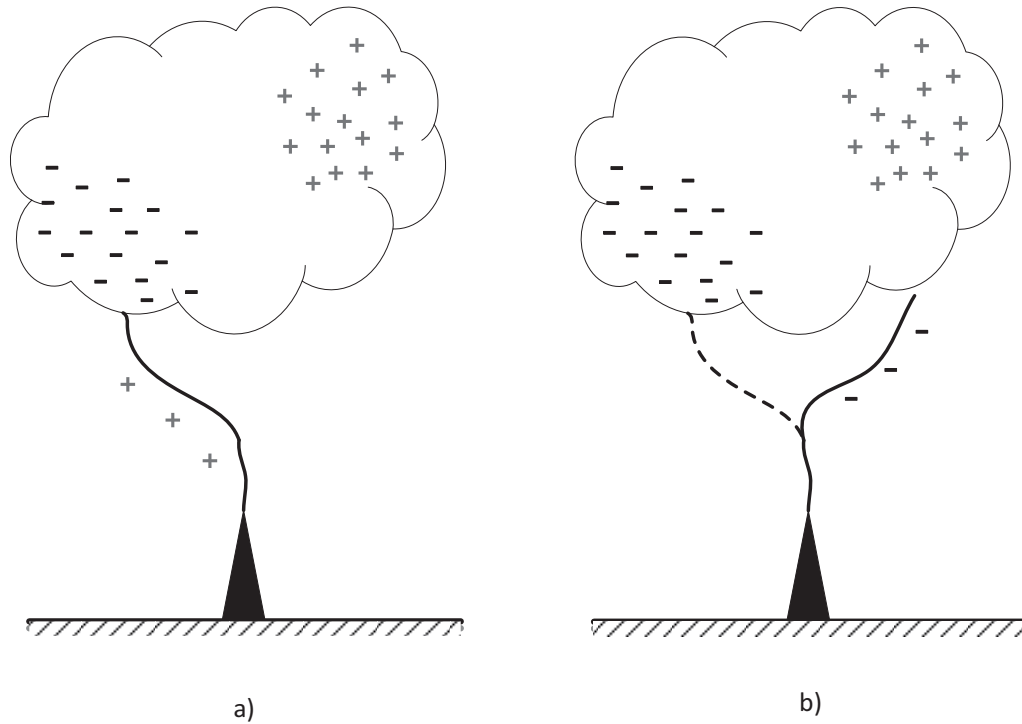


Figure 5-9. Bipolar flash that occurred on 7 May 2014. a) Overall current waveform. An expanded view of the current waveform corresponding to the upward negative leader is presented in the inset. b) Expanded view of the current waveform corresponding to the upward positive leader (UPL) and following ICC with superimposed pulses. This flash contained no return strokes (From [149]).

The initial stages of negative and positive upward flashes are associated with upward positive and upward negative leaders, respectively [31], [47]. The two observed flashes of Figure 5-8 and Figure 5-9 indicate that both, positive and negative upward leaders can be initiated from the tower on the time scale of one flash. Further, based on video observations of upward positive flashes, it has been inferred (e.g., [31]) that the pulse trains in the initial rising portion of the initial-stage current waveform are due to the stepping of an upward negative leader. The stepping-process signatures seen in the positive current waveforms in Figure 5-5, Figure 5-8 and Figure 5-9 are similar, although their durations differ by a factor of 5 or so. Since the upward negative leader shown in Figure 5-9 developed in virgin air, this similarity implies that the upward negative leader (shown in Figure 5-8) did not follow the same path as the preceding upward positive leader. Note, however, that it is conceivable that the negative stepped leader did not start from the tower tip, but from the previously-created channel carrying a 150 A steady current. To the best of our knowledge, this type of event has not been previously observed at an instrumented tower. Note, however, that a similar event was observed in triggered lightning experiments by Horii [161], [162]. That event is shown in figure 8.9 of [18], although no evidence of stepping is seen in the positive current waveform. Based on the above discussion, we hypothesize that two distinct upward leader channels of opposite polarity were involved in the development of the bipolar flash presented in Figure 5-8. Figure 5-10 shows a schematic diagram illustrating this hypothesis. The bipolar flash shown in Figure 5-9 might have followed a similar scenario, but in the reverse order.

The Category-Ib bipolar flashes can be defined as a sequence of two, and possibly more, upward leaders of different polarities, initiated from the tower less than 100 ms or so apart (See Figure 5-10). It is worth noting that Lu et al. have reported on two associated upward flashes of opposite polarity within a time interval of 45 ms [163]. However, those flashes initiated from two different towers separated by a distance of 375 m.

More data on upward leaders of opposite polarity initiated from the same tower within the same flash are required to improve our understanding of Category-Ib bipolar lightning.



**Figure 5-10. Schematic diagram illustrating the formation of the bipolar flash presented in Figure 8. It is essentially a sequence of two upward flashes separated by an unusually short time interval, the first one initiated by an upward positive leader (a) and the second one by an upward negative leader (b), (From [149]).**

## 5.4 Conclusion

We presented and discussed current waveforms associated with 13 bipolar flashes recorded at the Sântis Tower during the period from June 2010 to January 2015. A total of 427 flashes were recorded, of which 58 (13.5%) were classified as positive flashes and 13 (3.0%) as bipolar flashes.

The majority of the recorded bipolar flashes (10 out of 13) showed a polarity reversal during the initial continuous current, therefore belonging to Category I, according to [22]. Further, two flashes were characterized by different polarities of the initial stage current and the following return stroke or strokes (Category II) and one flash involved return strokes of different polarity (Category III).

Two of the ten Category-I bipolar flashes were each characterized by a sequence of two upward leaders of opposite polarity within the same flash, a scenario that has never been reported from previous observations at instrumented towers. The fact that two upward, opposite-polarity leaders can occur within tens of milliseconds of each other maybe of interest for lightning protection studies.

Further observations are needed to improve the traditional classification of bipolar flashes. Such observations should include the mapping of lightning channels inside the cloud to identify cloud charge structures and other conditions that can facilitate polarity changes in the course of the same flash.





# 6

## Lightning Interaction with the Ionosphere

### 6.1 Introduction

The ionosphere is known to contain significant number of electrons and ionized particles [164]. The presence of electrons and ions in the ionosphere causes a potential difference of about 300 kV with respect to the earth. This huge potential difference can be seen as an electrostatic field of about 100 V/m, which is measurable in fair-weather condition above the ground surface [67].

The ionosphere shows different characteristics during day time and night time conditions, indicating that along with solar ionization, non-solar ionization mechanisms such as precipitating energetic electrons, meteoric ionization, and cosmic rays must be involved in its formation and preservation [165]. In addition to temporal variation, the number of electrons and charged particles also varies as a function of altitude. Therefore, one can consider the ionosphere as a dynamic medium with characteristics varying in time and space. The characterization of the ionosphere was the subject of numerous studies since early nineteenth century (see a review in [166], [167]).

The ionosphere can be subdivided into three layers denominated as D, E, and F [165]. These layers differ one from another by their molecule content, which leads to their different response to the available ionization sources. It has been observed that the D layer mainly interacts with electromagnetic waves at the Extremely Low Frequency (ELF) and Very Low Frequency (VLF) ranges [166]. The D region of the ionosphere is known to vary drastically with the level of solar radiation and its altitude varies from 60 to 100 km. The altitude of this layer is too low for satellite measurements and too high for balloon soundings [168]. Due to the presence of free electrons and ionized particles, electromagnetic waves propagating through the D

layer of the ionosphere interact and inherit some of its features [169]. As a result, lightning electromagnetic radiation is found to be a valuable source of probing the D layer.

ELF and VLF electromagnetic field observations have been widely used to examine ionospheric reflection characteristics (e.g., [167]). The radiated electromagnetic fields from distant lightning flashes constitute a valuable source of ELF and VLF radiation which were widely used to inspect the properties of the ionosphere.

Various theoretical and numerical approaches have been proposed to model lightning-ionosphere interactions, which can be divided into four main types (see [170] and the references therein for a review).

The first approach proposed in [171], [172] is based on solving Maxwell's differential equations for slabs of horizontally stratified ionosphere. Another approach was suggested assuming the ionosphere and the earth as boundaries of a waveguide, the so-called Earth-Ionosphere waveguide. This method is based on finding eigenvalues and possible modes of propagation in the assumed waveguide [173]–[175].

A very accurate model was developed based on the solution of Fresnel equations for each slab of discretized layers of the ionosphere [176]–[178]. However, this method is computationally burdensome [168].

Finally, a 2D Finite Difference Time Domain (FDTD) method has been developed to solve Maxwell's equations in spherical coordinates in order to compute the electromagnetic field interaction with ionospheric layers [179]–[181]. This method is capable of considering a time varying ionosphere layer and nonlinearities.

In all previous studies, the knowledge of the exact lightning source is missing and this brings some level of uncertainty into the predicted ionosphere profiles (see [166] for a more thorough discussion). Simultaneous measurements of lightning currents at instrumented towers and remote electromagnetic fields have been reported in several studies (e.g., [33], [77], [87], [92], [105], [134], [182]). The longest previously reported distance at which fields from flashes to instrumented towers were measured simultaneously with their causative currents is about 100 km for the Gaisberg Tower [99].

Also, simultaneous measurements of lightning currents and electromagnetic fields associated with rocket-triggered lightning have been reported in the literature (e.g., [183]–[185]), but the distances generally varied from tens of meters to about 5 km and, hence, at least at later times, the fields were dominated by non-radiation field components. Dupree et al. [186] reported experimental observations of triggered lightning currents (at Camp Blanding, Florida) and their associated very long-distance ELF radio atmospherics in California, Greenland, and Antarctica. Note, however, that at such great distances (>3,000 km), the groundwave becomes

indiscernible and the identification of individual skywaves that overlap is impossible without sophisticated modeling [186], [187].

More recently, Carvalho et al. [188] presented electromagnetic field records associated with return strokes of upward negative triggered lightning at 209 km and 250 km away from the lightning current source. Using a Lightning Mapping Array (LMA), high speed video camera, and photodiode array, they presented as well the return stroke channel geometry and channel luminosity versus height and time, which can provide valuable and accurate information on the lightning source itself.

In this chapter, we present simultaneous current and wideband electric field waveforms at 380 km distance from the strike point associated with upward flashes initiated from the S antis Tower, which were recorded from April to October 2014. The dataset presented in this study represents, to the best of the author’s knowledge, the first simultaneous records of natural upward lightning currents and distant fields associated with natural upward flashes featuring ionospheric reflections.

The majority of our recorded electric field waveforms produced by individual strokes and ICC pulses feature one or two secondary “pulses” or “field excursions” inferred to be due to ionospheric reflections. These reflections were used to estimate the apparent ionospheric reflection heights.

The chapter contains a full-wave, Finite-Difference Time-Domain (FDTD) analysis of the field propagation. The effect of the ionospheric reflections is presented and the results are compared with the experimental data. Lightning electromagnetic fields were evaluated in spherical coordinates, within a two dimensional (2D) computational domain. The data obtained in this study can also be used to validate other models of lightning interaction with the ionosphere (e.g., [166], [168], [181], [189]).

Moreover, we present a novel semi-analytical simplified approach based on the ray tracing method to estimate radiated electric fields associated with lightning return strokes, taking into account ionospheric reflections.

The content of this chapter heavily draws from [190] and [191].

## 6.2 Obtained Experimental Data

During the period of analysis (April-October 2014), simultaneous records of currents and electric fields at 380 km were obtained for 29 flashes initiated from the S antis Tower. The detailed description of the electric field station was presented in Section 2.5. Among the 29 flashes, 4 were classified as upward bipolar and 25 as upward negative events.

We present an analysis of 11 negative upward flashes which contain 76 detectable current pulses (return strokes and fast ICC pulses, the latter being similar in their

waveform characteristics to return strokes [71] featuring secondary pulses above the noise level of the electric field records, which were identified (based on the wave shape and time of occurrence relative to the groundwave) as ionospheric reflections (skywaves). Nine flashes containing 69 pulses (with detectable skywaves) occurred during nighttime (sunset to sunrise) and two flashes containing 7 pulses (with detectable skywave) occurred during daytime (sunrise to sunset).

Figure 6-1 presents simultaneous records of the overall waveforms of current and E-field associated with an upward negative flash that occurred on 21 October 2014, during nighttime at 20:23:22 (local time). Note that the current waveform contains 5 return strokes, which followed an ICC not shown in Figure 6-1. It should be noted that, throughout this section, the positive-sign current corresponds to negative charge transfer to ground or, equivalently, positive charge transfer upward. Also, the physics sign convention (as opposed to the atmospheric electricity sign convention) according to which a downward directed electric field vector is negative, is used in the vertical electric field plots.

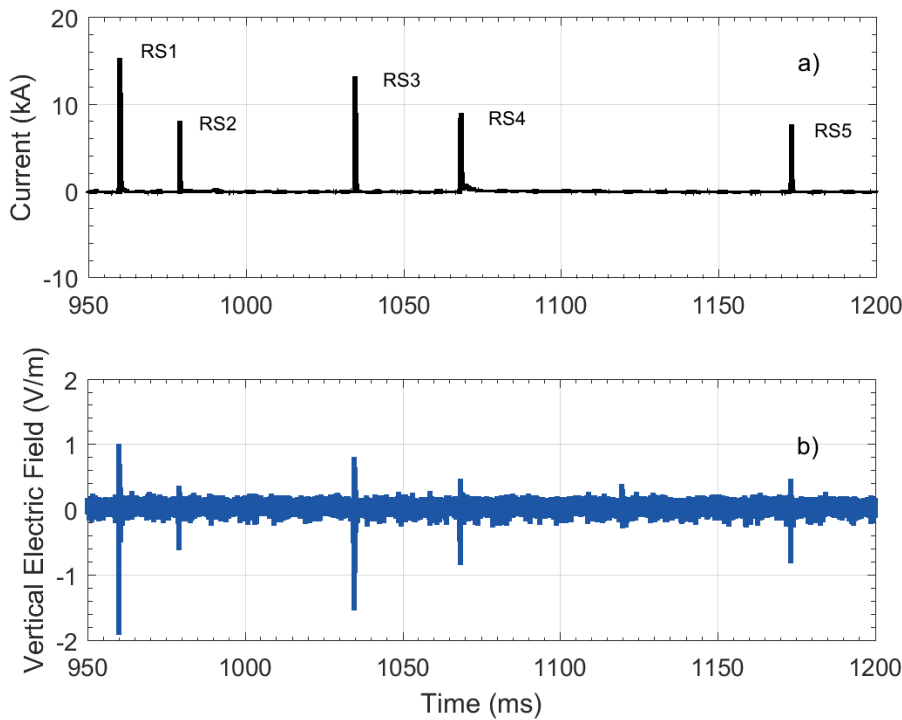


**Figure 6-1. Current and electric field waveforms produced by an upward negative flash that occurred on 21 October 2014, during nighttime at 20:23:22 (local time). a) Current waveform. b) Vertical electric field waveform at 380 km (From [190]).**

Figure 6-2 presents the current and field waveforms of one of the return strokes (RS1) of that flash. The current (Figure 6-2a) is characterized by a peak value of 15.3 kA, a risetime of 1.6  $\mu$ s and an FWHM (Full-Width at Half-Maximum) of 57  $\mu$ s. The field waveform (Figure 6-2b) exhibited the groundwave with a -1.9 V/m peak,

followed by first and second skywaves occurring about 155 and 487  $\mu\text{s}$ , respectively, after the groundwave.

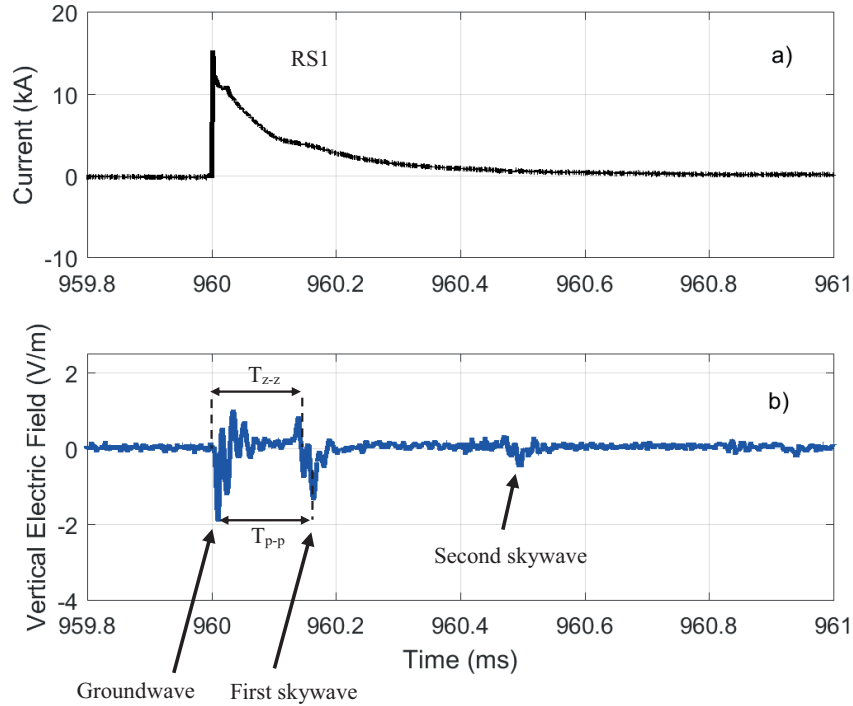


**Figure 6-2.** Current and electric field waveforms produced by the first subsequent return stroke of the nighttime upward negative flash whose overall waveforms are shown in Figure 6-1. a) Current waveform. b) Vertical electric field at 380 km. Zero-to-zero ( $T_{z-z}$ ) and peak-to-peak ( $T_{p-p}$ ), time intervals between the ground wave and the first skywave are indicated (From [190]).

Figure 6-3 shows the current and field waveforms of the return stroke of a single-stroke upward flash that occurred during daytime, on 11 May 2014, at 10:24:09 a.m. (local time). The time between the groundwave and the first skywave is shorter for this waveform than that for the nighttime skywaves seen in Figure 6-2. Also, the skywave-to-groundwave peak field ratio is much higher under nighttime conditions (0.72) compared to that under daytime conditions (0.32). This is because the ionospheric reflection during nighttime occurs at the E layer, in the absence of the high attenuation D layer, at which reflection occurs during daytime (e.g. [192]). These observations will be further discussed in the next section.

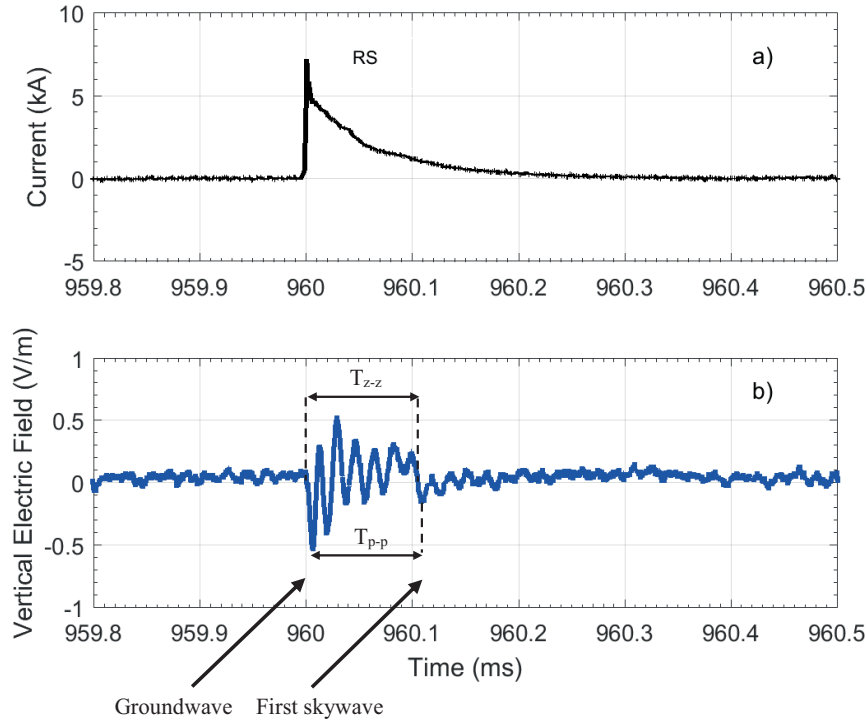


**Figure 6-3. Current and electric field waveforms produced by the only return stroke of a daytime upward flash that occurred on 11 May 2014 during daytime at 10:24:09 (local time). a) Current waveform. b) Vertical electric field waveform at 380 km. Zero-to-zero ( $T_{z-z}$ ) and peak-to-peak ( $T_{p-p}$ ), time intervals between the ground wave and the first skywave are indicated (From [190]).**

It should be noted that our field measuring system exhibited a high noise level at frequencies of 200, 300, 400 and 500 kHz. In order to reduce the noise, 20-kHz bandwidth notch filters centered at each of the above-mentioned frequencies were applied to all recorded signals. Figure 6-4 presents the raw and filtered electric field waveforms corresponding to the return stroke shown in Figure 6-2. It can be seen that the filtering appreciably reduced the noise, while preserving the main waveform characteristics.

Further, a 60-kHz ringing can be seen in the measured E-field waveform, whose origin is currently unknown and under investigation. It is worth noting that such ringing was not observed in measured (with the same instrumentation) field waveforms corresponding to lightning strikes to the Gaisberg Tower [73]. The ringing is therefore not associated with persistent local effects at the Neudorf field measuring station. On the other hand, since the Gaisberg and Säntis measurements were made on different dates, an interference source that was active only during the Säntis measurements cannot be ruled out. In any case, the ringing cannot be related to ionospheric effects, since it can also be seen on the groundwave. One possible reason could be the effect of the cable-car grounding wires of about 2.3 km in length

connecting the Säntis Tower to the mountain base. Those wires could form a half-wave resonator at a frequency of about 60 kHz. Note, however, that such ringing is not seen in the current waveform. This might be due to the fast attenuation of the upward reflected current pulses [193]. More thorough analyses is needed to confirm or refute this hypothesis.

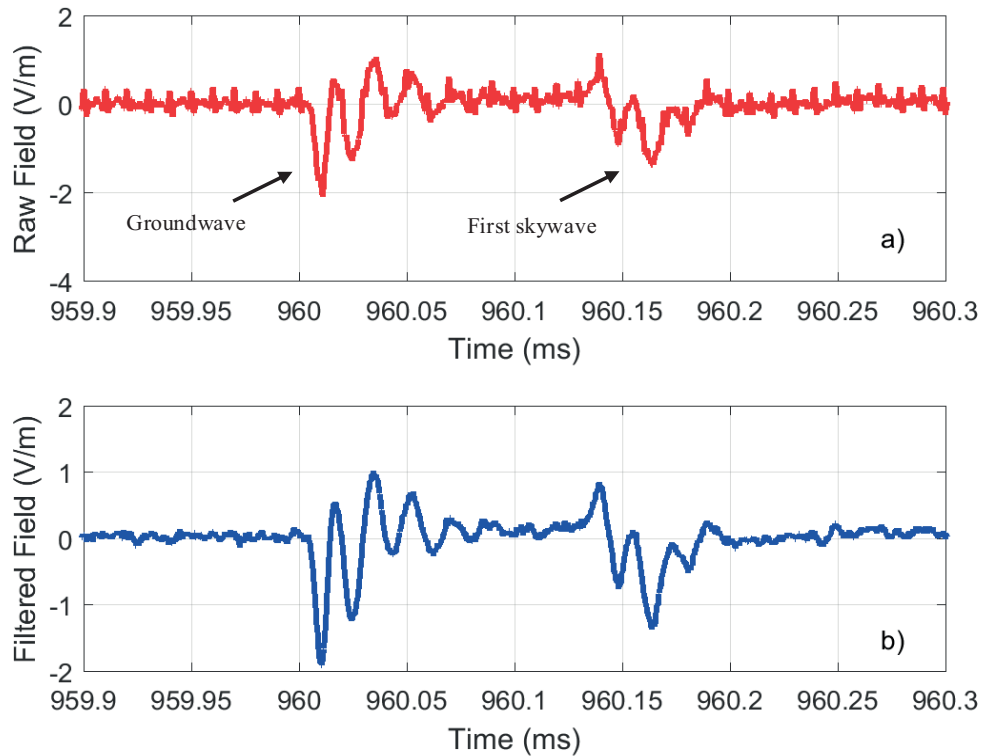


**Figure 6-4.** Raw (a) and filtered (b) E-field waveforms of the return stroke shown in Figure 6-2 (From [190]).

## 6.3 Reflection of Electromagnetic Fields from the Ionosphere

### 6.3.1 Height of Ionospheric Reflection

Figure 6-5 shows the schematic trajectories of the groundwave, first (one-hop) skywave and second (two-hop) skywave in green, blue and red, respectively. The ionospheric reflection of lightning electromagnetic pulses is a complex, frequency-dependent process. A rough and simple estimate of the ionospheric reflection height can be obtained using the difference in the times of arrival of the measured electric field groundwave and skywaves. Assuming a spherical Earth and using simple geometrical rules, the apparent height of the reflection of the first skywave ( $h_1$ ) can be estimated as:

$$h_1 = R_e \left[ \cos\left(\frac{d}{2R_e}\right) - 1 \right] + \sqrt{\left\{ R_e^2 \left[ \cos^2\left(\frac{d}{2R_e}\right) - 1 \right] + \left( \frac{ct_1 + d}{2} \right)^2 \right\}} \quad (7.1)$$

for which the propagation path is shown in blue in Figure 6-5. In equation (7.1),  $d$  is the distance from the lightning channel to the observation point along the surface of the Earth,  $R_e$  is the mean radius of the Earth,  $c$  is the speed of light, and  $t_1$  is the time interval between the groundwave and the first skywave.

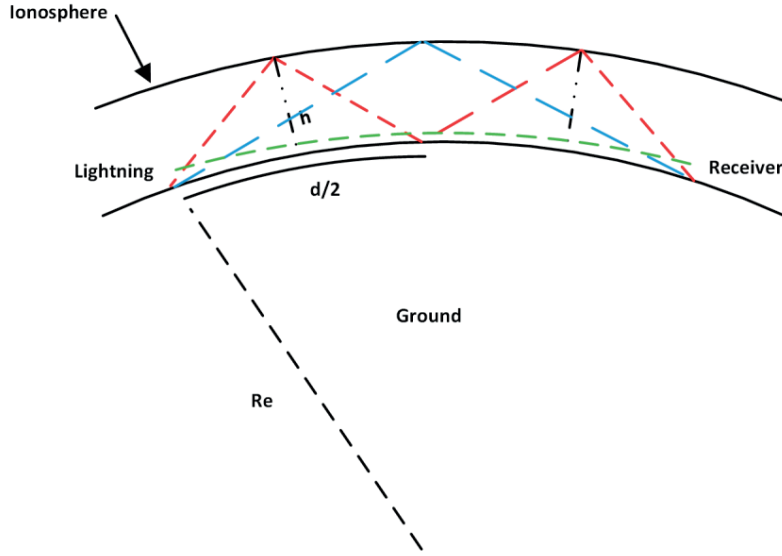


Figure 6-5. Schematic representation of the propagation paths of the ground-wave and the first two skywaves (the groundwave path is shown in green, the first skywave path in blue, and the second skywave path in red), (From [190]) .

Table 6-1. Height of the ionospheric reflection inferred from equation (7.1), (Adapted from [190]).

|           | Number of events | Height of the ionospheric reflection using peak-to-peak time interval(km) |                    |      |      | Height of the ionospheric reflection using zero-to-zero time interval(km) |                    |      |      |
|-----------|------------------|---|--------------------|------|------|---|--------------------|------|------|
|           |                  | Mean  | Standard deviation | Max  | Min  | Mean  | Standard deviation | Max  | Min  |
| Daytime   | 7                | 78.3  | 2.8                | 82.1 | 74.9 | 76.2  | 0.7                | 77.5 | 75.4 |
| Nighttime | 69               | 91.3  | 1.6                | 93.8 | 87   | 89.4  | 1.2                | 93.2 | 87.0 |

Haddad et al. proposed two approaches to roughly estimate the time interval  $t_1$  between the groundwave and the first skywave: the zero-to-zero approach and the peak-to-peak approach. We applied the two approaches to our data [194]. Table 6-1



presents the resulting arithmetic means of the height of the ionospheric reflection, determined separately for daytime and nighttime. It can be seen that, during daytime, the means of the estimates of the ionospheric reflection height, based on the two approaches, are 76 km and 78 km, corresponding to the D layer. On the other hand, the means of the reflection-heights estimates for nighttime are 91 km and 89 km, apparently corresponding to the reflection from the E layer.

Among the 76 recorded pulses for which ionospheric reflections were discernible in the electric field records, 14 pulses additionally showed a second ionospheric reflection above the noise level of the field measuring system. All of these pulses occurred during nighttime, which was expected due to the virtual absence of the D layer [192]. Similar to equation (7.1), it is straightforward to derive equation (7.2) to estimate the height ( $h_2$ ) of the ionospheric reflection using the second skywave (red path in Figure 6-5).

$$h_2 = R_e \times \left[ \cos\left(\frac{d}{4R_e}\right) - 1 \right] + \sqrt{\left\{ R_e^2 \times \left[ \cos^2\left(\frac{d}{4R_e}\right) - 1 \right] + \left( \frac{ct_2 + d}{4} \right)^2 \right\}} \quad (7.2)$$

In equation (7.2),  $t_2$  is the time interval between the groundwave and the second skywave. It should be noted that the heights of the first and second ionospheric reflections are assumed to be equal.

Table 2 presents the arithmetic means for the ionospheric reflection heights estimated using equation (7.2) and compares them with the reflection heights estimated using equation (7.1) for the same data set. It can be seen that the estimates obtained using equation (7.2) are in slightly better agreement with those of equation (7.1) when the zero-to-zero method is used.

**Table 6-2. Comparison between arithmetic means of the height of the ionospheric reflection inferred from equations (7.1) and (7.2). All the pulses occurred during nighttime (Adopted from [190]).**

|   | Number of events | Height of the ionospheric reflection (km) |                                  |
|---|------------------|---|----------------------------------|
|   |                  | using peak-to-peak time interval          | using zero-to-zero time interval |
| Eq. (7.1)   | 14               | 93  | 90                               |
| Eq. (7.2)   | 14               | 90  | 89                               |
| Maximum value of the difference between Eq. (7.1) and Eq. (7.2) | 14               | 4.4                                       | 3.7                              |

### 6.3.2 Variation of the Reflection Height as a Function of Stroke Order

Lightning discharges are known to be able to modify the electron density in the lower ionosphere (e.g. [195]), which would result in a change in the height of ionospheric reflections. Haddad et al. observed different daytime heights of ionospheric reflection for first and subsequent return strokes in downward flashes [194]. In a follow-up study, Somu et al. confirmed their daytime results (additionally reporting that the reflection heights tend to decrease with stroke order) and found that the trend was considerably less pronounced under nighttime conditions [189]. They also observed that the reflection height tended to increase with increasing the return-stroke peak current. A variation of electron density was mostly predicted for severe lightning return strokes with peak currents greater than about 60 kA [196], based on the theoretical study of Taranenko et al. [197].

Since there are no first strokes in upward flashes, we cannot compare reflection heights for first and subsequent strokes. However, in our dataset, we did not observe any significant variation of the estimated reflection height as a function of stroke order within a flash. This might be related to the fact that peak currents in our upward flashes ranged from 2.3 to 15.4 kA, much smaller than the downward flashes studied by Somu et al.

### 6.3.3 Peak Field Versus Peak Current for Groundwave and Skywaves

Figure 6-6 shows a scatterplot of the groundwave peak electric field versus the peak current for all the considered events. In this figure, pulses measured during daytime are shown in blue and those measured during nighttime are shown in red. As expected, no effect of the ionosphere (daytime or nighttime) on the groundwave is seen. Figure 6-7 shows the scatterplot of the first skywave peak electric field versus peak current. Again, pulses measured during daytime are shown in blue, while those measured during nighttime are shown in red. The best-fit linear regressions lines, forced to go through the origin, are also shown in Figure 6-6 and Figure 6-7. Unlike the groundwave, for which no clear distinction between nighttime and daytime pulses can be seen, Figure 6-7 indicates that daytime pulses appear to suffer stronger attenuation compared to nighttime pulses.

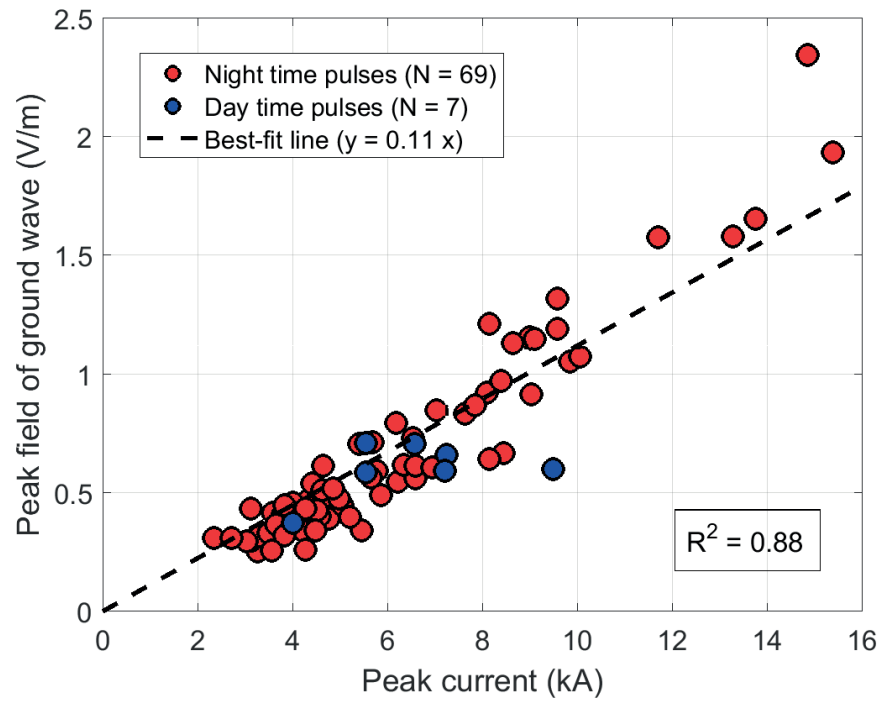


Figure 6-6. Peak current versus peak electric field for the groundwave at 380 km (Adopted from [190]).

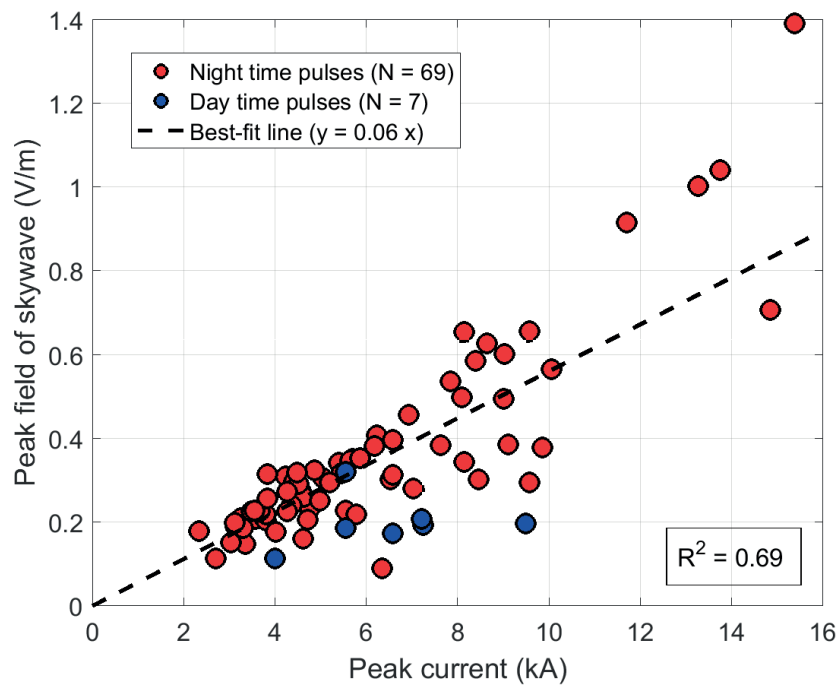


Figure 6-7. Peak current versus peak electric field of the first skywave at 380 km (Adopted from [190]).

## 6.4 FDTD Numerical Simulation of Wave Propagation in Earth-Ionosphere Waveguide

### 6.4.1 Methodology

In this section, a full-wave Finite-Difference Time-Domain (FDTD) model developed to analyze the propagation of lightning electromagnetic fields in the Earth-Ionosphere waveguide is presented. Lightning electromagnetic fields were evaluated in spherical coordinates, within a two dimensional (2D) computational domain lying on the plane defined by the center of the Earth, the tower base and the field measurement point [198], [199], as shown in Figure 6-8.

The working space of the 2D FDTD (point-centered) is  $1000 \text{ km} \times 100 \text{ km}$ , which is divided into 100-m quadrilateral cells. The time increment is set to  $0.19 \text{ } \mu\text{s}$ . In order to avoid reflections at the outer boundaries, we implemented the Uniaxial Perfectly Matched Layer (UPML) absorbing boundary conditions [116], [200], [201]. The lightning channel was placed on the symmetry axis of the model and the observation point is at distance  $d$  from the lightning channel (see Figure 6-8).

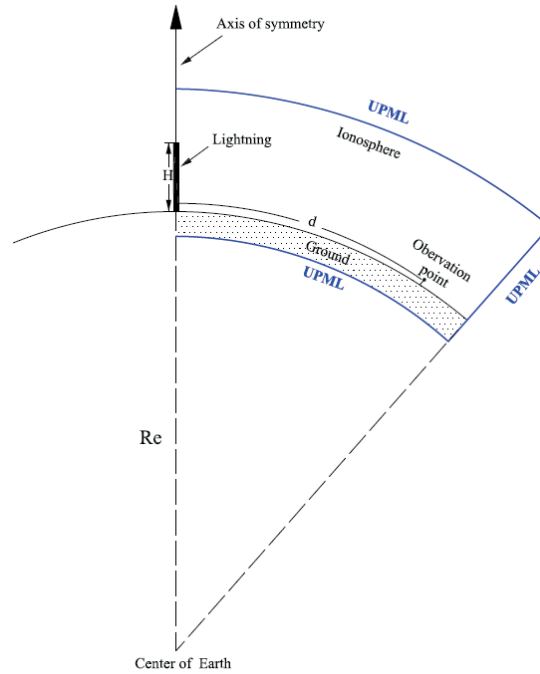


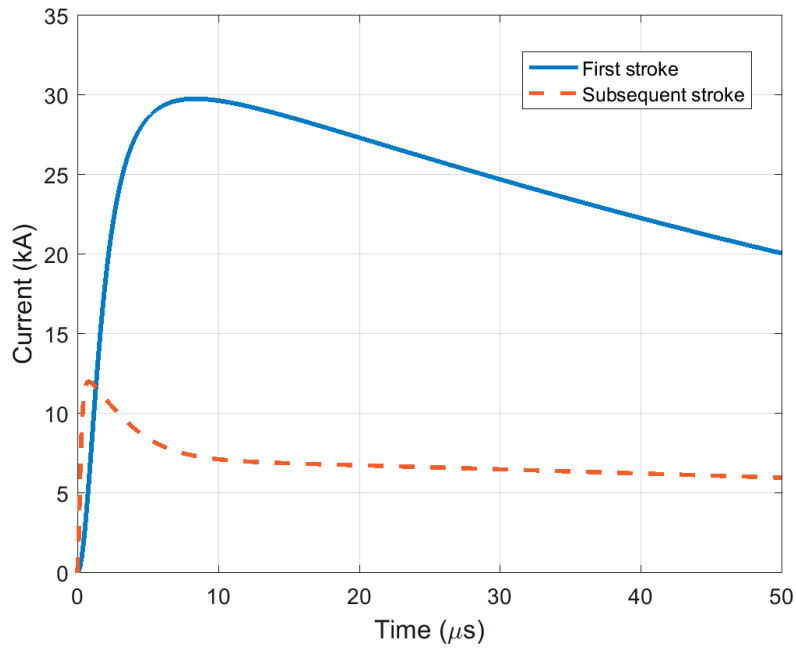
Figure 6-8. The geometry of the Computational domain of the FDTD model (From [190]).

In order to consider the ionospheric conductivity profile, we assume a vertically inhomogeneous, highly collisional, and isotropic ionosphere environment as presented by Said [170]. The conductivity of the ionospheric region varying with altitude is given by:

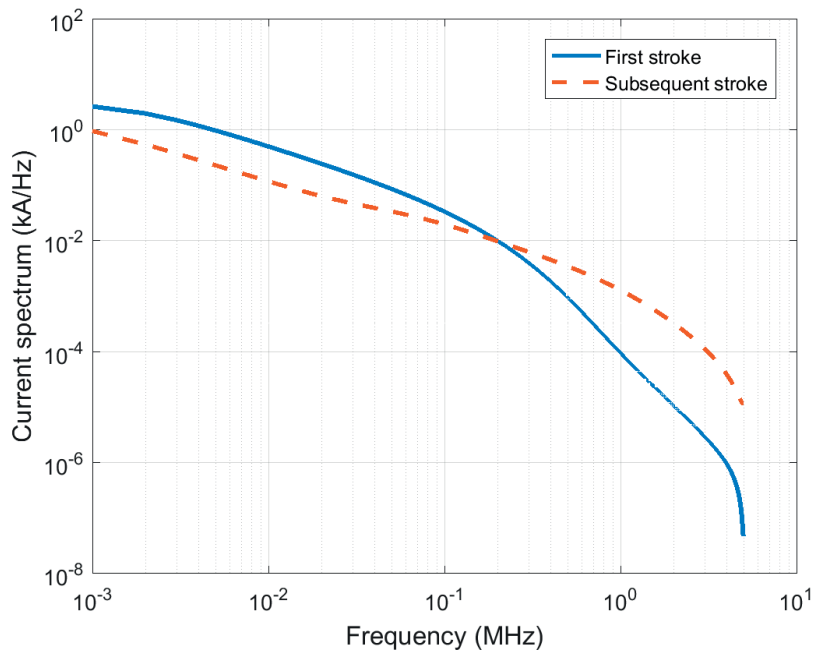
$$\sigma(z) = \varepsilon_0 (2.5 \times 10^5 \text{ s}^{-1}) e^{\beta(z-h')} \quad (7.3)$$

where  $\beta$  is the slope of the atmospheric conductivity profile with  $\beta = 0.3 \text{ km}^{-1}$  (daytime) or  $\beta = 0.7 \text{ km}^{-1}$  (nighttime) and  $h'$  is the reference reflection height which is equal to 80 km and 90 km for daytime and nighttime conditions, respectively [202]. The height of the lightning channel was assumed to be  $H = 8.0 \text{ km}$ , and the return stroke speed was set to  $v = 1.5 \times 10^8 \text{ m/s}$ . The homogeneous earth is characterized by a conductivity  $\sigma_g = 10^{-3} \text{ S/m}$  and relative permittivity  $\varepsilon_r = 10$ . Note that neither the effect of the geomagnetic field nor the presence of the tower nor the mountain were considered in the simulations.

The current distribution along the return stroke channel was specified according to the modified transmission line model with exponential current decay with height (MTLE) [117], [118], assuming a current decay constant  $\lambda = 2 \text{ km}$  [119]. The measured channel-base current waveform was represented using the sum of two Heidler's functions [121]. In the analysis, two channel-base current waveforms corresponding to typical first and typical subsequent strokes were considered. The parameters of the corresponding Heidler functions are given in [93]. The current waveforms and their frequency spectra are presented in Figure 6-9a and Figure 6-9b, respectively. It can be seen that the subsequent return-stroke spectrum is characterized by more significant higher-frequency content compared to the first return stroke.



(a)



(b)

Figure 6-9. Channel-base currents for typical first and subsequent return strokes. (a) Time domain wave forms. (b) Frequency spectra (From [190]).

### 6.4.2 Simulation Results

The electric fields were computed at three distances, 200 km, 380 km, and 700 km. The simulation results are presented in Figure 6-10 (first return stroke) and Figure 6-11 (subsequent return stroke). In each figure, the groundwave, the first skywave, and the second skywave are labeled G, S1, and S2, respectively.

Although the first and subsequent return stroke currents are characterized by different frequency spectra, the model-predicted E-field waveforms of the S1 and S2 skywaves shown in Figure 6-10 and Figure 6-11 exhibit similar features (including the delays relative to the ground wave). This was also demonstrated, using a different FDTD model, by Somu et al. ([189] , Figures 8 and 9).

At relatively short distances (less than 200 km), the effect of the ionospheric reflection on the electric field is relatively small for both daytime and nighttime conductivity profiles. At larger distances, the ionospheric reflections occur earlier in time with respect to the groundwave. At distance  $d=700$  km, the groundwave and the first skywave arrive almost simultaneously, particularly in the daytime.

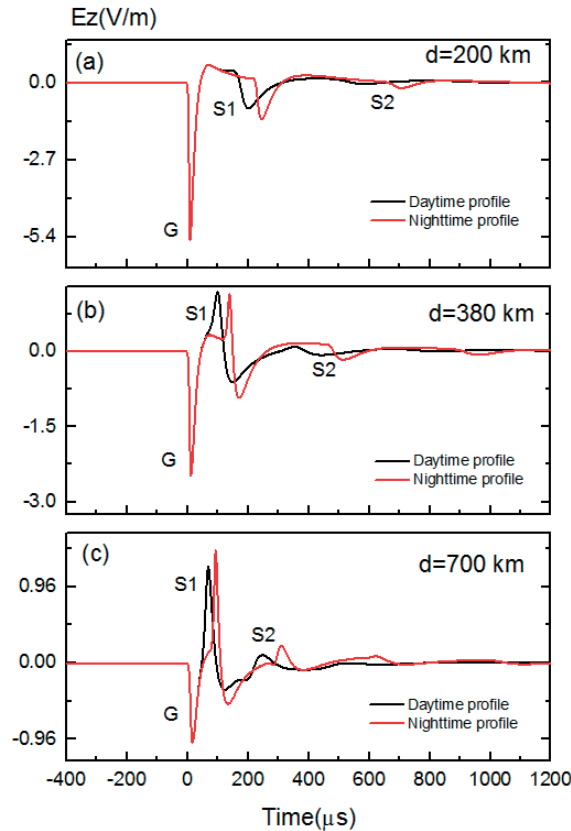


Figure 6-10. E-field waveforms at different distances (200 km (a), 380 km (b), and 700 km (c)) for the typical first return stroke and the daytime (black line) and nighttime (red line) ionospheric conductivity profiles. The groundwave, first ionospheric reflection, and second ionospheric reflection are labeled G, S1, and S2, respectively (From [190]).

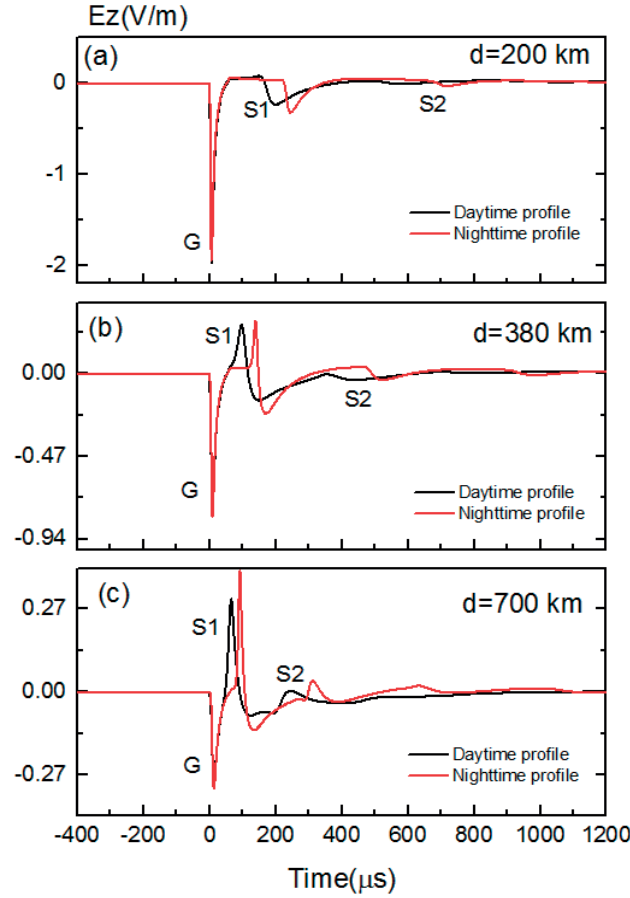


Figure 6-11. Same as Figure 6-10, but for the typical subsequent return stroke (From [190]).

#### 6.4.3 Comparison with Experimental Data

We present a comparison between the FDTD simulation results and the measured daytime and nighttime waveforms. The channel-base currents measured at the Säntis Tower could not be directly used in the FDTD simulations because of the superimposed noise [72]. To reduce the noise, we have smoothed the unusual waveforms using a 2-MHz low-pass filter. Figure 6-12a and Figure 6-13a show the current waveforms measured at the Säntis Tower (black line) and their low-pass filtered versions used in the FDTD computations (red line). Figure 6-12b and Figure 6-13b show the corresponding electric field waveforms at 380 km (Neudorf, Northern Austria). The event shown in Figure 6-12 corresponds to a return stroke of an upward flash that occurred during nighttime (shown in Figure 6-1). The event shown in Figure 6-13 corresponds to the single stroke of an upward flash that occurred during daytime (shown in Figure 6-3).



It can be seen that the FDTD model allows to reproduce fairly well the field waveshapes and the arrival times of the first and second skywaves relative to the ground wave for both the nighttime and daytime conductivity profiles.

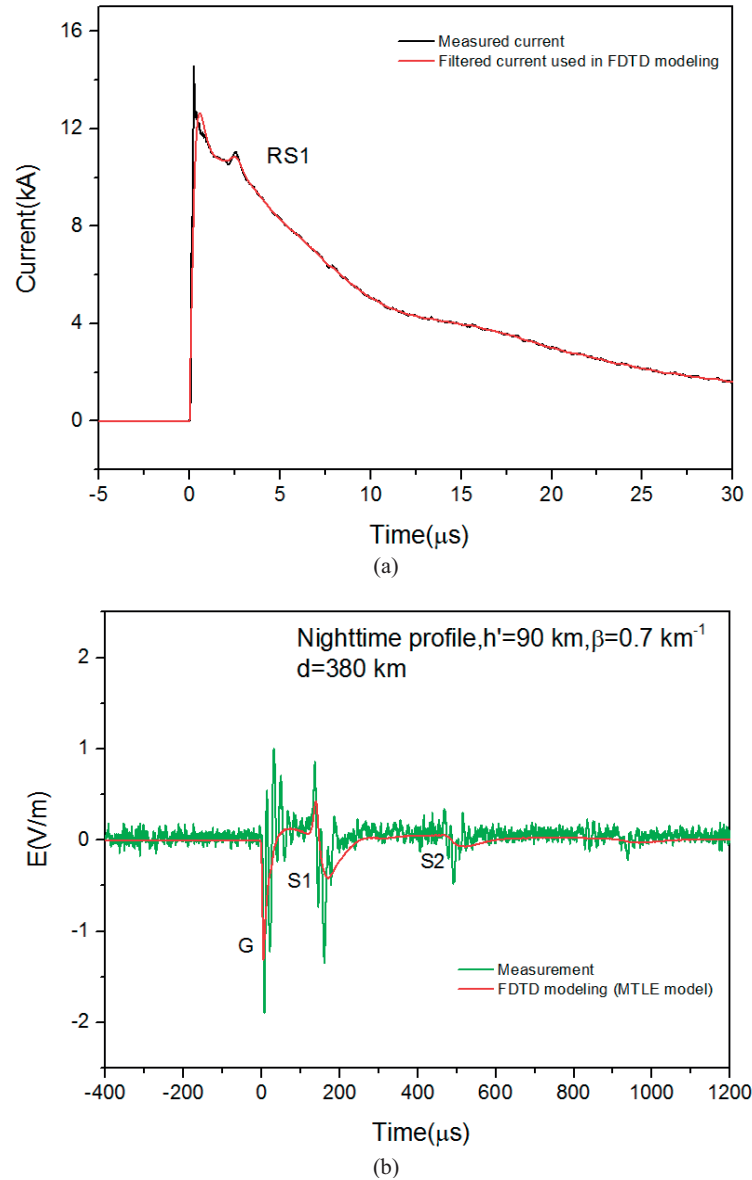


**Figure 6-12.** Current and electric field waveforms produced by the first return stroke of the nighttime upward flash that occurred on 21 October 2014 at 20:23:22. (a) Measured current (black) and 2-MHz low-pass filtered (red) current used in FDTD simulations. (b) Measured (green) and simulated (red) E-field waveforms at 380 km (From [190]).

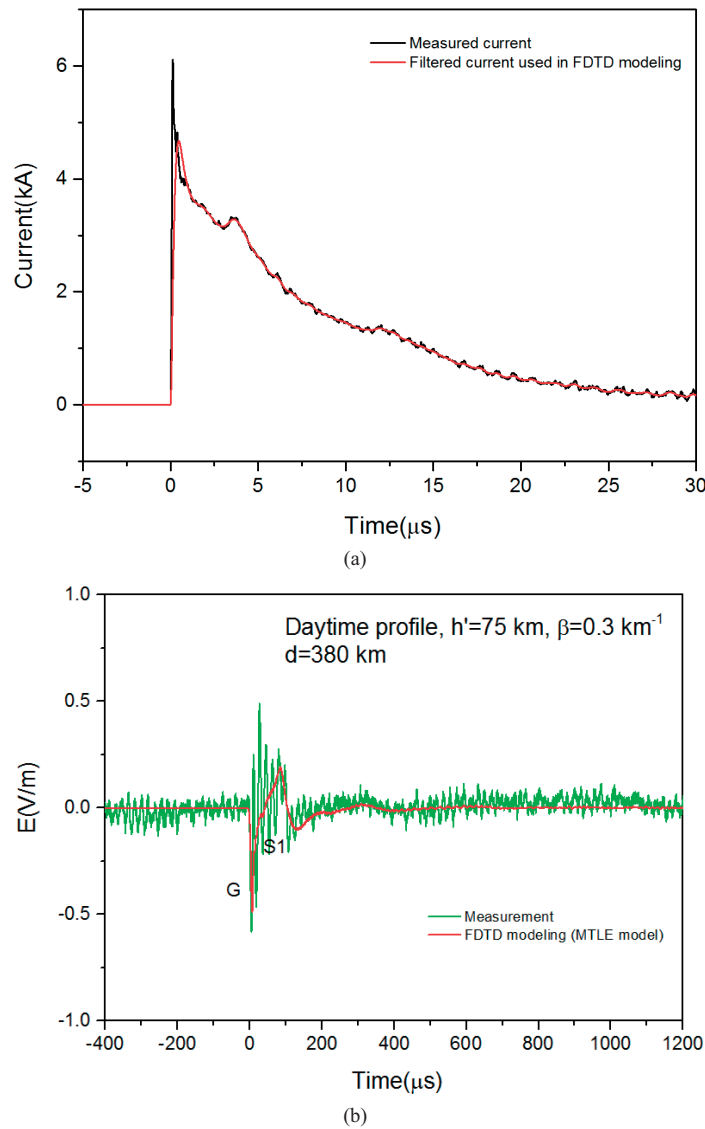


**Figure 6-13.** Current and electric field waveforms associated with the only return stroke in the daytime upward flash that occurred during daytime on 11 May 2014 at 10:24:09. (a) Measured current (black) and 2-MHz low-pass filtered current (red) used in FDTD simulations. (b) Measured (green) and simulated (red) E-field waveforms at 380 km (From [190]).

## 6.5 Ray Tracing Approach for Field Calculation of Electromagnetic Field Reflection from Ionosphere Layer

In this section, we present a semi-analytical simplified approach based on the ray tracing method to estimate radiated electric fields associated with lightning return strokes, taking into account ionospheric reflections.

The field transfer function at each frequency and each grazing angle is determined by applying the generalized Snell's law of refraction, and the antenna radiation pattern concept is used to obtain the source illumination efficiency, from which the radiated field is derived. The proposed method is validated using the full-wave FDTD simulations presented in section 6.4.

### 6.5.1 General Methodology and Simplifying Assumptions

Let us assume a vertical lightning channel of height  $H_0$  located along the  $z$  axis. As illustrated in Figure 6-14, the associated electromagnetic field radiates out from the channel in all directions and it depends both, on the frequency and on the direction. If the observation distance is sufficiently large compared to the channel length, the fields can be assumed to emanate from one point. The fields at any point in space can be obtained by the superposition of solutions at different frequencies and angles.

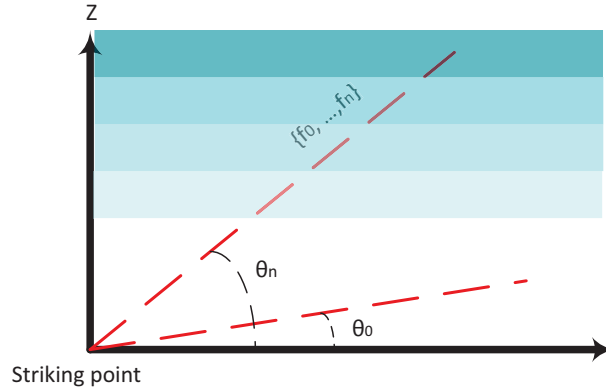


**Figure 6-14. Schematic diagram of frequency-angle solution space. The shaded area represents the considered discretized stratified medium (From [191]).**

The generalized Snell's law of refraction [203] along with the following simplifying assumptions were used to estimate the radiated electric field:

- An inhomogeneous, highly collisional and isotropic ionosphere environment is assumed (see Section 6.5.1.1 for more details).
- Multiple reflections between layers of the absorbing media representing the ionosphere are neglected and only the first reflection at half distance (from the striking location to the observation point) is considered (see Section 6.5.1.3 for more details).
- The MTLE return stroke model [117], [118] is used to compute the incident electric field, on which amplitude and phase corrections are applied to account for the presence of the ionosphere. Only the radiation field is considered in the analysis.
- The effect of the earth curvature is disregarded.

- The ground is assumed to be a perfectly-conducting half-space.

The applied methodology can be summarized as follows: First, the path of the field propagation is determined at each frequency and at each illumination angle (frequency-angle space) using Snell's law of refraction for absorbing media, and the phase delay of the path and its associated attenuation loss are calculated analytically. Then, the lightning source illumination efficiency is estimated using the antenna radiation pattern concept [204], from which the radiated field is derived. Figure 6-15 shows a flowchart of the detailed step-by-step procedure which will be explained in detail in Sections 6.5.1.1 to 6.5.1.6.

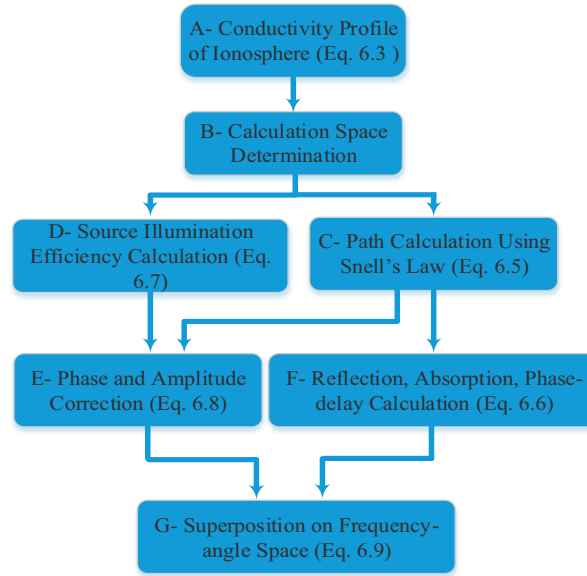


**Figure 6-15. Schematic diagram of the step-by-step procedure to estimate distant electric field (From [191]).**

#### 6.5.1.1 Conductivity Profile of the Ionosphere (Step A)

An isotropic, inhomogeneous, highly collisional environment as presented in equation (7.3), is considered with  $\beta = 0.7 \text{ km}^{-1}$  and  $h'$  is assumed to be 90 km (nighttime conditions).

#### 6.5.1.2 Calculation Space (Step B)

According to the adopted conductivity profile, the calculation space is represented as discrete, stratified horizontal layers with variation of conductivity values determined by equation (7.3). The vertical discretization step is assumed to be  $\lambda_{\min}/10$ , where  $\lambda_{\min}$  is the wavelength associated with the highest significant frequency of the source spectrum. For the sake of simplicity, we neglect the effect of the earth curvature and the finite ground conductivity in this preliminary study.

### 6.5.1.3 Path Calculation Using Snell's Law (Step C)

To calculate the path of the propagating field between the origin (lightning strike point) and the observation point, we use the generalized Snell's law of refraction for absorbing media to calculate field properties at the intersection of the adjacent layers.

A travelling plane wave with propagation direction  $\vec{r}$  can be written in the form  $\vec{E}(\omega) = \vec{E}_0(\omega)e^{-\vec{\gamma} \cdot \vec{r}}$  in the frequency domain, where:

$$|\vec{\gamma} \cdot \vec{\gamma}| = (j\omega\mu_0 \times (\sigma + j\omega\epsilon_0)) = (\alpha + j\beta)^2 = -|\vec{k} \cdot \vec{k}| \quad (7.4)$$

where  $\vec{k}$  is the wave vector,  $\epsilon_0$  and  $\mu_0$  are, respectively, the permittivity and the permeability of free space.

The generalized Snell's law of refraction at the interface of two absorbing media can be obtained using the following equation:

$$\begin{aligned} \beta_i^2 - \alpha_i^2 &= \omega^2 \mu_0 \epsilon_0 \\ \beta_i \times \sin \theta_i &= \beta_{i-1} \times \sin \theta_{i-1} \\ \alpha_i \times \sin \Psi_i &= \alpha_{i-1} \times \sin \Psi_{i-1} \\ \alpha_i \times \beta_i \times \cos(\theta_i - \Psi_i) &= \alpha_i \times \beta_i \times (\vec{e}_i \cdot \vec{f}_i) = \frac{\omega^2 \mu_0 \sigma}{2} \end{aligned} \quad (7.5)$$

where the incident field can be expressed in terms of the wave vector  $\vec{k}_{i-1} = \beta_{i-1} \vec{e}_{i-1} - \alpha_{i-1} \vec{f}_{i-1}$ , where  $\vec{e}_{i-1}$  and  $\vec{f}_{i-1}$  are perpendicular to the planes of constant phase and constant amplitude, respectively, in the  $(i-1)^{th}$  medium [203]. Assuming a propagation direction defined by the angle  $\theta_0$  as shown in Figure 3, when the two adjacent layers have very similar properties ( $\sigma_{i-1} \approx \sigma_i$ ), we expect a very small value for the reflection coefficient ( $\Gamma \ll 1$ ) at their interface. These higher order reflections are neglected in the analysis, since  $\Gamma^n \ll \Gamma \ll 1$  ( $n \geq 3$ ). As a result, for each illumination angle  $\theta_0$ , only one ray will reach the observation point (this ray is represented in bold in Figure 6-16 and corresponds to a reflection point at half distance).

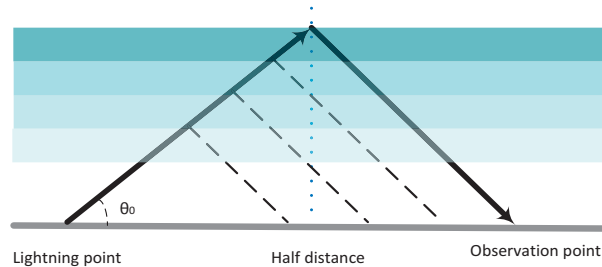


**Figure 6-16. Schematic diagram of the first-hand reflections, the dashed lines show the first-hand reflected rays which will not reach the observation point. The shaded area represents the considered discretized stratified medium (From [191]).**

#### 6.5.1.4 Reflection, Absorption, and Phase Delay

The field that passes through the dispersive ionosphere will be affected by reflection from the stratified layers ( $R_p$ ), as well as absorption losses (AL) and phase delay (PD), which are dependent on the incidence angle and frequency. The following set of equations allows to determine these parameters [203], [205]:

$$\begin{aligned}
 R_p(\theta, \omega) &= \frac{\tilde{n}_i^2 k_{i-1} - \tilde{n}_{i-1}^2 k_i}{\tilde{n}_i^2 k_{i-1} + \tilde{n}_{i-1}^2 k_i} \\
 AL(\theta, \omega) &= \\
 \exp(-2 \times \int_0^{L\_reflection} \alpha(l) \times l \times \cos(\theta(l) - \Psi(l)) \times dl) & \quad (7.6) \\
 PD(\theta, \omega) &= \\
 \exp(-2 \times \int_0^{L\_reflection} \beta(l) \times l \times dl) &
 \end{aligned}$$

in which  $\tilde{n}_i$  is the refractive index of the  $i$ th layer,  $k_i = \vec{n} \cdot \vec{k}_i$  ( $\vec{n}$  is the normal unit vector to the incident plane),  $l$  is the path of the wave determined by  $l_i = dh / \cos(\theta_i)$  and  $L\_reflection$  is the distance corresponding to  $x_i = \frac{d}{2}$ . The factor 2 in the exponent accounts for the fact that the path of the down-going wave is just the flipped version of the up-going one (at each frequency and at each illumination angle).

#### 6.5.1.5 Source Illumination Efficiency Calculation at Frequency-Angle Space (Steps D and E)

The current distribution along the return stroke channel was specified according to the modified transmission line model with exponential decay (MTLE) [117], [118], assuming a current decay constant of  $\lambda = 2$  km and a return stroke speed of  $1.5 \times 10^8$  m/s. The height of the lightning channel was set to 8 km. The incident radiation field of the lightning return stroke is calculated in the frequency domain using [206]:

$$E_z(r, z, \omega) = \int_{-H_0}^{H_0} \frac{-r^2}{4\pi\epsilon_0} \times \frac{j\omega}{c^2 R^3} \times I(z', \omega) \times \exp(-j\omega R/c) dz' \quad (7.7)$$

in which,  $r$  and  $z$  are the cylindrical coordinates of the observation point,  $R$  is the distance between each element of current along the channel from the observation point ( $R = \sqrt{r^2 + (z' - z)^2}$ ),  $I(z', t)$  is the Fourier transform of the current along the channel,  $c$  is the speed of light and  $\epsilon_0$  is the permittivity of free space.

First, we calculate the radiated electric field at far distance ranges in free space for all observation angles in the frequency domain using equation (7.7), from which one

can simply derive  $E_z(d/2, \theta, \omega)$ . The effect of propagation through the absorbing medium is accounted for using the following correction factors:

$$K_{amp}(\theta, \omega) = \frac{\int_0^{H_{reflection}} \frac{1}{\cos(\theta(h))} \times dh}{d/2 \sin(\theta_0)} \quad (7.8)$$

$$K_{phase}(\theta, \omega) = \exp \left[ j(\omega/c) \times (d/2 \sin(\theta_0)) \right]$$

in which  $H_{reflection}$  corresponds to  $x_i = \frac{d}{2}$ , and  $\theta_0$  is the illumination angle.

#### 6.5.1.6 Superposition in the Frequency-Angle Space (Step G)

Once the solution is obtained in the frequency-angle space, the total vertical electric field at the observation point can be evaluated superimposing all the contributions using:

$$E_z(d, z=0, t) = F^{-1} \left( \sum_{\theta} \sum_{\omega} E_z(d/2, \theta, \omega) \right. \\ \times K_{amp}(\theta, \omega) \times K_{phase}(\theta, \omega) \\ \left. \times R_p(\theta, \omega) \times AL(\theta, \omega) \times PD(\theta, \omega) \right) \quad (7.9)$$

### 6.5.2 Validation Using FDTD Simulation

Full-wave FDTD simulations [190] are used as reference to test the validity of the proposed approach. The vertical electric field radiated by a lightning discharge is evaluated at a distance of 380 km from the lightning channel. The channel-base current represented by the sum of two Heidler's functions is presented in Figure 6-17. This waveforms correspond to a recorded current of a subsequent return stroke of an upward flash recorded at the Säntis Tower [190]. The MTLE model with parameters presented in Section 6.5.1.5 was used to specify the current distribution along the lightning channel. Figure 6-18 shows the obtained results using the proposed approach, and those obtained using the FDTD method (the FDTD simulation parameters are described in [190]).

It can be seen from Figure 6-18 that the field predicted by the proposed semi-analytical approach is in reasonably good agreement with the FDTD results. The observed differences in the arrival time of the skywave can be explained by the fact that the earth curvature was considered in the FDTD simulations, but neglected in the semi-analytical approach. In addition, differences in the risetime and in the initial pulse width can be explained by the fact that in the FDTD simulations, the ground finite conductivity was accounted for ( $10^{-3}$  S/m).

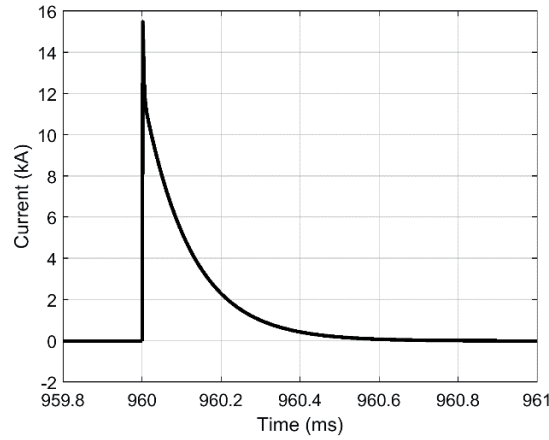


**Figure 6-17. Channel-base current of a subsequent return stroke recorded at the S antis Tower represented using Heidler’s functions (From [190]).**

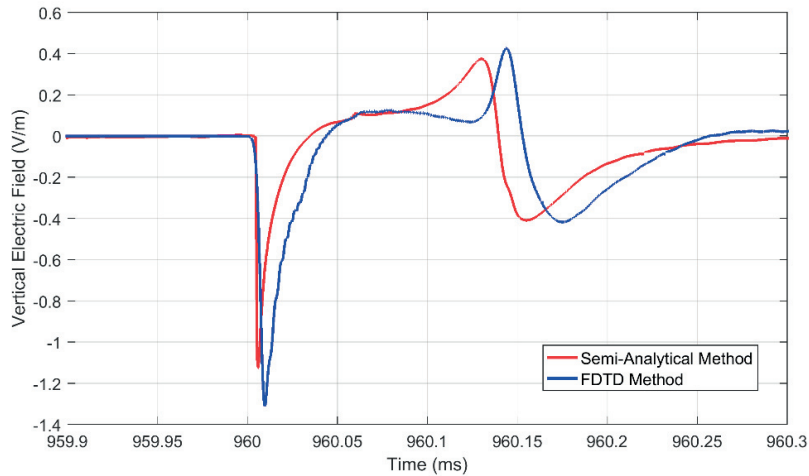


**Figure 6-18. Comparison of Simulated vertical electric field using the semi-analytical approach and FDTD method (From [191]).**

## 6.6 Conclusion

We presented simultaneous current and wideband electric field waveforms at 380 km associated with upward flashes initiated from the S antis Tower. To the best of our knowledge, the dataset presented in this study includes the first simultaneous records of lightning currents and associated fields featuring ionospheric reflections for upward flashes, and the longest distance at which upward lightning fields have been measured simultaneously with their causative currents.

Intervals between the ground wave and the skywaves were used to evaluate ionospheric reflection characteristics during daytime and nighttime based on the so-



called zero-to-zero and peak-to-peak methods. During daytime, the mean values of the estimated ionospheric reflection heights, using two different delay estimation approaches, are about 76 and 78 km, corresponding to the D layer. The mean estimated values for the reflection heights at nighttime are about 90 and 89 km, corresponding to the E layer.

We presented a full-wave, finite-difference time-domain (FDTD) analysis of the field propagation including the effect of the ionospheric reflection. The FDTD simulation results were compared with measured E-fields associated with upward flashes to the S antis Tower. It was found that the model reproduces fairly well the measured E-field waveforms and the times of arrival of the one-hop and the two-hop skywaves relative to the ground wave.

Finally, we presented a semi-analytical simplified approach based on the ray tracing method to estimate the radiated electric field associated with lightning return strokes, taking into account ionospheric reflections. The field transfer function at each frequency and each illumination angle was determined by applying the generalized Snell's law of refraction, and the antenna radiation pattern concept was used to obtain the source illumination efficiency, from which the radiated field was derived. The proposed method was validated using as reference full-wave FDTD simulations.



# 7

## Conclusions

### 7.1 Summary and Conclusions

The thesis is devoted to the study of upward lightning flashes. Upward lightning has received a great deal of attention in recent years essentially because it represents a major threat for modern wind turbines. The mechanism of initiation of upward discharges from tall structures is currently poorly understood and is the subject of various studies.

The thesis takes advantage of the data obtained at the unique experimental facility of the Sântis tower to study upward lightning discharges of different polarities (negative, positive and bipolar) and the modeling of its environmental electromagnetic effects.

The study of upward discharges is of great importance not only for engineering applications of lightning research (such as protection of power grids and wind turbines), but also to gain insight into the physics of this type of discharge and to infer the conditions of their initiation.

A summary of the topics covered in this dissertation is given in what follows.

**Chapter 1** presented the phenomenology of the lightning discharge including a summary of cloud electrification processes and various phases involved in different types of discharges. We reviewed cloud-to-ground lightning flash classifications based on the polarity and direction of the leader propagation. We briefly discussed various means of lightning observation including instrumented towers, triggered-lightning, and lightning location systems.

**Chapter 2** described the current measurement system at the Sântis Tower which has been operational since June 2010. We presented updates and upgrades which were

conducted during the course of this work in order to improve the performance of the system. In addition, the electric field measurement campaigns which were deployed at three different distance ranges, to record associated electric fields of lightning events, were described.

**Chapter 3** presented discussions on various aspects of upward negative lightning, which makes them different from their downward counterparts. We examined the superimposed pulses on the initial stage of upward negative flashes using simultaneous far field observations and current records at the Säntis Tower in order to find the involved charge transfer modes in their formation. Our investigation on the initial stage of upward negative flashes revealed that, in addition to the continuous current mode of charge transfer, negative charges will find their way to ground in both M-component and return stroke modes of charge transfer. These two types of charge transfer mode in the initial stage of upward negative events were found to be distinguishable by their associated electric-field signatures.

Superimposed pulses on the initial continuous current were identified: (1) M-component-type ICC-pulses, for which the microsecond-scale electric field pulse occurs significantly earlier than the onset of the current pulse, and, (2) RS-type ICC-pulses for which the onset of the field matches that of the current pulse.

Moreover, we investigated the ability of LLSs to locate and detect upward negative flashes. Different aspects of upward negative flashes, which might affect the evaluation performance of LLSs, were discussed. It was found that LLSs tend to overestimate the peak current values of RS pulses of upward negative flashes.

We presented a method to assess the propagation effect of lightning electromagnetic fields over a mountainous terrain. The propagation of lightning electromagnetic fields along the mountainous region around the Säntis tower was simulated using a full-wave approach based on the finite-difference time-domain method and using a two-dimensional topographic map along the direct path between the tower and our field measurement station. The results of our simulations revealed that considering the real irregular terrain, both the waveshape and amplitude of the simulated electric fields associated with return strokes and fast initial continuous current pulses are in excellent agreement with the measured waveforms.

**Chapter 4** was devoted to the study of upward positive flashes and the involved upward negative leader in their processes. In the first section, we presented a summary of occurrence characteristics of upward positive flashes recorded at the Säntis Tower.

In the following part of this chapter, using simultaneous channel-base current and vertical electric field records of Type-II flashes (initial-stage-only upward positive flashes), we distinguished two types of pulsations which must be due two distinct physical processes:

- Category A pulses with a bipolar E-field signature with mostly an initial positive half-cycle which usually can be correlated with a negative unipolar current pulse.

- Category B pulses, mainly unipolar positive or negative pulses which are not correlated with any major current pulse.

We have found that our Category A and B pulses are very similar to “Classical PBPs” and “Narrow PBPs” which have been observed in the initial stage of downward negative leaders.

Moreover, we investigated the overall electric field signature of our Type-II events and the occurrence of Category A and Category B pulses during the course of our Type-II events.

The overall field signature was found to be very similar to the Breakdown, Intermediate, Leader (BIL) phases of downward negative flashes. However, more extensive observations are needed to confirm this hypothesis.

Finally, we presented an engineering model to calculate electric fields radiated from pulses recorded during the first phase of discharges (Category A pulses) associated with upward negative stepped leaders. The predicted fields are in good agreement with experimental observations.

In **Chapter 5**, we presented and discussed current waveforms associated with 13 bipolar flashes recorded at the S antis Tower during the period from June 2010 to January 2015. The majority of the recorded bipolar flashes (10 out of 13) showed a polarity reversal during the initial continuous current, therefore belonging to Category I bipolar flashes. Two flashes were characterized by different polarities of the initial stage current and the following return stroke or strokes (Category II) and one flash involved return strokes of different polarities (Category III).

Two of the ten Category-I bipolar flashes were each characterized by a sequence of two upward leaders of opposite polarity within the same flash, a scenario that has never been reported from previous observations at instrumented towers. Our results suggest that the traditional classification of bipolar flashes should be modified to distinguish between two types of Category-I flashes: those in which the polarity reversal during the initial stage is associated with in-cloud processes (Category Ia) and those in which the polarity reversal is due to the initiation of two opposite-polarity leaders from the tower (Category Ib).

The fact that two upward, opposite-polarity leaders can occur within tens of milliseconds of each other is of interest for lightning protection studies.

In **Chapter 6**, we presented simultaneous channel-base current and wideband electric field waveforms at 380 km distance from the strike point associated with upward flashes initiated from the S antis Tower. The dataset presented in this study represents, to the best of the author’s knowledge, the first simultaneous records of lightning currents and distant fields associated with natural upward flashes featuring ionospheric reflections.

The chapter contains a full-wave, finite-difference time-domain (FDTD) analysis of the field propagation including the effect of the ionospheric reflections and the results are compared with experimental data.

Furthermore, we presented a novel semi-analytical simplified approach based on the ray tracing concept to estimate radiated electric fields associated with lightning return strokes, taking into account ionospheric reflections. The field transfer function at each frequency and each illumination angle was determined by applying the generalized Snell's law of refraction, and the antenna radiation pattern concept was used to obtain the source illumination efficiency, from which the radiated field was derived. The proposed method was validated using full-wave FDTD simulations.

## 7.2 Original Contributions

The main original contributions of the thesis can be summarized as follows:

- Our analysis on the superimposed ICC-pulses of upward negative flashes revealed that, both the M-component and return stroke modes of charge transfer can be involved in their formation, and they can be distinguished from each other by their radiated electric field signature.
- We evaluated the performance of the European Lightning Location System to detect and locate upward negative flashes recorded at the Säntis Tower. The flash and pulse detection efficiencies were found to be 97% and 73%, respectively.
- Using the Finite Difference Time Domain numerical approach and real topographical terrain data, we investigated the lightning electromagnetic field propagation along mountainous areas. Our analysis revealed that the radiated electric field is enhanced by propagation along mountainous terrain.
- We investigated radiated electric field pulses associated with upward negative leaders. We distinguished two types of pulsations in our records which are quite similar to classical PBP and narrow PBP pulses observed in the initial stage of downward negative flashes. Moreover, we hypothesize that the overall electric field signature of our Type-II events is very similar to the Breakdown, Intermediate, Leader (BIL) processes of downward negative events.
- Analysis of bipolar lightning flashes recorded at the Säntis Tower suggested a modification to the bipolar lightning classification. We have found two flashes of our database, each characterized by a sequence of two upward

leaders of opposite polarity within the same flash, a scenario that has never been reported from previous observations at instrumented towers.

- We presented the first simultaneous records of natural upward lightning channel-base current waveforms and their associated distant electric field featuring ionospheric reflections. We present a full-wave 2D FDTD analysis of the field propagation including the effect of the ionospheric reflections and the results are compared with the experimental data.
- We developed a novel semi-analytical approach based on the ray tracing concept to estimate radiated electric fields associated with lightning return strokes, taking into account ionospheric reflections.

### 7.3 Future Work:

The following suggestions can be considered as continuation of this dissertation:

*On the study of upward negative flashes:*

As it has been suggested in Chapter 3, one can distinguish RS-type ICC-pulses from M-component-type ICC pulses using their radiated electric field signature. We propose to use this criteria to obtain statistics of RS events and compare it with the conventional 2 kA and 8 microseconds criteria.

Furthermore, we propose to use Lightning Mapping Array (LMA) measurements to infer various processes involved in the formation of ICC-pulses and to make comparisons with those inferred from distant electric field measurements. LMA observations might help us as well to infer the cloud charge structures that facilitate the initiation of upward negative flashes.

*On the study of upward positive flashes:*

As we discussed in Chapter 4, two categories of pulsation can be observed in radiated electric field waveform of Type-II upward positive flashes. We propose to perform high-speed video observations along with simultaneous electric field measurements to correlate Category A and B pulses by positive and negative ends of leader progression, respectively, to confirm the hypothesis behind their formation.

We suggest as well conducting more sensitive channel-base current measurements along with radiated electric field observations. By inferring the cloud charge structure from LMA observations, one might be able to propose a more physical model for progression of upward negative leader.

Furthermore, the ability of Lightning Location Systems to detect and to locate upward positive flashes must be investigated.

*On the study of upward bipolar flashes:*

We suggest to use high-speed video cameras along with LMA measurements to study the involved processes in the formation of different types of upward bipolar events whose formation process is still not understood. LMA observations might as well suggest the favorable cloud charge structure for the occurrence of various types of bipolar lightning flashes.

*On the upward lightning-ionosphere interaction:*

We propose to further develop the presented semi-analytical approach in Chapter 6 to consider the earth curvature and the effect of the lossy ground. Moreover, considering channel-base current and electric field measurements, the inverse problem can be solved to infer conductivity profile of the ionosphere versus altitude





## Bibliography

- [1] V. Cooray, *The Lightning Flash*. The Institution of Engineering and Technology, Michael Faraday House, Six Hills Way, Stevenage SG1 2AY, UK: IET, 2003.
- [2] T. Takeuti and M. Nakano, "On Lightning Discharges in Winter Thunderstorm," in *Electrical Processes in Atmospheres*, Heidelberg: Steinkopff, 1976, pp. 614–617.
- [3] M. Brook, M. Nakano, P. Krehbiel, and T. Takeuti, "The electrical structure of the hokuriku winter thunderstorms," *J. Geophys. Res.*, vol. 87, no. C2, p. 1207, 1982.
- [4] E. Williams, "Lightning Activity in Winter Storms: A Meteorological and Cloud Microphysical Perspective," in *4th International Symposium on Winter Lightning*, 2017.
- [5] E. R. Jayaratne, C. P. R. Saunders, and J. Hallett, "Laboratory studies of the charging of soft-hail during ice crystal interactions," *Q. J. R. Meteorol. Soc.*, vol. 109, no. 461, pp. 609–630, Jul. 1983.
- [6] M. Roy, *The earth's electrical environment*, vol. 25, no. 1. Washington, D.C.: National Academies Press, 1988.
- [7] P. R. Krehbiel, "The electrical structure of thunderstorms in The Earth's Electrical Environment," in *Earth's Electrical Environment*, Washington, D.C: National Acad. Press, 1986, pp. 90–113.
- [8] N. Kitagawa and K. Michimoto, "Meteorological and electrical aspects of winter thunderclouds," *J. Geophys. Res.*, vol. 99, no. D5, p. 10713, 1994.
- [9] M. Stolzenburg, W. D. Rust, and T. C. Marshall, "Electrical structure in thunderstorm convective regions: 3. Synthesis," *J. Geophys. Res. Atmos.*, vol. 103, no. D12, pp. 14097–14108, Jun. 1998.
- [10] A. V. Gurevich, G. M. Milikh, and R. Roussel-Dupre, "Runaway electron mechanism of air breakdown and preconditioning during a thunderstorm," *Phys. Lett. A*, vol. 165, no. 5–6, pp. 463–468, Jun. 1992.
- [11] T. C. Marshall, M. P. McCarthy, and W. D. Rust, "Electric field magnitudes and lightning initiation in thunderstorms," *J. Geophys. Res.*, vol. 100, no. D4,

pp. 7097–7103, 1995.

- [12] V. Cooray, “Basic Physics of Electrical Discharges,” in *An Introduction to Lightning*, Dordrecht: Springer Netherlands, 2015, pp. 7–27.
- [13] E. M. Bazelyan and Y. P. Raizer, *Spark Discharge*. CRC Press, 1997.
- [14] I. Gallimberti and I. G. The, “The mechanism of the long spark formation,” *J. Phys. Colloq.*, vol. 40.
- [15] L. Arevalo and V. Cooray, “Preliminary study on the modelling of negative leader discharges,” *J. Phys. D. Appl. Phys.*, vol. 44, 2011.
- [16] I. Gallimberti, G. Bacchiega, A. Bondiou-Clergerie, and P. Lalande, “Fundamental processes in long air gap discharges,” *Comptes Rendus Phys.*, vol. 3, no. 10, pp. 1335–1359, 2002.
- [17] L. Arevalo, V. Cooray, D. Wu, and B. Jacobson, “A new static calculation of the streamer region for long spark gaps,” *J. Electrostat.*, vol. 70, no. 1, pp. 15–19, 2012.
- [18] V. A. Rakov and M. A. Uman, *Lightning Physics and Effects*. Cambridge University Press, 2003.
- [19] X. M. Shao and P. R. Krehbiel, “The spatial and temporal development of intracloud lightning,” *J. Geophys. Res. Atmos.*, vol. 101, no. D21, pp. 26641–26668, Nov. 1996.
- [20] W. P. Winn, G. D. Aulich, S. J. Hunyady, K. B. Eack, H. E. Edens, P. R. Krehbiel, W. Rison, and R. G. Sonnenfeld, “Lightning leader stepping, K changes, and other observations near an intracloud flash,” *J. Geophys. Res. Atmos.*, vol. 116, no. D23, Dec. 2011.
- [21] M. A. Uman, *The lightning discharge*. Dover, 1987.
- [22] V. A. Rakov, “A Review of Positive and Bipolar Lightning Discharges,” *Bull. Am. Meteorol. Soc.*, vol. 84, no. 6, pp. 767–776, Jun. 2003.
- [23] V. A. Rakov, “Initiation of lightning in thunderclouds,” *Proc. SPIE*, vol. 5975, p. 597512, 2006.
- [24] A. Nag and V. A. Rakov, “Pulse trains that are characteristic of preliminary breakdown in cloud-to-ground lightning but are not followed by return stroke pulses,” *J. Geophys. Res. Atmos.*, vol. 113, no. 1, pp. 1–12, 2008.
- [25] A. Nag and V. A. Rakov, “Some inferences on the role of lower positive charge region in facilitating different types of lightning,” *Geophys. Res. Lett.*, vol. 36, no. 5, pp. 1–5, 2009.
- [26] T. Marshall, W. Schulz, N. Karunarathna, S. Karunarathne, M. Stolzenburg, C. Vergeiner, and T. Warner, “On the percentage of lightning flashes that begin with initial breakdown pulses,” *J. Geophys. Res. Atmos.*, vol. 119, no. 2, pp. 445–460, Jan. 2014.
- [27] M. Stolzenburg, T. C. Marshall, S. Karunarathne, N. Karunarathna, L. E. Vickers, T. A. Warner, R. E. Orville, and H. D. Betz, “Luminosity of initial breakdown in lightning,” *J. Geophys. Res. Atmos.*, vol. 118, no. 7, pp. 2918–

2937, 2013.

- [28] D. Petersen and W. H. Beasley, “High-Speed video observations of the preliminary breakdown phase of a negative Cloud-to-Ground lightning flash,” in *XV International Conference on Atmospheric Electricity*, 2014, no. June, pp. 15–20.
- [29] K. Berger and E. Vogelsanger, “Photographische blitzuntersuchungen der jahre 1955–1965 auf dem Monte San Salvatore,” *Bull. Schweiz. Elektrotech.*, vol. 57, pp. 599–620, 1966.
- [30] A. Smorgonskiy, F. Rachidi, M. Rubinstein, G. Diendorfer, and W. Schulz, “On the proportion of upward flashes to lightning research towers,” *Atmos. Res.*, vol. 129–130, pp. 110–116, Jul. 2013.
- [31] M. Miki, V. A. Rakov, T. Shindo, G. Diendorfer, M. Mair, F. Heidler, W. Zischank, M. A. Uman, R. Thottappillil, and D. Wang, “Initial stage in lightning initiated from tall objects and in rocket-triggered lightning,” *J. Geophys. Res.*, vol. 110, no. D2, p. D02109, 2005.
- [32] C. Romero, “Instrumentation of the Säntis Tower for Lightning Current Measurement,” Swiss Federal Institute of Technology (EPFL), Lausanne, 2012.
- [33] H. Zhou, V. A. Rakov, G. Diendorfer, R. Thottappillil, H. Pichler, and M. Mair, “A study of different modes of charge transfer to ground in upward lightning,” *J. Atmos. Solar-Terrestrial Phys.*, vol. 125–126, pp. 38–49, Apr. 2015.
- [34] V. k. Berger, “Blitzstrom-Parameter von Aufwärtsblitzen,” *Bull. Schweiz. Elektrotech.*, vol. 69, pp. 353–360, 1978.
- [35] W. D. Rust, D. R. MacGorman, E. C. Bruning, S. A. Weiss, P. R. Krehbiel, R. J. Thomas, W. Rison, T. Hamlin, and J. Harlin, “Inverted-polarity electrical structures in thunderstorms in the Severe Thunderstorm Electrification and Precipitation Study (STEPS),” *Atmos. Res.*, vol. 76, no. 1, pp. 247–271, 2005.
- [36] R. E. Orville, G. R. Huffines, R. E. Orville, and G. R. Huffines, “Cloud-to-Ground Lightning in the United States: NLDN Results in the First Decade, 1989–98,” *Mon. Weather Rev.*, vol. 129, no. 5, pp. 1179–1193, May 2001.
- [37] H. Cui, X. Qie, Q. Zhang, T. Zhang, G. Zhang, and J. Yang, “Intracloud discharge and the correlated basic charge structure of a thunderstorm in Zhongchuan, a Chinese Inland Plateau region,” *Atmos. Res.*, vol. 91, no. 2, pp. 425–429, 2009.
- [38] P. R. Krehbiel, *An analysis of the electric field change produced by lightning*. Geophysical Research Center Research and Development Division New Mexico Institute of Mining and Technology, 1981.
- [39] X. Kong, X. Qie, and Y. Zhao, “Characteristics of downward leader in a positive cloud-to-ground lightning flash observed by high-speed video camera and electric field changes,” *Geophys. Res. Lett.*, vol. 35, no. 5, p. L05816, Mar. 2008.
- [40] C. Gomes and V. Cooray, “Radiation field pulses associated with the initiation of positive cloud to ground lightning flashes,” *J. Atmos. Solar-Terrestrial*

*Phys.*, vol. 66, no. 12, pp. 1047–1055, 2004.

- [41] V. Cooray, R. Montano, and V. Rakov, “A model to represent negative and positive lightning first strokes with connecting leaders,” *J. Electrostat.*, vol. 60, pp. 97–109, 2004.
- [42] V. A. A. Rakov, A. Borghetti, C. Bouquegneau, W. A. Chisholm, V. Cooray, K. Cummins, G. Diendorfer, F. Heidler, A. Hussein, M. Ishii, C. A. Nucci, A. Piantini, O. Pinto, X. Qie, F. Rachidi, M. M. F. Saba, T. Shindo, W. Schulz, R. Thottappillil, S. Visacro, and W. Zischank, “Lightning parameters for engineering applications,” Paris, 2014.
- [43] A. Nag and V. A. Rakov, “Positive lightning: An overview, new observations, and inferences,” *J. Geophys. Res. Atmos.*, vol. 117, no. D8, p. n/a-n/a, Apr. 2012.
- [44] K. Berger, “The Earth flash,” in *Lightning*, R. Golde, Ed. New York: Academic, 1977, pp. 119–190.
- [45] X. Liu, C. Wang, Y. Zhang, Q. Xiao, D. Wang, Z. Zhou, and C. Guo, “Experiment of artificially triggering lightning in China,” *J. Geophys. Res.*, vol. 99, no. D5, p. 10727, 1994.
- [46] F. H. Heidler, M. Manhardt, and K. Stimper, “Characteristics of Upward Positive Lightning Initiated From the Peissenberg Tower, Germany,” *IEEE Trans. Electromagn. Compat.*, vol. 57, no. 1, pp. 102–111, Feb. 2015.
- [47] M. Miki, T. Miki, A. Asakawa, and T. Shindo, “Characteristics of Negative Upward Stepped Leaders in Positive Upward Lightning,” *XV Int. Conf. Atmos. Electr. Norman, Oklahoma, U.S.A.*, no. June, pp. 15–20, 2014.
- [48] H. Zhou, G. Diendorfer, R. Thottappillil, H. Pichler, and M. Mair, “Characteristics of upward positive lightning flashes initiated from the Gaisberg Tower,” *J. Geophys. Res. Atmos.*, vol. 117, no. D6, Mar. 2012.
- [49] M. Azadifar, F. Rachidi, M. Rubinstein, M. Paolone, V. A. A. Rakov, D. Pavanello, S. Metz, and C. Romero, “Characteristics of electric fields of upward negative stepped leaders,” in *International Symposium on Lightning Protection (XIII SIPDA)*, 2015, pp. 32–36.
- [50] C. Romero, F. Rachidi, M. Rubinstein, M. Paolone, V. A. Rakov, and D. Pavanello, “Positive lightning flashes recorded on the Săntis tower from May 2010 to January 2012,” *J. Geophys. Res. Atmos.*, vol. 118, no. 23, pp. 12879–12892, 2013.
- [51] K. B. McEachron, “Lightning to the empire state building,” *J. Franklin Inst.*, vol. 227, no. 2, pp. 149–217, Feb. 1939.
- [52] J. H. Hagenguth and J. G. Anderson, “Lightning to the Empire State Building—Part III [includes discussion],” *Trans. Am. Inst. Electr. Eng. Part III Power Appar. Syst.*, vol. 71, no. 1, Jan. 1952.
- [53] D. A. Petersen and W. H. Beasley, “High-speed video observations of a natural negative stepped leader and subsequent dart-stepped leader,” *J. Geophys. Res. Atmos.*, vol. 118, no. 21, pp. 12110–12119, 2013.

- [54] A. Nag, M. J. Murphy, W. Schulz, and K. L. Cummins, "Lightning locating systems: Insights on characteristics and validation techniques," *Earth Sp. Sci.*, vol. 2, no. 4, pp. 65–93, Apr. 2015.
- [55] M. G. Ballarotti, M. M. F. Saba, and O. Pinto, "High-speed camera observations of negative ground flashes on a millisecond-scale," *Geophys. Res. Lett.*, vol. 32, no. 23, p. L23802, 2005.
- [56] V. Cooray, *Lightning electromagnetics*. Institution of Engineering and Technology, 2012.
- [57] K. Berger, "Novel observations on lightning discharges: Results of research on Mount San Salvatore," *J. Franklin Inst.*, vol. 283, no. 6, pp. 478–525, Jun. 1967.
- [58] K. Berger, R. B. Anderson, and H. Kroninger, "Parameters of lightning flashes," *Electra*, vol. 41, pp. 23–37, 1975.
- [59] G. Diendorfer, "Lightning initiated from tall structures — A review," in *27th International Symposium on Lightning Protection*, 2011, pp. 298–303.
- [60] A. Smorgonskii, "Advanced methods for the evaluation of lightning incidence over large areas, wind turbine parks and tall towers," EPFL, 2016.
- [61] G. Diendorfer, H. Pichler, and M. Mair, "Some parameters of negative upward-initiated lightning to the Gaisberg tower (2000-2007)," *IEEE Trans. Electromagn. Compat.*, vol. 51, no. 3 PART 1, pp. 443–452, Aug. 2009.
- [62] C. Schumann, M. M. F. Saba, A. Romão De Paiva, M. A. Da, S. Ferro, S. Jose, D. Campos, W. Schulz, G. Diendorfer, and T. A. Warner, "Analysis of terrain and atmospheric conditions for upward flashes in Sao Paulo-Brazil," in *International Symposium on Lightning Protection (XIII SIPDA)*, 2015, pp. 77–83.
- [63] R. Fieux, C. Gary, and P. Hubert, "Artificially triggered lightning above land," *Nature*, vol. 257, no. 5523, pp. 212–214, Sep. 1975.
- [64] V. A. Rakov, M. A. Uman, and K. J. Rambo, "A review of ten years of triggered-lightning experiments at Camp Blanding, Florida," *Atmos. Res.*, vol. 76, no. 1, pp. 503–517, 2005.
- [65] K. L. Cummins and M. J. Murphy, "An Overview of Lightning Locating Systems: History, Techniques, and Data Uses, With an In-Depth Look at the U.S. NLDN," *IEEE Trans. Electromagn. Compat.*, vol. 51, no. 3, pp. 499–518, Aug. 2009.
- [66] V. A. Rakov, "Lightning electromagnetic environment: From continuing-current fields to X-rays," in *3rd Intl. Conf. on Lightning Phys. and Effects*, 2008.
- [67] V. A. A. Rakov, A. Borghetti, C. Bouquegneau, W. A. Chisholm, V. Cooray, K. Cummins, G. Diendorfer, F. Heidler, A. Hussein, M. Ishii, C. A. Nucci, A. Piantini, O. Pinto, X. Qie, F. Rachidi, M. M. F. Saba, T. Shindo, W. Schulz, R. Thottappillil, S. Visacro, and W. Zischank, "Lightning Parameters for Engineering Applications," 2014.

- [68] C. Romero, A. Mediano, A. Rubinstein, F. Rachidi, M. Rubinstein, M. Paolone, P. Zweigacker, N. Mora, D. Pavanello, and B. Daout, "Measurement of Lightning Currents Using a Combination of Rogowski Coils and B-Dot Sensors," *J. Light. Res.*, vol. 4, pp. 71–77, 2012.
- [69] C. Romero, M. Paolone, M. Rubinstein, F. Rachidi, A. Rubinstein, G. Diendorfer, W. Schulz, B. Daout, A. Kälin, and P. Zweigacker, "A system for the measurements of lightning currents at the Säntis Tower," *Electr. Power Syst. Res.*, vol. 82, no. 1, pp. 34–43, 2012.
- [70] M. Azadifar, M. Paolone, M. Pavanello, D. Romero, C., Rachidi, F., Rubinstein, "An update on the instrumentation of the Säntis Tower in Switzerland for lightning current measurements and obtained results," in *CIGRE International Colloquium on Lightning and Power Systems*, 2014.
- [71] M. Azadifar, F. Rachidi, M. Rubinstein, V. A. Rakov, M. Paolone, D. Pavanello, and S. Metz, "Fast initial continuous current pulses versus return stroke pulses in tower-initiated lightning," *J. Geophys. Res. Atmos.*, vol. 121, pp. 6425–6434, 2016.
- [72] D. Li, M. Azadifar, F. Rachidi, M. Rubinstein, M. Paolone, D. Pavanello, S. Metz, Q. Zhang, and Z. Wang, "On Lightning Electromagnetic Field Propagation Along an Irregular Terrain," *IEEE Trans. Electromagn. Compat.*, vol. 58, no. 1, pp. 161–171, Feb. 2016.
- [73] H. Pichler, G. Diendorfer, and M. Mair, "Some parameters of correlated current and radiated field pulses from 339 lightning to the Gaisberg tower," *IEEE Trans. Electr. Electron. Eng.*, vol. 5(1), pp. 8–13, 2010.
- [74] W. Schulz, G. Diendorfer, S. Pedebay, and D. R. Poelman, "The European lightning location system EUCLID – Part 1: Performance analysis and validation," *Nat. Hazards Earth Syst. Sci.*, vol. 16, pp. 595–605, 2016.
- [75] D. R. Poelman, W. Schulz, G. Diendorfer, and M. Bernardi, "The European lightning location system EUCLID – Part 2: Observations," *Nat. Hazards Earth Syst. Sci.*, vol. 16, pp. 607–616, 2016.
- [76] M. Azadifar, F. Rachidi, M. Rubinstein, M. Paolone, G. Diendorfer, H. Pichler, W. Schulz, D. Pavanello, and C. Romero, "Evaluation of the performance characteristics of the European Lightning Detection Network EUCLID in the Alps region for upward negative flashes using direct measurements at the instrumented Säntis Tower," *J. Geophys. Res. Atmos.*, vol. 121, no. 2, pp. 595–606, Jan. 2016.
- [77] F. Fuchs, E. U. Landers, R. Schmid, and J. Wiesinger, "Lightning Current and Magnetic Field Parameters Caused by Lightning Strikes to Tall Structures Relating to Interference of Electronic Systems," *IEEE Trans. Electromagn. Compat.*, vol. 40, no. 4, 1998.
- [78] M. Guimaraes, P. Ramos, R. Sobreiro, and S. Visacro, "Lightning Measurements at Morro do Cachimbo Station: new results," in *2014 International Conference on Lightning Protection (ICLP)*, 2014, pp. 1695–1700.



- [79] V. Cooray, *Introduction to lightning*. SPRINGER, 2014.
- [80] N. Goelian, P. Lalande, and G. L. Bacchiega, "A simplified model for the simulation of positive-spark development in long air gaps," vol. 2441.
- [81] M. Azadifar, F. Rachidi, M. Rubinstein, V. A. Rakov, M. Paolone, D. Pavanello, and S. Metz, "Fast initial continuous current pulses versus return stroke pulses in tower-initiated lightning," *J. Geophys. Res. Atmos.*, vol. 121, no. 11, pp. 6425–6434, Jun. 2016.
- [82] M. Miki, T. Shindo, V. A. Rakov, M. A. Uman, G. Diendorfer, M. Mair, F. Heidler, W. Zischank, and R. Thottappillil, "Characterization of current pulses superimposed on the continuous current in upward lightning initiated from tall objects and in rocket-triggered lightning," in *28<sup>th</sup> International Conference on Lightning Protection*, 2006, pp. 83–88.
- [83] V. Mazur and L. H. Ruhnke, "Physical processes during development of upward leaders from tall structures," *J. Electrostat.*, vol. 69, no. 2, pp. 97–110, 2011.
- [84] S. Yoshida, C. J. Biagi, V. A. Rakov, J. D. Hill, M. V. Stapleton, D. M. Jordan, M. A. Uman, T. Morimoto, T. Ushio, Z.-I. Kawasaki, and M. Akita, "The initial stage processes of rocket-and-wire triggered lightning as observed by VHF interferometry," *J. Geophys. Res. Atmos.*, vol. 117, no. D9, May 2012.
- [85] V. A. Rakov, D. E. Crawford, K. J. Rambo, G. H. Schnetzer, M. A. Uman, and R. Thottappillil, "M-component mode of charge transfer to ground in lightning discharge," *J. Geophys. Res. Atmos.*, vol. 106, no. D19, pp. 22817–22831, 2001.
- [86] S. Mallick, V. A. Rakov, J. D. Hill, T. Ngin, W. R. Gamerota, J. T. Pilkey, C. J. Biagi, D. M. Jordan, M. A. Uman, J. A. Cramer, and A. Nag, "Performance characteristics of the NLDN for return strokes and pulses superimposed on steady currents, based on rocket-triggered lightning data acquired in Florida in 2004-2012," *J. Geophys. Res. Atmos.*, vol. 119, no. 7, pp. 3825–3856, Apr. 2014.
- [87] M. Azadifar, F. Rachidi, M. Rubinstein, V. A. Rakov, M. Paolone, D. Pavanello, and S. Metz, "Fast initial continuous current pulses versus return stroke pulses in tower-initiated lightning," *J. Geophys. Res. Atmos.*, vol. 121, no. 11, pp. 6425–6434, Jun. 2016.
- [88] M. D. Tran, V. A. Rakov, T. Ngin, W. R. Gamerota, J. T. Pilkey, M. A. Uman, and D. M. Jordan, "Microsecond-scale electric field pulses associated with lightning M-components," *Am. Geophys. Union, Fall Meet. 2013, Abstr. #AE13B-0356*, 2013.
- [89] X. M. Shao, P. R. Krehbiel, R. J. Thomas, and W. Rison, "Radio interferometric observations of cloud-to-ground lightning phenomena in Florida," *J. Geophys. Res.*, vol. 100, no. D2, p. 2749, 1995.
- [90] F. Rachidi and R. Thottappillil, "Determination of lightning currents from far electromagnetic fields," *J. Geophys. Res. Atmos.*, vol. 98, no. D10, pp. 18315–18321, Oct. 1993.

- [91] V. A. Rakov, "Lightning Return Stroke Speed," *J. Light. Res.*, vol. 1, pp. 80–89, 2007.
- [92] G. Diendorfer, "LLS performance validation using lightning to towers," in *International Lightning Detection Conference*, 2010.
- [93] F. Rachidi, W. Janischewskyj, A. M. Hussein, C. A. Nucci, S. Guerrieri, B. Kordi, and Jen-Shih Chang, "Current and electromagnetic field associated with lightning-return strokes to tall towers," *IEEE Trans. Electromagn. Compat.*, vol. 43, no. 3, pp. 356–367, 2001.
- [94] D. Pavanello, F. Rachidi, W. Janischewskyj, M. Rubinstein, A. M. Hussein, E. Petrache, V. Shostak, I. Boev, C. A. Nucci, W. A. Chisholm, M. Nyffeler, J. S. Chang, and A. Jaquier, "On return stroke currents and remote electromagnetic fields associated with lightning strikes to tall structures: 2. Experiment and model validation," *J. Geophys. Res. Atmos.*, vol. 112, no. D13, Jul. 2007.
- [95] D. Flache, V. A. Rakov, F. Heidler, W. Zischank, and R. Thottappillil, "Initial-stage pulses in upward lightning : Leader / return stroke versus M-component mode of charge transfer to ground," vol. 35, no. May, pp. 2–6, 2008.
- [96] V. Cooray and V. Rakov, "On the upper and lower limits of peak current of first return strokes in negative lightning flashes," *Atmos. Res.*, vol. 117, pp. 12–17, 2012.
- [97] C. Romero, F. Rachidi, M. Paolone, and M. Rubinstein, "Statistical distributions of lightning currents associated with upward negative flashes based on the data collected at the S antis (EMC) Tower in 2010 and 2011," *IEEE Trans. Power Deliv.*, vol. 28, no. 3, pp. 1804–1812, 2013.
- [98] D. Pavanello, F. Rachidi, W. Janischewskyj, M. Rubinstein, V. O. Shostak, C. A. Nucci, K. L. Cummins, A. M. Hussein, and J.-S. Chang, "On the Current Peak Estimates Provided by Lightning Detection Networks for Lightning Return Strokes to Tall Towers," *IEEE Trans. Electromagn. Compat.*, vol. 51, no. 3, pp. 453–458, Aug. 2009.
- [99] G. Diendorfer, H. Zhou, H. Pichler, R. Thottappillil, and M. Mair, "Currents and radiated E-fields of upward initiated lightning from the Gaisberg Tower in Austria," in *EGU General Assembly*, 2014, vol. 16.
- [100] F. Rachidi, J. L. Bermudez, M. Rubinstein, and V. A. Rakov, "On the estimation of lightning peak currents from measured fields using lightning location systems," *J. Electrostat.*, vol. 60, no. 2–4, pp. 121–129, Mar. 2004.
- [101] A. Nag, S. Mallick, V. A. Rakov, J. S. Howard, C. J. Biagi, J. D. Hill, M. A. Uman, D. M. Jordan, K. J. Rambo, J. E. Jerauld, B. A. DeCarlo, K. L. Cummins, and J. A. Cramer, "Evaluation of U.S. National Lightning Detection Network performance characteristics using rocket-triggered lightning data acquired in 2004–2009," *J. Geophys. Res.*, vol. 116, no. D2, p. D02123, Jan. 2011.
- [102] M. Azadifar, "Evaluation of the uncertainty associated with the current measurement system installed on the S antis Tower," 2015.



- [103] Y. Baba and V. A. Rakov, "Lightning electromagnetic environment in the presence of a tall grounded strike object," *J. Geophys. Res.*, vol. 110, no. D9, p. D09108, 2005.
- [104] Y. Baba and V. A. Rakov, "Lightning strikes to tall objects: Currents inferred from far electromagnetic fields versus directly measured currents," *Geophys. Res. Lett.*, vol. 34, no. 19, p. L19810, Oct. 2007.
- [105] J. L. Bermudez, F. Rachidi, M. Rubinstein, W. Janischewskyj, V. O. Shostak, D. Pavanello, J. S. Chang, A. M. Hussein, C. A. Nucci, and M. Paolone, "Far-Field-Current Relationship Based on the TL Model for Lightning Return Strokes to Elevated Strike Objects," *IEEE Trans. Electromagn. Compat.*, vol. 47, no. 1, pp. 146–159, Feb. 2005.
- [106] E. Soto, E. Perez, and C. Younes, "Influence of non-flat terrain on lightning induced voltages on distribution networks," *Electr. Power Syst. Res.*, vol. 113, pp. 115–120, Aug. 2014.
- [107] E. Soto, E. Perez, and J. Herrera, "Electromagnetic Field Due to Lightning Striking on Top of a Cone-Shaped Mountain Using the FDTD," *IEEE Trans. Electromagn. Compat.*, vol. 56, no. 5, pp. 1112–1120, Oct. 2014.
- [108] J. Paknahad, K. Sheshyekani, M. Hamzeh, and F. Rachidi, "Lightning electromagnetic fields and their induced voltages on overhead lines: the effect of a non-flat lossy ground," in *2014 International Conference on Lightning Protection (ICLP)*, 2014, pp. 591–594.
- [109] W. Schulz and Diendorfer. G, "Evaluation of a lightning location algorithm using an elevation model," in *25th International Conference on Lightning Protection (ICLP)*, 2000.
- [110] D. Li, M. Azadifar, F. Rachidi, M. Rubinstein, G. Diendorfer, K. Sheshyekani, Q. Zhang, and Z. Wang, "Analysis of lightning electromagnetic field propagation in mountainous terrain and its effects on ToA-based lightning location systems," *J. Geophys. Res. Atmos.*, vol. 121, no. 2, pp. 895–911, Jan. 2016.
- [111] T. Tachikawa, M. Kaku, A. Iwasaki, D. B. Gesch, M. J. Oimoen, Z. Zhang, J. J. Danielson, T. Krieger, B. Curtis, J. Haase, M. Abrams, and C. Carabajal, "ASTER Global Digital Elevation Model Version 2 - summary of validation results." 2011.
- [112] S. Visacro and F. H. Silveira, "Lightning current waves measured at short instrumented towers: The influence of sensor position," *Geophys. Res. Lett.*, vol. 32, no. 18, Sep. 2005.
- [113] A. Mosaddeghi, D. Pavanello, F. Rachidi, M. Rubinstein, and P. Zwiack, "Effect of Nearby Buildings on Electromagnetic Fields from Lightning," *J. Light. Res.*, vol. 1, no. 1, pp. 52–60, Dec. 2009.
- [114] Y. Baba and V. A. Rakov, "Electromagnetic Fields at the Top of a Tall Building Associated With Nearby Lightning Return Strokes," *IEEE Trans. Electromagn. Compat.*, vol. 49, no. 3, pp. 632–643, Aug. 2007.
- [115] G. Mur, "Absorbing Boundary Conditions for the Finite-Difference

- Approximation of the Time-Domain Electromagnetic-Field Equations,” *IEEE Trans. Electromagn. Compat.*, vol. EMC-23, no. 4, pp. 377–382, Nov. 1981.
- [116] A. Taflove and S. C. Hagness, *Computational electrodynamics : the finite-difference time-domain method*. Artech House, 2005.
  - [117] C. A. Nucci, C. Mazzetti, F. Rachidi, and M. Ianoz, “On lightning return stroke models for LEMP calculations,” in *19th International Conference on Lightning Protection*, 1988.
  - [118] F. Rachidi and C. A. Nucci, “On the Master, Uman, Lin, Standler and the Modified Transmission Line Lightning return stroke current models,” *J. Geophys. Res.*, vol. 95, no. D12, p. 20389, 1990.
  - [119] C. A. Nucci and F. Rachidi, “Experimental validation of a modification to the Transmission Line model for LEMP calculation,” in *8th Symposium and Technical Exhibition on Electromagnetic Compatibility*, 1989.
  - [120] D. Li, J. Paknahad, F. Rachidi, M. Rubinstein, K. Sheshyekani, Q. Zhang, and Z. Wang, “Propagation effects on lightning magnetic fields over hilly and mountainous terrain,” in *2015 IEEE International Symposium on Electromagnetic Compatibility (EMC)*, 2015, pp. 1436–1440.
  - [121] F. Heidler, “Traveling current source model for LEMP calculation,” in *6th Int. Zurich Symp. Electromagn. Compat.*, 1986, pp. 157–162.
  - [122] J. L. Bermudez, C. A. Pena-Reyes, F. Rachidi, and F. Heidler, “Use of genetic algorithms to extract primary lightning current parameters,” *Proc. EMC Eur. 2002. Int. Symp. Electromagn. Compat.*, 2002.
  - [123] V. A. Rakov, “Transient response of a tall object to lightning,” *IEEE Trans. Electromagn. Compat.*, vol. 43, no. 4, pp. 654–661, 2001.
  - [124] F. Rachidi, “Modeling Lightning Return Strokes to Tall Structures: A Review,” *J. Light. Res.*, vol. 1, pp. 16–31, 2007.
  - [125] A. Shoory, F. Rachidi, M. Rubinstein, R. Moini, and S. H. Hesamedin Sadeghi, “Analytical expressions for zero-crossing times in lightning return-stroke engineering models,” *IEEE Trans. Electromagn. Compat.*, vol. 51, no. 4, pp. 963–974, 2009.
  - [126] A. Shoory, A. Mimouni, F. Rachidi, V. Cooray, R. Moini, and S. H. Hesamedin Sadeghi, “Validity of simplified approaches for the evaluation of lightning electromagnetic fields above a horizontally stratified ground,” *IEEE Trans. Electromagn. Compat.*, vol. 52, no. 3, pp. 657–663, 2010.
  - [127] A. Shoory, A. Mimouni, F. Rachidi, V. Cooray, and M. Rubinstein, “On the accuracy of approximate techniques for the evaluation of lightning electromagnetic fields along a mixed propagation path,” *Radio Sci.*, vol. 46, 2011.
  - [128] M. Akbari, K. Sheshyekani, A. Pirayesh, F. Rachidi, M. Paolone, A. Borghetti, and C. A. Nucci, “Evaluation of Lightning Electromagnetic Fields and Their Induced Voltages on Overhead Lines Considering the Frequency Dependence of Soil Electrical Parameters,” *IEEE Trans. Electromagn. Compat.*, vol. 55, no.

6, pp. 1210–1219, Dec. 2013.

- [129] D. Cavka, N. Mora, and F. Rachidi, “A Comparison of Frequency-Dependent Soil Models: Application to the Analysis of Grounding Systems,” *IEEE Trans. Electromagn. Compat.*, vol. 56, no. 1, pp. 177–187, Feb. 2014.
- [130] C. A. Nucci, F. Rachidi, M. V. Ianoz, and C. Mazzetti, “Lightning-induced voltages on overhead lines,” *IEEE Trans. Electromagn. Compat.*, vol. 35, no. 1, pp. 75–86, 1993.
- [131] M. A. Uman and D. K. McLain, “Magnetic field of lightning return stroke,” *J. Geophys. Res.*, vol. 74, pp. 6899–6910, 1969.
- [132] V. A. Rakov and A. A. Dulzon, “A Modified Transmission Line Model for Lightning Return Stroke Field Calculations,” in *9th Int. Symp. Electromagn. Compat.*, 1991, pp. 229–235.
- [133] C. A. Nucci, G. Diendorfer, M. A. Uman, F. Rachidi, M. Ianoz, and C. Mazzetti, “Lightning return stroke current models with specified channel-base current: A review and comparison,” *J. Geophys. Res. Atmos.*, vol. 95, pp. 20395–20408, 1990.
- [134] D. Pavanello, V. A. Rakov, and J. L. Bermudez, “Return stroke current profiles and electromagnetic fields associated with lightning strikes to tall towers: Comparison of engineering models,” *J. Electrostat.*, vol. 65, no. 5, pp. 316–321, 2007.
- [135] C. J. Biagi, M. A. Uman, J. D. Hill, D. M. Jordan, V. A. Rakov, and J. Dwyer, “Observations of stepping mechanisms in a rocket-and-wire triggered lightning flash,” *J. Geophys. Res. Atmos.*, vol. 115, no. 23, pp. 2–7, 2010.
- [136] B. N. Gorin, V. I. Levitov, and A. V. Shkilev, “Some principles of leader discharge of air gaps with a strong non-uniform field,” in *IEE Conf. Publ.*, 1976, pp. 274–278.
- [137] A. Nag, B. A. DeCarlo, and V. A. Rakov, “Analysis of microsecond- and submicrosecond-scale electric field pulses produced by cloud and ground lightning discharges,” *Atmos. Res.*, vol. 91, no. 2–4, pp. 316–325, 2009.
- [138] D. E. Proctor, R. Uytendogaardt, and B. M. Meredith, “VHF radio pictures of lightning flashes to ground,” *J. Geophys. Res.*, vol. 93, no. D10, p. 12683, 1988.
- [139] L. Z. S. Campos and M. M. F. Saba, “Visible channel development during the initial breakdown of a natural negative cloud-to-ground flash,” *Geophys. Res. Lett.*, vol. 40, no. 17, pp. 4756–4761, 2013.
- [140] N. D. Clarence and D. J. Malan, “Preliminary discharge processes in lightning flashes to ground,” *Q. J. R. Meteorol. Soc.*, vol. 83, no. 356, pp. 161–172, Apr. 1957.
- [141] A. Nag and V. A. Rakov, “Electric Field Pulse Trains Occurring Prior to the First Stroke in Negative Cloud-to-Ground Lightning,” *IEEE Trans. Electromagn. Compat.*, vol. 51, no. 1, pp. 147–150, 2009.
- [142] M. Stolzenburg, T. C. Marshall, N. Karunarathna, and R. E. Orville, “Leader observations during the initial breakdown stage of a lightning flash,” *J.*

*Geophys. Res. Atmos.*, 2014.

- [143] S. Karunarathne, T. C. Marshall, M. Stolzenburg, and N. Karunarathna, "Modeling initial breakdown pulses of CG lightning flashes," *J. Geophys. Res. Atmos.*, vol. 119, no. 14, pp. 9003–9019, 2014.
- [144] S. Karunarathne, T. C. Marshall, M. Stolzenburg, and N. Karunarathna, "Modeling initial breakdown pulses of CG lightning flashes," *J. Geophys. Res. Atmos.*, vol. 119, no. 14, pp. 9003–9019, 2014.
- [145] K. Narita, Y. Goto, H. Komuro, and S. Sawada, "Bipolar lightning in winter at Maki, Japan," *J. Geophys. Res.*, vol. 94, no. D11, p. 13191, 1989.
- [146] M. M. F. Saba, C. Schumann, T. A. Warner, J. H. Helsdon, W. Schulz, and R. E. Orville, "Bipolar cloud-to-ground lightning flash observations," *J. Geophys. Res. Atmos.*, vol. 118, no. 19, p. 11,098–11,106, Oct. 2013.
- [147] A. C. V. Saraiva, L. Z. S. Campos, E. R. Williams, G. S. Zepka, J. Alves, O. Pinto, S. Heckman, T. S. Buzato, J. C. Bailey, C. A. Morales, and R. J. Blakeslee, "High-speed video and electromagnetic analysis of two natural bipolar cloud-to-ground lightning flashes," *J. Geophys. Res. Atmos.*, vol. 119, no. 10, pp. 6105–6127, May 2014.
- [148] M. Azadifar, F. Rachidi, M. Rubinstein, V. A. Rakov, M. Paolone, and D. Pavanello, "Bipolar Lightning Flashes Observed at the Săntis," in *33rd International Conference on Lightning Protection (ICLP)*, 2016.
- [149] M. Azadifar, F. Rachidi, M. Rubinstein, V. A. Rakov, M. Paolone, and D. Pavanello, "Bipolar lightning flashes observed at the Săntis Tower: Do we need to modify the traditional classification?," *J. Geophys. Res. Atmos.*, vol. 121, no. 23, p. 14,117–14,126, Dec. 2016.
- [150] P. Hubert and G. Mouget, "Return stroke velocity measurements in two triggered lightning flashes," *J. Geophys. Res.*, vol. 86, no. C6, p. 5253, 1981.
- [151] K. Nakahori, T. Egawa, and H. Mitani, "Characteristics of Winter Lightning Currents in Hokuriku District," *IEEE Power Eng. Rev.*, vol. 11, pp. 37–38, 1982.
- [152] B. Gorin and A. Shkilev, "Measurements of lightning currents at the Ostankino tower," *Elektrichestvo*, vol. 8, pp. 64–65, 1984.
- [153] H. Akiyama, K. Ichino, and K. Horii, "Channel reconstruction of triggered lightning flashes with bipolar currents from thunder measurements," *J. Geophys. Res. Atmos.*, vol. 90, no. D6, pp. 10674–10680, Oct. 1985.
- [154] F. Heidler, W. Zischank, and J. Wiesinger, "Statistics of lightning current parameters and related nearby magnetic fields measured at the Peissenberg Tower," in *Proc. 25th Int. Conf. on Lightning Protection*, 2000, pp. 78–83.
- [155] M. Miki, A. Wada, and A. Asakawa, "Observation of upward lightning in winter at the coast of Japan Sea with a high-speed video camera," in *Proc. 27th Int. Conf. Lightning Protection*, 2004, pp. 63–67.
- [156] J. Jerauld, M. A. Uman, V. A. Rakov, K. J. Rambo, and D. M. Jordan, "A triggered lightning flash containing both negative and positive strokes,"

*Geophys. Res. Lett.*, vol. 31, no. 8, p. L08104, 2004.

- [157] D. Wang and N. Takagi, “Characteristics of upward bipolar lightning derived from simultaneous recording of electric current and electric field change,” in *Proceedings of the XXIX General Assembly of the International Union of Radio Science*, 2008.
- [158] H. Zhou, G. Diendorfer, R. Thottappillil, H. Pichler, and M. Mair, “Characteristics of upward bipolar lightning flashes observed at the Gaisberg Tower,” *J. Geophys. Res.*, vol. 116, no. D13, p. D13106, Jul. 2011.
- [159] V. A. Rakov, “Lightning Flashes Transporting Both Negative and Positive Charges to Ground,” in *Recent Progresses in Lightning Physics*, Ed. C. Pon., 2005, pp. 9–21.
- [160] W. Schulz and G. Diendorfer, “Bipolar flashes detected with lightning location systems and measured on an instrumented tower,” in *Proceedings of the VII International Symposium on Lightning Protection (SIPDA)*, 2003, pp. 6–9.
- [161] K. Horii, “Experiment of artificial lightning triggered with rocket,” *Mem. Fac. Eng.*, vol. 34, pp. 77–112, 1982.
- [162] K. Horii, “Experiment of triggered lightning discharge by rocket,” in *In Proc. Korea–Japan Joint Symp. on Electrical Material and Discharge*, 1986.
- [163] W. Lu, D. Wang, Y. Zhang, and N. Takagi, “Two associated upward lightning flashes that produced opposite polarity electric field changes,” *Geophys. Res. Lett.*, vol. 36, no. 5, p. L05801, Mar. 2009.
- [164] C. O. Hines and J. Aarons, “Physics of the Earth’s Upper Atmosphere,” *Phys. Today*, vol. 18, no. 11, pp. 63–63, Nov. 1965.
- [165] J. K. Hargreaves, *The solar-terrestrial environment: an introduction to geospace--the science of the terrestrial upper atmosphere, ionosphere, and magnetosphere*. Cambridge University Press, 1992.
- [166] S. A. Cummer, “Lightning and Ionospheric Remote Sensing Using VLF/ELF Radio Atmospheric | Stanford VLF Group,” Stanford University, 1997.
- [167] U. S. Inan, S. A. Cummer, and R. A. Marshall, “A survey of ELF and VLF research on lightning-ionosphere interactions and causative discharges,” *J. Geophys. Res. Sp. Phys.*, vol. 115, no. A6, p. n/a-n/a, Jun. 2010.
- [168] A. R. Jacobson, X.-M. Shao, and R. Holzworth, “Full-wave reflection of lightning long-wave radio pulses from the ionospheric *D* region: Numerical model,” *J. Geophys. Res. Sp. Phys.*, vol. 114, no. A3, p. n/a-n/a, Mar. 2009.
- [169] A. R. Jacobson, R. Holzworth, E. Lay, M. Heavner, and D. A. Smith, “Low-frequency ionospheric sounding with Narrow Bipolar Event lightning radio emissions: regular variabilities and solar-X-ray responses,” *Ann. Geophys.*, vol. 25, no. 10, pp. 2175–2184, Nov. 2007.
- [170] R. K. Said, “Accurate and Efficient Long-Range Lightning Geo-Location Using a VLF Radio Atmospheric Waveform Bank | Stanford VLF Group,” Stanford University, 2009.



- [171] M. L. V. Pitteway, "The Numerical Calculation of Wave-Fields, Reflexion Coefficients and Polarizations for Long Radio Waves in the Lower Ionosphere. I.," *Philos. Trans. R. Soc. London A Math. Phys. Eng. Sci.*, vol. 257, no. 1079, 1965.
- [172] W. R. Piggott, M. L. V. Pitteway, and E. V. Thrane, "The Numerical Calculation of Wave-Fields, Reflexion Coefficients and Polarizations for Long Radio Waves in the Lower Ionosphere. II," *Philos. Trans. R. Soc. London A Math. Phys. Eng. Sci.*, vol. 257, no. 1079, 1965.
- [173] k. G. Budden, *The Waveguide Mode Theory of Wave Propagation*, Logos Pres. London: Logos Press, 1961.
- [174] K. G. Budden, *The propagation of radio waves: the theory of radio waves of low power in the ionosphere and magnetosphere*. Cambridge University Press, 1988.
- [175] R. A. Pappert and J. A. Ferguson, "VLF/LF mode conversion model calculations for air to air transmissions in the earth-ionosphere waveguide," *Radio Sci.*, vol. 21, no. 4, pp. 551–558, Jul. 1986.
- [176] I. Nagano, M. Mambo, and G. Hutatsuishi, "Numerical calculation of electromagnetic waves in an anisotropic multilayered medium," *Radio Sci.*, vol. 10, no. 6, pp. 611–617, Jun. 1975.
- [177] W. Xiang-Yang, I. Nagano, B. Zong-Ti, and T. Shimbo, "Numerical simulation of the penetration and reflection of a whistler beam incident on the lower ionosphere at very low latitude," *J. Atmos. Terr. Phys.*, vol. 58, no. 10, pp. 1143–1159, Jul. 1996.
- [178] I. Nagano, S. Yagitani, K. Miyamura, and S. Makino, "Full-wave analysis of elves created by lightning-generated electromagnetic pulses," *J. Atmos. Solar-Terrestrial Phys.*, vol. 65, no. 5, pp. 615–625, 2003.
- [179] M. Cho and M. J. Rycroft, "Computer simulation of the electric field structure and optical emission from cloud-top to the ionosphere," *J. Atmos. Solar-Terrestrial Phys.*, vol. 60, no. 7, pp. 871–888, 1998.
- [180] W. Hu and S. A. Cummer, "An FDTD Model for Low and High Altitude Lightning-Generated EM Fields," *IEEE Trans. Antennas Propag.*, vol. 54, no. 5, pp. 1513–1522, May 2006.
- [181] T. H. Thang, V. A. Rakov, Y. Baba, and V. B. Somu, "2D FDTD Simulation of LEMP Propagation Considering the Presence of Conducting Atmosphere," in *2016 Asia-Pacific International Symposium on Electromagnetic Compatibility (APEMC)*, 2016, pp. 19–21.
- [182] F. H. Heidler, M. Manhardt, and K. Stimper, "The Slow-Varying Electric Field of Negative Upward Lightning Initiated by the Peissenberg Tower, Germany," *IEEE Trans. Electromagn. Compat.*, vol. 55, no. 2, pp. 353–361, Apr. 2013.
- [183] J. C. Willett, J. C. Bailey, V. P. Idone, A. Eybert-Berard, and L. Barret, "Submicrosecond intercomparison of radiation fields and currents in triggered lightning return strokes based on the transmission-line model," *J. Geophys. Res.*, vol. 94, no. D11, p. 13275, 1989.

- [184] B. Bador, A. Bonamy, M. A. Uman, and V. A. Rakov, "Leader properties determined with triggered lightning techniques," *J. Geophys. Res. Atmos.*, vol. 103, no. 97, pp. 109–115, 1998.
- [185] M. Rubinstein, F. Rachidi, M. A. Uman, R. Thottappillil, V. A. Rakov, and C. A. Nucci, "Characterization of vertical electric fields 500 m and 30 m from triggered lightning," *J. Geophys. Res. Atmos.*, vol. 100, no. D5, pp. 8863–8872, 1995.
- [186] N. A. Dupree, R. C. Moore, and A. C. Fraser-Smith, "ELF Sferics Produced by Rocket-Triggered Lightning and Observed at Great Distances," *Am. Geophys. Union, Fall Meet. 2013, Abstr. #AE33A-0333*, 2013.
- [187] R. C. Moore, N. A. Dupree, J. T. Pilkey, D. M. Jordan, and M. A. Uman, "An analysis of ELF sferics produced by rocket-triggered lightning," in *2014 XXXIth URSI General Assembly and Scientific Symposium (URSI GASS)*, 2014, pp. 1–1.
- [188] F. L. Carvalho, M. A. Uman, D. M. Jordan, J. D. Hill, S. A. Cummer, D. A. Kotovsky, and R. C. Moore, "Triggered lightning sky waves, return stroke modeling, and ionosphere effective height," *J. Geophys. Res. Atmos.*, vol. 122, no. 6, pp. 3507–3527, Mar. 2017.
- [189] V. B. Somu, V. A. Rakov, M. A. Haddad, and S. A. Cummer, "A study of changes in apparent ionospheric reflection height within individual lightning flashes," *J. Atmos. Solar-Terrestrial Phys.*, vol. 136, pp. 66–79, 2015.
- [190] M. Azadifar, D. Li, F. Rachidi, M. Rubinstein, G. Diendorfer, W. Schulz, V. A. Rakov, M. Paolone, and D. Pavanella, "Analysis of Lightning-Ionosphere Interaction Using Simultaneous Records of Source Current and 380-km Distant Electric Field," *J. Atmos. Solar-Terrestrial Phys.*, 2017.
- [191] M. Azadifar, D. Li, M. Rubinstein, and F. Rachidi, "A Semi-Analytical Simplified Approach to Compute Lightning Radiated Electric Fields at Long Distances Taking into Account Ionospheric Reflection," in *32nd URSI GASS, Montreal*, 2017.
- [192] A. P. Nickolaenko and M. Hayakawa, *Resonances in the earth-ionosphere cavity*. Kluwer Academic Publishers, 2002.
- [193] A. Shoory, F. Vega, P. Yutthagowith, F. Rachidi, M. Rubinstein, Y. Baba, V. A. Rakov, K. Sheshyekani, and A. Ametani, "On the Mechanism of Current Pulse Propagation Along Conical Structures: Application to Tall Towers Struck by Lightning," *IEEE Trans. Electromagn. Compat.*, vol. 54, no. 2, pp. 332–342, Apr. 2012.
- [194] M. A. Haddad, V. A. Rakov, and S. A. Cummer, "New measurements of lightning electric fields in Florida: Waveform characteristics, interaction with the ionosphere, and peak current estimates," *J. Geophys. Res. Atmos.*, vol. 117, no. D10, May 2012.
- [195] X.-M. Shao, E. H. Lay, and A. R. Jacobson, "Reduction of electron density in the night-time lower ionosphere in response to a thunderstorm," *Nat. Geosci.*, vol. 6, pp. 29–33, Dec. 2012.

- [196] Z. Cheng, S. A. Cummer, H.-T. Su, and R.-R. Hsu, "Broadband very low frequency measurement of D region ionospheric perturbations caused by lightning electromagnetic pulses," *J. Geophys. Res. Sp. Phys.*, vol. 112, no. A6, Jun. 2007.
- [197] Y. N. Taranenkov, U. S. Inan, and T. F. Bell, "Interaction with the lower ionosphere of electromagnetic pulses from lightning: Heating, attachment, and ionization," *Geophys. Res. Lett.*, vol. 20, no. 15, pp. 1539–1542, Aug. 1993.
- [198] J.-P. Béranger, "FDTD computation of vlf-lf propagation in the Earth-ionosphere waveguide," *Ann. Des Télécommunications*, vol. 57, no. 11–12, pp. 1059–1090.
- [199] M. ThÈvenot, J.-P. BÈrenger, T. MonediÈre, and F. Jecko, "A FDTD scheme for the computation of VLF-LF propagation in the anisotropic earth-ionosphere waveguide," *Ann. Des Télécommunications*, vol. 54, no. 5–6, pp. 297–310.
- [200] F. Collino and P. Monk, "The Perfectly Matched Layer in Curvilinear Coordinates," *SIAM J. Sci. Comput.*, vol. 19, no. 6, pp. 2061–2090, Nov. 1998.
- [201] S. D. Gedney, "An Anisotropic PML Absorbing Media for the FDTD Simulation of Fields in Lossy and Dispersive Media," *Electromagnetics*, vol. 16, no. 4, pp. 399–415, Jul. 1996.
- [202] J. R. Wait and K. P. Spies, *Characteristics of the earth-ionosphere waveguide for VLF radio waves*. US Dept. of Commerce, National Bureau of Standards: for sale by the Supt. of Doc., US Govt. Print. Off., 1964.
- [203] P. C. Y. Chang, J. G. Walker, and K. I. Hopcraft, "Ray tracing in absorbing media," *J. Quant. Spectrosc. Radiat. Transf.*, vol. 96, no. 3, pp. 327–341, 2005.
- [204] C. A. Balanis, *Antenna theory: analysis and design*, 4th ed. Wiley, 2016.
- [205] R. F. Harrington, *Time-harmonic electromagnetic fields*. IEEE Press, 2001.
- [206] M. Rubinstein and M. A. Uman, "Methods for calculating the electromagnetic fields from a known source distribution: Application to lightning," *IEEE Trans. Electromagn. Compat.*, vol. 31, no. 2, pp. 183–189, 1989.



# Curriculum Vitae

## Mohammad Azadifar

Electromagnetic Compatibility Laboratory (EMC)  
École Polytechnique Fédérale de Lausanne (EPFL)

Born in 14<sup>th</sup> Sept, 1987, Lahijan, Iran

Email: mhaazadifar@gmail.com

Tel : +41 78 963 8691

Address: Chemin de Riant-Mont 3, 1030  
Bussigny, Switzerland

### Education

---

- |           |   |
|-----------|---|
| 2013-2017 | <b>Ph.D. in Electrical Engineering</b> , <i>Swiss Federal Institute of Technology (EPFL)</i> , Switzerland.<br><b>Thesis:</b> Characteristics of Upward Flashes .   |
| 2009-2012 | <b>Master of Science in Electrical Power Engineering</b> , <i>AmirKabir University of Technology (Tehran Polytechnic)</i> , Iran.<br><b>Thesis:</b> Modeling and Analysis of Electromagnetic Susceptibility of Rectangular Cavity Loaded With PCBs by Hybrid Numerical Methods of FDFD-MoM.   |
| 2005-2009 | <b>Bachelor of Science in Electrical Engineering</b> , <i>AmirKabir University of Technology (Tehran Polytechnic)</i> , Iran.<br><b>Thesis :</b> Modeling, Analysis and Measurement of Shielding Effectiveness of an Enclosure with Finite Wall Thickness against Oblique Plane Wave by GMMOM (Generalized Modal Method of Moment). |

### Professional Experience

---

- |           |   |
|-----------|---|
| 2013-2017 | <b>Doctoral assistant</b> , Electromagnetic Compatibility Laboratory (EMC),<br>Lausanne, Switzerland. |
| 2012-2013 | <b>Research Assistant</b> , K. N. Toosi University, Iran.   |
-

## Research Interests

---

- Electromagnetic Compatibility and Lightning.
- Computational Electromagnetic.
- Antenna and Wave Propagation

## Language Skills:

---

- Persian (Native)
- English (Fluent, IBT: 96/120)
- French (Intermediate, B1)

## Awards and Scientific Recognitions

---

|      |  |
|------|--|
| 2017 | Young Scientist Award, XXXIrd International Union of Radio Science.  |
| 2017 | Best Presentation Award, 4rd International Symposium on Winter Lightning.  |
| 2016 | Best Paper Award of IEEE Transactions on EMC.  |
| 2016 | Diploma for High Quality of Presentation and notable contribution to the field of lightning research of 33rd International Conference on Lightning Protection. |
| 2009 | Scholarship for graduate education, Amirkabir University of Technology (Tehran Polytechnic).   |

## Publications

---

### Journal Papers

---

- 1- **M. Azadifar**, D. Li, F. Rachidi, M. Rubinstein, G. Diendorfer, W. Schulz, ... & D. Pavanello, Analysis of lightning-ionosphere interaction using simultaneous records of source current and 380-km distant electric field, in Journal of Atmospheric and Solar-Terrestrial Physics, 2017.
- 2- D. Li, **M. Azadifar**, F. Rachidi, M. Rubinstein and M. Paolone et al. On Lightning Electromagnetic Field Propagation Along an Irregular Terrain, in IEEE Transactions on Electromagnetic Compatibility, vol. 58, num. 1, p. 161-171, 2016.

- 3- D. Li, **M. Azadifar**, F. Rachidi, M. Rubinstein and G. Diendorfer et al. Analysis of lightning electromagnetic field propagation in mountainous terrain and its effects on ToA-based lightning location systems, in *Journal of Geophysical Research: Atmospheres*, vol. 121, num. 2, p. 895-911, 2016.
- 4- **M. Azadifar**, F. Rachidi, M. Rubinstein, V. A. Rakov and M. Paolone et al. Bipolar Lightning Flashes Observed at the S antis Tower: Do We Need to Modify the Traditional Classification?, in *Journal of Geophysical Research: Atmospheres*, vol. 121, 2016.
- 5- **M. Azadifar**, F. Rachidi, M. Rubinstein, V. A. Rakov and M. Paolone et al. Fast Initial Continuous Current Pulses vs Return Stroke Pulses in Tower-initiated Lightning, in *Journal of Geophysical Research: Atmospheres*, vol. 121, 2016.
- 6- **M. Azadifar**, F. Rachidi, M. Rubinstein, M. Paolone and G. Diendorfer et al., Evaluation of the performance characteristics of the European Lightning Detection Network EUCLID in the Alps region for upward negative flashes using direct measurements at the instrumented S antis Tower, in *Journal of Geophysical Research: Atmospheres*, vol. 121, num. 2, p. 595-606, 2016.
- 7- **M. Azadifar**, P. Dehkhoda, S. H. H. Sadeghi, R. Moini, A Hybrid FDFD-MoM Technique for Susceptibility Evaluation of a Transmission Line Inside a Perforated Enclosure, *Electromagnetic Compatibility, IEEE Transactions on* , vol.PP, no.99, pp.1,6, Jul. 2014.
- 8- P. Dehkhoda, A. Tavakoli, **M. Azadifar**, Shielding Effectiveness of an Enclosure With Finite Wall Thickness and Perforated Opposing Walls at Oblique Incidence and Arbitrary Polarization by GMMoM, *Electromagnetic Compatibility, IEEE Transactions on* , vol.54, no.4, pp.792,805, Aug. 2012.

## Conference Proceedings

---

- 1- **M. Azadifar**, Dongshuai Li, M. Rubinstein and F. Rachidi. A Semi-Analytical Approach to Compute Lightning Radiated Electric Fields at Long Distances Taking into Account Ionospheric Reflection. 32nd URSI General Assembly, Canada, 2017.
- 2- A. Mostajabi, **M. Azadifar**, F. Rachidi, M. Rubinstein, G. Diendorfer et al. Simultaneous Records of Current and 380-km Distant Electric Field of a Bipolar Lightning Flash. XIV International Symposium on Lightning Protection SIPDA, Brazil, 2017.
- 3- R. Daher, **M. Azadifar**, A. Smorgonsky, J. Zuber, M. Rubinstein, G. Diendorfer, F. Rachidi. A study of Upward Flashes Initiated at the S antis Tower. Asia Electromagnetic International Symposium ASIAEM, India, 2017.
- 4- **M. Azadifar**, G. Diendorfer, M. Paolone, D. Pavanello, F. Rachidi, V. A. Rakov, ... & W. Schulz. A Large Bipolar Event Recorded at the S antis Tower. In 4th International Symposium on Winter Lightning, Japan, 2017.

- 
- 5- **M. Azadifar**, F. Rachidi, M. Rubinstein, G. Diendorfer, H. Pichler, W. Schulz. Simultaneous Currents and Electric Fields at Two Distances Associated with an Upward Flash to the Säntis Tower, In 10th Asia-Pacific International Conference on Lightning, Thailand, 2017.
- 6- **M. Azadifar**, F. Rachidi, M. Rubinstein, V. A. Rakov and M. Paolone et al. Bipolar Lightning Flashes Observed at the Säntis Tower. 33rd International Conference on Lightning Protection (ICLP), Estoril, Portugal, 2016.
- 7- M. Stojilovic, **M. Azadifar**, M. Rubinstein and F. Rachidi. Lightning Location Systems and Interstroke Intervals: Effects of Imperfect Detection Efficiency. 33rd International Conference on Lightning Protection (ICLP), Estoril, Portugal, 2016.
- 8- **M. Azadifar**, M. Lagasio, E. Fiori, F. Rachidi and M. Rubinstein et al. Occurrence of Downward and Upward Flashes at the Säntis Tower: Relationship with -10 degrees C Temperature Altitude. European Electromagnetics International Symposium EUROEM 2016, London, UK, 2016.
- 9- **M. Azadifar**, D. Li, M. Paolone, D. Pavanello and F. Rachidi et al. An Update on the Measurements of Lightning Currents and Electromagnetic Fields Associated with Flashes to the Säntis Tower in Switzerland. International Colloquium on Lightning and Power Systems, Bologna, Italy, 2016.
- 10- **M. Azadifar**, D. Li, F. Rachidi, M. Rubinstein and G. Diendorfer et al. Simultaneous Current and Distant Electric Field Waveforms from Upward Lightning: Effect of Ionospheric Reflection. 24th International Lightning Detection Conference (ILDC), San Diego, California, 2016.
- 11- **M. Azadifar**, F. Rachidi, M. Rubinstein, M. Paolone and D. Pavanello. An Update on Experimental Data Obtained at the Säntis Tower. IEEE 15th International Conference on Environment and Electrical Engineering (EEEIC), Rome, 2015.
- 12- **M. Azadifar**, F. Rachidi, M. Rubinstein, M. Paolone and V. A. Rakov et al. Characteristics of Electric Fields of Upward Negative Stepped Leaders. XIII International Symposium on Lightning Protection (SIPDA), Balneario Camboriu, Brazil, 2015.
- 13- **M. Azadifar**, M. Paolone, D. Pavanello, F. Rachidi and V. Rakov et al. An Update on the Characteristics of Positive Flashes Recorded on the Säntis Tower. 32nd International Conference on Lightning Protection (ICLP), Shanghai, China, 2014.
- 14- **M. Azadifar**, M. Rubinstein, F. Rachidi, M. Paolone and D. Pavanello. On the Influence of Measuring Instruments Bandwidth Limitations on the Inferred Statistical Parameters for Lightning Currents. 31st URSI General Assembly and Scientific Symposium, Beijing, China, 2014.

---

15- **M. Azadifar**, M. Stojilovic, M. Rubinstein and F. Rachidi. Influence of LLS Detection Efficiency on the Measured Distribution of Interstroke Intervals. American Electromagnetics International Symposium (AMEREM), Albuquerque, New Mexico, USA, 2014.

16- **M. Azadifar**, M. Paolone, D. Pavanello, F. Rachidi and C. Romero et al. An Update on the Instrumentation of the Säntis Tower in Switzerland for Lightning Current Measurements and Obtained Results. CIGRE International Colloquium on Lightning and Power Systems, Lyon, France, 2014.

17- **M. Azadifar**, P. Dehkhoda, S.H.H. Sadeghi, R. Moini, "Shielding effectiveness evaluation of a loaded perforated enclosure by hybrid FDFD-MoM," Electromagnetic Compatibility (EMC), 2013 IEEE International Symposium on , vol., no., pp.167,170, 5-9 Aug. 2013.



